

UNIVERSITY OF OKLAHOMA

GRADUATE COLLEGE

INVESTIGATION OF POLARIMETRIC MEASUREMENTS OF RAINFALL AT
CLOSE AND DISTANT RANGES

A DISSERTATION

SUBMITTED TO THE GRADUATE FACULTY

in partial fulfillment of the requirements for the

degree of

Doctor of Philosophy

By

SCOTT EDWARD GIANGRANDE

Norman, Oklahoma

2007

UMI Number: 3291249



UMI Microform 3291249

Copyright 2008 by ProQuest Information and Learning Company.
All rights reserved. This microform edition is protected against
unauthorized copying under Title 17, United States Code.

ProQuest Information and Learning Company
300 North Zeeb Road
P.O. Box 1346
Ann Arbor, MI 48106-1346

INVESTIGATION OF POLARIMETRIC MEASUREMENTS OF RAINFALL
AT CLOSE AND DISTANT RANGES

A DISSERTATION APPROVED FOR THE
SCHOOL OF METEOROLOGY

BY

Dr. Michael Biggerstaff

Dr. Alexander Ryzhkov

Dr. Jerry Straka

Dr. Guifu Zhang

Dr. Mark Yeary

© Copyright by SCOTT EDWARD GIANGRANDE 2007
All Rights Reserved.

ACKNOWLEDGEMENTS

I would like to extend my sincerest thanks to the numerous individuals who have helped me complete this work. To begin, this work would not have been possible without the guidance of my primary research advisor, Dr. Alexander Ryzhkov. His leadership and patience were instrumental throughout this process. I would also like to extend my gratitude to the other members of my committee: Drs. Michael Biggerstaff (Co-Chair and primary OU School of Meteorology advisor), Guifu Zhang, Jerry Straka, and Mark Yeary. The reviews performed by these individuals strengthened this work.

I also thank the members of the Radar Research and Development Division (RRDD) at the National Severe Storms Laboratory (NSSL), which includes Drs. Douglas Forsyth, Dusan Zrnic, Dick Doviak, Allen Zahrai, Terry Schuur, Pam Heinselman, Valery Melnikov, Sebastian Torres, Pengfei Zhang and Svetlana Bachmann. The above individuals contributed in some manner to the theoretical background, the securing of funding and the collection of the data for this study. This work would also not have been possible without the support of current and former RRDD members including John Krause, Dan Suppes, Mark Askelson, Christopher Godfrey, Paul Schlatter, Darren Clabo, Mi-Young Kang, Roel Linszen, Hyang-Suk Park and Matt Kumjian.

The support of the numerous employees at the north campus NSSL building and the new NSSL/National Weather Center is also acknowledged. These individuals

offered computer and programming assistance, maintained the radar system(s) and provided other necessary services that often go without praise. In particular, Mike Baldwin and Kevin Manross were instrumental in the gathering of RUC model output for use in chapter 2 this work. I also thank J.J. Gourley and Kevin Scharfenberg for thorough review of chapters 2 and 3.

Additional appreciation is extended for the financial support provided by The Cooperative Institute for Mesoscale Meteorological Studies (CIMMS) and the assistance of the CIMMS office staff and management. Not to be overlooked, the office staff at the OU School of Meteorology was also very helpful throughout this process. I also wish to thank the Oklahoma Climatological Survey (OCS) for providing the high-quality gage data utilized in this study. Special thanks in particular to Andrew Reader, Chris Fiebrich and Mark Shafer at the OCS.

Finally, to my family, friends and past/current professors: Without your support, this work would not have been possible.

TABLE OF CONTENTS

| | |
|---|------|
| LIST OF TABLES | viii |
| LIST OF FIGURES | ix |
| ABSTRACT | xx |
| | |
| 1. INTRODUCTION | 1 |
| 1.1 Overview of Polarimetric Radar Measurements | 5 |
| 1.1.1 Reflectivity Factor, Z | 5 |
| 1.1.2 Differential Reflectivity, Z_{DR} | 7 |
| 1.1.3 Correlation Coefficient, ρ_{HV} | 9 |
| 1.1.4 Differential Phase, Φ_{DP} , and Specific Differential Phase, K_{DP} | 10 |
| 1.1.5 Radar Measurands for Canted Hydrometeors | 11 |
| 1.2 Processing Polarimetric Data | 15 |
| 1.3 Review of Radar Rainfall Estimation Techniques | 17 |
| 1.3.1 Conventional Z-R Relations | 18 |
| 1.3.2 Polarimetric Rainfall Estimation | 20 |
| 1.4 Review of Polarimetric Echo Classification | 22 |
| 1.4.1 Fuzzy Logic Classification | 22 |
| 1.4.2 Class Designation | 24 |
| 1.5 Outline of the Study | 26 |
| | |
| 2. AUTOMATIC DESIGNATION OF THE MELTING LAYER AND POLARIMETRIC ECHO CLASSIFICATION | 28 |
| 2.1 Description of the MLDA | 30 |
| 2.1.1 Input Radar Data | 31 |
| 2.1.2 Identification of Melting Snow | 32 |
| 2.1.3 Designation of Melting Layer Boundaries | 34 |
| 2.1.4 Justification of the Thresholds in the MLDA Procedure | 35 |
| 2.1.5 Additional Considerations | 37 |
| 2.2 Validation of Melting Layer Designation | 38 |
| 2.2.1 Comparison with Radiosonde Observations | 39 |
| 2.2.2 Comparison with RUC Model Analysis Output | 39 |
| 2.2.3 Temporal Dependencies | 41 |
| 2.3 Discussion | 41 |
| 2.4 Summary | 43 |
| | |
| 3. ESTIMATION OF RAINFALL BASED ON THE RESULTS OF | 46 |

| | |
|--|-----|
| POLARIMETRIC ECHO CLASSIFICATION | |
| 3.1 Radar Dataset, Preprocessing and Echo Classification | 49 |
| 3.2 Rainfall Estimates Associated with Different Echo Types | 54 |
| 3.2.1 Rainfall Relation Comparisons in Rain | 55 |
| 3.2.2 Rainfall Relation Comparisons in Wet Snow | 58 |
| 3.2.3 Conventional Relation Performance Above the Melting Layer | 60 |
| 3.3 Radar Algorithms and Their Performance as a Function of Range | 62 |
| 3.4 Summary | 67 |
| 4. POLARIMETRIC MEASUREMENTS AT MULTIPLE ELEVATION ANGLES | 70 |
| 4.1 Comparisons of Multiple Elevation Angles | 74 |
| 4.2 The Use of Low or Blocked Elevation Angles for Rainfall Estimation | 77 |
| 4.3 Partial Beam Blockage Detection and Correction | 81 |
| 4.3.1 Z_{DR} Observations in the Presence/Absence of Partial Beam Blockage | 84 |
| 4.3.2 Methodology for Z_{DR} Calibration in the Presence of a Partial Beam Blockage | 90 |
| 4.3.3 Z Calibration in the Presence of a Partial Beam Blockage | 93 |
| 4.3.4 Summary of Partial Beam Blockage Detection and Correction | 101 |
| 4.4 Recommendations In The Presence of a Partial Beam Blockage | 104 |
| 5. MODELING OF THE MELTING LAYER: POSSIBILITIES FOR POLARIMETRIC VPR CORRECTION | 107 |
| 5.1 Polarimetric Melting Layer Signatures | 109 |
| 5.1.1 Data and Analysis Methods | 110 |
| 5.1.2 Polarimetric Bright Band Parameters | 111 |
| 5.2 Model of the Melting Layer | 114 |
| 5.2.1 Thermodynamic Background of the Model | 115 |
| 5.2.2 Snowflake/Drop Size Distribution | 120 |
| 5.2.3 Shape and Dielectric Properties of Melting Snowflakes | 121 |
| 5.2.4 Comparisons of Model Profiles with Observed Melting Layer Signatures | 124 |
| 5.2.5 Improvements to the Melting Layer Model and Polarimetric VPR Implications | 131 |
| 5.3 Summary and Implications for Rainfall Estimation | 137 |
| BIBLIOGRAPHY | 140 |
| APPENDIX A: TABLES | 158 |
| APPENDIX B: FIGURES | 163 |

LIST OF TABLES

| | |
|---|-----|
| Table 1: KOUN data listing and available verification for melting layer designation..... | 158 |
| Table 2: Listing of KOUN events and the hours of observation..... | 159 |
| Table 3: The results of echo classification for the Oklahoma Mesonet dataset. Percentages exclude nonecho/null classifications. $\langle R \rangle$ and $\langle Z_{DR} \rangle$ are mean values of rainfall rate (Z capped at 53 dBZ) and differential reflectivity over gage locations for the corresponding echo class. The standard NEXRAD $R(Z)$ relation (23) is used to estimate the relative contribution to the total radar-estimated rain depth in the far right column..... | 160 |
| Table 4: Listing of KOUN events and the hours of observation in the subset for which 0.0° and 0.5° rainfall results are examined..... | 161 |
| Table 5: Values of ρ_{HV} and Z_{DR} for different aggregation intensities defined by factor C . Λ_r and Λ_s are the slopes of the bi-exponential distribution for rain and snow portions, respectively..... | 162 |

LIST OF FIGURES

- Fig. 1: Geometry of scattering as adapted from Ryzhkov (2001). Shaded area represents polarization plane. Direction N denotes orientation of the symmetry axis of the particle, k represents the direction of wave propagation, z is the true vertical, α denotes the canting angle and ψ is the orientation angle with respect to the direction of propagation k163
- Fig. 2: Trapezoidal membership function shape164
- Fig. 3: Illustration of radar beam interaction with the melting layer. Solid curve represents the mean beam height of the 0.5° elevation angle tilt with a 1° beam width (bounded by dashed curves).165
- Fig. 4: KOUN measurement PPI images of Z , Z_{DR} , and ρ_{hv} on May 13, 2005 at the 4.5° elevation angle.166
- Fig. 5: An example of average slant range dependences of Z , Z_{DR} , and ρ_{hv} at the 4.5° elevation angle for the case illustrated in Fig. 3. Z measurements are displayed with thin solid lines, Z_{DR} and ρ_{hv} are displayed with thick solid lines. MLDA ρ_{hv} thresholds are depicted with dashed lines.167

Fig. 6: (A) Example of ML points mapped on the height-azimuth plane. The 80% (ML top) and 20% (ML bottom) height contours are overlaid on the image in solid lines. (B) Corresponding surface Oklahoma Mesonet temperature (Celsius) and KOUN radar reflectivity factor from the 0.5° elevation angle. Highest surface temperatures and higher ML tops are located in directions ahead of the convective line.....168

Fig. 7: Normalized histograms of KOUN radar measurements of (A) ρ_{hv} , (B) Z, and (C) Z_{DR} for wet snow (dotted line), dry snow (thin solid line) and light-to-moderate rain (thick solid line)(adapted from Park et al. (2007), 29 hours of observation). Vertical dashed lines indicate thresholds used in the MLDA.....169

Fig. 8: Intrinsic model (thick solid line) and smoothed (dotted lines) vertical profiles of ρ_{hv} demonstrating the impacts of beam broadening and radial smoothing on polarimetric melting layer signatures at elevation angles 4.5° and 10.0°. Environmental melting level height is approximately 3.7 km (thin horizontal line).....170

Fig. 9: Scatterplot of ML top heights obtained from the MLDA versus radiosonde-derived 0°C observations.....171

Fig. 10: As in Fig. 9, but utilizing RUC model analysis output temperatures for validation. Hours with questionable RUC or MLDA performance for convective events are noted with asterisks.....172

Fig. 11: Histogram of the temperature of the ML top retrieved from the radar as revealed by RUC model analysis output.....173

Fig. 12: As in Fig. 11, but for ML bottom heights.....174

Fig. 13: Histogram of the ML thickness retrieved from the MLDA.....175

Fig. 14: Temporal dependencies of the height of the ML top estimated from the radar (crosses), RUC model output (diamonds) and soundings ('S' symbol, bottom of the symbol) for 4 different days of observation.....176

Fig. 15: A map of the observation network in central Oklahoma.....177

Fig. 16: Histogram of ranges associated with different classes of hydrometeors observed at the 0.5° elevation.....178

Fig. 17: Hourly radar-gage rainfall accumulation scatterplots for rain type I over Oklahoma Mesonet gage locations: (a) R(Z), (b) R(K_{DP}), (c) R(Z,Z_{DR}).....179

Fig. 18: Hourly radar-gage rainfall accumulation scatterplots for rain type I over ARS network gage locations: (a) $R(Z)$, (b) $R(K_{DP})$, (c) $R(Z, Z_{DR})$180

Fig. 19: As in Fig. 17, but for rain type II over Oklahoma Mesonet gages.....181

Fig. 20: As in Fig. 18, but for rain type II over ARS network gages.....182

Fig. 21: An example of hourly rain accumulation maps obtained using an (a) $R(K_{DP})$ relation and (b) $R(Z)$ relation.....183

Fig. 22: As in Fig. 17, but for Wet Snow over Oklahoma Mesonet gages: (a) $R(Z)$, (b) $R(K_{DP})$, (c) $R(Z, Z_{DR})$, and (d) $0.6 * R(Z)$ that minimizes bias.....184

Fig. 23: Vertical cross-section of $R(Z)$, Z_{DR} , $R(K_{DP})$ and ρ_{HV} through a thunderstorm illustrating loose connection between $R(K_{DP})$ and Z_{DR} aloft and rain at the surface.....185

Fig. 24: Performance of the conventional $R(Z)$ algorithm if Dry Snow and Crystals are identified in the radar resolution volume; (a) All distances and heights of the radar volume are included, (b) the radar volume is at or below the freezing level, (c) the radar volume is above the freezing level.....186

Fig. 25: Performance of the conventional R(Z) algorithm if the radar volume is filled with graupel or hail and is located above the freezing level.....187

Fig. 26: Mean bias (top) and RMS error (bottom) of different radar estimates as a function of range (43 rain events, 179 hours of observation).....188

Fig. 27: As in Fig. 26, but for stratiform events with an absence of convective signatures (9 rain events, 26 hours of observation).....189

Fig. 28: Polarimetric variables for various elevation angles measured at the 110° azimuth for the 11/18/04 case. Tick marks in Z (Z_{DR}) plots represent 1 dB (0.1 dB). ρ_{HV} is plotted with 0.01 tick marks. Tick marks in Φ_{HV} profiles are in 1° increments190

Fig. 29: Illustration of the beam blockage cause by the surface. θ_0 is the elevation angle at the middle of the beam (here drawn as 0.0°), θ_b is the elevation angle for the top of the blocking obstacle, h is the height of the radar tower, a_e is the effective radius of the earth, h_e is the equivalent mean beam height above the surface.....191

Fig 30: Hourly radar-gage rainfall accumulation scatterplots over ARS (cross-hairs) and Oklahoma Mesonet (stars) network gage locations for the R(Z) relation at the 0.0° tilt and the 0.5° tilt.....192

Fig. 31: As in Fig. 30, but for $R(K_{DP})$193

Fig. 32: Image of the Cimarron radar taken during the Fall of 2002. Top left corner image shows the radar after an ice storm in February 2003.....194

Fig. 33: Mean $Z-Z_{DR}$ dependencies obtained from the radar for different rain regimes and from the disdrometer using different assumptions about raindrop shapes. “Radar” curves are derived from the KOUN WSR-88D measurements. “Disd” curves are based on the 2D video disdrometer statistics. “LD” and “SD” curves correspond to rain regimes dominated by large and small drops, respectively. Simulations from disdrometer measurements are made using assumptions about drop shape following Beard and Chuang (1987) measurements, Brandes et al. (2002), and Bringi et al. (2003).....195

Fig. 34: (a) Azimuthal dependencies of Z_{DR} measured by the Cimarron radar at the 0.5° elevation angle for 5 rain events. (b) Mean azimuthal dependence for these events. Error bars indicate the range of Z_{DR} variations for all cases.....196

Fig. 35: Same as Fig. 34, but for 7 snow events.....197

Fig. 36: (a) Difference between the mean azimuthal dependencies of Z_{DR} at the 1.5° and 0.5° elevation angles for 5 events. (b) Mean azimuthal dependence for all 5 events. Error bars indicate the range of variation in the difference field.....198

Fig. 37: Same as Fig. 36, but for 4 events observed by the KOUN radar.....199

Fig. 38: Location of radars and the ARS network rain gauges in central Oklahoma.....200

Fig. 39: Bias of Z measured by the Cimarron radar as a function of azimuth for 5 rain events. Diamonds and dashed lines indicate results of direct comparisons of Z from the Cimarron and WSR-88D data. The solid curves represent results of consistency-based retrievals.....201

Fig. 40: Relative bias of Z as determined from the difference of $R(K_{DP})$ and $R(Z)$ rainrates projected into Z as a function of azimuth for 4 rain events.....202

Fig. 41: Mean azimuthal dependence of the Z bias for the events featured in Fig. 40.....203

Fig. 42: Diagram of polarimetric measurement profiles and several parameters that are extracted from these profiles.....204

Fig. 43: Scatterplot of the Z in snow versus the value of Z in the rain beneath the melting layer as revealed from analysis of 30 typical profiles of polarimetric radar variables in 10 different storms with pronounced bright band observed with the NSSL's S-band polarimetric radar.....205

Fig. 44: Scatterplot of Z in rain versus the peak value of Z within the melting layer as in Fig. 43.....206

Fig. 45: Scatterplot of Z_{DR} in snow versus Z_{DR} in rain beneath the melting layer as in Fig. 43.....207

Fig. 46: As in Fig. 43, the scatterplot of the Z_{DR} in rain versus the peak in Z_{DR} within the melting layer.....208

Fig. 47: As in Fig. 43, the scatterplot of the Z_{DR} peak within the melting layer versus the minimum in ρ_{HV}209

Fig. 48: As in Fig. 43, the scatterplot of the Z peak within the melting layer versus the minimum in ρ_{HV}210

Fig. 49: As in Fig. 43, the scatterplot of the Z peak within the melting layer versus the value of Z_{DR} in rain beneath.....211

Fig. 50: As in Fig. 43, the scatterplot of the enhancement in Z within the melting layer versus the Z_{DR} in the rain beneath.....212

Fig. 51: As in Fig. 43, the scatterplot of melting layer thickness versus the value of Z in rain.....213

Fig. 52: As in Fig. 43, scatterplot of melting layer thickness versus the height of the melting layer top (based on ρ_{HV} observations).....214

Fig. 53: Terminal velocity of melting snowflakes as a function of melted water diameter for six values of mass water fraction: 0, 20, 40, 60, 80, and 100% in the case of unrimed and heavily rimed snow.....215

Fig. 54: Maximal diameter of raindrops versus fall distances from the top of the melting layer. Rainrate R is set at 5 mm hr^{-1}216

Fig. 55: Size distributions of raindrops and partially melted snowflakes at the top of the melting layer (upper curve) and at the levels 200, 400, 600, and 800 m below the top.....217

Fig. 56: Terminal velocities of raindrops and partially melted snowflakes at the top of the melting layer (bottom curve) and at the levels 200, 400, 600, and 800 m below the top. Rainrate R is set at 5 mm hr^{-1}218

Fig. 57: Model profiles of Z_H through the melting layer. Z_H based on dielectric Model A (water with snow inclusions) is depicted with a solid line, Model B (snow with water inclusions) is depicted with a dotted line, and Model C (mixture of Models A,B) is depicted with a dashed lines. Rain rate is 3 mm hr^{-1}219

Fig. 58: As in Fig. 57, but for model profiles of Z_{DR} through the melting layer.....220

Fig. 59: As in Fig. 57, but for model profiles of ρ_{HV} through the melting layer.....221

Fig. 60: As in Fig. 57, model profiles of Z_H for heavily rimed particles entering the melting layer.....222

Fig. 61: As in Fig. 57, model profiles of Z_{DR} for heavily rimed particles entering the melting layer.....223

Fig. 62: As in Fig. 57, model profiles of ρ_{HV} for heavily rimed particles entering the melting layer.....224

Fig. 63: Volume fraction of water dependence on melting particle diameter. The maximal size of raindrops D_{rs} is 6 mm. Solid curve is the dependence that matches well with the thermodynamic model in Eq. (90). Dashed lines are for increasing aggregation factors as in Eq. (107).225

Fig. 64: Resonance factor $D_m |\epsilon_m|^{1/2} / \lambda$ dependence on melting particle diameter. Solid curve corresponds to dielectric constants determined using the output of the thermodynamic model without aggregation. Dashed lines are for increasing aggregation factors.....226

Fig. 65: Modification of the bi-exponential particle size distribution via aggregation.....227

ABSTRACT

As part of continuous modernization of operational weather radar systems, several government agencies have explored adding polarimetric capability to existing networks. Polarimetric measurements of rain have been previously shown robust with respect to drop size distribution variations, hail contamination, and offer improved echo classification capabilities. Other advantages of polarimetric measurements of rain include an immunity to radar miscalibration, attenuation in rain and partial beam blockage.

Whereas the existing literature overwhelmingly recommends polarimetric methods for weather radar applications, the majority of dual-polarization studies have been conducted on datasets collected at relatively close distance to the radar. However, it is well-known that the quality of radar measurements and rainfall estimates degrades with distance due to factors including beam broadening, the effect of Earth curvature and the overshooting of precipitation.

This study is motivated by the lack of validation for polarimetric rainfall applications with respect to coverage and accuracy demands of the operational weather community. To address these concerns, the quality of polarimetric measurements and rainfall estimation is investigated over a broad range of distances. Several new methods to identify regions of known radar bias and improve radar rainfall measurements in operations are provided.

1. INTRODUCTION

The importance of accurate precipitation estimation is well known. Real-time rainfall observations impact weather forecasting operations and aid in the initialization of broad-scale hydrologic models. Since the earliest applications of weather radar, researchers have sought precipitation measurements from widespread radar networks. Radar rainfall estimation techniques provide rapid observations and extensive coverage which distinguish these methods from the limitations of surface-based gage data.

Despite known advantages, the reliability of radar-based rainfall measurements remains a fundamental concern. The pitfalls of radar rainfall methods that utilize reflectivity factor Z are well documented (e.g., Wilson and Brandes 1979; Fabry et al. 1992; Doviak and Zrnic 1993; Ryzhkov and Zrnic 1995, Smith et al. 1996; Fulton et al. 1998). Modest calibration errors may produce severe deficiencies in the accuracy of radar products such as rainfall estimation and hydrometeor classification (e.g., Ryzhkov et al., 2005a). Blockage and attenuation of the radar beam further exacerbates the problem of accurate precipitation measurements from radar.

Domestic and foreign meteorological agencies mandate accurate radar rainfall estimation over large coverage areas to ensure the safety of life and property. In particular, the United States National Weather Service (NWS) requires estimates of rainfall at ranges up to 230 km from the radar (e.g., WSR-88D System Specification, Section 3.7.2.2.1). In addition to the aforementioned deficiencies in reflectivity

factor-based rainfall measurements, the quality of radar rainfall estimates degrade with distance as a result of beam broadening, the effect of Earth curvature and the overshooting of precipitation (e.g., Doviak and Zrnic 1993). Radar rainfall estimation at longer distances is further complicated by radar resolution volumes that are more likely filled with mixed-phase or frozen hydrometeors, which may be loosely related to the rainfall reaching the surface.

Several studies discuss the quality of conventional (single polarization) radar measurements of rainfall to far distances and over complex terrain (e.g., Koistinen 1991, Fabry et al. 1992, Andrieu and Creutin 1995, Smith et al. 1996, Andrieu et al. 1997, Kitchen 1997, Seo et al. 2000, Dinku et al. 2002, Kucera et al. 2004, Langston and Zhang 2004, Krajewski and Ciach 2005). These studies indicate that accurate radar rainfall estimation to longer distance is challenging and necessitates the concurrent application of several techniques to overcome the fundamental limitations of conventional radar systems. Emphasis is placed on reducing the errors in radar rainfall estimates associated with drop size distribution (DSD) variability, melting layer and hail contamination, and radar beam blockage from larger-scale topographical features. Recommended conventional methodologies to improve radar rainfall estimation include the vertical profiling of the radar reflectivity factor (VPR), ‘mean-field’ gage bias adjustments, and the use of digital terrain models to determine the blockage of the radar beam. Validation of these techniques is limited as it requires long-term comparisons between radar rainfall estimates and sparse surface rain gage network accumulations.

The above techniques to improve conventional radar rainfall estimates to long distance remain the subject of ongoing research and are not without limitation. For example, VPR techniques are sensitive to precipitation variability including changes in storm type (e.g., stratiform versus convective) and temporal/spatial changes in the VPR (Zawadzki 2006). Similarly, partial beam blockage (PBB) correction contingent on digital terrain models is questionable for significant blockages ($> 60\%$ beam occultation), as the degree of beam blockage depends on atmospheric refractive conditions (e.g., Bech et al. 2003). In addition to the large-scale terrain features captured by terrain models, unresolved smaller-scale anthropogenic structures (e.g., towers, buildings) and nearby trees cause additional occultation of the radar beam.

Polarization diversity promises to mitigate conventional radar shortcomings for rainfall estimation as numerous theoretical and validation studies show (e.g., Ryzhkov and Zrnich 1996; May et al. 1999; Bringi and Chandrasekar 2001; Brandes et al. 2002; Matrosov et al. 2005; Ryzhkov et al. 2005a). Polarimetric rainfall relations are more robust with respect to DSD variations and the presence of hail than conventional relations. Measurements of specific differential phase K_{DP} , which is immune to radar miscalibration, attenuation, and PBB, benefit precipitation estimation by providing methods to correct Z bias or through the direct estimation of rainfall using $R(K_{DP})$ relations (e.g., Zrnich and Ryzhkov 1996). In addition, polarimetric radar is uniquely suited for discriminating between different classes of meteorological and nonmeteorological echo (e.g., Zrnich and Ryzhkov 1999).

As part of continuous modernization of the nationwide network of the Weather Surveillance Radar- 1988 Doppler (NEXRAD WSR-88D) weather radars,

the NWS has decided to add polarimetric capability to existing operational radars. The operational proof-of-concept was held on the National Severe Storms Laboratory's (herein, NSSL) prototype polarimetric KOUN WSR-88D radar in Norman, Oklahoma (herein, KOUN). A primary selling point for the nationwide deployment of polarimetric weather radar was the demonstration of enhanced radar rainfall estimation capabilities within existing radar coverage areas.

Although the strengths of polarimetric measurements have been previously established and successfully sold to government agencies including the NWS, the majority of dual-polarization studies (rainfall or otherwise) have been conducted on data collected during warm season precipitation (characterized by strong or hail producing storms and high freezing levels) and at distances within 100 km of the radar. Because of the stringent NWS range requirements for the delivery of operational radar rainfall products to ranges of 230 km, a primary motivation of this study is to investigate and verify the quality of polarimetric rainfall estimation over a broad range of distances. The study is further motivated to improve upon the quality of existing polarimetric methods for operational rainfall estimation through the exploration of new methods that further capitalize on the unique microphysical insights afforded by polarimetric radar measurements.

1.1 Overview of Polarimetric Radar and Measurements

The primary data source for this study is the KOUN dual-polarization S-band radar maintained by the NSSL. To determine the merits of polarization diversity, it is important to understand the governing measurands of radar rainfall estimation. This overview addresses four fundamental polarimetric variables measured by the KOUN radar: the reflectivity factor Z , differential reflectivity Z_{DR} , correlation coefficient $\rho_{HV}(0)$, and differential phase Φ_{DP} .

1.1.1 Reflectivity Factor, Z

Noting historical significance and relevance to forecasting applications, perhaps the most widely recognized radar quantity is reflectivity factor, Z . Reflectivity factor is proportional to the backscattering cross-section per unit volume. A generalized form of the reflectivity factor for horizontal or vertical polarizations is

$$Z_{H,V}[mm^6 / m^3] = \frac{\lambda^4}{\pi^5 |(\epsilon - 1)/(\epsilon + 2)|^2} \int \sigma_{H,V} N(D) dD, \quad (1)$$

where σ is the backscatter cross-section of individual drops at two orthogonal polarizations, λ is the radar wavelength, ϵ is the dielectric constant, and $N(D)$ is the drop size distribution (Doviak and Zrnich 1993). The backscatter cross-section in (1) may be expressed as

$$\sigma_{H,V}[mm^2] = 4\pi |f_{H,V}|^2, \quad (2)$$

with $f_{H,V}$ denoting the backscattering amplitudes of individual hydrometeors for the two orthogonal polarizations. The expression in (2) is valid for equioriented drops with an axis of rotation along the vertical.

For a Rayleigh scattering regime in which the equivalent-volume diameter of raindrops, D_e , is much smaller than the radar wavelength ($D_e \ll \lambda$, a condition suitable for most weather radar scatterers at S-band),

$$f_{H,V}[mm] = \frac{\pi^2 D_e^3}{6\lambda^2} \zeta_{H,V}, \quad (3)$$

where $\zeta_{H,V}$ is the polarizability factor

$$\zeta_{H,V} = \frac{1}{L_{H,V} + \frac{1}{\epsilon - 1}}, \quad (4)$$

with $L_{H,V}$ representing the horizontal and vertical factors depending solely on the shape of the scatterer. For oblate spheroids with axis ratio b/a , where a is the minor axis and b is the major axis, these shape factors can be expressed as

$$L_V = \frac{1 + A^2}{A^2} \left(1 - \frac{\arctan^{-1} A}{A}\right), \quad L_H = \frac{(1 - L_V)}{2}, \quad (5)$$

where

$$A = \sqrt{(b/a)^2 - 1}. \quad (6)$$

Assuming spherical raindrops with an axis ratio of unity, (5) reduces to one-third.

Applying this assumption by substituting these shape factors into (4), and replacing ζ in (3) with (4)

$$\sigma_H[mm^2] = \sigma_V = \frac{\pi^5 D_e^6}{\lambda^4} \frac{|\epsilon - 1|^2}{|\epsilon + 2|^2}. \quad (7)$$

Therefore, for spherical drops under the Rayleigh approximation (denoted in (7)), (1) simplifies to

$$Z_H[mm^6 / m^3] = Z_V = \int D_e^6 N(D_e) dD , \quad (8)$$

highlighting the familiar dependence of reflectivity factor on diameter raised to the sixth power. Because reflectivity factor measurements span many orders of magnitude for weather scatterers, a logarithmic scale $10 \log_{10} Z$ is commonly adopted (Doviak and Zrnic 1993).

Reflectivity factor is directly linked to the received backscattered power for an illuminated volume through the weather radar equation (e.g., Doviak and Zrnic 1993). Blocked or attenuated waves will exhibit diminished power returns. These returns produce lower Z measurements, thereby impacting subsequent precipitation and hydrometeor classification applications.

1.1.2 Differential Reflectivity, Z_{DR}

The definition of Z in (8) assumes spherical, equioriented drops that are small relative to radar wavelengths. While this assumption is sufficient for general weather radar applications, deviations from this ideal situation are common, particularly as drop sizes increase. Several forces alter falling hydrometeor shape, with drops becoming oblate with increased volume (e.g., Doviak and Zrnic 1993). Because larger drops are often associated with heavier rainfall, knowledge of these deviations in drop shape may provide complementary information for rainfall and hydrometeor classification applications.

The literature provides several estimates of axis ratio behavior. An estimate of the axis ratio response to increasing equivalent volume drop diameter provided by Beard and Chuang (1987) is

$$a/b = 1.0048 - 0.0057D_e - 2.628D_e^2 + 3.682D_e^3 - 1.677D_e^4, D_e[\text{cm}]. \quad (9)$$

Differential reflectivity is defined as

$$Z_{DR} = 10 \log Z_{dr}, \quad (10)$$

where Z_{dr} is the ratio of reflectivity factors measured at the horizontal and vertical polarizations

$$Z_{dr} = \left(\frac{\int \sigma_H N(D) dD}{\int \sigma_V N(D) dD} \right). \quad (11)$$

Herein Z_{dr} is expressed in linear units and Z_{DR} is expressed in dB. Through inspection of (2)-(6), it is apparent that the expression for Z_{dr} is predominantly influenced by changes to the backscatter cross-section of individual drops, and therefore directly linked to individual axis ratio and dielectric constant of the scatterers.

The connection between differential reflectivity and the canting, axis ratio and dielectric constant of the scatterers provides useful links between the measured Z_{DR} and select hydrometeor populations. For example, liquid precipitation is characterized by higher dielectric constants than frozen precipitation and larger raindrops have larger axis ratios than smaller raindrops. It follows that the expected value of Z_{DR} should differ predictably in response to these changes in the apparent axis ratio and dielectric constant. Hydrometeor orientation also impacts Z_{DR} , as randomly oriented scatterers produce a net spherical appearance resulting in an apparent axis ratio of unity.

A classic example of Z_{DR} application is the discrimination of hail from large rain scatterers. It has been suggested that hail tumbles while falling to the surface, rather than maintaining a net oblate form. The tumbling produces a random hail orientation that presents a net spherical appearance relative to radar polarizations. Reflectivity factor measurements of large raindrops and small hail for a horizontal polarization are typically similar given the comparable horizontal dimensions. However, following (11), the net spherical shape for hail results in low expected Z_{DR} value relative to large raindrops with net oblate shapes, allowing delineation of hail using Z_{DR} and Z fields.

1.1.3 Correlation Coefficient, ρ_{HV}

Correlation coefficient ρ_{HV} measures the correlation between the horizontally and vertically polarized signals at zero lag time. Qualitatively, ρ_{HV} may be interpreted as a measure of the particle diversity in the radar resolution volume. ρ_{HV} characterizes the differences in size, shape, orientation, and refractive index of the particles, and is very informative for classification of meteorological and non-meteorological scatterers. A simplified expression for the magnitude of the correlation coefficient is

$$\rho_{HV} = \frac{\left\langle \left| E_H^s E_V^{s*} \right| \right\rangle}{\sqrt{\left\langle \left| E_H^s \right|^2 \right\rangle \left\langle \left| E_V^s \right|^2 \right\rangle}} \approx \frac{\left| \sum_{i=1}^N \sqrt{\sigma_{Hi}} \sqrt{\sigma_{Vi}} e^{j\delta_i} \right|}{\sqrt{\sum_{i=1}^N \sigma_{Hi} \sum_{i=1}^N \sigma_{Vi}}}, \quad (12)$$

where E^s represents a scattered electric field component, with denotations for both horizontal and vertical polarization, and δ is the differential phase upon scattering (e.g., Bringi and Chandrasekar 2001). The expression in (12) is valid for equioriented

drops with an axis of rotation along the vertical. ρ_{HV} remains unaffected by blockage or attenuation due to the division of like-biases during its calculation.

Factors influencing the correlation coefficient include dielectric properties of scatterers, differential phase shifts upon scattering, canting angles, irregular hydrometeor shapes, and hydrometeor mixtures. Spherically shaped hydrometeors exhibit higher ρ_{HV} approaching unity. Mixtures of hydrometeors such as rain and hail lower the correlation coefficient. Non-meteorological scatterers including insects, birds, and ground clutter are characterized by substantially lower ρ_{HV} than hydrometeors (e.g., Zrníc and Ryzhkov 1999).

1.1.4 Differential Phase, Φ_{DP} , and Specific Differential Phase, K_{DP}

EM waves undergo phase shifts caused by particles impeding forward wave propagation. Hydrometeor concentration and sizes along the propagation path directly cause this phase shift. Isotropic scatterers equally affect microwave radiation at orthogonal polarizations. Non-spherical raindrops exhibit a larger net physical dimension in the horizontal perspective, therefore horizontally polarized waves experience an increased phase shift relative to vertically polarized waves when propagating through rain. Differential phase, Φ_{DP} , tracks the phase discrepancy that accumulates during two-way wave propagation in such medium. An expression for differential phase is

$$\Phi_{DP}[\text{deg}] = \delta + 2 \int_0^r K_{DP}(r) dr \quad (13)$$

where

$$K_{DP}[\text{deg km}^{-1}] = \frac{180\lambda}{\pi} \int_0^{\infty} \text{Re}[f_H(D) - f_V(D)]N(D)dD = \frac{1}{2} \frac{d\Phi_{DP}}{dr}, \quad (14)$$

and f_H and f_V in (14) are the forward scattering amplitudes at the horizontal and vertical polarizations (identical to the expression in (3) if the Rayleigh approximation is valid). Once again, expressions (13) and (14) are applicable for oriented drops with an axis of rotation along the vertical.

Φ_{DP} is related to the drop concentration, shape, and the orientation of drops. Subsequently, Φ_{DP} is also related to rainfall along the radial (e.g., Jameson 1985; Sachidananda and Zrnica 1986). Specific differential phase K_{DP} in (14) is defined as the range derivative of the differential phase, e.g., whereas Φ_{DP} represents the cumulative phase change, K_{DP} describes the phase change per unit range interval. It follows from (3), (13), and (14) that K_{DP} is related to the concentration and shape of particles associated with phase changes within a select range interval. Therefore, K_{DP} has important implications for estimating rainfall (e.g., Ryzhkov and Zrnica 1995a; Ryzhkov and Zrnica 1996; Vivekanandan et al. 1999) and attenuation losses (e.g., Bringi et al. 1990; Ryzhkov and Zrnica 1995b, Smyth and Illingworth 1998).

1.1.5 Radar Measurands for Canted Hydrometeors

Although the radar variable expressions outlined in the previous section are useful for illustrative purposes, it is known that meteorological scatterers are canted and that the orientation of particles has an impact on polarimetric variables. In particular, an increase in the canting of particles will result in a drop of Z_{DR} and ρ_{HV} . For more sophisticated radar calculations as in chapter 5 of this study, expressions

valid for canted hydrometeor populations are required. These expressions are as follows

$$Z_h = C \sum_j [I_1^j - 2A_2^j \operatorname{Re} I_2^j + A_4^j I_3^j], \quad (15)$$

$$Z_v = C \sum_j [I_1^j - 2A_1^j \operatorname{Re} I_2^j + A_3^j I_3^j], \quad (16)$$

$$\rho_{hv} = \frac{C \left| \sum_j [I_1^j + A_5^j I_3^j - A_1^j I_2^j - A_2^j I_2^{*j}] \right|}{Z_h^{\frac{1}{2}} Z_v^{\frac{1}{2}}}, \quad (17)$$

and

$$K_{DP} = C' \left\{ \left[\sum_j A_6^j I_4^j \right]^2 + \left[\sum_j A_7^j I_4^j \right]^2 \right\}^{\frac{1}{2}}, \quad (18)$$

where 'j' is the index of the species, $Z_{h,v}$ are expressed in $[\text{mm}^6 \text{m}^{-3}]$, Z_{dr} is equal to Z_h/Z_v and K_{DP} is in $[\text{deg}/\text{km}]$. In the above expressions, the constants C and C' are defined as

$$C = \frac{4\lambda^4}{\pi^4 \left| \frac{\epsilon - 1}{\epsilon + 2} \right|^2}, \quad (19)$$

$$C' = \frac{0.18\lambda}{\pi}, \quad (20)$$

where λ is the radar wavelength [in mm]. In expressions (15) - (18), the moments denoted with 'I' are related to the scattering amplitudes and the particle size distribution as

$$I_1 = \int N(D) |f_b|^2 dD, \quad (21)$$

$$I_2 = \int N(D) f_b^* (f_b - f_a) dD, \quad (22)$$

$$I_3 = \int N(D) |f_b - f_a|^2 dD, \quad (23)$$

$$I_4 = \int N(D) (f_b - f_a) dD, \quad (24)$$

where the scattering amplitudes in (21) - (23) correspond to backward scattering amplitudes and the scattering amplitudes in (24) are forward scattering amplitudes (function of diameter). The angular moments $A_1 - A_7$ in (15) - (18) are defined following Ryzhkov (2001) as

$$A_1 = \langle \sin^2 \psi \cos^2 \alpha \rangle, \quad (25)$$

$$A_2 = \langle \sin^2 \psi \sin^2 \alpha \rangle, \quad (26)$$

$$A_3 = \langle \sin^4 \psi \cos^4 \alpha \rangle, \quad (27)$$

$$A_4 = \langle \sin^4 \psi \sin^4 \alpha \rangle, \quad (28)$$

$$A_5 = \langle \sin^4 \psi \cos^2 \alpha \sin^2 \alpha \rangle, \quad (29)$$

$$A_6 = \langle \sin^2 \psi \sin 2\alpha \rangle, \quad (30)$$

$$A_7 = A_1 - A_2 = \langle \sin^2 \psi \cos 2\alpha \rangle, \quad (31)$$

where the angle α is the canting angle and angle ψ is the orientation angle with respect to the direction of propagation k , as illustrated in Fig. 1.

Radar calculations in chapter 5 assume a two-dimensional axisymmetric Gaussian distribution of particle orientations

$$p(\psi, \alpha) = \frac{1}{2\pi\sigma\sigma_\alpha} \exp \left[-\frac{(\psi - \langle \psi \rangle)^2}{2\sigma^2} - \frac{(\alpha - \langle \alpha \rangle)^2}{2\sigma_\alpha^2} \right] \quad (32)$$

where the angles $\langle\psi\rangle$ and $\langle\alpha\rangle$ determine the mean orientation of particles and parameters σ and

$$\sigma_\alpha = \frac{\sigma}{\sin\langle\psi\rangle} \quad (33)$$

define the width of the angular distribution along ψ and α directions, respectively. The approximation of the axisymmetric Gaussian distribution of orientations allows averaging over angles ψ and α independently, therefore angular moments A_i can be expressed as products of the following factors:

$$\langle\sin^2\psi\rangle = \frac{1}{2}(1 - r \cos 2\langle\psi\rangle), \quad (34)$$

$$\langle\sin^4\psi\rangle = \frac{3}{8} - \frac{1}{2}r \cos 2\langle\psi\rangle + \frac{1}{8}r^4 \cos 4\langle\psi\rangle, \quad (35)$$

$$\langle\cos^2\alpha\rangle = \frac{1}{2}(1 + r_\alpha \cos 2\langle\alpha\rangle), \quad (36)$$

$$\langle\sin^2\alpha\rangle = \frac{1}{2}(1 - r_\alpha \cos 2\langle\alpha\rangle), \quad (37)$$

$$\langle\cos^4\alpha\rangle = \frac{3}{8} + \frac{1}{2}r_\alpha \cos 2\langle\alpha\rangle + \frac{1}{8}r_\alpha^4 \cos 4\langle\alpha\rangle, \quad (38)$$

$$\langle\sin^4\alpha\rangle = \frac{3}{8} - \frac{1}{2}r_\alpha \cos 2\langle\alpha\rangle + \frac{1}{8}r_\alpha^4 \cos 4\langle\alpha\rangle, \quad (39)$$

$$\langle\cos^2\alpha \sin^2\alpha\rangle = \frac{1}{8}(1 - r_\alpha^4 \cos 4\langle\alpha\rangle), \quad (40)$$

$$\langle\sin 2\alpha\rangle = r_\alpha \sin 2\langle\alpha\rangle, \quad (41)$$

where,

$$r = \exp(-2\sigma^2), \quad (42)$$

and

$$r_\alpha = \exp(-2\sigma_\alpha^2). \quad (43)$$

At grazing angles for a zero mean canting angle of hydrometeors ($\langle\alpha\rangle = 0$) and mean axis of symmetry (N in Fig. 1) along the vertical

$$\begin{aligned} A_1 &= \frac{1}{4}(1+r)^2, & A_2 &= \frac{1}{4}(1-r^2), & A_3 &= \left(\frac{3}{8} + \frac{1}{2}r + \frac{1}{8}r^4\right)^2, \\ A_4 &= \left(\frac{3}{8} - \frac{1}{2}r + \frac{1}{8}r^4\right)\left(\frac{3}{8} + \frac{1}{2}r + \frac{1}{8}r^4\right), & A_5 &= \frac{1}{8}\left(\frac{3}{8} + \frac{1}{2}r + \frac{1}{8}r^4\right)(1-r^4). \\ A_6 &= \frac{1}{2}r(1+r) \end{aligned} \quad (44)$$

The radar calculations in chapter 5 utilize (44) for different values of the canting angle distribution σ that vary contingent on the type (rain, mixed-phase, frozen) of hydrometeor. A typical value of σ in rain is 10-20°. In wet snow/hail/graupel, values for σ may vary between 5° and 50°

1.2 Processing Polarimetric Data

An important consideration for the interpretation of polarimetric radar measurements is radar data collection and processing. For this study, raw KOUN measurements of Z , Z_{DR} , Φ_{DP} , and ρ_{HV} were measured at a radial resolution of 0.250 - 0.267 km using a short dwell time (48 radar samples) to satisfy NEXRAD antenna rotation rate (3 rpm) and azimuthal resolution (1°) requirements. Volume update time for polarimetric rainfall and echo classification products varied between 2 and 6 minutes. Data processing includes a radial (boxcar) smoothing procedure using a 3-gate averaging window for Z (0.5 km) and a 5-gate window for Z_{DR} and ρ_{HV} (1.0 km).

Due to the noisiness inherent in phase measurements of precipitation, these measurements require stringent processing routines. Two smoothed radial profiles of Φ_{DP} are obtained: a “lightly filtered” Φ_{DP} with an approximate 2 km radial resolution (9 range gates) and a “heavily filtered” Φ_{DP} with roughly 6 km radial resolution (25 gates). Φ_{DP} de-aliasing complicates phase measurement processing, however the task was simplified following an upgrade of the KOUN radar to an RVP8 processor (2004) with an aliasing interval of 360° . Measurements of Φ_{DP} rarely exceed 360° at S-band, although aliasing may occur if the system differential phase drifts with time. The separation of “data” from “noise” gates is performed along a radial by identifying locations where raw ρ_{hv} values exceed 0.9. Valid smoothing intervals for Φ_{DP} contain at least 9 successive gates classified as data in the case of light filtering and 25 successive data gates for heavy filtering. A median filter is used for smoothing of Φ_{DP} values in these intervals. Filling in the gaps between valid intervals in Φ_{DP} profiles is accomplished by linear interpolation using the valid Φ_{DP} values at the beginning and ending gates of gaps.

Two estimates of K_{DP} are obtained from the lightly and heavily filtered radial profiles of Φ_{DP} , $K_{DP}^{(9)}$ and $K_{DP}^{(25)}$, as a slope of a least squares fit for two range averaging intervals corresponding to 9 and 25 gates, respectively. To determine the value of K_{DP} at any particular range gate, the estimate $K_{DP}^{(9)}$ is selected if $Z > 40$ dBZ, otherwise $K_{DP}^{(25)}$ is used.

Radar reflectivity measured by KOUN for this study was matched with Z obtained from the nearby KTLX WSR-88D radar, which was assumed to be well calibrated. Z_{DR} was calibrated using polarimetric signatures of dry aggregated snow

above the melting level following Ryzhkov et al. (2005b). Attenuation correction of Z and Z_{DR} was performed using values of differential phase and the relations: $\Delta Z(\text{dB}) = 0.04 \Phi_{DP}$ (degrees) and $\Delta Z_{DR}(\text{dB}) = 0.004 \Phi_{DP}$ (degrees) (Ryzhkov and Zrnich 1995). Measurements of Z_{DR} and ρ_{HV} are affected by noise if the signal-to-noise ratio (SNR) is below 20 dB. A simple correction is applied for both measurements in such low SNR regions.

Texture parameters $SD(Z)$ and $SD(\Phi_{DP})$ characterize the intensity of small-scale fluctuations of Z and Φ_{DP} along the radar ray. These measurements are useful in radar echo classification to discriminate meteorological from nonmeteorological echo. To obtain $SD(Z)$, raw Z data are averaged along a radial using a 5-gate averaging window. The smoothed estimates of Z are then subtracted from the original Z values and the texture parameter is determined as the standard deviation of the difference. A similar procedure is used for computing $SD(\Phi_{DP})$, however the averaging window is two times wider.

1.3 Review of Radar Rainfall Estimation Techniques

Despite the limitations of radar-based rainfall measurements, a strong connection exists between rainfall rate and radar parameters (Doviak and Zrnich 1993). Conventional techniques solely involve reflectivity factor, whereas proposed operational techniques capitalize on polarization diversity.

1.3.1 Conventional Z-R Relations

Conventional methods use radar reflectivity factor to measure rain. While there is no universal relation between these quantities, a strong association exists between regions of mutual high values (Doviak and Zrnic 1993). Current operational radars exploit this connection for real-time rainfall estimation practices.

The development of single parameter Z-R rainfall estimates is straightforward. Making the proper assumptions, the reflectivity factor from (8) is related to the number concentration of drops and the equivalent volume diameter of these drops to the 6th power. The rainfall rate is measured as the depth of water per unit time, which may be expressed as

$$R = \left(\frac{\pi}{6}\right) \int_0^{\infty} D^3 N(D) w_t(D) dD, \quad (45)$$

where w_t is the terminal velocity of a raindrop (Doviak and Zrnic 1993).

Typically, a DSD is approximated by a Gamma function (e.g., Ulbrich 1983)

$$N(D) = N_0 D^{\mu} \exp(-\Lambda D), \quad (46)$$

where slope (Λ) is related to the median volume diameter D_0 by

$$\Lambda \approx \frac{3.67 + \mu}{D_0}, \quad (47)$$

with parameter μ typically having values between -3 and 8 , and D_0 is the solution of the equation

$$\int_0^{D_0} D^3 N(D) dD = \frac{1}{2} \int_0^{\infty} D^3 N(D) dD. \quad (48)$$

Assuming an empirical terminal velocity relation of the form (see Doviak and Zrníc, 1993)

$$w_t = 3.78D^{0.67}, \quad (49)$$

obtained through a best-fit of experimental data, (8) and (45) may be combined to form a power-law relation

$$Z = aR^b, \quad (50)$$

with coefficients a and b primarily depending on the type of DSD. Historically, the first Z-R relation was suggested by Marshall and Palmer (e.g., Marshall et al. 1947; Marshall and Palmer 1948)

$$Z = 200R^{1.6}, \quad (51)$$

where Z is in $\text{mm}^6 \text{m}^{-3}$ and R is in mm hr^{-1} . Z-R relations similar to (51) are often determined empirically as DSDs are rarely known. Battan (1973) cited no fewer than 69 empirically derived Z-R relations, which vary with region, storm structure, and cloud microphysical properties. Changes to the coefficients can be considerable, particularly in response to stratiform, convective, tropical, and different rain regimes (e.g., Battan 1973). Current NWS WSR-88Ds operate with two distinct default empirical Z-R relations (Fulton et al. 1998)

$$\begin{aligned} Z &= 300R^{1.4} && \left(\textit{for midlatitudes} \right) \\ Z &= 250R^{1.2} && \left(\textit{tropical type events} \right) \end{aligned} \quad (52)$$

In addition to errors associated with DSD uncertainty and variability of terminal velocities, conventional Z-R relations are prone to contamination due to ground

clutter, anomalous propagation, hail, partial radar beam blockage, incomplete beam filling, and radar miscalibration.

For this study, conventional relationship performance is assessed using the relation

$$R(Z) = 1.7 \times 10^{-2} Z^{0.714}. \quad (53)$$

The conventional relation in (53) is the inversion of the standard NEXRAD continental formula from (52) where Z is in $\text{mm}^6 \text{m}^{-3}$ and R is in mm hr^{-1} . Although commonly referred to as the ‘conventional’ relation, it is noted that the Z measurements to be utilized in (53) capitalize on polarimetric methods for calibration and quality control prior to rainfall estimation.

1.3.2 Polarimetric Rainfall Estimation

Polarimetric methods for rainfall estimation have been introduced during the past few decades and utilize different combinations of polarimetric measurements including the differential reflectivity factor Z_{DR} and specific differential phase K_{DP} (e.g., Ryzhkov et al. 2005a). Rainfall relations have been obtained for different radar wavelengths using simulated or measured DSDs and various assumptions about the size and shapes of raindrops. Estimate performance has been tested on extensive data sets from Oklahoma (Ryzhkov and Zrnice 1996, Ryzhkov et al. 2002, Ryzhkov et al. 2005b), Colorado and Kansas (Brandes et al. 2001), Florida (Brandes et al. 2002) for S-band radars, Australia (May et al. 1999) for C-band radar, and Virginia (Matrosov et al. 2002) for X-band radar. These studies demonstrate that there is an improvement in rainfall estimation if dual-polarization radar is used. Further, it has been

demonstrated that polarimetric rainfall estimation techniques are more robust with respect to DSD variations than conventional relations.

The following polarimetric $R(K_{DP})$ and $R(Z, Z_{DR})$ relations have been selected for analysis in this study

$$R(K_{DP}) = 44.0|K_{DP}|^{0.822}\text{sign}(K_{DP}), \quad (54)$$

and

$$R(Z, Z_{DR}) = 1.42 \times 10^{-2} Z^{0.770} Z_{dr}^{-1.67}. \quad (55)$$

where R is in mm hr^{-1} and K_{DP} in (54) is expressed in $^{\circ} \text{km}^{-1}$. The $\text{sign}(K_{DP})$ term allows negative values of R . Polarimetric relations (54) and (55) are selected because of their optimum performance in rain for central Oklahoma during the JPOLE field campaign (e.g., Ryzhkov et al. 2005a). Coefficients in (54) and (55) were determined using collected disdrometer data for the central Oklahoma region and assuming drop shape characteristics specified by (9) (e.g., Schuur et al. 2001, Ryzhkov et al. 2005a).

It is unlikely any single conventional or polarimetric radar relation will produce high quality precipitation estimates at different distances from the radar and for different types of hydrometeors filling the radar resolution volume. The idea of using multiple polarimetric relations to optimize rainfall estimation was explored by Ryzhkov et al (2005a). According to the “synthetic” approach developed in that study, the choice of a polarimetric rainfall relations is determined by the radar reflectivity Z or $R(Z)$, i.e., rain rate computed from Z . Chapter 3 expands on the idea of a polarimetric “synthetic” approach and tests a new formulation that capitalizes on the results of echo classification (e.g., Zrnic 1996).

1.4 Review of Polarimetric Echo Classification

In addition to anticipated improvements in quantitative precipitation estimation (QPE), another primary selling point of the operational polarimetric WSR-88D upgrade is the ability to automatically distinguish echo type. Several studies have demonstrated that polarimetric signatures are useful in pinpointing hail and graupel regions in convective storms, for delineation of meteorological and nonmeteorological scatterers including tornadic debris, melting layer designation, and determining ice crystal type. Echo classification may also be beneficial for optimizing QPE and forecast/warning applications.

1.4.1 Fuzzy Logic Classification

A fuzzy logic approach has been adopted for the initial deployment of operational polarimetric echo classification (e.g., Straka et al. 1996, Vivekanandan et al. 1999, Straka et al. 2000). The JPOLE field campaign validated the performance of this approach for discrimination of nonmeteorological echoes and the designation of hail (Ryzhkov et al. 2005). As opposed to classification based on conditional statements (if-then-else) or rigid boundaries between echo classes, fuzzy logic schemes allow boundaries between classes to overlap through the use of weighting (membership) functions (e.g., Straka et al. 1996, Liu and Chandrasekar 2000). ‘Fuzzy’ boundaries are particularly useful for weather echo that feature similar polarimetric signatures across several polarimetric measurement fields.

In the fuzzy logic approach adopted for this study, we identify a radar echo by selecting the echo class type with a maximal aggregation score. Aggregation values (or scores) for each of i -th class are determined as

$$A_i = \frac{\sum_{j=1}^n W_{ij} P^{(i)}(V_j)}{\sum_{j=1}^n W_{ij}} \quad (56)$$

where $P^{(i)}(V_j)$ is a membership function of the i^{th} class and j^{th} variable. W_{ij} is a weight between 0 and 1 assigned to the i^{th} class and j^{th} variable that characterizes the importance or rank of each variable for a particular class. More sophisticated classification schemes may incorporate quality control devices to devalue radar measurements with known biases. Maximal aggregation values may be below a predetermined critical threshold or the difference between the maximal aggregation value and that of the next highest aggregation value too small. In these situations, confidence in the results of echo classification may be low and the classification deemed unreliable.

Membership functions $P^{(i)}(V_j)$ in the operational echo classification algorithm are trapezoidal in shape and exhibit a maximal value of 1 and minimal value of 0. An example of a trapezoidal membership function is illustrated in Fig. 2. Each trapezoidal function is described by 4 parameters, denoted on Fig. 2 as: x_1 , x_2 , x_3 , and x_4 . Parameters of the membership functions are often experimentally determined and still a subject of ongoing research.

1.4.2 Class Designation

Membership functions for several classes including light rain and dry aggregate snow are significantly overlapped because of small polarimetric contrasts between these media. In these situations, consistency checks of the designated class with ancillary information including melting layer location and Doppler velocity signatures may alleviate glaring discrepancies. For example, rain (dry snow aggregates) identified above (below) the melting layer is apparently an incorrect designation.

The proposed operational echo classification algorithm distinguishes between 10 classes of radar echo, including AP and Ground Clutter (AP / GC), Biological Scatterers (BS), Light to Moderate Rain (RA), Heavy Rain (HR), Rain/Hail (RH), Big Drops (BD), Graupel (GR), Wet Snow (WS), Dry Snow (DS), and Ice Crystals (CR). In order to properly designate these classes, it is necessary to identify the slant ranges R_b and R_t corresponding to the bottom and the top of the melting layer. These ranges are defined as

$$\begin{aligned} R_b &= [2H_b a_e + a_e^2 (\sin \theta)^2]^{1/2} - a_e \sin \theta \\ R_t &= [2H_t a_e + a_e^2 (\sin \theta)^2]^{1/2} - a_e \sin \theta \end{aligned} \quad (57)$$

where the heights H_b and H_t represent the heights of the bottom and top of the melting layer [in km] and are inputs to the classification routine. These heights are often azimuthally dependent. θ in (57) is the elevation angle and $a_e = 8500$ km is equivalent Earth radius.

The slant ranges R_b and R_t in (57) correspond to simple geometric projections of the melting layer onto the current tilt provided that the antenna beam is infinitesimally small. However, melting layer contamination occurs over a broad

range interval if the antenna beam has a finite width (as illustrated in Fig. 3). The ranges R_{bb} and R_{tt} for a finite beam width of 1° are determined as

$$\begin{aligned} R_{bb} &= [2H_b a_e + a_e^2 (\sin(\theta + 0.5))^2]^{1/2} - a_e \sin(\theta + 0.5) \\ R_{tt} &= [2H_t a_e + a_e^2 (\sin(\theta - 0.5))^2]^{1/2} - a_e \sin(\theta - 0.5) \end{aligned} \quad (58)$$

To determine a final echo classification in the proposed echo classification scheme, particular subsets of classes are allowed within the five slant range intervals established in the relations (57) and (58) as

| | | |
|--------------------|-----------------------------------|------|
| $0 < R < R_{bb}$ | GC/AP, BS, BD, RA, HR, RH | |
| $R_{bb} < R < R_b$ | GC/AP, BS, WS, GR, BD, RA, HR, RH | |
| $R_b < R < R_t$ | GC/AP, BS, DS, WS, GR, BD, RH | (59) |
| $R_t < R < R_{tt}$ | GC/AP, BS, DS, WS, CR, GR, BD, RH | |
| $R > R_{tt}$ | DS, CR, GR, RH. | |

In general, the class designation outlined in (59) allows liquid and biological / nonmeteorological classes near or below the freezing level and frozen hydrometeor categories aloft. Big drops and hail echo are allowed at all slant ranges (e.g., allows for convective updrafts extending above environmental freezing level). In addition to these designations, GC/AP is assumed stationary. If GC/AP is identified, the absolute value of mean Doppler velocity V is checked for consistency. If this value is larger than 1 m/s, the class designation is made for the echo with the next highest aggregation score.

1.5 Outline of the Study

Whereas the existing literature overwhelmingly recommends polarimetric methods for weather radar applications at close distance to the radar, the primary goal of this study is to investigate and improve the performance of polarimetric rainfall estimation to longer distances. This work is motivated by the lack of studies that validate polarimetric rainfall applications with respect to the coverage and accuracy demands of the operational weather community. The four chapters of the study contain the four major research themes used to drive improved polarimetric rainfall estimation and subsequent algorithm transition into operations.

In order to investigate and automatically adjust operational radar rainfall measurement fields for the effects of ‘bright band’ contamination, the boundaries of the melting layer should be known in real-time. Melting layer boundary designation is also necessary for successful delineation of rain from mixed-phase and frozen hydrometeor regions in operational echo classification routines. Chapter 2 presents a new melting layer detection algorithm suitable for operational implementation on the polarimetric WSR-88D. Melting layer designations are validated using radiosonde and model temperature analysis.

Chapter 3 examines the quality of current conventional and polarimetric radar rainfall estimation for a broad range of distances from the polarimetric prototype of the WSR-88D radar. The results of polarimetric echo classification have been integrated into the study to investigate the performance of radar rainfall estimation contingent on hydrometeor type. A new methodology for operational rainfall

estimation that capitalizes on the results of polarimetric echo classification (EC method) is suggested. It is shown that this new approach exhibits better performance than the conventional WSR-88D algorithm and several popular polarimetric algorithmic formulations to distances of 200 km from the radar.

Melting layer contamination and beam blockage are two primary sources of error in radar rainfall estimates to longer distances. For conventional radar rainfall algorithms, there is often a tradeoff between observing Z at low elevation angles to extended the slant range of observations in rain below the melting layer and the Z bias attributed to surface beam blockage. Since polarimetric measurements of K_{DP} are immune to partial beam blockage, it may be possible to capitalize on K_{DP} measurements from lower tilts for direct rainfall estimation or the calibration of other radar measurements. Chapter 4 explores these issues and further refines the operational rainfall strategy to optimize rainfall algorithm performance to longer distance and in blocked regions.

High resolution modeling of the melting layer may provide valuable insight into the microphysical processes that affect the vertical profiles of polarimetric variables. Another approach for future improvements to rainfall estimation at or beyond the melting layer may be to incorporate polarimetric measurement insight into current VPR techniques. Chapter 5 explores the value of polarimetric VPR techniques through basic physical modeling efforts and comparisons with radar observations for various rain regimes.

2. AUTOMATIC DESIGNATION OF THE MELTING LAYER AND POLARIMETRIC ECHO CLASSIFICATION

Accurate melting layer (ML herein) designation is useful for several operational radar applications. ML identification is needed for accurate QPE because mixed-phase and frozen hydrometeors may contaminate radar rainfall estimates at longer distances from the radar. Knowledge of ML location is also important for microphysical characterization of the cloud, including the separation of liquid from frozen hydrometeors and evaluation of icing potential.

Melting hydrometeors often produce a discernable signature in conventional radar reflectivity factor Z known as the radar “bright band”. Gourley and Calvert (2003) describe an operational technique for bright band detection that scans columns of Z for spatially consistent maxima. The technique is recommended for stratiform precipitation events in which bright band signatures are often well-pronounced and associated with melting snow aggregates. However, the transition between frozen and liquid hydrometeors in convective regions featuring melting graupel or hail is not well-marked with a pronounced Z signature. The lack of pronounced signatures is a significant challenge to conventional radar-based ML designation in convective situations.

Polarimetric radar provides a unique capability to delineate the ML. Polarimetric measurements including Z_{DR} , ρ_{HV} , K_{DP} , and linear depolarization ratio L_{DR} exhibit well-pronounced ML signatures both in stratiform and convective situations (e.g., Zrnic et al., 1993). Moreover, polarimetric measurements are

sensitive to melting hydrometeors in situations where Z alone does not exhibit bright band signatures. It is known that the ML in stratiform clouds is characterized by a drop in ρ_{HV} and peaks in Z_{DR} and L_{DR} measurements. Brandes and Ikeda (2004) capitalize on these strong and complementary polarimetric signatures in stratiform precipitation for freezing level designation with accuracy to within 200 m. The Brandes and Ikeda (2004) technique matches observed polarimetric radar measurement profiles with idealized model profiles of Z , L_{DR} and ρ_{HV} expected in the ML. Tabary et al. (2006) present a similar technique for operational ML identification capitalizing solely on profiles of ρ_{HV} .

ML designation is an integral part of product generation for the KOUN radar. The current fuzzy logic hydrometeor classification algorithm (HCA) mandates accurate ML designation for successful delineation of several hydrometeor types. QPE for the polarimetric WSR-88D may also be contingent on reliable radar echo classification such that different rainfall relations are utilized for different classes of hydrometeors in the radar resolution volume.

This chapter presents an algorithm for operational polarimetric ML detection (MLDA). The technique differs from the Brandes and Ikeda (2004) and Tabary et al. (2006) methodology in that the algorithm does not attempt to match model profiles or rely on measurements of the linear depolarization ratio L_{DR} . The MLDA utilizes Z_{DR} instead of L_{DR} since the KOUN radar does not measure L_{DR} in its primary mode of operation for which H and V waves are transmitted and received simultaneously (SHV mode). The proposed method designates a ML top and bottom rather than

producing a single estimate of the freezing level height. The MLDA is integrated with the HCA in the operational system.

Verification of the proposed MLDA was performed for 18 events observed by the KOUN radar using 136 hours of comparisons with Rapid Update Cycle (RUC) model output and National Weather Service radiosonde data when available.

2.1 Description of the MLDA

The proposed algorithm capitalizes on radial dependencies of Z , Z_{DR} and ρ_{HV} at elevation angles between 4° and 10° to estimate the boundaries of the ML. These radial dependencies reflect vertical profiles of the three radar variables which exhibit well pronounced maxima in Z and Z_{DR} and minima in ρ_{HV} . The heights of these signatures generally do not coincide. Typically, the maximum of Z is observed at a higher altitude (i.e., at a larger slant range) than the maximum of Z_{DR} and minimum of ρ_{HV} . This can be explained by the fact that Z depends on concentration of melting snowflakes whereas Z_{DR} and ρ_{HV} measurements do not. Indeed, the vertical profile of Z within the melting layer is determined by three factors: (1) a change in particle size, (2) a change in particle refractive index, and (3) a change in particle concentration. As melting snowflakes fall through the melting layer, their size may initially increase due to possible aggregation and eventually decreases when a snowflake melts into a water drop. Concurrently, refractive index monotonically increases while concentration decreases as a result of a rapid increase in terminal velocity. Since Z_{DR} does not

depend on concentration, the decrease in concentration does not offset the increase in Z_{DR} due to possible aggregation and wetting of snowflakes. Hence, the maximum of Z_{DR} is observed closer to the bottom of the melting layer than the Z maximum. Similar considerations can be applied to ρ_{HV} .

Examples of ML signatures at the elevation 4.5° are presented for a PPI and for a mean radial profile from the May 13, 2005 event in Figs. 4 and 5. These examples confirm that the ρ_{HV} signature provides the most effective discrimination of melting hydrometeors. ML signatures are explored in greater detail in chapter 5 of this study.

2.1.1 Input Radar Data

For the WSR-88D precipitation volume coverage pattern (VCP-11), the MLDA incorporates six elevation angles: 4.5° , 5.5° , 6.5° , 7.5° , 8.7° and 10.0° . Such a choice of elevation angles is dictated by a compromise between radar resolution and areal coverage for observing melting signatures. At elevation angles lower than 4° , ML signatures are smeared due to beam broadening and may be contaminated by nonuniform beam filling (NBF) or partial beam blockage (e.g., Sanchez-Diezma et al. 2000, Ryzhkov 2007, Giangrande and Ryzhkov 2005). The widening of ML signatures at grazing angles due to beam broadening may be even more significant for polarimetric measurements (e.g., Ryzhkov 2007). The impact of beam broadening is discussed in further detail in section 2.1.4. At elevation angles greater than 10° , the expected number of range gates that reside within a typical ML decreases rapidly. In

addition, at higher elevation angles, the ML signature is expected at closer slant ranges which are more likely contaminated with ground clutter.

Ground clutter and nonmeteorological scatterers such as birds and insects may exhibit signatures similar to melting hydrometeors in the fields of Z , Z_{DR} and ρ_{HV} . Therefore, the results of radar echo classification obtained with the HCA are used to minimize spurious designations from nonmeteorological media. Doppler clutter filtering (not currently performed on KOUN) will also mitigate spurious designations associated with precipitation mixed with nonmeteorological echo.

2.1.2 Identification of Melting Snow

The MLDA searches for gate locations exhibiting polarimetric signatures of melting snow. Identification is performed on preprocessed radial data. Data preprocessing for the KOUN radar is standard as outlined in section 1.2. Identification of melting snow is performed as follows

1. For each radial, the algorithm identifies gates where ρ_{HV} falls between 0.90 and 0.97. These gates may not necessarily belong to the ML. Ground clutter and biological scatterers may exhibit similar ρ_{HV} signatures. To mitigate contamination from scatterers other than melting snowflakes, locations with polarimetric signatures of nonmeteorological echo are filtered. A climatological ML height constraint is enforced to ensure melting snowflakes are not identified above 6 km (adaptable threshold).
2. The ρ_{HV} ML signature should be consistent with Z and Z_{DR} maxima in the vicinity of the gate where the ρ_{HV} drop occurs. The algorithm searches for

Z and Z_{DR} maxima in a 500 meter window above gate locations matching the ρ_{HV} signature from step (1). The equivalent slant range distance for this window varies with elevation angle.

3. If the maximum value of Z falls between 30 dBZ and 47 dBZ and the maximum value of Z_{DR} is within the interval 0.8 dB to 2.5 dB for the 500 m window, then the gate of the ρ_{HV} signature is considered a ML point.
4. The corresponding azimuth and height of the ML points are stored in a two-dimensional array which contains the total number of ML points in a height-azimuth grid. The proposed MLDA utilizes a grid resolution of 0.1 km in height and 1° resolution in azimuth for this array. Fig. 6 provides an example of the ML point locations on a height-azimuth plane after all azimuths and elevations between 4° and 10° are examined for a single radar volume (13 May 2005 event from the dataset, 0848 UTC).
5. ML signatures at higher elevations are less smeared by the radar beam and thus better pronounced. The total number of possible ML points is smaller at higher elevations. In light of this, the MLDA can be modified to weight data collected at higher elevation angles more than the data collected at lower elevation angles.
6. Although censoring of ground clutter at lower heights is performed for regions with nonmeteorological polarimetric signatures, we found it useful to further mitigate possible contamination from ground clutter by removing ML points detected more than 1 km below the ML bottom height of the previous scan.

2.1.3 Designation of the Melting Layer Boundaries

Designation of ML boundaries is performed if the total count of ML points in the array exceeds a predetermined threshold (currently 1500 ML points). Typically, a high threshold produces more accurate results, but requires a longer time for data accumulation. ML boundaries are determined using the following methodology:

1. In order to capture azimuthal variability of the ML boundaries, the height-azimuth array of ML points is partitioned using a running (boxcar) 21° sector window ($\pm 10^\circ$ around the azimuth of MLDA designation). If the total number of ML points in a sector exceeds an adaptable threshold, then ML designation will be performed for that particular sector. If not, designation is not possible for this sector.
2. The heights that encompass a majority of the ML points are determined. In the proposed algorithm, the ML top is determined as the height below which 80% of ML points reside. Similarly, the ML bottom is determined as the height below which 20% of the ML points reside. Example ML boundaries are presented with solid lines in Fig. 6.
3. Missing designations (e.g., directions not meeting the threshold requirements) are filled using valid ML radar retrievals. For example, if only a single sector qualifies for a valid designation, that designation is utilized for all azimuths.

2.1.4 Justification of the Thresholds in the MLDA Procedure

The ρ_{hv} thresholds serve as the primary criteria for ML point identification along a radial. The lower MLDA ρ_{hv} threshold of 0.90 mitigates contamination from nonmeteorological scatterers. The upper ρ_{hv} threshold was selected to ensure the best discrimination between wet snow (within the melting layer) and light-to-moderate rain (below the melting layer) or dry snow (above the melting layer). The separation between these three categories of hydrometeors in terms of ρ_{hv} , as well as Z and Z_{DR} is illustrated in Fig. 7. The histograms in Fig. 7 summarize the results of polarimetric hydrometeor classification for a large set of the KOUN data including 29 hours of observations for 6 storm events in central Oklahoma (Park et al. 2007). Fig. 7a presents normalized histograms of ρ_{hv} for the two types of snow and rain. It is evident from Fig. 7a that the best separation of wet snow (ML) from dry snow and rain is achieved if the demarcation value of $\rho_{\text{hv}} = 0.974$ is used. This value is very close to the upper $\rho_{\text{hv}} = 0.97$ threshold. The Z and Z_{DR} histograms for the three classes in Fig. 7bc also substantiate the choice of the relevant Z and Z_{DR} thresholds in the MLDA.

We also consider the impact of radial smoothing and antenna beam broadening on the vertical profile of ρ_{hv} in justification of the ρ_{hv} thresholds. In order to evaluate such an impact, we take a model profile of intrinsic ρ_{hv} (solid line in Fig. 8) and compute the corresponding profiles modified by radial smoothing and beam broadening for elevation angles 4.5° and 10° (dotted lines in Fig. 8) following the methodology suggested by Ryzhkov (2007). The shape of the model profile was obtained from KOUN measurements at very high elevation angles (between 10° and 45°) without any radial smoothing for the case on April 7, 2002 (see Ryzhkov et al.

(2005b)). The height of the melting level (3.7 km) is adjusted to be more consistent with an average climatological value for central Oklahoma.

Although the model ρ_{hv} profile is almost symmetric, there is more broadening on the upper side because of very different vertical gradients of radar reflectivity factor above and below the melting layer. As expected, the broadening is more significant at elevation 4.5° . If the vertical profile of ρ_{hv} is not widened at all, then using the MLDA threshold of 0.97 (dashed vertical line) would result in about 0.25 km underestimation of the melting level height. Beam broadening and radial smoothing at elevations of 10° and 4.5° for this example causes about 0.1 km of underestimation and overestimation of the freezing level height, respectively. Hence, at least a fraction of the ML points from a typical melting layer are expected at heights above the melting level. If all ML points are counted, overestimation of the melting level height is inevitable. This is one of the reasons for discarding ML points above the 80% percentile for estimation of the ML top.

The choice of the cutoff percentiles in the height distribution of ML points is quite subjective. Apparently, retaining too many ML points in the distribution tails leads to increasing statistical errors in determination of the ML top and bottom. On the other hand, decreasing the interval between the two cutoff percentiles too much would produce an artificially narrow melting layer (however, mitigating the impacts of beam broadening and radial smoothing). We believe that 20% and 80% is a reasonable compromise. Ultimately, an empirical correction is likely needed for any choice of the cutoff percentiles (see section 2.3).

2.1.5 Additional Considerations

In addition to the use of multiple elevation angles to improve ML designation, the MLDA procedure retains information from previous volume scans to alleviate sparse data intervals in time and space and improve time continuity of the designation. This is accomplished by combining arrays of ML points corresponding to the current and two previous radar volume scans. With update times of 5 minutes, this translates to approximately a 15-minute averaging window. From operational testing, the 15-minute window reflects the shortest time averaging interval which consistently produces spatially continuous ML boundaries. Previous studies by Gourley and Calvert (2003) indicate success with the use of a 30-minute window.

For some events, it is possible that no pronounced ML signatures exist, the lowest radar tilt in the MLDA may overshoot storms/ML signatures at distance greater than 60 km, or the ML signature may be embedded in ground clutter hindering proper interpretation with KOUN. Because the MLDA capitalizes on the polarimetric signatures of melting snowflakes and not those associated with melting graupel or hail, ML designation is not available in convective events with an absence of surrounding regions of melting snow. For situations where a ML cannot be determined, model output temperatures, radiosonde and surface temperature data, or user-defined values are necessary to supplement the operational products or until sufficient radar melting signatures can be accumulated. Such considerations allow for uninterrupted application of ML designation for generation of other polarimetric radar products.

2.2 Validation of Melting Layer Designation

Following the Glossary of Meteorology, the melting layer is defined as the altitude interval throughout which ice-phase precipitation melts as it descends. The melting level is defined as the lowest 0°C constant temperature surface and the top of the melting layer (Glickman 2000). In stratiform and widespread precipitation events, it is expected that the retrieved ML top should coincide well with the location of the melting level since the onset of snowflake melting is typically at temperatures of 0°C or slightly warmer. The height of the ML bottom is variable and may be several hundred meters below the melting level at temperatures warmer than 5°C depending on humidity, particle concentration or density (e.g., Stewart et al. 1984, Pruppacher and Klett 1998, Willis and Heymsfield 1989, Fabry and Zawadzki 1995). The thickness of the ML has been observed close to 500 meters according to long-term ML observations (e.g., Fabry and Zawadzki 1995).

The performance of the MLDA has been tested for several precipitation events in central Oklahoma. A list of the 18 events and the validation sources for these events is provided in Table 1. Designations of the top and bottom of the ML have been checked against high frequency Rapid Update Cycle (RUC) model analysis output (e.g., Benjamin et al. 2004). ML top designations have also been validated against radiosonde observations. Areal averaged ML top heights (average ML top height designation from all valid azimuthal directions) retrieved from the KOUN radar are compared to the heights of the lowest 0°C level from these sources. Radiosonde data are obtained from the Norman, Oklahoma (OUN) NWS radiosonde

site that is within 200 meters of the KOUN radar site. RUC model analysis output from the closest model grid points is interpolated over the KOUN radar location.

2.2.1 Comparison with Radiosonde Observations

Radiosonde temperature and height measurements from the NWS Norman, OK (OUN) location are available at 0000 and 1200 UTC (Vaisala RS80 radiosonde equipment). The nearest valid radar-based designation (to within an hour and a half of the OUN sounding) is utilized for comparisons. Because of the limited sounding frequency, radiosonde-derived 0°C levels in close temporal proximity are not available for all events listed in Table 1. TELEX field campaign high-resolution balloon launch data supplement OUN soundings for select events during summer 2004 (as noted in Table 1).

Areal averaged ML top heights from the MLDA are plotted against the radiosonde-derived melting level heights in Fig. 9. The plot contains all available hours of comparison (16 hours total). The bias of the radar estimate for this dataset is -0.18 km with a RMS error of 0.28 km and standard deviation of 0.21 km. The correlation between ML top obtained from the radar and radiosonde-derived 0°C height is 0.92.

2.2.2 Comparison with RUC Model Analysis Output

Operational forecast models may provide accurate estimates of the melting level height to within a few hundred meters, particularly in uniform precipitation events (e.g., Mittermaier and Illingworth 2003). An advantage of the RUC model is

the high spatial and temporal resolution of its output. Hence, longer series of continuous radar-based ML designations can be validated.

A comparison of areal averaged ML top height and RUC model analysis output 0°C height is presented in Fig. 8. The plot contains 136 hours of RUC-radar comparisons for the 18 events in Table 1. Although the majority of points in Fig. 10 group very well along the 45° line, there is a separate cluster of points denoted with asterisks for which the radar shows a substantially lower height of the melting level compared to the RUC model. These points are associated with a few warm season convective events for which the RUC output may not be a reliable verification source. The reliability of RUC output is discussed in more detail in the next section. After these spurious hours are removed, a subset of 115 hours remains. For this subset, the bias is -0.16 km with an RMS error of 0.27 km and standard deviation of 0.22 km. The correlation between ML top heights and RUC model-derived melting level height is 0.93.

Fig. 11 displays a histogram of the RUC model temperature associated with the heights of the ML top designations for the hours of available RUC model output. The histogram is plotted at 0.5°C temperature bin intervals. Similar analysis was performed for ML bottom designations in Fig. 12. ML bottom designation indicates a wider range of associated temperatures, with the ML bottom often identified between RUC 2°C and 6°C. Events with extremely warm ML bottom designations (e.g., RUC temperature greater than 5°C) are typically associated with mature warm-season convective line events featuring trailing precipitation regions and/or questionable RUC or ML retrieval performance. A histogram of MLDA ML depth (ML top minus

ML bottom) for the hours of the RUC model dataset is presented in Fig. 13. ML thickness is typically less than 500 meters, consistent with long-term ML thickness observations by Fabry and Zawadzki (1995).

2.2.3 Temporal Dependencies

Checking temporal and spatial continuity of ML retrievals is a simple test of the algorithm performance. Since the radar ML designations in the dataset were updated every 5 minutes for the periods of several hours, it was possible to trace general trends and sharp changes in the characteristics of air masses associated with frontal passage or convective lines (Fig. 14). Temporal dependencies of areal averaged ML top heights are provided in Fig. 14 for four long-duration events in the dataset. Crosshairs on the image indicate results of the radar retrieval. NWS radiosonde-derived melting level heights are denoted with an ‘S’ symbol. Melting level heights obtained from the RUC are shown with diamonds. Error bars for the radar estimates reflect the degree of azimuthal variability.

2.3 Discussion

Overall, areal averaged height of the melting level (ML top) estimated from the MLDA correlates very well (at the level of 0.92-0.93) with heights obtained from soundings or RUC model analysis output except for a few outliers typically associated with mature warm-season MCSs. If the outliers are excluded, then the

radar algorithm yields a negative bias between 0.16 and 0.18 km. Most bias is attributed to the cut-off percentile choice of 80% for the ML top. One may reduce or eliminate most bias if a higher percentile threshold is chosen. However, an increase of this threshold may result in noisier retrievals. Thus, we prefer to use the 80% percentile level for the ML top designation and add an empirically derived correction of 0.16 km. This would ensure the unbiased estimate and the RMS error of 0.22 km. An offset (although perhaps less pronounced) is expected for ML bottom retrievals, however limited observations are available to validate this offset.

Several additional factors may also contribute to a discrepancy between the areal averaged estimates of the ML heights from radar, soundings and model analysis output. One of them is azimuthal variability of the ML height that is not captured by spatially sparse NWS soundings and quite often is not well reproduced in RUC model output. In the case of widespread radar echo typical for large frontal systems or trailing stratiform regions of MCS events, the polarimetric radar demonstrates a unique capability to track spatial variations in the depth and height of the ML including small-scale undulations of the melting level (e.g., due to localized convection or the passage of convective lines, as highlighted in the lower panel of Fig. 6). As error bars in Fig. 14 indicate, spatial variability of the MLDA-retrieved height exceeds 300 m for several events. The radar provides ML retrievals only in the areas of radar echo, whereas many soundings used for validation were collected in precipitation free air.

MLDA update frequency can provide a significant improvement over RUC model analysis output which is available hourly with observational data assimilation

“cut-off” times that may delay the analysis output by 20-50 minutes after the analysis time. RUC model analyses rely on the previous 1-h forecast which may exhibit errors, particularly in convective regimes. A benefit of high resolution radar ML retrieval is well illustrated with an example of the 13 May 2005 event (Fig. 14d) featuring an intense convective line and trailing precipitation region in the vicinity of the KOUN radar location. As the system approaches the radar location, the RUC 0°C height and radar areal averaged ML heights significantly differ. By 1200 UTC, the RUC 0°C height and the overall temperature profile change markedly following the RUC assimilation of the 1200 UTC OUN sounding. The change is indicative of prior questionable performance of the RUC model for this event. For the 1200 UTC analysis time, the MLDA top height is in best agreement with RUC model 0°C height and the OUN sounding. It is noted that the 1200 UTC OUN sounding was most likely launched into a relatively precipitation-free environment behind the trailing stratiform region, which may account for the observed mismatch of about 400 m between the OUN and MLDA designations.

2.4 Summary

1. A new melting layer detection algorithm (MLDA) has been developed for use with the polarimetric WSR-88D radar. The algorithm estimates the top and bottom boundaries of the ML using radar reflectivity factor Z ,

differential reflectivity Z_{DR} , and cross-correlation coefficient ρ_{HV} measured at antenna elevations between 4° and 10° .

2. The suggested algorithm was validated using sounding data and the output of the RUC model for 18 events encompassing 136 hours of observations in central Oklahoma. The height of the top of the ML retrieved from the radar was compared to the height of the lowest 0°C isotherm obtained from soundings and the RUC model.
3. In 85% of cases the MLDA yields unbiased estimates of the height of the melting level with an RMS error of 0.22 km. The correlation coefficient between the radar estimates and the ones from soundings and the RUC model output was as high as 0.92 and 0.93, respectively, for this category of events (mainly widespread stratiform rain).
4. The remaining 15% of the cases were primarily associated with mature warm-season mesoscale convective systems for which radar-derived ML heights were occasionally 1 km lower than the RUC model prediction. There is a strong indication that the radar might provide more reliable designation of the ML than the RUC model in these situations.
5. It was found that the temperature of the bottom of the ML varies in a wide range from 2°C to 6°C . According to MLDA retrievals, the depth of the ML changed from 100 to 900 m with a median value of about 400 m in the dataset used for validation.
6. The MLDA product updated every 5 minutes exhibiting solid temporal continuity and consistency with model output and soundings.

7. It is demonstrated that the MLDA captures the azimuthal and spatial variability of the height of the ML in the cases of widespread precipitation.
8. The MLDA is considered as an essential part of the operational polarimetric radar echo classifier to be used with polarimetric-upgraded WSR-88D radars.

3. ESTIMATION OF RAINFALL BASED ON THE RESULTS OF POLARIMETRIC ECHO CLASSIFICATION

Accurate rainfall estimates are vital for most hydrologic applications. The U.S. National Weather Service requires estimates of rainfall at ranges up to 230 km from the radar. However, the quality of radar measurements and rainfall estimates degrades with distance as a result of beam broadening and the effect of Earth curvature (e.g., Smith et al. 1996; Sanchez-Diezma et al. 2000; Ryzhkov 2007). At longer distances from the radar (typically beyond 100 km at base tilt), the radar resolution volume is more likely filled with mixed-phase or frozen hydrometeors. The radar measurements aloft are also quite loosely related to rainfall near the ground as a result of drastic changes in microphysical properties of precipitation in the vertical due to sublimation, riming, aggregation, evaporation, coalescence, break-up and advection (e.g., Doviak and Zrníc 1993, Sec. 8.4)

Contamination from nonliquid hydrometeors is especially pronounced in colder climates where the melting layer (or bright band) is particularly low. Even in relatively warm climates, this contamination generally occurs over a significant portion of the required NWS radar rainfall coverage area. For a typical warm-season melting level height in central Oklahoma (~3 km AGL), contamination of radar rainfall estimates at the 0.5° elevation angle due to the presence of mixed-phase and frozen hydrometeors is usually observed as close as 120 km from the radar. As a result, the accuracy of rain estimation may be compromised in over two-thirds of the radar rainfall coverage area required by the NWS.

Several studies discuss the quality of conventional rainfall estimation with single-polarization radar to large distances (e.g., Fabry et al. 1992; Smith et al. 1996; Seo et al. 2000; Krajewski and Ciach 2005). To obtain accurate surface rainfall measurements at longer distances, it is necessary to address the impact of melting layer and frozen hydrometeor contamination on radar measurements. For conventional radars, emphasis has been on establishing characteristic vertical profiles of reflectivity (VPR) to account for the reflectivity behavior through regions of melting hydrometeors (e.g., Koistinen 1991; Andrieu and Creutin 1995; Kitchen 1997). Although methods capitalizing on the knowledge of the VPR yield improved rainfall estimates at longer distance, these techniques are sensitive to precipitation variability including changes in storm type (e.g., stratiform versus convective) and temporal/spatial changes in the VPR (e.g., Zawadzki 2006). In this chapter, we suggest an alternate approach that capitalizes on polarimetric classification of radar echo rather than vertical profiles of reflectivity.

Polarimetric radar provides new opportunities to improve the accuracy of rain measurements. A number of different polarimetric algorithms for rainfall estimation have been recently validated in an operational environment during the Joint Polarization Experiment (JPOLE) field campaign, which was held in central Oklahoma in 2002-2003 (Ryzhkov et al. 2005a,b). In the JPOLE study, it was shown that the so-called “synthetic algorithm,” which utilizes different polarimetric relations depending on the value of Z , outperforms all other relations at the distances less than 90 km from the radar (Ryzhkov et al. 2005a). The performance of the synthetic algorithm (as well as other rainfall algorithms) at longer ranges was not investigated

in that study. Preliminary analysis by Giangrande and Ryzhkov (2003) and Ryzhkov et al. (2005b) demonstrated statistical improvement in the accuracy of rain measurements at longer distances (between 100 and 200 km) if the $R(K_{DP})$ relation is used instead of $R(Z)$. We are not aware of any other substantial effort to validate polarimetric rainfall algorithms beyond the range of 100 km, and the quality of polarimetric rainfall measurements at longer distances (where the radar samples mixed-phase and frozen hydrometeors) is largely unknown. One of the major objectives of this chapter is to examine the performance of polarimetric algorithms for rain estimation up to the distance of 250 km from the radar using a large dataset collected with the polarimetric prototype of the WSR-88D radar (KOUN herein) and Oklahoma Mesonet gage network.

Previous studies indicate that regardless of range interval it is unlikely any single radar relation would produce high quality precipitation estimates at different distances from the radar and for different types of hydrometeors filling the radar resolution volume (e.g., Jameson 1991; Chandrasekar et al. 1993; Cifelli et al. 2002; Ryzhkov et al. 2005a). According to the Ryzhkov et al. (2005a) synthetic approach, the segregation between different polarimetric relations is based on radar reflectivity factor. Following Zrnich (1996), we suggest using results of polarimetric hydrometeor classification for such a segregation.

This chapter emphasizes the quality of polarimetric rainfall estimation for a broad range of distances from the radar. The data were collected with the KOUN radar in central Oklahoma. Polarimetric echo classification has been integrated into this study to investigate the performance of radar rainfall estimation contingent on the

type of hydrometeors that fill the radar resolution volume. Hourly Agricultural Research Service (ARS) Micronet and Oklahoma Mesonet rain gage accumulations are used to validate conventional and polarimetric radar rainfall measurements (e.g., Brock et al. 1995, Shafer et al. 2000). The ARS and Mesonet gages used in this study are well calibrated and located at distances between 25 km and 250 km from the KOUN radar (e.g., Shafer et al. 2000; Fiebrich et al. 2006; McPherson et al. 2007).

3.1 Radar Dataset, Preprocessing and Echo Classification

A total of 43 events observed by the KOUN radar between the years of 2002 and 2005 have been selected for analysis. The dataset includes gage observations from over 100 Oklahoma Mesonet stations and comprises 179 hours of radar data. Concurrent gage observations were available from the densely-spaced ARS network stations located at ranges of 50-88 km from the KOUN radar. The total number of ARS gages with an average spacing of about 5 km is 42 (24 after 2004 when some gages were decommissioned). Over the ARS network, comparisons between the performance of radar-based rainfall retrievals are mainly affected by DSD variability and the possible presence of hail rather than ground clutter or contamination from melting layer or frozen hydrometeors (e.g., Ryzhkov et al. 2005a). A map of the observation network in central Oklahoma is presented in Fig. 15. A complete list of rain events and hours of observation is provided in Table 2. The dataset includes warm-season convective storms containing hail, mesoscale convective systems

(MCS) with intense squall lines and trailing stratiform precipitation, widespread cold-season stratiform rain, and select tropical storm remnants. The Mesonet and ARS gages (shielded Met One tipping-bucket type) used in the study are unheated, therefore we exclude the data associated with frozen and/or mixed phase precipitation recorded at gage level.

Radar rainfall estimates and echo classification results were obtained from the KOUN radar using data collected at the 0.5° elevation scan. Radar reflectivity measured by KOUN was matched with Z obtained from the nearby KTLX WSR-88D radar, which was assumed to be well calibrated based on the results of our previous studies (e.g., Ryzhkov et al. 2005c; Giangrande and Ryzhkov 2005). Z_{DR} was calibrated using polarimetric signatures of dry aggregated snow above the melting level following Ryzhkov et al. (2005c). A minimum $\rho_{hv} = 0.85$ threshold was applied as an additional check to filter echoes of nonmeteorological origin. Radar reflectivity was capped at 53 dBZ to mitigate hail contamination.

In this study, hourly gage and radar rainfall accumulations over gage locations within 250 km of KOUN are compared. Hourly radar accumulations are defined as an hourly rainfall estimate averaged over an area centered on an individual gage. Radar rainrates are averaged using 5 gates centered over the gage location and two closest azimuths separated by 1 degree. Such averaging produces a radial resolution of 1.0 km and transverse resolution that varies with range.

When comparing radar and gage rain estimates, one must be mindful of the errors of tipping bucket (TB) gage measurements (e.g., Zawadzki 1975, Wilson and Brandes 1979, Austin 1987, Ciach 2003). The errors in gage accumulations

associated with high wind undercatch and splashing may exceed 12% for intense MCS events in central Oklahoma (Duchon and Essenberg 2001). These errors are not common and/or typically have a lesser impact on the hourly rain total. Quality assurance meteorologists at the Oklahoma Mesonet perform regular gage maintenance and event-based analysis to detect and remove accumulation reports from malfunctioning and apparently biased gages. Thus, we believe that the intrinsic gage errors in the hourly rain total are well below the expected errors of radar rainfall measurements.

To establish the quality of the conventional and polarimetric radar rainfall algorithms, absolute differences between radar and gage estimates (expressed in mm) are examined rather than standard fractional errors, which are heavily weighted towards small accumulations. Rainfall estimates are characterized by the bias $B = \langle \Delta \rangle$ and the rms error $RMSE = \langle |\Delta|^2 \rangle^{1/2}$, where $\Delta = T_R - T_G$ is the difference between radar and gage hourly totals for any given radar-gage pair and brackets imply averaging over all such pairs.

A second objective is to examine the quality of radar rain measurements as a function of radar echo type and to explore the value of polarimetric hydrometeor classification for quantitative precipitation estimation. For this purpose, the type of scatterers in the radar sampling volume corresponding to a particular gage location was identified using a polarimetric classification algorithm based on fuzzy logic principles. The classification algorithm utilized herein is close to the one described by Ryzhkov et al. (2007) and Park et al. (2007) (as in Chapter 1, section 4). The membership functions in the fuzzy logic scheme are consistent with those in the

literature (e.g., Liu and Chandrasekar 2000; Lim et al. 2005). The classifier distinguishes between 10 classes of radar echo, including Anomalous Propagation and Ground Clutter (AP / GC), Biological Scatterers (BS), Light to Moderate Rain (RA), Heavy Rain (HR), Rain/Hail (RH), Big Drops (BD), Graupel (GR), Wet Snow (WS), Dry Snow (DS), and Ice Crystals (CR). The classification algorithm in this study utilizes four radar variables: Z , Z_{DR} , ρ_{HV} and a texture parameter $SD(Z)$, i.e., the standard deviation of small-scale fluctuations of Z along a radial. $SD(Z)$ is primarily used to distinguish meteorological and nonmeteorological echo. Melting level height, which is required as an input into the classification scheme, is determined from the closest available NWS sounding in Norman, OK.

The classification code distinguishes between 4 types of rain: RA, HR, RH, and BD. The membership functions in the fuzzy logic scheme for 4 classes of rain overlap significantly in terms of all 4 radar variables and are constructed in such a way that distinction between light to moderate rain (RA) and heavy rain (HR) is primarily based on Z using a 45 dBZ borderline. This corresponds to a rain rate of approximately 25-30 mm hr⁻¹. Rain-hail mixture (RH), on the other hand, is recognized and distinguished from heavy rain (HR) with the same Z by significantly lower values of Z_{DR} and ρ_{HV} . Rain associated with significant presence of big drops and/or a relative deficit of small drops is usually characterized by anomalously high Z_{DR} (for a given Z) and is identified as BD in the echo classifier. Rain belonging to the BD category is commonly observed in the updraft areas of the storms where vigorous size sorting of raindrops occurs. BD designations may also be found beneath

mature bright bands associated with the melting of large snowflakes in the stratiform regions of an MCS.

Table 3 and Fig. 16 summarize results of echo classification at Oklahoma Mesonet gage locations up to 250 km from the KOUN radar for the entire dataset containing 43 rain events and 179 hours of observation. On average, a radar echo over a particular gage was strong enough to be classified during 30% of the observation period.

The second column in Table 3 shows the percentage of occurrence for different echo types at elevation 0.5° in the 250 km radius area for the whole dataset. These data indicate that about 53% of radar echoes observed at the lowest elevation scan are associated with liquid hydrometeors (raindrops or raindrops mixed with hail), while mixed-phase or frozen particles are responsible for 23% of these echoes. Classification performed over the ARS gages shows an absence of frozen and mixed-phased echo over these locations for the events in the dataset.

For the classifications over Oklahoma Mesonet gage locations, the light to moderate rain (RA) category is the dominant echo type and classified to the distances of 170 km. Although convective rain categories including Heavy Rain, Big Drops, and Rain/Hail only account for approximately 10% of the valid classifications, their contribution to total rain amount exceeds 40% (if estimated from the standard WSR-88D R(Z) relation) because of higher rain rates. Echoes related to frozen and mixed-phase hydrometeors are typically observed at distances beyond 100 km. Wet Snow is a prevalent category among nonrain class designations owing to several MCSs with trailing stratiform precipitation in the dataset.

Echo classification is performed over each gage location during every radar scan, whereas radar and gage rainfall accumulations are computed for each hour. Because classification results generally change from scan to scan at the same location, several class designations may be associated with a single hourly rain total. To quantify the accuracy of hourly rainfall estimation for individual echo classes, we prefer to assign the hourly rain total to a single, dominant echo class for that hour. For example, a particular hourly gage accumulation is associated with light and moderate rain (RA) if the corresponding radar echo is classified as RA for at least 70% of radar scans constituting this hour. We refer to this type of echo as rain type I.

Other categories of rain (BD, HR, RH) are relatively infrequent (see Fig. 16 and Table 3) and the number of hours and gages over which such signatures are dominant is too small for obtaining reliable statistics. For this reason, we combine these rain categories in a single class of rain called rain type II. An hourly gage total is associated with rain type II if either RA, BD, HR or RH (or all of them together) are detected for at least 70% of time and one of the three categories (BD, HR, or RH) are identified for no less than 20% of time.

3.2 Rainfall Estimates Associated with Different Echo Types

The performance of different rainfall relations is investigated contingent on the results of polarimetric echo classification. It is known that conventional radar rainfall estimates obtained from $R(Z)$ relations deteriorate in the presence of mixed-phase and frozen hydrometeors. Previous studies have shown that the $R(Z, Z_{DR})$

relation is less prone to DSD variability, but it is not immune to hail contamination and is not efficient in situations of melting layer contamination and precipitation overshooting (e.g., Aydin et al. 1990; Ryzhkov and Zrníc 1995; Brandes et al. 2002; Ryzhkov et al. 2005a,b). Rainfall algorithms based on K_{DP} are more robust in the presence of hail, but are not optimal for light rain (e.g., Chandrasekar et al. 1990; Ryzhkov and Zrníc 1995). Giangrande and Ryzhkov (2003) demonstrate that $R(K_{DP})$ outperforms $R(Z)$ in melting layer regions, but the improvement may be fortuitous and requires further clarification. The results of polarimetric echo classification can be utilized to further investigate the nature of the errors inherent to all three types of rainfall relations ($R(Z)$, $R(Z, Z_{DR})$, $R(K_{DP})$) depending on the type of radar echo. We examine the performance of different rainfall relations separately in rain below the melting layer, within the melting layer where wet snowflakes are the dominant scatterers, and in frozen hydrometeors including graupel, hail, dry snow, and crystals above the melting layer where the direct application of radar rainfall relations is questionable.

3.2.1 Rainfall Relation Comparisons in Rain

Rain is most often classified at relatively close distances from the radar. For this reason, both Oklahoma Mesonet and ARS Micronet gage network accumulations are available to validate radar rainfall algorithms in rain. In this study, the offered relations $R(Z)$, $R(K_{DP})$ and $R(Z, Z_{DR})$ follow the relations found in (53) – (55), respectively.

Scatterplots of hourly rainfall totals obtained from the radar relations (53) - (55) versus hourly gage accumulations are displayed in Figs. 17–20. Figs. 17 and 18 illustrate radar – gage comparisons using Oklahoma Mesonet and ARS gages if rain is classified as rain type I as specified in Section 3.2. Similar plots highlighting the performance of the three rainfall relations for more convective and/or heavier rain type II (as specified in the previous section) are provided in Figs. 19 and 20 for the same gage networks.

For rain type I, the tested relations show similar performance with respect to both gage networks. A modest improvement in the rms errors is observed for all three rainfall relations if the ARS network is utilized for validation. This may be attributed to the improved spatial resolution of the KOUN radar measurements over these gages (all 42 ARS gages are located to within 88 km, as compared to 20 Mesonet gages). As Figs. 17 and 18 show, the $R(Z, Z_{DR})$ relation is relatively unbiased and has the lowest rms errors over both networks, consistent with the Brandes et al. (2002) findings. The improvement yielded by the $R(Z, Z_{DR})$ is relatively modest for rain type I and is more pronounced over the ARS network (Fig. 18c).

There is a clear benefit in polarimetric rainfall estimation in rain type II. The sizable reduction in bias and rms error (as compared to rain type I) for the $R(Z, Z_{DR})$ and $R(K_{DP})$ relations is an indication that these relations are less susceptible to hail contamination and DSD variability. The conventional $R(Z)$ relation significantly overestimates rain type II even though radar reflectivity is capped at 53 dBZ level to mitigate hail contamination. This overestimation is attributed to large raindrops and/or melting hailstones, which are typical for convective storms during warm

season in Oklahoma (e.g., Ryzhkov et al. 2005a). High values of Z in the $R(Z, Z_{DR})$ relation from (55) are offset by large intrinsic Z_{DR} for big drops and/or small melting hail.

The performance of the $R(K_{DP})$ and $R(Z, Z_{DR})$ relations for rain type II is comparable, and network-relative performance is similar to the case of rain type I (Figs. 17,18). At closer distances from the radar where the radar estimates are validated against ARS rain gages (Fig. 20b,c), the $R(K_{DP})$ relation yields slightly higher bias and rms error compared to $R(Z, Z_{DR})$. The opposite is true in the broader range of distances where validation is performed using Oklahoma Mesonet gages (Fig. 19b,c). K_{DP} measurements are already heavily filtered in range which may explain why these measurements are less sensitive to the additional beam broadening/filling effects in rain over Mesonet gages.

The choice between $R(K_{DP})$ and $R(Z, Z_{DR})$ in rain type II is affected by the quality of absolute calibration of Z and Z_{DR} , severity of the nonuniform beam filling (NBF) effects, and required spatial resolution of rain estimates. For example, the $R(Z, Z_{DR})$ relation cannot be applied in rain/hail mixtures (RH) if the increase in Z is not compensated by the proportional increase of Z_{DR} in (55). One has to distinguish between situations where rain is mixed with relatively small melting hail having high Z_{DR} and large hail characterized by low Z_{DR} . According to our classification algorithm, only the latter situation is qualified as hail / rain mixture. This is confirmed by the difference in the $2^\circ \times 1$ km average values of $R(Z)$ and Z_{DR} for Heavy Rain and Rain / Hail in Table 3. In rain / hail mixture, higher Z is associated with lower Z_{DR} and the $R(K_{DP})$ relation produces smaller bias.

Specific differential phase is immune to radar miscalibration and attenuation in rain, making $R(K_{DP})$ algorithms attractive choice for rainfall estimation.. However, because estimates of K_{DP} are noisier and more prone to NBF, the fields of $R(K_{DP})$ and even corresponding hourly totals may contain spurious perturbations and “holes” associated with unphysical negative rain rates or accumulations. An example of these “holes” in a rainfall accumulation display is presented in Fig. 21a. The reflectivity-based relation generally produces less noisy, “hole-free” fields of rain totals and may be favorable for operational forecast/warning applications, which require high spatial and temporal resolution (Fig. 21b). The $R(K_{DP})$ relation may be preferred in hydrological applications, which need unbiased estimates of rain integrated over large spatial / temporal domain.

3.2.2 *Rainfall Relation Comparisons in Wet Snow*

Wet Snow echoes are associated with (but not limited to) locations of pronounced bright band signatures in Z . Wet snow is identified with greater confidence if Z is supplemented with polarimetric variables Z_{DR} and ρ_{hv} . For the KOUN radar, Wet Snow echoes are best characterized by values of ρ_{hv} between 0.90 and 0.97 and Z_{DR} values exceeding 0.7 dB.

The comparison between hourly rain totals obtained from Eq (53) – (55) and Oklahoma Mesonet gages in the cases when the radar samples Wet Snow above the gages is illustrated in Fig. 22. Again, an hourly rain total is associated with Wet Snow if the radar echo is classified as Wet Snow for at least 70% of the scans within the hour. At elevation 0.5° , Wet Snow in the radar resolution volume is usually classified

at distances beyond 80 km from the radar and beyond the ARS Micronet gage network (Fig. 15). Thus, ARS network accumulations cannot be used for validation in the case of Wet Snow echoes.

The use of a single $R(Z)$ rainfall relation through rain, mixed-phase and snow regions is a common practice in conventional NEXRAD operations. However, no reasonable expectation exists that a single relation developed for the rain medium would be applicable to longer distance and through mixed phase regions. As Fig. 22a shows, the conventional $R(Z)$ relation applied over Wet Snow echo gages significantly overestimates surface rainfall. Slight improvement in terms of the bias and rms error is observed if polarimetric relations are used (Fig. 22b,c). Such an improvement may be explained by the fact that K_{DP} is less affected by the contribution from large wet snowflakes than Z . Also, because Z_{DR} is high in wet snow, the combined use of Z and Z_{DR} helps to partially mitigate the overestimation inherent to $R(Z)$. However, the peaks in the vertical profiles of Z and Z_{DR} through the bright band generally do not coincide in height and Z and Z_{DR} do not correlate to the extent typical for ordinary rain. In addition, both K_{DP} and Z_{DR} are quite prone to the NBF effects in the presence of very strong vertical gradients in the melting layer (Ryzhkov 2007) and are rather noisy due to low ρ_{hv} . Thus, the use of Eqs. (54) - (55) in Wet Snow are not as beneficial as in rain.

In view of these considerations, we recommend using a modified $R(Z)$ relation, as opposed to polarimetric relations, if the radar echo is classified as Wet Snow. Such a modification implies multiplying the right side of (53) by a factor that can be determined empirically by minimizing the bias and rms error in the rain

estimate. In the case of Wet Snow for this dataset, this factor was determined to be 0.6, i.e., the relation $R = 0.6 R(Z)$ works the best (Fig. 22d).

3.2.3 *Conventional Relation Performance Above the Melting Layer*

The echo classification routine used in this study classifies four hydrometeor species above the melting layer: Dry Snow, Crystals, Graupel, and Rain/Hail. Dry Snow and Crystals encompass most polarimetric echo designations exhibiting low Z (generally less than 35 dBZ) and ρ_{hv} greater than 0.97. Discrimination between Dry Snow and Crystals is primarily based on the magnitudes of Z and Z_{DR} . Discrimination between Graupel and Rain/Hail above the melting layer is primarily based on the magnitudes of Z and ρ_{HV} .

As illustrated by a polarimetric radar cross-section through a typical Oklahoma thunderstorm (Fig. 23), the two polarimetric variables K_{DP} and Z_{DR} measured above the melting layer are noisy, often negative, and seem loosely connected with rain on the ground. Although microphysical processes in the frozen part of the cloud directly impact rain formation and polarimetric measurements undoubtedly provide insight into the nature of such processes and snow type, the quantitative use of the polarimetric variables measured above the melting layer for precipitation estimation on the ground has not yet been justified. At the moment, the use of modified $R(Z)$ relations may be the most reasonable option provided that the type of the radar echo above the melting layer is determined using a polarimetric classification algorithm.

Fig. 24a shows that the conventional relation (53) heavily underestimated rain at the surface if the hydrometeors in the radar resolution volume are identified as Dry Snow and Crystals. Note, the classification routine allows for Dry Snow to be designated if part of the radar volume is below the freezing level. The errors are smaller at closer distances where the height of the radar resolution volume is at or below the freezing level (Fig. 24b). Z measurements in these regions often closely resemble those in the rain beneath (e.g., Fabry and Zawadski, 1995). As the height of radar echo progressively increases with distance, rain underestimation becomes overwhelming (Fig. 24c).

In order to minimize the bias in the estimate of rain when dry snow / crystals are sampled by the radar at longer distances, we introduce an additional factor of 2.8 to conventional $R(Z)$ relation (53)

$$R(Z) = 2.8 * R(Z) = 4.76 \times 10^{-2} Z^{0.714} \quad (60)$$

The intercept in (60) is between the intercepts of the $Z - S$ relations recommended by Super and Holroyd (1998)

$$S = 3.86 \times 10^{-2} Z^{0.5}, \quad (61)$$

and Vasiloff (2001)

$$S = 5.46 \times 10^{-2} Z^{0.5}, \quad (62)$$

for estimating snow water equivalent rate S on the operational NEXRAD network if snow near the surface is dry.

The performance of the conventional $R(Z)$ relation for a limited subset of cases when the radar echo was classified as Graupel / Hail above the freezing level is illustrated in Fig. 25. Because K_{DP} and Z_{DR} are usually small for dry graupel and hail

aloft, it is hard to expect rainfall estimation improvement if these two polarimetric variables are used directly. Instead, we recommend to use the modified $R(Z)$ relation for Graupel / Hail aloft with the multiplying factor 0.8 which minimizes the bias and rms error for this data subset.

3.3 Radar Algorithms and Their Performance as a Function of Range

As in section 3.2, there is benefit in the use of different rainfall relations for different classes of radar echo. The idea of using multiple relations to optimize rainfall estimation as suggested by Chandrasekar et al. (1993), Cifelli et al. (2002), and Matrosov et al. (2005) was further explored by Ryzhkov et al (2005a) in JPOLE studies. According to the “synthetic algorithm” developed by Ryzhkov et al. (2005a), the choice between various polarimetric rainfall relations is determined solely by the radar reflectivity Z or $R(Z)$, i.e., rain rate computed from Z using Eq (53). Ryzhkov et al. (2005a) recommend using the $R(Z, Z_{DR})$ relation in light rain ($R(Z) < 6$ mm/h), $R(K_{DP}, Z_{DR})$ relation in moderate-to-heavy rain ($6 < R(Z) < 50$ mm/h), and $R(K_{DP})$ relation in heavy rain ($R(Z) > 50$ mm/h). The three relations were optimized based on the comparison with the ARS gages for rain events during JPOLE in 2002 – 2003. In Ryzhkov et al. (2005a), the “synthetic algorithm” was validated only at distances less than 90 km from the radar, where the contamination from mixed-phase and frozen hydrometeors is minimal. Note that the $R(Z, Z_{DR})$ relation in the “synthetic

algorithm” is different from the one given by (25). The $R(Z, Z_{DR})$ relation in Ryzhkov et al. (2005a) was optimized for light rain where $R(Z) < 6 \text{ mm hr}^{-1}$.

We suggest another version of a “synthetic algorithm” which is based on the results of polarimetric classification rather than on Z and is applicable for a wide range of distances from the radar. This algorithm is constructed as follows.

$$\begin{aligned}
 R &= 0 && \text{-- if nonmeteorological echo is classified,} \\
 R &= R(Z, Z_{DR}) && \text{-- if Light/Moderate Rain is classified,} \\
 R &= R(Z, Z_{DR}) && \text{-- if Heavy Rain or Big Drops are classified,} \\
 R &= R(K_{DP}) && \text{-- if Rain/Hail is classified and the echo is below} \\
 &&& \text{the freezing level,} \\
 R &= 0.6 * R(Z) && \text{-- if Wet Snow is classified,} \\
 R &= 0.8 * R(Z) && \text{-- if Graupel or Rain/Hail is classified and the radar} \\
 &&& \text{volume is above the freezing level,} \\
 R &= R(Z) && \text{-- if Dry Snow is classified and the radar volume is} \\
 &&& \text{below the freezing level,} \\
 R &= 2.8 * R(Z) && \text{-- if Dry Snow or Crystals are classified and the} \\
 &&& \text{radar volume is above the freezing level,}
 \end{aligned} \tag{63}$$

where the $R(Z)$, $R(Z, Z_{DR})$, and $R(K_{DP})$ relations are specified by (53) – (55) above, Z values are capped at 53 dBZ and rain rate is set to zero if $\rho_{hv} < 0.85$ to ensure minimal contamination from nonmeteorological echoes. The set of equations in (63) comprises an echo classification (EC) rainfall estimation algorithm. In the current version of the EC algorithm, we use two very different $R(Z)$ relations for Dry Snow below and above the freezing level. In the future, a more gradual change of the

intercept parameter in the $R(Z)$ relation for Dry Snow / Crystals as function of range (or radar volume height) might be needed, similar to what was suggested by Hunter et al. (2001) for WSR-88D snow accumulation algorithm or what is usually employed in the conventional VPR methods. This algorithm was tested on the entire dataset along with the individual relations (53) - (55) and the “synthetic algorithm” by Ryzhkov et al. (2005a).

The mean biases and RMS errors for 5 algorithms are plotted as functions of range for the entire dataset in Fig. 24. The distances from gauges have been partitioned into 50 km wide range bins to smooth the plotting. Due to significant radar rainfall accumulations associated with intense convective lines (MCS) and hail-producing storms, convective warm season events dominate the overall performance statistics in Fig. 26. Separate statistics were obtained for widespread “stratiform” rain events that we define as the events with an absence of convective signatures and for which the bright band played a significant role (Fig. 27). This subset includes 26 hours of Oklahoma Mesonet gage observations during 9 widespread cold-season precipitation events.

As was claimed by Ryzhkov et al. (2005b) and Giangrande and Ryzhkov (2003), the conventional WSR-88D algorithm tends to overestimate rainfall in a wide range of distances up to 200 km from the radar and underestimate it beyond 200 km because of the progressive overshooting of precipitation at longer ranges (Figs. 26, 27). The overestimation at ranges below 100 km is primarily due to the impact of large drops and melting hail, which are very common in Oklahoma storms (Ryzhkov et al. 2005a). At ranges between 100 and 200 km, contamination from the bright band

is another factor contributing to the positive bias of the conventional rainfall estimate. Depending on the height of the freezing level, the impact of the bright band is strongest in the range interval 130 – 180 km. Conclusions regarding the performance of the conventional WSR-88D $R(Z)$ relation in this paper are consistent with the results of independent statistical study by Krajewski and Ciach (2005), who examined a massive amount of radar data collected by the operational KTLX WSR-88D radar in the same region, i.e., central Oklahoma.

The performance of rainfall relations at close distances from the radar (< 100 km) reaffirms initial JPOLE findings, which suggest that polarimetric methods and “synthetic” algorithms in particular outperform the conventional $R(Z)$ relation for most precipitation regimes. Three polarimetric algorithms: the Ryzhkov et al. (2005a) “synthetic”, EC-based, and $R(K_{DP})$ demonstrate similar performance at the ranges up to 130 km with the EC algorithm producing the lowest bias and the “synthetic” one yielding smallest rms errors for all rain events combined (Fig. 26).

The EC algorithm significantly outperforms others in the range interval between 130 and 200 km in terms of the rms error. However, this result is not necessarily surprising since the tuned $R(Z)$ relations in mixed phase and frozen hydrometeors in the proposed EC-method (63) were developed by minimizing the bias and rms errors using subsets associated with different hydrometeor classes within the same multi-year dataset. Although our 4-year dataset is rather large and encompasses a high variety of different storms, independent testing and validation of the method in different climate regions is required to check stability of the suggested $R(Z)$ relations for nonrain hydrometeors. There is little chance to find a single $R(Z)$

relation which will perform satisfactory for all classes of mixed-phase and frozen hydrometeors. Polarimetric classification combined with the use of multiple $R(Z)$ relations provides a better opportunity to reduce uncertainty in rainfall measurements in a wide range of distances from the radar.

Utilizing the classification-based polarimetric algorithm (EC) instead of the conventional $R(Z)$ relation results in a reduction of the bias and rms errors of hourly rainfall estimates up to 200 km from the radar (Fig. 26, 27). At distances within 50 km, the rms error is reduced by roughly a factor of 2, largely attributed to improved polarimetric performance in the presence of heavy rain and convective echo. This result echoes the Ryzhkov et al. (2005a) report of a factor of 1.7 reduction for the cases observed in central Oklahoma during JPOLE. The improvement gradually phases out with increasing distance from the radar. The degree of the rms error reduction exceeds 50% at ranges up to 140 – 150 km and drops to about 20% at 200 km.

For the cold season, non-convective events, the EC-algorithm also outperforms the conventional one, but to a lesser degree. Polarimetric methods capitalizing on the combined use of Z and Z_{DR} offer only modest improvement at close ranges. The most tangible improvement is achieved at longer distances from the radar where the impact of the bright band is maximized (Fig. 27).

The EC-algorithm is designed to use specific differential phase K_{DP} more sparingly compared to the “synthetic” algorithm which implies more aggressive use of K_{DP} . This is dictated by the need to mitigate noisiness in rain fields and the appearance of negative accumulations related to noisy and negative K_{DP} . However, in

some instances the K_{DP} -based algorithms may produce less bias if substantial averaging over time and space is performed. For example, the “synthetic algorithm” shows slightly smaller bias at shorter distances than the EC-algorithm. Nevertheless, we believe that the overall performance of the EC-algorithm is better and the approach is the better suited for implementation on the polarimetric NEXRAD. An advantage of the EC-based methodology is that it can be easily adapted to incorporate the ideas of traditional VPR correction which will benefit from polarimetric classification.

3.4 Summary

1. The performance of the conventional and various polarimetric algorithms for rainfall estimation has been validated at a wide range of distances from the radar. This was accomplished using a large dataset that included radar data collected with polarimetric prototype of the WSR-88D radar and gage data from the ARS Micronet and Oklahoma Mesonet networks in Oklahoma. The type of radar echo in the radar resolution volume over gage locations was identified using the polarimetric classification algorithm. The accuracy of rainfall estimation was assessed separately for different classes of radar echo including liquid, mixed-phase, and frozen hydrometeors.

2. A new algorithm that utilizes multiple polarimetric relations and modified $R(Z)$ relations depending on a radar echo class has been developed. According to this strategy, quantitative precipitation estimation should be preceded by and contingent on results of hydrometeor classification. The $R(Z, Z_{DR})$ relation is utilized if the radar echo is classified as rain and $R(K_{DP})$ relation is used if large hail is mixed with rain. At longer distances, where the radar resolution volume is filled with mixed-phase and frozen hydrometeors, the polarimetric radar is primarily used as a classifier. $R(Z)$ relations with additional multiplicative factors (or intercept parameters) are applied if the radar scatterers are identified as wet snow, dry snow, crystals, as well as graupel and hail above the melting layer. These factors were optimized for our dataset and further testing of the method using independent data in different climate regions will be needed to assess their variability. We do not exclude that in the future that the $R(Z)$ relations should be modified according to the height of the radar resolution volume above ground or melting layer similar to the approach recommended by Hunter et al. (2001) for improvements of the WSR-88D snow accumulation algorithm.
3. A validation study that incorporates a 4-year polarimetric dataset containing 43 rain events and 179 hours of observations demonstrates that the performance of the suggested algorithm, which is based on echo classification (EC-algorithm), is superior in terms of both bias and rms error. The most significant improvement, as compared to the conventional

WSR-88D algorithm, is found in convective storms where the rms error of hourly rain estimate is reduced by a factor of 2 at distances less than 50 km from the radar.

4. The degree of improvement for all relations gradually decreases with range and becomes insignificant at distances beyond 200 km. It is shown that the EC method exhibits better performance than the conventional WSR-88D algorithm with 1.5 – 2 times reduction in the rms error of one-hour rainfall estimates up to distances of 150 km from the radar. In regions with bright band contamination, the rms error for the EC-method is reduced by a factor of 1.25 as compared with the conventional method. Only modest improvement in rms error is observed compared to the conventional relation in snow above the melting layer.
5. As opposed to the “synthetic” algorithm suggested by Ryzhkov et al. (2005a), the EC-algorithm uses specific differential phase K_{DP} sparingly. This was done to avoid noisiness inherent to most of the K_{DP} -based algorithms.

4. POLARIMETRIC MEASUREMENTS AT MULTIPLE ELEVATION ANGLES

The advantages of polarimetric methods for improving radar rainfall estimation to longer distances were discussed in the previous chapter. The quality of several published and a proposed EC-based rainfall algorithm was assessed for a single elevation angle (0.5°) that is the most relevant for standard NWS rainfall applications. A main conclusion was that the performance of the tested rainfall algorithms deteriorates with range in the locations of mixed-phase and frozen hydrometeors. Although it was demonstrated that the knowledge of polarimetric echo classification may improve rainfall algorithm performance, the results point to an unavoidable limitation of radar-based rainfall estimation to distant ranges; as range from the radar increases, the radar beam height and volume size increase such that the measured bulk hydrometeor characteristics are increasingly less representative of the underlying surface precipitation.

It was not unexpected that close-distance Mesonet and ARS network gage accumulation comparison studies reaffirmed the superiority of polarimetric methods in rain. However, the EC-methodology calls for the use of modified $R(Z)$ relations at ranges with mixed phase and frozen echo. This implies polarimetric rainfall estimation at these locations only capitalizes on polarimetric insight *indirectly* through echo classification. It is further cautioned that tuned $R(Z)$ relations have not been extensively tested and are not likely to be universally applicable.

As an alternative to the use of modified $R(Z)$ relations, it may be beneficial to capitalize on the data collected at lower radar tilts to extend the range interval where the radar samples rain, thereby minimizing the role of tuned $R(Z)$ relations in an EC-based methodology. The potential advantage of data collection at lower radar tilts is illustrated by the following example: A beam from the KOUN radar system with base tilt at the 0.5° elevation angle intersects the bottom of the melting layer to within 120 km during the typical warm-season central Oklahoma MCS events (e.g., chapter 3, Figs. 26, 27). Under similar atmospheric conditions for a 0.0° tilt, simple beam geometric considerations dictate the radar beam would intersect the melting layer near 170 km. Here, the lower radar tilt provides an additional 50 km of radar observations in rain beneath the melting layer where polarimetric relations are best suited (100% areal coverage increase). Such an ability to probe liquid hydrometeors to much longer distances provides strong incentive to pursue the use of a lower base tilt in operations.

A major limitation for data collection at lower tilts is that the radar measurements at these elevation angles are susceptible to partial beam blockage and ground clutter contamination. Maddox et al. (2002) highlight the limits of radar coverage for the operational NEXRAD WSR-88D network. The study notes that radar coverage below 3 km AGL in the western United States is sparse, with prominent low-level blockage significantly compromising available radar data. Owing to partial beam blockage and public safety considerations, the WSR-88D network operates with a minimum elevation angle of 0.5° to ensure unobstructed and high quality measurements of Z under typical atmospheric conditions. For low-lying

radar systems and/or radar located in mountainous terrain as in the Maddox et al. (2002) paper, higher base tilts are necessary to collect uncontaminated data near the radar and/or beyond larger surface blockages. It is clear that such data collection at higher tilts precludes longer-range precipitation coverage. In this way, the availability of unbiased measurements of precipitation or accurate calibration of radar measurements in the presence of a PBB is intimately linked with the challenge of capitalizing on the lowest available grazing angles for precipitation estimation to longer distances.

Several studies offer methods to improve conventional precipitation measurements over complex terrain (e.g., Andrieu et al. 1997, Seo et al. 2000, Dinku et al. 2002, Kucera et al. 2004, Langston and Zhang 2004). A common practice is the use of Digital Elevation Models (DEM) to identify the larger-scale topographical features responsible for significant partial beam blockage bias in the reflectivity factor Z . The accuracy of such DEM-based Z correction procedures strongly depends on the extent of beam blockage and often requires the transition to less obstructed radar measurements from higher tilts (as in hybrid scanning schemes) when blockage exceeds 60%. In many situations, smaller sub DEM-scale anthropogenic structures (e.g., towers, buildings) and nearby trees may cause significant occultation of the radar beam and lower the quality of Z bias retrievals for these methods. As a further complication, the degree of beam blockage also depends on atmospheric refractive conditions. This may result in large errors in Z calibration procedures, particularly if anomalous propagation occurs (Bech et al. 2003).

Polarimetric measurements offer several avenues for precipitation measurements in the presence of a PBB. Most notably, polarimetric measurements of K_{DP} and ρ_{HV} are immune to partial beam blockage. Such blockage immunity may provide an opportunity for viable rainfall estimation in mountainous terrain as well as rainfall estimation at lower elevations more representative of near ground hydrometeors (e.g., Zrníc and Ryzhkov 1996). Radar calibration techniques drawing from polarimetric self-consistency (e.g., Goddard et al. 1994, Scarchilli et al. 1996) and the polarization properties of some natural scatterers (e.g., Smyth and Illingworth 1998) may also be adapted to enhance the quality of Z and Z_{DR} measurements for subsequent radar rainfall applications to longer distances and in the presence of a PBB.

To this point, the study has solely focused on the data collected by the KOUN polarimetric prototype of the WSR-88D. Although the KOUN radar is well-suited for most radar rainfall studies, PBB investigations with KOUN are challenging since the radar is relatively unobstructed at standard WSR-88D VCP 11/12 grazing angles. Nevertheless, it is possible to capitalize on the flexible scanning strategies of KOUN, as it is a research radar system. Specifically, the KOUN radar routinely scans at a 0.0° base tilt that is partially obstructed by the Earth surface. Since the KOUN 0.5° tilt is largely unobstructed, relative comparisons between the 0.0° and 0.5° tilts may provide an adequate proxy for the PBB attributed to modest terrain features. However, in light of limited KOUN radar blockage, the studies in this chapter are supplemented by the large archive of radar data collected by the low-lying NSSL Cimarron polarimetric radar that is more prone to the bias by PBB.

Several applications of polarimetric radar measurements at multiple, low, and partially blocked elevation angles are addressed in this chapter. As an initial inroad into the value of radar observations at various tilts, the first section examines changes in radial profiles of polarimetric variables at several low grazing angles collected during a widespread precipitation event. Following the procedures outlined in chapter 3, the second section provides KOUN point comparisons for conventional and polarimetric rainfall estimates at the 0.0° (blocked) elevation angle and the 0.5° (unblocked) tilt. These comparisons explore the immunity of polarimetric rainfall methods in the presence of PBB. The third section discusses methods for the calibration of conventional and polarimetric radar measurements in the presence of a PBB that may be beneficial for subsequent operational weather radar applications. The chapter concludes with an outline of the recommended changes to operational strategies for improved rainfall estimation in partially blocked regions.

4.1 Comparison of Multiple Elevation Angles

Radial profiles of polarimetric variables through the melting layer provide the initial insight into the benefits of lower elevation angles for rainfall estimation. Fig. 28 displays KOUN radial measurements at the 0.0° , 0.5° , 1.5° and 2.5° elevation angles for a volume scan from the 11/18/04 JPOLE stratiform rainfall event (00:40Z). Profiles are obtained along the 110° azimuth in the direction of modest precipitation. As described in chapter 2, the heights of the freezing level and the 4°C level from the

00Z NWS OUN sounding may reasonably approximate the boundaries of the melting layer in cold season events. For this event, the available sounding indicates that pronounced polarimetric melting signatures are likely between 2.0 km – 3.0 km AGL. Concurrent results from the operational MLDA (performed as in chapter 2) designate a melting layer between these heights.

Polarimetric signatures through the melting layer (Fig. 28) are in general agreement with the conceptual model for melting hydrometeors outlined in chapter 2. Melting signatures are more pronounced at higher elevation angles, attributed to the improved transverse resolution of the measurements. The reflectivity factor exhibits a characteristic ‘bright band’ peak, although some ambiguity exists (at the lower tilts) which is attributed to localized precipitation variability and the impacts of beam broadening. Higher elevation angles resolve these ambiguities and a pronounced increase in Z is found at slant ranges that correspond to a mean radar beam height of 2.5 km.

Along differential reflectivity profiles, a sharp increase is observed once the radar beam encounters the melting layer. This increase is most pronounced along the highest tilts, with a relative enhancement of 0.8-1.0 dB found along the 2.5° tilt. As with Z measurement profiles, the Z_{DR} enhancements are less well-defined at the lower elevation tilts, which is also attributed to precipitation variability, smoothing and beam broadening.

As stated in chapter 2, the cross-correlation coefficient ρ_{HV} is sensitive to small concentrations of mixed-phase hydrometeors and provides the best signal for the onset of melting layer contamination in radar rainfall fields. In contrast to Z and

Z_{DR} measurement profiles, there is clear evidence of melting layer signature along ρ_{HV} profiles for all tilts in Fig. 28. At the 0.5° tilt, previously defined as the radar tilt most applicable for current operational rainfall algorithms, there is a significant 0.04 - 0.05 drop over 50 km originating at the slant range of 85 km. For the 85 km slant range, the beamwidth of a WSR-88D radar at the base 0.5° tilt is approximately 1.5 km with the center of the radar beam at a height of 1.1 km above the surface. Recall that the melting layer bottom is placed slightly below 2.0 km AGL based on available sounding and MLDA results. In contrast to Z and Z_{DR} profiles, the onset of the pronounced ρ_{HV} drop along the profile is more readily attributed to the interaction of the top portion of the radar beam with the melting layer bottom. Similar arguments can be applied with respect to the other tilts shown in Fig. 28. These observations confirm that ρ_{HV} is more sensitive to melting layer contamination than Z and Z_{DR} , with particular emphasis on the response of the measurement at lower tilts where Z and Z_{DR} signatures are ambiguous.

Statistical errors of differential phase measurements increase with decreasing ρ_{HV} within the melting layer. This explains the noisy measurements of Φ_{DP} and K_{DP} and these regions. In the previous chapter, it was highlighted that fluctuations in differential phase translate to noisy measurements of K_{DP} and contribute to artificially low, nonphysical and/or negative rainfall accumulations. Since the impact of low ρ_{HV} associated with the melting layer and melting layer contamination at the lowest elevation angle occurs at larger distances, there is a sizable 30 - 40 km gain in range where K_{DP} may be safely used for rainfall estimation.

4.2 The Use of Low or Blocked Elevation Angles for Rainfall Estimation

A new radar rainfall algorithm suitable for the polarimetric WSR-88D was formulated in chapter 3 and shown to improve rainfall estimation performance to the distances mandated by the NWS. The proposed EC-methodology capitalizes on the sensitivity of polarimetric measurements to meteorological echo and applies a different rainfall relation contingent on echo type. An unstated limitation of the methodology for immediate operational implementation is that rainfall relation recommendations were based on KOUN radar studies that assume well-calibrated radar in the absence of PBB. Therefore, to successfully apply the proposed EC-methodology for rainfall estimation across the entire WSR-88D network, an operational algorithm must be flexible so as to identify and apply necessary corrections (which includes adopting different rainfall relations) when the radar is miscalibrated and/or partial beam blockage may impact rainfall variables.

If the location and extent of beam blockage is known or radar miscalibration is a concern, perhaps the simplest modification to the proposed EC-methodology would be to adopt rainfall relations that heavily capitalize on polarimetric measurements of K_{DP} that are immune to PBB. This section explores the usefulness of direct rainfall estimation with a $R(K_{DP})$ relation for partially blocked and unblocked tilts. As an additional reference, the performance of the $R(K_{DP})$ relation is compared to the performance from the standard $R(Z)$ relation that will experience bias due to PBB at the 0.0° tilt. We may determine the extent of partial beam blockage (%) for the KOUN radar at the 0.0° tilt using the expression

$$\alpha = 100 \frac{\theta_b - \theta_0 + \Omega/2}{\Omega}, \quad (64)$$

where the center of the radar beam is at elevation angle $\theta_0 = 0.0^\circ$ and the top of the blocking obstacle (surface of the earth) is defined by the elevation angle θ_b (as illustrated in Fig. 29). Ω is the radar beamwidth, which is 1.0° for the KOUN radar. Based on the KOUN tower height $h = 20$ meters and assuming standard atmospheric conditions, the value of θ_b can be determined based on simple beam geometry as

$$\theta_b = -\left(\frac{2h}{a_e}\right)^{\frac{1}{2}} = -\frac{(2 * 2 \cdot 10^{-2} \text{ km})}{8.5 \cdot 10^3 \text{ km}} = -0.124^\circ. \quad (65)$$

Substituting the value for θ_b into (64), the degree of beam blockage at the lowest KOUN tilt is roughly 37.5%.

In the presence of a partial beam blockage, Z may be expressed as the product of a shielding factor F_{shield} of the obstacle and the unobstructed value for Z

$$Z_{\text{blocked}} = Z_{\text{unblocked}} F_{\text{shield}} = Z_{\text{unblocked}} \frac{1}{\sqrt{\pi}} \int_x^\infty e^{-t^2} dt, \quad (66)$$

where a Gaussian antenna pattern is assumed with $x = 1.18\left(\frac{\alpha}{50} - 1\right)$ and the reflectivity factors expressed in linear units. Following (66) for the KOUN 0.0° blockage of 37.5%, a 1.8 dBZ bias of Z is predicted.

Twenty hours of KOUN rainfall measurements have been identified for the investigation of $R(Z)$ and $R(K_{\text{DP}})$ relations at low, blocked tilts. The subset was selected from the larger JPOLE dataset in the previous chapter and required observations during hours when the data from both the 0.0° (lowest, blocked tilt

available from KOUN) and 0.5° tilt were available. A list of the events and the hours of observations (as in Table 2) is provided in Table 4.

Hourly rainfall accumulation comparisons are performed over ARS and Mesonet network gages using the conventional $R(Z)$ and the polarimetric $R(K_{DP})$ relations from (53) and (54), respectively. To isolate errors associated with PBB on rainfall estimate performance, gages beyond 100 km have been removed to mitigate melting layer contamination. Hail contamination is a factor for some events in the dataset (based on the results of echo classification), however hail contamination will not significantly alter the interpretation of $R(K_{DP})$ relations. The corresponding gage-radar accumulation scatterplots for the 0.0° and 0.5° elevation angles are shown in Figs. 30 and 31, respectively. The images combine the results from the Oklahoma Mesonet (star symbols) and ARS (cross-hair symbols) network hourly gage comparisons.

It is not surprising that there is a relative underestimation of the hourly rainfall accumulation from the conventional $R(Z)$ relation at 0.0° as compared to the 0.5° tilt (Fig. 30). At the 0.0° tilt, the conventional relation underestimates rainfall with a bias of -0.64 mm and an rms error of 1.95 mm. For the unobstructed KOUN 0.5° tilt, there is overestimation of the rainfall with a bias of 0.74 mm and an rms error of 2.20 mm. The findings for the unobstructed 0.5° tilt are consistent with the performance of the $R(Z)$ relation in rain types I and II over the larger JPOLE rainfall dataset in chapter 3. While there is slight improvement in the rms errors at the blocked tilt, the gain is likely fortuitous and the improvement is attributed to hail contamination outliers that are partially offset by PBB.

In contrast to the performance of the conventional $R(Z)$ relation, $R(K_{DP})$ accumulations are unbiased by PBB. Bias and rms error statistics at the 0.0° elevation angle are of the same sign and similar magnitude to those obtained at the higher, unobstructed tilt (Fig. 31). For the blocked 0.0° tilt, the $R(K_{DP})$ relation underestimates rainfall with a bias of -0.7 mm and an rms error of 1.8 mm. There is a slight improvement in the performance of the $R(K_{DP})$ relation at the higher tilt that exhibits a bias of -0.6 mm and an rms error of 1.56 mm. However, if considering only higher gage accumulations (> 5 mm) as a means to mitigate noisiness inherent in K_{DP} measurements of light rain, the bias and rms errors at both the unblocked and blocked elevation angles are nearly identical.

The results indicate is that $R(Z)$ relations are biased by the presence of PBB, however there is no substantial change in the performance of the $R(K_{DP})$ relation. It is noteworthy that the $R(K_{DP})$ relation applied for the blocked tilt outperforms the standard $R(Z)$ relation at the unblocked tilt, as it is less sensitive to DSD variability and the presence of melting hail. However, noisiness in K_{DP} measurements still limits the viability of $R(K_{DP})$ relations in light rain. Therefore, although the use of K_{DP} -based relations may be beneficial in operations when compared to a Z -based relation from higher or obstructed tilts, successful application of $R(K_{DP})$ relations demands situations of moderate to heavier precipitation. Z -based rainfall measurements in light rain situations that benefit from cursory blockage correction procedures may be ideal if the blockage is not too severe.

4.3 Partial Beam Blockage Detection and Correction

Regular operation of weather radar mandates frequent calibration to ensure accurate measurements. Even modest calibration errors in the measurements of Z and Z_{DR} may produce severe deficiencies in the accuracy of radar products such as rainfall estimation and hydrometeor classification (e.g., Ryzhkov et al., 2005a). As with the errors introduced by system miscalibration or attenuation in rain, partial blockage of the radar beam further exacerbates the problem of accurate radar measurements.

The impact of partial beam blockage and radar miscalibration on reflectivity-based rainfall relations calls into question the robustness of the proposed EC-methodology in mixed phase and frozen echo. One of the advantages of polarimetric radar is its ability to measure specific differential phase K_{DP} that is immune to radar system miscalibration, attenuation in rain, and partial beam blockage. In addition to direct applications of K_{DP} measurements for rainfall estimation (as in section 4.2), it may be possible to capitalize on the unique properties of K_{DP} for radar calibration including Z and Z_{DR} calibration in the presence of a PBB to an accuracy sufficient for operational rainfall applications.

Improvements in radar data quality was a motivating factor for the polarimetric upgrade to the WSR-88D network. Several studies explore polarimetric methods for radar calibration. Ryzhkov et al. (2005b) examined the idea of self-consistency among Z , K_{DP} , and differential reflectivity Z_{DR} (e.g., Goddard et al. 1994, Scarchilli et al. 1996, Vivekanandan et al. 2003) for the KOUN radar. The calibration technique originally suggested in Goddard et al. (1994) was modified by introducing

an area-time integration approach over a large spatial/temporal domain and by incorporating multiple consistency relations for the central Oklahoma region. This calibration methodology was tested on a large dataset during the JPOLE field campaign (Ryzhkov et al. 2005c), and exhibited an accuracy to within 1 dB of the well-calibrated KTLX WSR-88D reference radar.

Application of the above consistency technique for Z calibration stipulates unbiased measurements of Z_{DR} and K_{DP} . As opposed to K_{DP} , Z_{DR} may also be significantly biased by PBB (Ryzhkov et al. 2002). This bias of Z_{DR} caused by blockage is usually manifested by an apparent azimuthal modulation of Z_{DR} in uniform precipitation. Hence, Z_{DR} should be corrected for the effects of PBB prior to calibration of Z if a consistency technique is to be utilized.

Different methods for absolute Z_{DR} calibration are discussed by Gorgucci et al. (1999), Bringi and Chandrasekar (2001), Hubbert et al. (2003), and Ryzhkov et al. (2005c) among others. They include the measurement of solar radiation at the two orthogonal polarizations and the use of natural scatterers of known polarimetric properties such as light rain and dry aggregated snow. However, none of these techniques address the assessment and correction of the Z_{DR} bias caused by PBB.

The section is organized as follows. First, observational evidence of the Z_{DR} bias caused by PBB is presented. The evidence includes data collected over a multiyear period from two polarimetric radars located in central Oklahoma. A Z_{DR} calibration technique is proposed and utilizes radar measurements of Z_{DR} in light rain and dry aggregated snow at unblocked and blocked elevations. This calibration technique was tested for the NSSL Cimarron radar that suffers from PBB at the 0.5°

tilt, and the KOUN radar that does not experience significant PBB at this tilt. Once an estimate of Z_{DR} bias has been established, a methodology for the calibration of Z in the presence of PBB will be presented following the operational self-consistency approach presented by Ryzhkov et al. (2005c). Integration is partitioned into small azimuthal sectors to assess the azimuthal modulation of the Z bias. The suggested technique is validated by direct comparisons of Z measured by the Cimarron radar and the unobstructed KTLX WSR-88D radar near Oklahoma City.

Although self-consistency studies have demonstrated the usefulness of these techniques for absolute radar calibration of Z , the proposed techniques are often difficult to implement in operations. A simple consistency method for relative blockage and radar miscalibration assessment is also provided. Motivated by the results in section 4.2, the technique examines the ratio of the rainrates from a polarimetric $R(K_{DP})$ relation that is unbiased by PBB to those from the conventional $R(Z)$ relation that is biased by PBB. For this approach, we utilize KOUN radar rainfall rates from the 0.5° tilt that is unbiased due to PBB and compare these to the rainrates from the 0.0° tilt that experiences blockage due to beam blockage by the Earth surface (e.g., Figs. 30, 31). Radar miscalibration is determined by projecting rainrate discrepancies between the blocked and unblocked tilts into Z offsets.

4.3.1 Z_{DR} Observations in the Presence/Absence of Partial Beam Blockage

4.3.1.1 Blocked radar (Cimarron)

It is often difficult to recognize the adverse effects of beam blockage on the quality of radar measurements if the blockage is not well pronounced. This was precisely the case for the Cimarron polarimetric radar. Although the Cimarron radar sits relatively low compared to the surrounding terrain (Fig. 32), the impact of PBB on the quality of dual-polarization measurements was not immediately apparent. The most common manifestations of the problem include persistent radial ‘valleys’ and ‘ridges’ in the Z or Z_{DR} fields in cases of uniform precipitation like stratiform rain and snow. Another indication of this phenomenon is a repetitive negative bias of Z -based rainfall estimates in particular azimuthal sectors. The latter can be revealed only after analysis of long-term statistics of radar-gauge comparisons. The natural spatial variability of the radar variables often obscures blockage-related azimuthal modulations of Z and Z_{DR} over shorter time frames.

The use of meteorological scatterers of known polarimetric properties provides one possible approach to investigate Z_{DR} bias (e.g., Bringi and Chandrasekar 2001, Hubbert et al. 2003, Ryzhkov et al. 2005c). Light drizzle-type rain and dry aggregate snow are possible natural calibration targets. Nearly spherical drizzle particles should exhibit Z_{DR} close to zero (in dB scale, e.g., Smyth and Illingworth 1998, Bringi and Chandrasekar 2001). However, JPOLE studies indicate that drizzle constitutes only a small portion of light rain with intensity less than 5 mm hr^{-1} , resulting in Z_{DR} values for light rain quite different from zero and dependent on drop

size distributions (Ryzhkov et al. 2005c). Fig. 33 illustrates a summary of the mean Z_{DR} - Z dependencies for central Oklahoma obtained from multi-year disdrometer data and measurements from the well-calibrated KOUN WSR-88D polarimetric radar that does not experience beam blockage problems. If highly convective events (thick black line) are excluded, the mean Z_{DR} values for light rain with intensities between 1 and 5 mm hr⁻¹ (Z between 25 and 35 dBZ) commonly vary in the range between 0.4 and 0.8 dB with median values around 0.5-0.7 dB (which are rather different than zero). Fig. 33 represents the $Z_{DR} - Z$ dependencies averaged over large number of different rain events with different DSDs. For given value of Z , the mean Z_{DR} in light rain can vary considerably from storm to storm depending on the type of DSD. Such variations can be as high as 0.6 – 0.7 dB (Ryzhkov et al. 2005c). Measurements in dry aggregated snow near the ground usually exhibit Z_{DR} below 0.3 dB with much lower variability than in light rain provided that wet snow and pristine snow crystals are excluded (Ryzhkov and Zrnica 1998a, 2003).

Because of high variability of Z_{DR} in light rain, dry snow appears to be a better calibration target for absolute calibration of Z_{DR} than rain observed at low antenna elevations. However, the impact of DSD on Z_{DR} in stratiform rain can be substantially reduced if one examines the difference between Z_{DR} at two adjacent elevations (e.g., 0.5° and 1.5°). Such difference is usually small in light stratiform rain provided that both elevations are not blocked. The partial beam blockage at lower elevation can be recognized by an increased value of the Z_{DR} difference. Identification of the areas of light rain (with rain rates between 1 and 5 mm hr⁻¹)

requires radar rainfall estimates that are unbiased by beam blockage. This is guaranteed by the use of K_{DP} , which is immune to PBB.

It is reasonable to expect that in the absence of PBB the mean value of Z_{DR} in range gates where $1 < R(K_{DP}) < 5 \text{ mm hr}^{-1}$ should not depend on azimuth provided that the averaging procedure is performed over a sufficiently large volume of data. To confirm this notion, rain rates were computed using the relation in (54) for the Cimarron data collected at the lowest tilt of 0.5° . For several rain events, we identify range gates where $1 < R(K_{DP}) < 5 \text{ mm h}^{-1}$ and partition these range gates into 1° azimuthal intervals. Recall that for light rain ($Z < 40 \text{ dBZ}$), the estimate of K_{DP} is made using a window of 25 successive gates, which corresponds to a radial resolution of about 6 km. The standard deviation of such a K_{DP} estimate is about $0.05 - 0.1 \text{ deg km}^{-1}$ (Ryzhkov and Zrnich 1996). Although the relatively large errors of K_{DP} estimation may incorrectly classify range gates as containing “light rain”, the impact of this is minimized when a large number of radials are summed. Since attenuation is nearly linearly proportional to Φ_{DP} , these measurements can also be used to correct Z_{DR} for attenuation in rain (e.g., Bringi et al. 1990). Mean Z_{DR} values for this rainrate interval are computed and examined as a function of azimuth.

Prior to Z_{DR} averaging, range gates with a cross-correlation coefficient ρ_{HV} lower than 0.7 are removed. In pure light rain or dry snow, ρ_{HV} usually varies between 0.98 and 0.997 if the dual-polarization radar is well designed. Because of quantization noise in the Cimarron data processor, the measured values of ρ_{HV} are negatively biased, and these high values have never been attained (Ryzhkov and Zrnich 1998b). This should be taken into account when interpreting the Cimarron

polarimetric data. Although the absolute values of ρ_{HV} are not reliable, relative changes are still trustworthy. Previous studies indicate that for the Cimarron radar, the 0.7 ρ_{HV} threshold is useful to discriminate between meteorological and nonmeteorological scatterers and to avoid melting layer contamination (e.g., Ryzhkov and Zrnic 1998b). To further mitigate potential melting layer contamination, only gates located within 100 km of the radar were examined. Data from the first 12 km have been removed to limit ground clutter contamination. Polarimetric bright band detection performed at higher, unobstructed elevation angles (e.g., Giangrande and Ryzhkov 2004, chapter 2) also helps reduce contamination from mixed phase hydrometeors.

The results of this analysis for 5 stratiform rain events are presented in Fig. 34a,b. Each event contains a minimum of 3 continuous hours of stratiform rainfall observations that include between 13,000 and 21,000 radials of data at the elevation of 0.5°. It is clear that averaged values of Z_{DR} at the 0.5° elevation exhibit a repetitive azimuthal dependency. In addition, the magnitude of Z_{DR} for nearly all azimuths is much lower than the expected 0.4 - 0.8 dB in Fig. 33. The composite curve in Fig. 34b shows that the standard deviation of the Z_{DR} bias estimates for each azimuth is about 0.2 dB.

Similar dependencies of Z_{DR} have been obtained for a number of snow events (Fig. 35a,b). Each of the 7 events contained a minimum of 2.5 continuous hours of snowfall data. For several of these cases, the number of azimuths exceeded 12,000 individual radials per event, however individual radial counts on the order of 5,000 were more typical due to changes in radar scanning strategy. In fact, the results in Fig.

35 exhibit a striking resemblance with the azimuthal modulation observed for light rain events, with Z_{DR} values about 0.3 dB lower as expected. The composite curve (Fig. 35b) once again shows that the standard deviation of the difference between individual curves is about 0.2 dB.

The hypothesis that PBB is responsible for the observed azimuthal modulation was confirmed by the fact that a pronounced azimuthal modulation was not revealed at the next available and mostly unblocked elevation angle of 1.5° . The difference of Z_{DR} measured at the unblocked (1.5°) and blocked (0.5°) elevation angles is shown in Fig. 36a,b. Unfortunately, data at 1.5° were not available for all of the events illustrated in Figs. 34 and 35. For the cases shown in Fig. 36, however, the observed difference between the elevation angles remains relatively stable for several years. The mean standard deviation of the Z_{DR} difference at each azimuth for these events is 0.12 dB. Analysis of reflectivity data during this period shows that the Z difference between 1.5° and 0.5° is typically within 3 dB. This suggests that the radar blockage is usually less than 50% in most directions.

As Fig. 36 shows, the Z_{DR} bias due to PBB is unacceptably high and approaches 0.8 dB in certain azimuthal sectors. This magnitude of the bias is particularly noteworthy for radar located in the Great Plains, without rugged or mountainous terrain in close proximity. In order to estimate rainfall with an acceptable accuracy, the required accuracy of Z_{DR} measurements should be 0.2 dB for moderate-to-heavy rainfall, and 0.1 dB for light rain (Ryzhkov et al. 2005c). Therefore, the correction for possible PBB must be performed before polarimetric rainfall estimation is made.

The origin of the Z_{DR} bias associated with PBB may stem from a variety of sources. First, the antenna beams at the H and V polarizations are not perfectly identical, and therefore may be obstructed differently by the same obstacle. A second possible cause is multipath propagation with different characteristics for H and V radio waves. Finally, semitransparent obstacles (like nearby trees) might have different degrees of transparency for H and V radiation similar to polarimetric grids. Note that the spike at $Az = 45^\circ$ in Fig. 35a almost disappeared on 02/05/2002 following an extreme ice storm responsible for breaking several large trees in the vicinity of the radar. Minor seasonal variations might be potentially attributed to the presence/absence of foliage on nearby trees.

4.3.1.2 Unblocked radar (KOUN WSR-88D)

The same methodology was applied to the KOUN WSR-88D polarimetric radar data presumed much less affected by PBB at the 0.5° elevation angle. A summary of 4 events (rain on 09/19/2002, 10/08/2002, 10/24/2002, and snowfall on 02/06/2003) is presented in Fig. 37a,b where the difference between Z_{DR} at the 1.5° and 0.5° elevation angles is displayed as a function of azimuth (four individual curves and one composite curve). Regions of light rain were identified using the fuzzy logic classification algorithm described by Schuur et al. (2003), as in chapter 1. As with the Cimarron data, only gates in which $1 < R(K_{DP}) < 5 \text{ mm hr}^{-1}$ were examined.

The difference in the mean Z_{DR} at the two elevations for the light rain events is particularly small and does not exhibit a pronounced azimuthal dependence. The mean value does not differ from zero by more than 0.1-0.2 dB. The only exceptions

are the azimuthal directions of 36° and 157° at which a tower of another WSR-88D radar and large University of Oklahoma buildings are located. The mean standard deviation of the Z_{DR} difference at each azimuth is 0.06 dB. This result confirms that the KOUN radar does not experience noticeable bias due to PBB except for a few isolated directions where high towers or buildings are located.

Out of the four snowfall events observed during the JPOLE project, the 02/06/2003 event was selected for analysis because of its large spatial extension and uniformity. Frequent ground observations were also available during this case, which confirm that the snow consisted primarily of large dry aggregates. Similar to the rain events, the difference in Z_{DR} between the lowest two elevation angles is within 0.1 dB.

4.3.2 Methodology for Z_{DR} Calibration in the Presence of a Partial Beam Blockage

The suggested calibration of Z_{DR} in the presence of PBB can be formulated as follows:

1. Absolute calibration of Z_{DR} has to be performed at high (unobstructed) elevation angles as described by Ryzhkov et al. (2005c). This calibration implies the measurements of solar radiation at the two orthogonal channels and/or the use of polarimetric properties of dry aggregated snow above the melting layer. These techniques demonstrate an ability to calibrate Z_{DR} with an accuracy of 0.2 dB, which is sufficient for most hydrological applications.

2. Regions of light rain should be identified using a polarimetric classification algorithm and K_{DP} measurements that are immune to PBB. An algorithm based on the fuzzy logic approach as in chapter 1 and that utilizes Z , Z_{DR} , ρ_{HV} , and texture parameters of Z and/or Φ_{DP} , $SD(Z)$, and $SD(\Phi_{DP})$, is recommended. The cross-correlation coefficient ρ_{HV} is not affected by PBB provided that the signal-to-noise ratio is sufficiently high. Because the distinction between rain and nonrain echo (e.g., bright band, ground clutter, biological scatterers) is mostly affected by ρ_{HV} , $SD(Z)$ and $SD(\Phi_{DP})$ and to a lesser extent by Z and Z_{DR} , the moderate biases of Z and Z_{DR} due to PBB do not dramatically impact the results of such rain-versus-nonrain classification. Zero weights can be assigned to Z and Z_{DR} measurements if very large biases are expected.
3. Classification should be performed for all elevation angles examined. The selection of range gates with $1 < R(K_{DP}) < 5 \text{ mm hr}^{-1}$ provides further confidence that only the data associated with light rain are chosen for subsequent averaging of Z_{DR} . An alternate option is to use more reliable and unbiased Z and Z_{DR} data at higher elevation angles to identify regions of light rain. This option implies that light rain is present at both elevations.
4. In the case of snow, one has to ensure that the snow type is suitable for Z_{DR} calibration, i.e., it has intrinsic Z_{DR} of a few tenths of a dB. Such Z_{DR} is usually observed for dry aggregated snow (Ryzhkov and Zrnic 1998a, 2003). Classification of this type of snow is more challenging than the

classification of light rain, and is often contingent on additional observational data (surface temperatures, soundings, etc.). Crystallized snow is characterized by high values of Z_{DR} and K_{DP} , whereas wet aggregated snow is associated with low ρ_{HV} combined with high Z_{DR} and moderate K_{DP} (similar to the bright band).

5. Once appropriate scatterers (light rain or dry snow aggregates) are identified, the mean value of Z_{DR} corresponding to these scatterers should be computed as a function of azimuth at the potentially blocked and unblocked elevations. The dataset should be large enough to ensure acceptable statistical error in the mean Z_{DR} value for every azimuthal interval defined by radar resolution in azimuth. In this study, 1-4 hours of data were used for such estimation. Further investigations are required to evaluate more objectively the amount of data that are needed.
6. It is very likely that in the case of snow the intrinsic Z_{DR} might exhibit a pronounced increase with height (Ryzhkov and Zrnich 1998a). If this happens and the mean Z_{DR} at the lowest unblocked elevation angle exceeds 0.3 dB, then it is recommended that only Z_{DR} data from the lowest (blocked) elevation be used.

For each azimuth, the Z_{DR} bias caused by PBB is determined as

$$\Delta Z_{DR} = \langle Z_{DR}(\text{blocked}) \rangle - \langle Z_{DR}(\text{unblocked}) \rangle \quad (64)$$

in the case of rain and snow (if $\langle Z_{DR}(\text{unblocked}) \rangle$ in snow is less than 0.3 dB) and

$$\Delta Z_{DR} = \langle Z_{DR}(\text{blocked}) \rangle - 0.2 \text{ dB} \quad (65)$$

in the case of snow if $\langle Z_{DR}(\text{unblocked}) \rangle$ is larger than 0.3 dB. It is assumed in (65) that the average intrinsic value of Z_{DR} in snow is equal to 0.2 dB.

4.3.3 *Z Calibration in the Presence of a Partial Beam Blockage*

This section describes two methods for the calibration of Z in the presence of a PBB. Once Z_{DR} is calibrated (e.g., using a technique described in the previous section), the principle of self-consistency among Z , Z_{DR} , and K_{DP} in the rain medium can be applied as a means to estimate Z bias that is expected to change with azimuth as a function of PBB. This approach allows for an absolute calibration of Z in the presence of a PBB. In addition to the above self-consistency methodology, a simple consistency calibration technique that compares the rainfall rates from $R(K_{DP})$ and $R(Z)$ relations is used to explore relative Z bias as a function of PBB.

4.3.3.1 *Self-Consistency Z Calibration Approach in the Presence of PBB*

To investigate the Z bias caused by PBB for the Cimarron radar, we adopt a modified version of the self-consistency approach offered by Ryzhkov et al. (2005c). According to the consistency principle, the radar reflectivity factor in rain can be roughly estimated from Z_{DR} and K_{DP} using the relation

$$Z = a + b \log(K_{DP}) + c Z_{DR}, \quad (66)$$

where a , b , and c are constant coefficients, Z is expressed in dBZ, K_{DP} is in deg km^{-1} , and Z_{DR} is in dB. Then, the area-time integrals of the measured K_{DP} and the K_{DP}

estimated from Z and Z_{DR} using (66) are matched by adjusting Z . This type of Z adjustment has to be performed separately for different azimuthal intervals. Since the relation (66) is valid for rain only, all nonrain echoes should be identified and filtered out prior to application of the consistency technique.

The coefficients in (66) are usually derived from large statistics of disdrometer measurements or direct radar observations in rain. A large number of the consistency relations can be found in the literature. Comparative analyses of the performance of different consistency formulas have been performed by Ryzhkov et al. (2005c) on the extensive polarimetric radar dataset obtained during JPOLE. Ryzhkov et al. (2005c) found that additional improvement could be achieved if more than one consistency relation was used. The study recommends two relations that work best for central Oklahoma rain events:

$$Z = 46.0 + 9.55 \log(K_{DP}) + 1.68 Z_{DR}, \quad (67)$$

and

$$Z = 44.0 + 12.2 \log(K_{DP}) + 2.32 Z_{DR}. \quad (68)$$

The need to use more than one consistency relation is dictated by a very high diversity of rain regimes and associated DSDs in Oklahoma. There is no unique consistency formula that “matches” all rain types. Equation (67) works better in the cases of DSDs dominated by small drops and (68) is preferable for DSDs that are characterized by a prevalence of large drops with a relative deficit of small drops. Two estimates of the Z bias are derived from (67) and (68), with only one accepted for a particular rain event using criteria formulated in Ryzhkov et al. (2005c).

In this study, the Z biases caused by PBB are examined in a limited azimuthal sector between 180° - 220° that contains the ARS micronet gauges (Fig. 38). The ARS area was also used for independent verification of the Cimarron radar calibration using the data from the operational KTLX WSR-88D radar that is located 20 km off the Cimarron radar.

Consistency relations (67) and (68) were applied separately for 5° azimuthal sectors within the 180° - 220° interval to compute two sets of estimates of the Z bias as a function of azimuth. The 5° increment was assumed adequate to resolve most details of the expected azimuthal modulation of Z bias attributed to PBB for several reasons. Although Z_{DR} biases were obtained for 1° increments, mean azimuthal dependencies (e.g., Fig. 34) indicate that resolving most modest changes in the Z_{DR} bias (excluding the larger towers) does not require such a high level of detail. In addition, since the consistency technique utilizes area-time integrals of K_{DP} , an increase in the sector size should decrease the collection time for a valid calibration to be performed.

Alternate estimates of the bias in the Cimarron reflectivity factor were obtained via direct comparison of reflectivity factors measured by the Cimarron and KTLX radars. Direct comparison of the instantaneous Z fields from the Cimarron and WSR-88D radars is not the best way to quantify the bias that is a function of azimuth with respect to the Cimarron radar. Instead, we compare point estimates of one-hour rainfall accumulation for each of the 42 rain gages constituting the ARS network from both radars using a conventional WSR-88D $R(Z)$ algorithm and determine how the difference between the two is projected into a difference in Z .

4.3.3.2 Results of Self-Consistency Z Calibration

Fig. 39 represents a summary of the Z bias estimates obtained from the consistency method (solid lines) and direct KTLX-Cimarron comparisons (diamonds and dashed lines) for 5 widespread rain events. Each event contains a minimum of two consecutive hours of hourly KTLX-Cimarron rainfall comparisons and a minimum of 3 hours of accumulated radar data for the consistency-based calibration. Every diamond in Fig. 39 indicates the result of the KTLX-Cimarron comparison obtained from one hour of observations for a particular rain gage. The dashed lines represent the mean azimuthal dependencies of the Z bias obtained from the direct KTLX-Cimarron comparisons.

Similar to Z_{DR} , the bias of Z exhibits a well-pronounced azimuthal modulation, even within a relatively narrow sector of less than 40° . The azimuthal dependencies of the bias obtained from the consistency method and direct KTLX-Cimarron comparisons show good agreement in 4 out of 5 events (except the event on 10/23/1997). In the case on 10/25/2000, the two estimates of the Z offset show very similar azimuthal dependencies, but the absolute values of the biases are about 3 dB off for all azimuths examined.

A general increase in the magnitude of the negative Z bias during the 4-year period is well captured by both methods. Note that such degradation is mostly related to the system problems with the Cimarron radar. As mentioned previously, partial beam blockage between the Cimarron 1.5° and 0.5° tilts is responsible for no more than 3 dB of the azimuthally modulated offset.

It is very difficult to quantify the accuracy of the suggested technique for Z calibration using direct comparisons of reflectivity factors from the KTLX and Cimarron radars. This is because the direct method shows significant uncertainty. There are also indications that the operational KTLX radar could be noticeably miscalibrated itself. Comparison of rainfall estimates from gauges and both radars using conventional and polarimetric rainfall algorithms shows that reflectivity from the KTLX radar was likely negatively biased prior to Fall 2000 and positively biased after that (Ryzhkov et al. 2001b).

The RMS difference between the two estimates of Z bias obtained from the consistency technique and direct comparisons of reflectivity factor measured by the KTLX and Cimarron radar is about 2.4 dB for all 5 cases combined.

4.3.3.3 Rainfall Consistency Z Calibration Approach in the Presence of PBB

The self-consistency Z calibration approach outlined above provides an estimate of the absolute radar miscalibration if sufficient data are collected in moderate rain. In the absence of a pronounced PBB, Z self-consistency techniques are straightforward to automate and may complement existing calibration procedures. Unfortunately, establishing the Z bias attributed to the combined impacts of PBB and system miscalibration is more complex and requires additional testing. In particular, Z_{DR} measurements are biased due to PBB and these biases may translate into large errors in absolute Z calibration retrievals. Because the Z_{DR} bias from blockage is often difficult to accurately assess, one approach is to consider longer-term Z retrievals in the vicinity of a PBB *relative* to known unblocked radials/regions. In this

manner, consistency methods that deemphasize or avoid Z_{DR} measurements may be equally suited.

A simplified consistency approach is proposed to investigate the relative Z bias attributed to PBB. The method examines the rainrates obtained from a conventional $R(Z)$ relation to those from a polarimetric $R(K_{DP})$ relation over blocked and unblocked regions. The operational quality KOUN radar was selected to test this approach because the system is assumed well calibrated. Since the KOUN radar is relatively unobstructed at the 0.5° elevation angle, the proposed technique compares KOUN rainfall relations between the blocked 0.0° tilt and the unblocked 0.5° tilt.

Results from previous section indicate that the polarimetric $R(K_{DP})$ rainfall relations produce unbiased rainfall accumulations at both the unblocked and blocked KOUN radar tilts. The results indicate that conventional $R(Z)$ accumulations are biased at the 0.0° tilt compared with the 0.5° tilt, which is attributed to PBB by the Earth's surface. We may express the bias in the conventional $R(Z)$ relation as

$$R(Z_b) = R(Z) * 10^{0.0714 * \Delta Z}, \quad (69)$$

where ΔZ is the bias [in dBZ], Z_b is the biased reflectivity factor = $Z \pm \Delta Z$, and R is in mm hr^{-1} . The ratio of $R(K_{DP})$ to $R(Z_b)$ from (69) is

$$[R(K_{DP})/R(Z_b)] = [R(K_{DP})/R(Z)] * 10^{-0.0714 * \Delta Z}. \quad (70)$$

For unblocked, well-calibrated radar measurements in regions of light to moderate rain, the ratio of rainrates in (70) should be close to unity. Taking the logarithm of both sides of (70) and multiplying by 10, the projected bias in Z measurements ΔZ can be expressed as

$$\Delta Z = -14 \log [R(K_{DP})/R(Z_b)]. \quad (71)$$

In the presence of a PBB, $R(Z)$ should underestimate the rainrate as compared to $R(K_{DP})$. Underestimation results in a negative value for ΔZ in (71). The expression for Z bias in (71) is straightforward and easily adapted to explore of azimuthally dependant blockages.

In practice, several factors impede the ability to obtain accurate Z bias retrievals with the method proposed in (71). It is known that $R(K_{DP})$ rainfall rate estimates are noisy and possibly negative in regions of light rain. To avoid issues associated with negative or unrepresentative rainfall rate measurements, it is suggested that the proposed method in (71) retrieves Z bias from the median ratio obtained over a large dataset. As an additional constraint, we avoid negative $R(K_{DP})$ values and consider only the retrievals for K_{DP} -based rainfall rates and corresponding polarimetric signatures consistent with light to moderate rain echo (e.g., rainrate between 1 to 10 mm hr⁻¹, high ρ_{HV}) to minimize hail contamination.

$R(K_{DP})$ rainfall relations are less sensitive to DSD variability than $R(Z)$ relations and have been found to underestimate rainfall in light to moderate precipitation. Therefore, despite K_{DP} quality control efforts, the ratio of rainfall relations in (71) is not necessarily unity. These factors limit the accuracy of Z bias retrievals, especially over short data collection intervals. It is for this reason we do not recommend the methodology in (71) for absolute radar calibration. However, the relative difference of Z bias retrievals from unblocked and blocked KOUN tilts is meaningful over longer intervals and may provide a Z correction for PBB in a manner similar to Z_{DR} calibration in (64) and (65).

In light to moderate precipitation, vertical changes in the profile of precipitation are assumed minor for small increases in the elevation angle. It was demonstrated in sections 4.1 and 4.2 that differential phase profiles and the performance of $R(K_{DP})$ is largely unchanged between the lowest KOUN tilts in rain. Rewriting the Z bias equation in (71) as a difference between the median values from the blocked (0.0°) and unblocked (0.5°) elevation angles

$$\Delta Z' = \Delta Z_{0.0} - \Delta Z_{0.5} = 14 \left(\text{median} \left[\log \left(\frac{R(K_{DP}^{0.5})}{R(Z^{0.5})} \right) \right] - \text{median} \left[\log \left(\frac{R(K_{DP}^{0.0})}{R(Z^{0.0})} \right) \right] \right). \quad (72)$$

The relation in (72) may be evaluated over various area (azimuthal) and time domains as necessary for relative blockage mapping.

4.3.3.4 Results of Rainfall Consistency Z Calibration

Fig. 40 summarizes Z bias estimates obtained from the rainfall consistency method from (72) for 4 widespread rain events during JPOLE. Each event contains a minimum of three consecutive hours of KOUN data from the 0.0° and 0.5° elevation angles. Fig. 41 plots the combined median difference between the unblocked and blocked radar tilts for all events in Fig. 40.

Similar to KOUN Z_{DR} bias mapping (Fig. 37), the bias of Z for the events in Fig. 38 exhibits a pronounced azimuthal modulation with repeatable azimuthal dependencies in several directions. Consulting the composite Z bias observations in Fig. 41, the most pronounced directions of blockage (in excess of the anticipated offset expected between the tilts) occur along azimuthal directions of roughly 60° , 90° , 157° , 200° - 270° , 315° and 345° . As with Z_{DR} , it is often difficult to attribute

these offsets to specific terrain features or towers. It is noted that directions of 60° , 157° , and 315° feature pronounced peaks for both Z and Z_{DR} long-term KOUN observation maps and are in the direction of larger towers and university buildings. There is also a relative valley in Z_{DR} measurements and a relative peak of Z between the directions of 200° - 270° , consistent with the location of a terrain ridge that is a prominent fixture on ground clutter maps within 20 km of the KOUN radar (e.g., Fig. 3, Bachmann and Zrnic 2007).

On an event-by-event basis, absolute values of the Z bias based on the method in (72) may vary significantly. As previously stated, partial beam blockage attributed to the Earth surface ($Z_{0.5^\circ} - Z_{0.0^\circ}$) is responsible for not more than 2 dB. For three events in Fig. 40, these statements are reasonable compared to mean Z bias observations for relatively unobstructed KOUN radar viewing directions, e.g., 180° . During the event on June 11, 2003, the median difference along most directions is greater than 4 dBZ. For this case, radar observations were collected in the wake of a strong squall line passage over the radar location. It is possible that the sharp temperature drop at the lowest levels of the atmosphere behind this line was conducive for additional ducting/bending of the lower radar beam into the surface. This additional ducting may explain the 2 dBZ discrepancy between the Z bias observations from this event and the other events.

4.3.4 Summary of Partial Beam Blockage Detection and Correction

Partial beam blockage (PBB) causes biases in radar reflectivity factor Z and differential reflectivity Z_{DR} . Such biases manifest themselves as azimuthal

modulations of Z and Z_{DR} in spatially uniform precipitation such as stratiform rain and snow. The biases may stem from larger terrain features (e.g., hills and mountains) or smaller obstructions in close proximity of the radar (towers, tall buildings, trees, etc.). The suggested methodologies for calibration might be helpful to improve the quality of radar data collected at blocked low antenna elevations that are beneficial to perform rainfall measurements less affected by bright band contamination, to detect regions of convection initiation associated with surface based gust fronts, and for more efficient polarimetric tornado detection (Ryzhkov et al. 2005d).

In order to recognize PBB, it is recommended to examine azimuthal dependences of the mean Z_{DR} for light rain with intensity between 1 and 5 mm h⁻¹ or dry aggregated snow at several elevation angles including potentially blocked and unblocked elevations. Identification of the areas containing light rain should be performed using polarimetric classification of radar echoes and measurements of specific differential phase K_{DP} that is not affected by PBB. Dry aggregated snow should be distinguished from other snow types such as pristine ice crystals and wet aggregates that are not efficient for recognition of PBB.

Regular observations with the Cimarron polarimetric radar reveal azimuthal modulations of Z_{DR} at the elevations of 0.5° with the depth up to 0.8 dB. No such modulation was observed for the polarimetric prototype of the WSR-88D radar. The Z_{DR} bias caused by PBB is estimated as a difference between mean values of Z_{DR} measured in light rain or dry aggregated snow at lowest unblocked and blocked elevations. Such a difference can be estimated with an accuracy of about 0.1 dB provided that the dataset is sufficiently large. Absolute calibration of Z_{DR} at higher,

unblocked elevations can be performed using the methods described in the literature (e.g., Gorgucci et al. 1999, Bringi and Chandrasekar 2001, Hubbert et al. 2003, Ryzhkov et al. 2005a).

Once Z_{DR} is corrected for effects of PBB, a self-consistency approach capitalizing on interdependency of Z , Z_{DR} , and K_{DP} in rain can be applied to calibrate Z at every azimuthal interval. The Z bias estimates obtained from the self-consistency approach in the presence of PBB have been validated using direct comparisons of radar reflectivity measured by the Cimarron radar and unobstructed operational KTLX WSR-88D radar. The two techniques exhibit similar azimuthal dependencies of the Z bias resulting from PBB. The RMS difference between the biases of Z obtained from the two methods is about 2.4 dB for all 5 cases examined. The technique does not require using digital elevation maps of terrain and does not rely on any assumptions about refractive conditions in the atmosphere. Although in the case of the Cimarron radar the occultation of the radar beam at elevation 0.5° was relatively moderate (generally less than 50%), we expect that the proposed method is applicable in the presence of more severe blockage.

Simple, consistency-based calibration techniques for relative Z biases may also prove beneficial for operational blockage detection and correction. An advantage of these methods is that they are simple to implement and avoid the issues with Z_{DR} calibration in the presence of a PBB. It was demonstrated that these approaches may also capture the situations of beam bending/ducting for individual events.

4.4 Recommendations In The Presence of a Partial Beam Blockage

To improve the recommended EC-methodology to satisfy the additional demands for an operational radar network, the suggested methodology for rainfall estimation in the presence of PBB can be modified as follows:

1. Correction of radar variables affected by PBB must be performed prior to application of echo classification routines and radar rainfall estimation. There are several methods to calibrate Z and Z_{DR} measurements that are affected by PBB, including the use of DEM-based correction procedures, examining Z and Z_{DR} differences between obstructed and nearest unobstructed beam directions (both in azimuth and elevation) in uniform precipitation, and by checking the consistency between Z , Z_{DR} , and K_{DP} in rain. As in section 4.3, the later two methods typically require long-term observations at the particular radar site before reliable estimates of the Z and Z_{DR} biases can be established. The use of DEM information is not sufficient if PBB is caused by man-made targets or trees near the radar (as with the Cimarron radar).
2. As a first step for Z calibration, a simple approach based solely on pure geometric considerations is recommended, i.e., on the degree of beam occultation based on DEM or other terrain models following (64) - (66). The “default” Z_{DR} bias should be set to zero. More accurate estimates of the PBB-related biases of Z and Z_{DR} using techniques outlined in section

4.3 can be performed after sufficient amount of the radar data becomes available at the radar site.

3. According to the proposed EC-methodology, the $R(Z, Z_{DR})$ relation should be primarily used in rain and heavy rain echo, $R(K_{DP})$ used in rain / hail, and various modifications to $R(Z)$ relations in mixed phase and frozen hydrometeors above the melting layer. The recommendations were established for unobstructed KOUN radar measurements of Z and Z_{DR} . In the presence of PBB, echo classification is questionable and measurements of Z and Z_{DR} may be less reliable than K_{DP} . In these situations, Z and Z_{DR} measurements should be used more sparingly. There are several possible combinations for the use of standard $R(Z)$ and polarimetric relations contingent on echo classification and the degree of beam blockage. We recommend the following

- i. If the beam blockage parameter $\alpha < 20\%$ (e.g., Z bias due to PBB is roughly less than 1 dB), the EC-methodology should remain unchanged.
- ii. If the blockage is $20\% < \alpha < 70\%$, we recommend that the EC-method be modified to utilize the $R(Z, Z_{DR})$ relation if the echo behind obstruction is classified as light/moderate rain, but to switch to the $R(K_{DP})$ relation if the echo is classified as heavy rain or rain / hail (HR or RH). Modified $R(Z)$ relations are still applied above the melting layer, however the quality of all relations is questionable.

- iii. If the blockage $\alpha > 70\%$, we recommend avoiding the elevation angle for classification and rainfall estimation behind the obstruction. As in hybrid scanning strategies, we recommend switching to the next highest elevation and reassessing the blockage.

5. MODELING OF THE MELTING LAYER: POSSIBILITIES FOR POLARIMETRIC VPR CORRECTION

Widespread radar observations in melting layer regions are noteworthy given limited and costly laboratory or *in situ* sampling of the melting process and hydrometeor characteristics therein (e.g., Stewart et al. 1984, Willis and Heymsfield 1989, Mitra et al. 1990, Barthazy et al. 1998, Oraltay and Hallett 2005). Many studies have linked conventional radar melting layer or bright band signatures, as well as the prominence of these signatures, to hydrometeor type and precipitation microphysics (e.g., Atlas 1957, Fabry and Zawadzki 1995, Drummond et al. 1996). A detailed understanding of the atmospheric conditions and important hydrometeor interactions/properties that produce polarimetric radar signatures within the melting layer may provide critical information for improving radar rainfall estimates beneath.

High resolution modeling of the melting layer may offer valuable insight into the microphysical processes that affect vertical profiles of polarimetric variables. Previous studies directly compare model output to conventional radar reflectivity factor observations (e.g., Ekpenyong and Srivastava 1970, Klaassen 1988, Szyrmer and Zawadzki 1999). Few studies have expanded these efforts in an attempt to reproduce polarimetric measurements for comparison with observed polarimetric radar data (e.g., Russchenberg and Ligthart 1996, D'Amico et al. 1998) and eventual improvements in rainfall estimation.

This chapter explores polarimetric observations of the melting layer and provides a simple melting layer model to gain a better understanding of the important

physical processes within. The motivation for this effort is in the potential for improvements to conventional VPR methods for rainfall estimation to longer distance through the addition of polarimetric insight. The working hypothesis to be tested is as follows. Aggregation increases the median size of raindrops beneath the melting layer (that ultimately reach the surface), whereas riming tends to decrease this median size. Therefore, for the same value of reflectivity factor Z aloft, traditional VPR-based rainfall estimates overestimate for the cases of strong aggregation and underestimate for cases of intense riming. However, aggregation and riming differently affect the polarimetric parameters of the melting layer, such as those for Z_{DR} and ρ_{HV} , which may be modeled. In this manner, our knowledge of the behavior of the polarimetric measurement profiles through the melting layer could be directly applicable to improve rainfall estimation in the rain medium below.

The chapter is organized into two major parts. In the first section, we examine vertical profiles of polarimetric measurements and explore the relationship between conventional and polarimetric bright band signatures. Such long-term polarimetric observations are necessary to evaluate the performance of melting layer modeling efforts. A basic statistical analysis of these profiles will also complement the existing literature documenting the behavior of the conventional radar reflectivity factor through the melting layer (e.g., Fabry and Zawadzki 1995). KOUN radar observations for several events featuring prominent melting layer signatures have been compiled for this analysis.

In the second section, we provide the theoretical background and results for a polarimetric melting layer model. The basic thermodynamic framework for this

model follows directly from several previous published efforts. A goal is to reproduce cases of strong aggregation and riming. To differentiate this work from the previous melting layer modeling studies, our results focus on the ability to reproduce key polarimetric signatures with such models. The strengths and limitations of the model, as well as additional methods to improve the accuracy of the model, are discussed.

5.1 Polarimetric Melting Layer Signatures

Long-term melting layer observations of the conventional reflectivity factor are widely documented in the literature (e.g., Fabry and Zawadzki 1995), however systematic observations of polarimetric variables within the melting layer are largely unavailable. The motivation for compiling polarimetric radar observations of melting is similar to that for Z . Longer-term polarimetric observations from a wide range of precipitation regimes may allow for the quantification of the contributions from various microphysical processes responsible for bright band signatures. The importance of different microphysical processes may also be determined indirectly through comparisons of long term signatures with microphysical modeling efforts. Following the Fabry and Zawadzki (1995) model, the calculation and relationships between several key polarimetric parameters of the melting layer have been examined below.

5.1.1 Data and Analysis Methods

As an initial effort toward documenting long-term polarimetric melting signatures, an analysis has been performed for 10 events observed by the KOUN radar during the JPOLE field campaign. All selected events feature prominent, widespread polarimetric melting layer signatures and were selected for analysis based on the frequency and duration for which MLDA results were available. Characteristic profiles of Z , Z_{DR} , and ρ_{HV} were obtained in the directions of the most pronounced melting layer signatures for each event. To reduce the impact of beam broadening / smoothing on the interpretation of polarimetric signatures, three higher KOUN elevation angles of 19° , 16° , and 10° were utilized. A list of the events is in Table 5.

Several parameters of the melting layer have been obtained from the set of measurement profiles. The definitions of these parameters largely follow Fabry and Zawadzki (1995) for conventional Z measurement profiles. A ‘typical’ set of Z , Z_{DR} , ρ_{HV} profiles is shown in Fig. 42. This image contains a description and the location of several key polarimetric parameters. For this analysis, the radar parameters are determined as follows. For each profile of ρ_{HV} , we determine the heights at which ρ_{HV} drops below 0.99 in the vicinity of the melting layer (based on MLDA results). These locations serve as a proxy for the top and bottom of the melting layer. We noted that this definition differs from the one utilized by Fabry and Zawadzki (1995) that is based on the change in the slope of the Z profile. It is again argued that the drop in ρ_{HV} is more sensitive to the presence/absence of melting particles and has a stronger physical basis for top/bottom designation.

Once the melting layer boundaries along a profile are established, parameters including the height and magnitudes of peaks/extremes in Z , Z_{DR} , and ρ_{HV} are easily determined. The parameter values for Z and Z_{DR} in snow aloft and rain beneath the melting layer are specified 50 meters from boundary locations. In this analysis, the melting layer thickness is defined as the difference between the melting layer top and bottom heights and based on ρ_{HV} signatures as in Fig. 40.

5.1.2 Polarimetric Bright Band Parameters

A scatterplot of Z in the regions of snow above the melting layer versus the corresponding values in the rain medium beneath is shown in Fig. 43. Similar to the findings of Fabry and Zawadzki (1995), the Z values found in both regions are comparable and straddle the 1:1 line on the plot. The median value of Z is higher for rain (31.7 dBZ) than in snow (31.3 dBZ), although Z is largely conserved at the peripheries of the melting layer. The findings for these events support arguments that aggregation and breakup in the melting layer accounts for less than a 1 dB change in Z (e.g., Fabry and Zawadzki 1995, Szyrmer and Zawadzki 1999).

Fig. 44 contains a scatterplot of Z in rain versus the corresponding peak Z in the melting layer. As anticipated, there is a substantial melting layer Z enhancement ($\Delta Z = Z_{\text{peak}} - Z_{\text{rain}}$) for all profiles examined. The mean and median enhancement in Z is 9 dB and varies between 4 dB and 16 dB. These bright band enhancements are comparable to the values observed by Fabry and Zawadzki (1995) for modest rainrates ($R < 3 \text{ mm hr}^{-1}$). However, since the observations of Fabry and Zawadzki (1995) were performed with an X-Band radar system, caution is advised when

comparing relative magnitudes of Z enhancements that depend on radar wavelength. While a large peak Z is typically associated with a larger value of Z in rain, the enhancement ΔZ does not strongly correlate with Z in rain (e.g., Klaassen 1988, Fabry and Zawadzki 1995).

The interpretation of conventional melting layer signatures may be aided by the addition of polarimetric parameters. Fig. 45 shows a scatterplot of Z_{DR} in snow versus rain as was plotted for Z . Unlike measurements of Z , Z_{DR} measurements exhibit very different values at the boundaries of the melting layer. Low density dry snow aggregates aloft exhibit low Z_{DR} with a mean and median of 0.47 dB (consistent with chapter 4). Mean and median Z_{DR} values in rain are higher and exceed 0.8 dB.

The Z_{DR} enhancement ΔZ_{DR} in the melting layer as compared with the value of Z_{DR} in the underlying rain is shown in Fig. 46. The average profile exhibits a 0.7 dB enhancement in the melting layer, with relative peak values ranging from 0.3 dB to 1.2 dB above the value in rain. The magnitude of the Z_{DR} peak generally exceeds 1.0 dB for the event profiles. Several events recorded peak Z_{DR} in excess of 2 dB in the melting layer, indicative of large melting snow aggregates. Mean and median peak Z_{DR} exceed 1.5 dB and are significantly higher than the mean and median values observed in rain or snow. High peak Z_{DR} values are associated with higher Z_{DR} values in rain, which is not unexpected if aggregation that generates large hydrometeors within the melting layer is responsible for an increase in median drop size in the rain beneath.

Minimum values of ρ_{HV} within the melting layer ranged between 0.81 and 0.97 for the profiles in the dataset, with a mean and median value of 0.91. Among the

polarimetric parameters, the most pronounced relationship between parameters was found for these minimum values of the correlation coefficient and peak Z_{DR} (Fig. 47). This result is expected since both Z_{DR} and ρ_{HV} are not weighted by concentration and extreme values for both are sensitive to the presence of resonance-sized melting aggregates (those with a resonance factor $(D |\epsilon|^{1/2}) / \lambda \sim 1$). There is loose connection between Z peak and ρ_{HV} (Fig. 48) because Z depends on concentration whereas ρ_{HV} does not.

Cross-comparisons between Z and Z_{DR} parameters reveal additional, nontrivial connections. While the relationship between ρ_{HV}/Z_{DR} and Z parameters is often weaker, large peak Z values are often associated with high Z_{DR} in the rain beneath the melting layer (Fig. 49). Large ΔZ enhancements also trend toward high Z_{DR} measurements in rain (Fig. 50). However, the opposite is not true, e.g., large or pronounced peaks in Z_{DR} provide less insight into the value of Z for rain, attributed to sensitivity of Z_{DR} to resonance-sized particles.

In chapter 2, it was argued that the peak values of Z_{DR} and ρ_{HV} should reside at heights equal to or below the height of the peak in Z . On the average, the relative height of the Z peak was located just slightly above the middle of the melting layer, similar to the findings of Fabry and Zawadzki (1995). As confirmation of the statements in chapter 2, the height of the Z_{DR} peak was found at/below the height of the ρ_{HV} minimum for all event profiles and always located below the height of Z peak. The typical separation between peak heights was on the order of 100 meters for the profiles examined.

The thickness of the melting layer (depth of the ρ_{HV} drop) ranged between 0.6 km and 1.2 km with a mean and median of 0.9 km. As suggested in Fabry and Zawadzki (1995), deeper melting layers typically corresponded to higher rainrates (values of Z) in the rain beneath (Fig. 51). For this dataset, thickness was strongly linked to the absolute height of the melting layer top (Fig. 52). The result is a likely indication that the warm season MCS events in the dataset with higher freezing levels also often featured deep, low relative humidity layers below the melting layer favorable for extended melting layer depths (e.g., see theoretical melting layer discussion in the next section.).

5.2 Model of the Melting Layer

This section outlines a simple model of the melting layer capable of reproducing polarimetric radar measurement profiles. Validation of the model may be performed against observed polarimetric radar measurement profiles and parameters as shown in the previous section. The model assumes that one snowflake produces one raindrop (e.g., Ohtake 1969, Mitra et al. 1990, Szrymer and Zawadzki 1999). This assumption greatly simplifies the modeling problem by avoiding the need to numerically solve the stochastic collection or breakup equations for melting particles. In our initial simulations, melting hydrometeors are treated as Rayleigh scatterers to simplify calculations of radar measurements. For melting layer models of the conventional reflectivity factor Z profiles, the above assumptions have produced

reasonable results (e.g., Klaassen 1988, Szrymer and Zawadzki 1999). However, several field studies indicate the presence of large melting aggregates within the melting layer resulting from collisions in the upper portion of the melting layer as well as breakup in the lower sections (e.g., Stewart et al. 1984, Willis and Heimsfield 1989, Barthazy et al. 1998, Goeke and Waldvogel 1998). Although aggregation and breakup processes may offset by the lower boundary of the melting layer, such particle interactions may be critical for the accurate replication of polarimetric profiles and parameters within the layer.

5.2.1 Thermodynamic Background of the Model

The heat balance equation for a melting snowflake / small graupel can be expressed as (e.g., Klaassen 1988)

$$L_f m \frac{df}{dt} = 2\pi D_m F_m [K(T - T_0) + D_v L_v (\rho - \rho_0)], \quad (73)$$

where m is a mass of melting snowflake, $f = m_w/m$ is mass fraction of melted water, D_m is the diameter of a melting snowflake (assumed spheroid), K is the thermodynamic conductivity of air, D_v is the diffusivity of water vapor in air, L_f is the latent heat of fusion of water, L_v is the latent heat of vaporization, F_m is the ventilation coefficient, and $(T - T_0)$ and $(\rho - \rho_0)$ are the temperature and vapor density differences between the air and the surface of the melting particle.

The vapor density difference from (74) may be expressed as

$$\rho - \rho_0 = \frac{e(T)}{R_v T} - \frac{e_s(T_0)}{R_v T_0} = \frac{RH}{100} \frac{e_s(T)}{R_v T} - \frac{e_s(T_0)}{R_v T_0}, \quad (74)$$

where e is the water vapor pressure, e_s is saturation (equilibrium) vapor pressure, RH is the relative humidity (expressed in %), and R_v is the gas constant for water vapor.

Expanding the saturation vapor pressure $e_s(T)$ as

$$e_s(T) = e_s(T_0) + \frac{de_s}{dT}(T - T_0) \quad (75)$$

and using the Clausius – Clapeyron equation

$$\frac{de_s}{dT} = \frac{L_v e_s}{R_v T^2}, \quad (76)$$

the vapor density difference in (75) may be expressed as

$$\rho - \rho_0 \approx \left(\frac{RH}{100} - 1 \right) \frac{e_s(T_0)}{R_v T_0} + \frac{RHL_v e_s(T_0)}{100 R_v^2 T_0^3} (T - T_0). \quad (77)$$

The expression in (77) may be substituted into (73) as

$$L_f m \frac{df}{dt} = 2\pi D_m F_m \left[\left(\frac{RH}{100} - 1 \right) \frac{D_v L_v e_s(T_0)}{R_v T_0} + \left(K + \frac{RHD_v L_v^2 e_s(T_0)}{100 R_v^2 T_0^3} \right) (T - T_0) \right]. \quad (78)$$

For the expression in (78), it is assumed that the surface temperature of the melting snowflake is 0°C. Therefore, the melting of a snowflake starts immediately at $T = 273^\circ\text{K}$ (0°C) if $RH = 100\%$, e.g., the air is saturated. If the air is subsaturated ($RH < 100\%$), snowflake melting begins at slightly positive temperature T_m for which right-hand side of (78) is equal to zero (e.g., Mitra et al. 1990). For several JPOLE events with prominent melting layer signatures, the relative humidity from available soundings within melting layer regions was observed below 100%. In the presence of strong entrainment of dry ambient air (e.g., trailing stratiform sections of MCS events), the RH can drop as low as 60 – 70 %. Under these conditions, the onset of

melting may be delayed until the ambient air temperature is in excess of 2°C (e.g., Rasmussen and Pruppacher 1982).

Eq. (78) may be simplified as

$$L_f m \frac{df}{dt} = 2\pi D_m F_m \left(K + \frac{RH D_v L_v^2 e_s(T_0)}{100 R_v^2 T_0^3} \right) (T - T_m). \quad (79)$$

Substituting known constants $K = 2.428 \cdot 10^{-2} \text{ J m}^{-1} \text{ s}^{-1} \text{ K}^{-1}$, $D_v = 2.26 \cdot 10^{-5} \text{ m}^2 \text{ s}^{-1}$, $L_v = 2.5 \cdot 10^6 \text{ J kg}^{-1}$, $R_v = 461.5 \text{ J K}^{-1} \text{ kg}^{-1}$, $e_s(T_0) = 611 \text{ kg m}^{-1} \text{ s}^{-2}$, and $T_0 = 273 \text{ K}$ into (79) yields

$$L_f m \frac{df}{dt} = 2\pi D_m F_m \left(2.4310^{-2} + \frac{RH}{100} 1.9910^{-2} \right) (T - T_m). \quad (80)$$

Noting that

$$\frac{df}{dt} = \frac{df}{dh} \frac{dh}{dt} \quad \text{and} \quad \frac{df}{dh} = \frac{df}{dt} \frac{1}{U_m}, \quad (81)$$

then (80) can be expressed as

$$\frac{df}{dh} = \frac{2\pi D_m F_m}{L_f m U_m} \left(2.4310^{-2} + \frac{RH}{100} 1.9910^{-2} \right) (T - T_m). \quad (82)$$

In (81) – (82), h is height and U_m is terminal velocity of melting snowflake.

Szyrmer and Zawadzki (1999) showed that the product $D_m F_m$ in (82) can be expressed using the melted diameter of snowflake D_w

$$D_m F_m = B_m D_w^{A_m} \quad (83)$$

where $A_m = 1.7$ and $B_m = 6.58$, with D_w and D_m expressed in mm. Szyrmer and Zawadzki (1999) and Zawadzki et al. (2005) recommend expressing terminal velocity of melting snowflakes U_m using the terminal velocity of the corresponding raindrops (to which snowflakes melt) U_r and the mass melted water fraction f as

$$U_m = \frac{U_r(D_w)}{g(f)} = \frac{U_r(D_w)}{a - bf(1+f)}, \quad (84)$$

where

$$a = 1.26\rho_s^{-1/3}, \quad b = (a - 1)/2, \quad (85)$$

and ρ_s is a density of dry snowflake in g/cm^3 prior to melting.

For this model, we adopt the approximation of Brandes et al. (2002) for the terminal velocity of raindrops

$$U_r(D_w) = \left(\frac{\rho_0}{\rho} \right)^{1/2} (-0.1021 + 4.932D_w - 0.9551D_w^2 + 0.07934D_w^3 - 0.002362D_w^4). \quad (86)$$

In (86), ρ is the density of air at arbitrary height, ρ_0 is the density of air at 1000 mb (hPa), D_w is expressed in mm and U_r is in m/s.

The density of dry snowflakes depends on snowflake size and the degree of riming f_{rim} . In this model, the following formula for ρ_s is used (adopted from Brandes et al. 2007)

$$\rho_s = 0.178f_{rim}D_w^{-0.922}, \quad (87)$$

where D_w is expressed in mm and ρ_s is in g/cm^3 . For unrimed snow, $f_{rim} = 1$. If snow is rimed, then it is assumed that $f_{rim} > 1$ does not change across the size spectrum, but that the snow density can not exceed 0.5 g/cm^3 (Zawadzki et al. 2005). As riming increases, the density of the snowflake and its terminal velocity increases. Fig. 53 illustrates the change in the terminal velocity of a melting snowflake depending on the melted water diameter and degree of riming for six values of mass water fraction: 0, 20, 40, 60, 80, and 100%.

In the model, we assume a linear dependence of ambient temperature with height (no interaction between the melting particles and the environment)

$$T - T_m = \gamma(h - h_m), \quad (88)$$

such that the balance equation in (82) may be expressed as

$$\frac{df}{dh} = \frac{12B_m g(f, D_w, f_{rim}) \gamma}{L_f \rho_w D_w^{3-A_m} U_r(D_w)} \left(2.4310^{-2} + \frac{RH}{100} 1.9910^{-2} \right) (h - h_m), \quad (89)$$

where ρ_w is density of water. Taking into consideration that $A_m = 1.7$ (e.g., Szyrmer and Zawadzki 1999), $U_m(D_w) \sim D_w^{0.67}$ and $g \sim D_w^{0.37}$, the rate of melting is approximately proportional to D_w^{-2} and $(f_{rim})^{-1/3}$. Moreover, the expression in (89) indicates that bigger and/or rimed snowflakes melt faster. With respect to the initial environmental conditions, not surprisingly the rate of melting slows in dry, low relative humidity air and for low lapse rates γ . If we note that $L_f = 336.1 \cdot 10^3 \text{ J kg}^{-1}$, a further simplification of (89) yields

$$\frac{df}{dh} = 5.71 \cdot 10^{-6} \left(1 + 0.82 \frac{RH}{100} \right) \frac{g(f, D_w, f_{rim}) \gamma}{D_w^{1.3} U_r(D_w)} (h - h_m). \quad (90)$$

In (90), D_w is expressed in mm, U_r is in m/s, γ is in $^{\circ}\text{km}^{-1}$, and h is in m. The model in (90) is a nonlinear differential equation which can be solved numerically. The diameter and density of melting snowflake are functions of the mass water fraction f

$$D_m = D_w \left[\frac{\rho_w}{\rho_s} \left(1 - f + \frac{\rho_s}{\rho_w} f \right) \right]^{1/3} \quad (91)$$

and

$$\rho_m = \frac{\rho_s \rho_w}{f \rho_s + (1 - f) \rho_w}. \quad (92)$$

5.2.2 Snowflake/Drop Size Distribution

Computations in the model are performed assuming that the raindrop size distribution at the bottom of the melting layer is Marshall – Palmer exponential form

$$N(D_w) = 8000 \exp(-\Lambda_w D_w) \quad (93)$$

where the slope $\Lambda_w = 4.1 R^{-0.21}$ (R is the rainrate in mm hr^{-1}), D_w is expressed in mm and $N(D_w)$ is in $\text{m}^{-3}\text{mm}^{-1}$. The distribution is truncated such that the largest allowable raindrop size is 8 mm.

Recall that for this simple model approach, there is a one-to-one correspondence between the snowflakes and raindrops to which these snowflakes melt. Thus, the smaller snowflakes in the model melt faster than the larger snowflakes and produce smaller raindrops beneath the melting layer. This also implies that the largest particles are present at the very top of the melting layer, which contradicts the observations of several studies (e.g., Barthazy et al. 1998, Goeke and Waldvogel 1998). For this model, the maximal diameter of raindrops originated from fully melted snowflakes is shown as function of the fall distance from the top of the melting layer in Fig. 54. At any given height level, raindrops originating from fully melted snowflakes and partially melted snowflakes have very distinct size distributions as Fig. 55 demonstrates. It is assumed that mass flux is conserved along the height in each bin of the snowflake melted diameter. The size distribution of melted snowflakes $N(D_m)$ is expressed as

$$N(D_m) = N(D_w) [a - bf(1+f)] \frac{dD_m}{dD_w}. \quad (94)$$

In (94), $N(D_w)$ is determined by (93) and the mass fraction of melted water is obtained as a solution of (90). Following Fig. 55, it is clear that the size distribution

of hydrometeors is close to exponential only at the peripheries of the melting layer. Within the melting layer, the size distribution is close to bi-exponential, which agrees with the observations of Barthazy et al. (1998) and Goeke and Waldvogel (1998). The slope of DSD for the rain part of size spectrum ($\Lambda = 2.92 \text{ mm}^{-1}$) is much larger than the corresponding slope for the snow part ($\Lambda \approx 0.5 \text{ mm}^{-1}$). It is no surprise that the terminal velocities of the hydrometeors are also very different in the rain, mixed-phase and snow parts of the spectrum (Fig. 56).

5.2.3 *Shape and Dielectric Properties of Melting Snowflakes*

For the KOUN polarimetric prototype of the WSR-88D, observational studies in section 5.1 considered vertical profiles and profile parameters of the three primary polarimetric variables useful for understanding microphysical processes within the melting layer: reflectivity factor Z_H at horizontal polarization, differential reflectivity Z_{DR} , and cross-correlation coefficient ρ_{hv} . As described in chapter 1, these radar variables depend on the size distribution of the hydrometeors, hydrometeor shape, particle orientation, and phase composition (i.e., density and water content). These radar variables can be calculated from Eqs. (15) – (18) based on the output of the cloud model described in the preceding sections and by using several assumptions about the shapes and orientations of hydrometeors of different types.

For model radar computations, a zero mean canting angle of hydrometeors is assumed. The width of the canting angle distribution σ is allowed to vary with particle size and depends on mass water fraction f

$$\sigma = \sigma_s + f(\sigma_r - \sigma_s) \quad (95)$$

where σ_r is the width of canting angle distribution for raindrops, whereas σ_s is the corresponding value for dry snowflakes. Suitable values of σ_r and σ_s are 10° and 40° , respectively.

For the initial run of the model, all liquid, frozen and mixed-phase hydrometeors are assumed oblate spheroids (horizontal axis greater than or equal to the vertical axis) that justify use of the Rayleigh approximation (e.g., $D_m|\epsilon_m|^{1/2}/\lambda \ll 1$). In the Rayleigh approximation, scattering amplitudes are estimated following chapter 1 Eqs. (3) – (6). The axis ratio of raindrops beneath the melting layer follows from Brandes et al. (2002). For snowflakes throughout the melting process, the axis ratio is assumed to vary linearly as a function of the melted water mass fraction from a value of 0.8 in dry snow aggregates to a final value for rain as predicted by the Brandes et al. (2002) study. This axis ratio dependence of a melting snowflake may be expressed as

$$\frac{a}{b} = 0.8 + f (A_r - 0.8), \quad (96)$$

where A_r is the axis ratio of the raindrop size to which the snowflake eventually melts.

At S band for a temperature $T = 0^\circ\text{C}$, the dielectric constant of bulk ice is $\epsilon_i = 3.17 - j 8.54 \cdot 10^{-3}$ and the dielectric constant of water is $\epsilon_w = 79.7 - j 25.2$. For dry graupel or snowflakes in this study, the dielectric constant of the snowflakes entering the melting layer can be obtained as

$$\epsilon_s = 1 + \frac{3 \frac{\rho_s}{\rho_i} \frac{\epsilon_i - 1}{\epsilon_i + 2}}{1 - \frac{\rho_s}{\rho_i} \frac{\epsilon_i - 1}{\epsilon_i + 2}}. \quad (97)$$

In (74), the dielectric model of snowflakes follows Maxwell Garnett mixing formulas for the basic topology of uniformly mixed spherical ice inclusions in an air matrix (e.g., Bohren and Battan 1982, Meneghini and Liao 1996). Here, $\rho_i = 0.92 \text{ g/cm}^3$ is density of bulk ice and the snowflake density ρ_s is determined from (87). Note from (97) that if snowflake density is equal to that of bulk ice, ε_s reduces to ε_i . For dry snow above the melting layer, the dielectric constant found in (97) may be substituted into (15) – (18) to estimate radar variables.

For melting snowflakes (e.g., within melting layer regions), the dielectric constant of depends on the snow density and volume fraction of water in the snowflake. In addition, the manner with which the melted water is distributed within the melting snowflake (topology) also affects the value of ε . Previous studies by Fabry and Szyrmer (1999) describe at least 6 different models for the topology of melting snowflakes. For this modeling study, three dielectric models are adopted following Maxwell Garnett mixing formulas for three component mixing (e.g., Meneghini and Liao 1996). In the first model (Model A), the dielectric constant of a melting snowflakes is given by

$$\varepsilon_{ws} = \varepsilon_w \left[1 + \frac{3(1-fv) \frac{\varepsilon_s - \varepsilon_w}{\varepsilon_s + 2\varepsilon_w}}{1 - (1-fv) \frac{\varepsilon_s - \varepsilon_w}{\varepsilon_s + 2\varepsilon_w}} \right]. \quad (98)$$

where ε_s is first obtained by substituting the expression in (74). In Model A, the topology of melting snowflakes is that of a water matrix with snow (ice in an air matrix) inclusions. For the above expression, fv is volume fraction of water. The value of fv is easily computed from the mass fraction of water f as

$$fv = \frac{\rho_s f}{\rho_w - \rho_w f + \rho_s f}. \quad (99)$$

For the second dielectric model (Model B), the dielectric constant of melting snowflakes is determined as

$$\varepsilon_{ws} = \varepsilon_s \left[1 + \frac{3(fv) \frac{\varepsilon_w - \varepsilon_s}{\varepsilon_w + 2\varepsilon_s}}{1 - (fv) \frac{\varepsilon_w - \varepsilon_s}{\varepsilon_w + 2\varepsilon_s}} \right]. \quad (100)$$

In Model B, the topology of the melting snowflakes is that of a snow matrix (air matrix with ice inclusions) with spherical water inclusions.

For the third model (Model C), a mixture of the previous models is adopted. The relative contribution from Models A and B is determined based on the volume fraction of water and the error function (e.g., Meneghini and Liao 1996)

$$\varepsilon_{ws} = \frac{1}{2} [(1-t)\varepsilon^A + (1+t)\varepsilon^B], \quad (101)$$

$$t = \text{Erf}\left(\frac{1-fv}{fv} - 0.2\right) \quad \text{if } fv > 0.01, \quad (102)$$

where ε^A and ε^B represent the dielectric constants determined from Models A and B, respectively. This model aims for a more realistic topology of melting snowflakes consistent with laboratory studies (e.g., Mitra et al. 1990). For small volume fractions of water ($t \approx 1$), the dielectric constant is weighted towards the value of Model B (snow matrix with water inclusions). For higher volume fractions of water, the relative dielectric constant is weighted toward that of Model A (water matrix with ice inclusions).

5.2.4 Comparisons of Model Profiles with Observed Melting Layer Signatures

i. A Low Density Aggregate Example

For the initial set of melting layer radar measurement profile simulations, the density of snowflakes entering the melting layer follows (87) with the riming factor set at 1. A riming factor of 1 implies low density aggregates are entering the melting layer. For the model runs, the relative humidity has been set at 100% to initiate the melting of snow at the height of the freezing level. The lapse rate for these model runs is assumed moist adiabatic. Individual snowflakes melt to form a Marshall-Palmer size distribution (recall, maximum raindrop size beneath the melting layer is 6 mm) of raindrops consistent with a rainfall rate of 3 mm hr^{-1} .

Fig. 57 shows the vertical profiles for the reflectivity factor Z corresponding to the scattering Models A (solid curve), B (dotted curve) and C (dashed curve). Z profiles in Fig. 57 exhibit bright band enhancements ranging in intensity from 2 to 15 dB. The most pronounced enhancement in Z is observed for scattering Model A, the one which models the topology of melting snowflakes as a water matrix with snow inclusions. The Z enhancement for this dielectric model of 15 dB seems too high for the 3 mm hr^{-1} rainrate. Qualitative performance measures such as the profile shape and the relative location of peak Z are also questionable compared with radar observations, with peak Z located closer to the freezing level than long-term observation dictate.

A substantially weaker response in the simulated Z profile is obtained through the application of dielectric Model B, the model that reverses the roles of snow and water in snowflake topology. The 2 dB bright band enhancement is also in poor

agreement with long-term KOUN radar observations. Profile shape and the height of peak Z for Model B are also not significantly improved over Model A when compared with KOUN radar observations.

Dielectric Model C offers a reasonable compromise to the performances of Models A and B for simulated Z profiles. The enhancement in Z is 10 dB, in good agreement with long-term radar observations from the previous section. Qualitatively, relative Z peak location and the shape of the Z profile are more consistent with the radar observations than for the other models.

The general performance of the three scattering models with respect to the previous literature on conventional melting layer Z profile simulations is comparable. The bright band signatures in Model A are too intense, a common response of scattering models that use water as the dominant media for the matrix and snow as inclusions (e.g., Fabry and Szrymer 1999). Water-dominant or concentric sphere dielectric models may be appropriate for melting hail or graupel for which water tends to soak around or coat the ice during melting. However, this topology for the distribution of melt water is not as typical for melting snowflakes, especially at the beginning stages of melting (e.g., Mitra et al. 1990). It follows from (98) that even for relatively small volume fractions of water, the dielectric constant for melting snowflakes increases rapidly to that of water. In contrast, although the topology in dielectric Model B may better represent the early stage of melting (water flowing down branches of snowflakes toward the center of the particle), this topology is inadequate to capture the enhancement associated with the eventual collapse of the ice crystal structure in a mixed-phase particle before forming a water droplet (e.g.,

Mirta et al. 1990). It is as no surprise that Model C is optimal, as it blends the behavior of both the initial and final stages of melting snowflakes.

Although the simulated Z profiles capitalizing on dielectric Model C perform well under the initial simulation conditions, the sensitivity of these profiles to the model input parameters should be briefly considered. For example, low values for the lapse rate and relative humidity decrease the melting rate, which broadens the modeled bright band signatures. It is easy to demonstrate with the thermodynamic model in (90) that a $1\text{-}2^\circ \text{ km}^{-1}$ change in the lapse rate is comparable to a RH drop from 100% to 50%. In the current thermodynamic framework, the only qualitative difference introduced by these parameters is that RH controls the temperature at which snowflake melting initiates. It is worth noting that for the current model, simple changes to the RH and lapse rate do not impact the magnitude of the Z peak or the relative peak location. A broadening of the melting layer signatures is observed with higher input rainrates (smaller slope Λ), consistent with the presence of additional and larger snowflakes entering the melting layer (recall, the raindrop DSD is truncated by a maximum raindrop size of 8 mm). The increase in the rainrate also leads to an increase in the value of Z proportional to the increase in the number of medium to larger diameter snowflakes falling into the melting layer. However, the bright band enhancement ($Z_{\text{peak}} - Z_{\text{rain}}$) for the model is largely insensitive to changes in rainrate beneath the layer. This is attributed to the lack of aggregation and the inability of the current model to retain/generate large snowflake sizes in the middle of the melting layer (largest particle size is always at the top of the layer).

Although the capability of this simple model to replicate Z signatures appears adequate compared to KOUN radar observations, the performance of the combined thermodynamic and radar scattering model for the simulation of polarimetric Z_{DR} and ρ_{HV} profiles indicates several deficiencies in the current approach. Simulated Z_{DR} vertical profiles for the three dielectric models are shown in Fig. 58. For the dielectric models using water a matrix (Models A and C), enhancements of 0.3-0.6 dB are typical for Z_{DR} using realistic values of RH, lapse rate and modest rainrates. These dielectric models capture the shape and relative location of peak Z_{DR} , several hundred meters beneath the height of peak Z . The results are less reasonable for the Z_{DR} vertical profile based on dielectric Model B, as only a gradual increase in Z_{DR} is observed between small values for dry snow aggregates and slightly higher values in rain.

It is clear that the coupled thermodynamic/radar model underestimates the Z_{DR} enhancement. To approach the 0.7 - 1.2 dB Z_{DR} melting layer enhancements consistent with typical KOUN radar observations, there are two mechanisms in the current modeling approach without aggregation or sophisticated scattering computations. First, it is possible to increase the peak Z_{DR} by increasing the input rainrate, which increases the number of medium to larger snowflakes entering the melting layer. This approach is reasonable since the number and size of the largest melting aggregates is likely underrepresented within the melting layer due to the absence of aggregation. However, an artificial increase in the rainrate directly limits the viability of the corresponding Z profiles. The second approach to increase the Z_{DR} enhancement is to modify the initial axis ratio parameter or widths of the canting

angle distribution for the snowflakes/raindrops. For example, we note that a decrease in the axis ratio of 0.1 - 0.2 increases the relative peak in Z_{DR} by 0.1 - 0.2 dB at modest rainrates.

The results for Z_{DR} vertical profiles argue that a more accurate treatment of large melting aggregates is necessary to reproduce the desired signatures in radar measurement profiles. The necessity for more sophisticated scattering computations is further augmented since melting hydrometeors are of resonance size, i.e., if the factor $D |\epsilon_m|^{1/2}/\lambda$ becomes comparable to 1. At large sizes, the Rayleigh approximation becomes invalid for the estimation of the scattering amplitudes such that more complex computations based on the T-matrix method are required. Section 5.2.5 explores the impact of resonance scattering and the rapid increase in Z_{DR} measurements for larger drop sizes. The discrepancies in model Z_{DR} profile shape and peak enhancement may also be attributed to neglecting aggregation in this simplified model.

One of the clear manifestations of the limitation of the current model without aggregation is its inability to reproduce realistic vertical profiles of the cross-correlation coefficient (Fig. 59). The minimal value of ρ_{hv} for all dielectric models is higher than 0.996, whereas KOUN observations often indicate that the cross-correlation coefficient may drop below 0.90.

ii. Rimed Particle Example

To simulate rimed/accreted particles typical of weak convective storm regimes, the density of snowflakes entering the melting layer is increased by setting

the riming factor in Eq. (87) to 10. A riming factor of 10 forces the initial bulk density of nearly all particles to a value typical of graupel, 0.5 g cm^{-3} . Fig. 60 illustrates the vertical profiles for the reflectivity factor Z corresponding to the scattering Models A (solid curve), B (dotted curve), and C (dashed curve). Similar plots for the riming example have been provided for the simulated profiles of Z_{DR} (Fig. 61) and ρ_{HV} (Fig. 62).

For higher density rimed particles entering the melting layer, the simulations are in general agreement with the available observations for weak convection (e.g., Fabry and Zawadzki 1995). The profiles for convective cells feature no clear bright band signature and a rapid change in Z near the freezing level consistent with the onset of melting. These signatures imply that there is only minimal change in the velocity of the falling particles during melting.

For the simulated Z profiles, all dielectric models lack the pronounced bright band signature and feature a quick transition between lower Z values in snow and higher Z values in the rain beneath the melting layer. Z_{DR} measurements in the profiles gradually evolve from low values in dry snow aloft to higher values in rain. Changes to the dielectric model dictate the nature of the transitions. Specifically, water-matrix dominant dielectric models (Models A and C) favor the transition in Z and Z_{DR} to higher values at heights closer to the freezing level than the snow-matrix model (Model B). Model values of ρ_{HV} for rimed snow are closer to unity than for unrimed snow, but the magnitudes of the cross-correlation coefficient are still at variance with radar observations.

5.2.5 *Improvements to the Melting Layer Model and Polarimetric VPR Implications*

An understanding of the conditions necessary to reproduce the observed polarimetric melting layer profiles is required for the potential inclusion of polarimetric measurements into VPR techniques. It is suggested that the discrepancy between model profiles and KOUN observations in the previous sections implies that the proposed thermodynamic / radar scattering model of the melting layer without aggregation / breakup does not adequately account for wet snow particles of resonance sizes. Moreover, these hydrometeors are responsible for the observed enhancements in Z_{DR} as well as the pronounced minimums of ρ_{hv} .

The conditions in the upper sections of the melting layer are favorable for aggregation and the generation of hydrometeors of larger size than the aggregates entering the top of the melting layer. This is because raindrops and/or smaller wet snowflakes will have a much higher terminal velocity than larger snowflakes that require additional time to melt. As a result, smaller particles may be collected by partially melted, larger snowflakes given that particle sticking capacity should be high at positive temperatures. In support of such claims, observational studies confirm that wet snow aggregates in portions of the melting layer may reach sizes 2 – 3 times that of the largest dry snowflake observed entering into the top of the melting layer (e.g., Barthazy et al. 1998). However, it is unclear whether such giant aggregates (> 20 mm) found in the upper to middle sections of the melting layer are associated with the most pronounced polarimetric signatures. Presumably, these particles become increasingly unstable as melting progresses, collapse and/or are prone to collision or spontaneous breakup. Regardless, such a melting morphology is in sharp contrast to

the melting layer model without aggregation for which the largest particles are located at the top of the melting layer.

Future modeling efforts should incorporate aggregation / breakup and appropriate scattering computation methods for large wet hydrometeors. It is suggested that aggregation and breakup of melting snowflakes be treated in a rigorous manner which implies solving stochastic collection equations (e.g., Mitchell 1988)

$$\begin{aligned}
\frac{\partial n(m)}{\partial t} &= \frac{\partial}{\partial z} [w - v(m)]n(m) + \\
&+ \frac{1}{2} \int_0^m n(m-m')n(m')K(m-m',m')g(T)q(m-m',m')dm' - \\
&- n(m) \int_0^\infty n(m')K(m,m')g(T)q(m,m')dm' + \\
&+ \frac{1}{2} \int_0^\infty \int_0^\infty S(m/m',m'')n(m')n(m'')K(m',m'')[1-q(m',m'')]dm'dm'' - \\
&- n(m) \int n(m')K(m,m')[1-q(m,m')]dm'
\end{aligned} \tag{103}$$

where n is the concentration, m is mass, w is vertical air velocity, $v(m)$ is terminal velocity, $g(T)$ is temperature-dependent probability of aggregation, $q(m',m'')$ is mass-dependent probability of aggregation when two particles collide, $S(m/m',m'')$ is a number of fragments with masses between m and $m+dm$ formed when particles with masses m' and m'' collide and break up, and $K(m',m'')$ is a collection kernel determined as

$$K(m',m'') = \frac{\pi}{4} (D'+D'')^2 E_c |v(D') - v(D'')| \tag{104}$$

where E_c is collision efficiency, D' and D'' are diameters of particles with masses m' and m'' . It is noted that the second and third lines in (103) describe the process of

aggregation, whereas the fourth and fifth lines describe breakup on collision. For example, if the probability of aggregation q is set as 1, then only aggregation takes place.

Several studies suggest numerical and approximation techniques for solving (103) for rain (e.g., Kovetz and Olund 1969, Tzivion et al. 1987) and snow (e.g., Passarelli 1978). However, solving (103) within the melting layer is computationally nontrivial and beyond the scope of this study. Rather, it is much easier to explore a realistic spectrum of melting snowflakes with rigorous scattering computations at larger particle sizes for which the Rayleigh approximation becomes invalid (e.g., > 8 mm). This exercise is useful to demonstrate the ingredients responsible for a sharp increase of Z_{DR} and a more realistic drop in ρ_{HV} as in KOUN observations. As noted in section 5.2.2 and shown in Fig. 55, particle distributions within the melting layer are often observed close to bi-exponential. In this section, we examine polarimetric Z , Z_{DR} and ρ_{HV} measurements using such a bi-exponential model for a melting layer particle size distribution.

Polarimetric radar measurements are sensitive to the volume fraction of water for the melting particles. The volume fraction of water for a population of melting particles at a given height is an output of the thermodynamic model (90). While examining solutions of (90), the volume fraction of water for melting particles (thermodynamic model without aggregation) was well approximated by a power law relation

$$f_v \approx \left(\frac{D_m}{D_{rs}} \right)^\beta \quad (105)$$

where D_{rs} is the diameter of the largest completely melted particle and $\beta = -2$ best matches the model in (90). For a bi-exponential distribution, this implies that particles with a size $D_m \leq D_{rs}$ have completely melted into raindrops and the volume fraction of water f_v is set at 1 for these sizes. The dependence of the f_v on diameter of melting particles from (105) is shown as the solid curve in Fig. 63. The value of D_{rs} is 6 mm, which is realistic for the lower part of the melting layer.

It is easy to demonstrate that a melting layer model with volume fractions of water following (105) may not adequately handle particles of resonance sizes responsible for the observed signatures in Z_{DR} and ρ_{hv} . Resonance effects become increasingly important as the ratio of $D_m |\epsilon_m|^{1/2} / \lambda$ approaches 1. Fig. 64 plots this resonance factor as a function of melting snowflake diameter D_m . In this plot, the solid curve is based on dielectric constants calculated using the value of f_v that is specified by (105) for $D_{rs} = 6$ mm and a dielectric model that assumes a water matrix with snow inclusions. Although melting particle size may be large relative to the KOUN radar wavelength, large melting snowflakes have smaller dielectric constants closer to that of snow (low volume fractions of water). For such reasons, it is unlikely to reproduce the observed drop in the cross-correlation coefficient ρ_{hv} with the current thermodynamic model that does not feature high volume fractions of water on medium-sized melting particles.

In the process of aggregation/accretion, larger-size wet snowflakes collect smaller raindrops that have originated from smaller-size snowflakes. In this manner, aggregation should lead to an increase in the water content of melting snowflakes relative to the values predicted by (105). Such a redistribution of melt water can be

quantified using Eq. (104) for a kernel $K(m', m'')$ in the stochastic collection equation (103). The volume of water $\Delta V(D_m)$ collected by a snowflake with diameter D_m during certain time interval Δt may be estimated as the integral

$$\Delta V(D_m) = C \int_0^{D_{rs}} D^3 (D_m + D)^2 |U(D_m) - U(D)| N(D) dD \quad (106)$$

where D is diameter of collected raindrop, D_{rs} is a maximal diameter of the available raindrops, U is terminal velocity of the particles, $N(D)$ is the size distribution of raindrops in the interval $(0, D_{rs})$, and C is a constant depending on collision efficiency and Δt . It is noted that $N(D)$ in (106) relates to the liquid portion of a bi-exponential distribution with slope Λ_r that depends on the rain rate below the melting layer. The multiplicative aggregation factor C in the integral (106) is a point of uncertainty and a temporary solution to a problem that requires a more rigorous treatment of the aggregation process via solving the stochastic collection equation.

Collected water increases both the volume of a snowflake and its volume water fraction. A modified volume water fraction $f_v^{(m)}(D_m)$ of the melting snowflake is given as

$$f_v^{(m)}(D_m) = \frac{\frac{\pi}{6} D_m^3 f_v(D_m) + \Delta V(D_m)}{\frac{\pi}{6} D_m^3 + \Delta V(D_m)} \quad (107)$$

where $f_v(D_m)$ is initial volume water fraction (in the absence of aggregation) as calculated from the thermodynamic model and provided in (105). The dependencies of $f_v^{(m)}$ for different aggregation factors C (aggregation intensity) are compared with the original model from (105) in Fig. 63 (dashed curves). Size dependencies of the corresponding resonance factors for $C = 30, 60, 90,$ and 120 are shown in Fig. 64

(dashed lines). It is clear that more intense aggregation increases the likelihood of resonance effects for medium particle sizes typically observed within the melting layer.

It is expected that aggregation/accretion also alters the melting particle size distribution. In Fig. 65, the initial bi-exponential distribution (without aggregation) is depicted by a solid line, whereas a distribution modified due to aggregation as in (106) is depicted by dashed lines. In this image, the modified spectrum (after aggregation) is also assumed bi-exponential, but with smaller slopes in both the rain and snow portions. That is, liquid water from the rain part of the size distribution is taken out and redistributed in the snow part.

The argument that aggregation/accretion is necessary to reproduce the observed signatures in the melting layer is further tested by computation of radar variables radar using bi-exponential distributions and a T-Matrix approach for improved scattering computations (e.g., Mishchenko 2000). For these calculations, we assume a starting distribution with largest raindrop size $D_{rs} = 6$ mm and maximum particle size of 20 mm. Axis ratios and the canting angle distribution spread are as outlined in section 5.2.3. The dielectric model assumes a water matrix with snow inclusions as in Model A. This dielectric model should provide a realistic topology for partially-to-completely melted snowflakes in the bottom half of the melting layer. Table 5 contains ρ_{HV} and Z_{DR} calculations for the nonaggregation case ($C = 0$) and the cases for an increasing aggregation factor ($C = 30, 60, 90, 120$). In the nonaggregation case, the slopes of the size distribution are $\Lambda_r = 2.92$ (rain) and $\Lambda_s =$

0.5 (snow) for a rain rate of 5 mm hr^{-1} below the melting layer (see section 5.2.2.). Aggregation implies lower values for Λ_r and Λ_s , as listed in Table 5.

It appears that incorporating aggregation/accretion into the microphysical model is necessary to reproduce the observed polarimetric signatures within the melting layer. As expected, in the absence of aggregation case ($C = 0$) the results of T-Matrix computations are similar to those from the previous section where simplified Rayleigh formulas are utilized, i.e., the T-Matrix approach makes little difference. To replicate polarimetric enhancements in Z_{DR} and the minimums in ρ_{HV} close to KOUN observations, it is required to take into account aggregation with relatively high values of C . High values of C imply a more rigorous redistribution of melt water onto the larger particles within the melting layer, thereby enhancing resonance effects. The most pronounced polarimetric signatures are associated with high concentrations of wet particles at sizes close to 0.1λ . Further, a strong relationship is found between the calculated values of Z_{DR} and ρ_{HV} . That is, the lowest values of ρ_{HV} are associated with the highest values of Z_{DR} . This relationship and the magnitudes of Z_{DR} and ρ_{HV} compare well with KOUN observations in section 5.1 (Fig. 47).

5.3 Summary and Implications for Rainfall Estimation

Based on the long-term KOUN radar observations and initial melting layer modeling efforts, significant information applicable for rainfall estimation is

contained in the shape of polarimetric radar measurement profiles. A summary of important findings for radar rainfall estimation through mixed-phase regions is as follows:

1. Aggregation and riming differently affect the polarimetric measurement profiles and parameters of Z , Z_{DR} and ρ_{HV} . The cases of moderate to intense aggregation favor a pronounced enhancement in polarimetric profiles and parameters of Z , Z_{DR} , and a sharp drop in ρ_{HV} . Riming suggests a weaker melting layer signature for all variables.
2. As hypothesized, long-term Z_{DR} observations and Z_{DR} model profiling indicates aggregation increases the median size of raindrops. Riming tends to decrease this median size.
3. The strongest connection between polarimetric profile parameters is observed between peak Z_{DR} and the minimum in ρ_{HV} . Pronounced Z_{DR} and ρ_{HV} signatures typically occur below the height of Z peak where wet snowflakes with high contents of water and resonance sizes of roughly 0.1λ are generated.
4. Understanding polarimetric signatures within the melting layer may be useful to improve VPR-based rainfall estimation. Initially, we recommend a simple approach that capitalizes on peak values of Z , Z_{DR} and ρ_{HV} within the melting layer. A pronounced increase in Z and Z_{DR} associated with a significant drop in ρ_{HV} indicates the presence of large aggregates and an increase in medium raindrop size. If riming is a dominant mechanism for

snow formation, then polarimetric signatures in the melting layer are weaker. Since vertical profiles of precipitation flux and radar variables are very different in the cases of aggregation and riming, the VPR correction should be performed differently in these situations.

BIBLIOGRAPHY

- Andrieu H., and J. D. Creutin, 1995: Identification of vertical profiles of radar reflectivity for hydrological applications using an inverse method. Part I: Formulation. *J. Appl. Meteor.*, **34**, 225–239.
- , J. D. Creutin, G. Delrieu, and D. Faure, 1997: Use of weather radar for the hydrology of a mountainous area. Part I: radar measurement interpretation. *J. Hydrol.*, **193**, 1-25.
- Atlas, D., 1957: Drop size and radar structure of a precipitation streamer. *J. Atmos. Sci.*, **14**, 261–271.
- Austin, P.M., 1987: Relation between measured radar reflectivity and surface rainfall. *Mon. Wea. Rev.*, **115**, 1053–1070.
- Aydin, K., Y. Zhao, and T. Seliga, 1990: A differential reflectivity radar hail measurement technique: observations during the Denver hailstorm of 13 june 1984. *J. Atmos. Oceanic Technol.*, **7**, 104–113.
- Bachmann, S., and D. Zrnica, 2007: "Suppression of Clutter Residue in Weather Radar Reveals Birds' Corridors over Urban Area", *Geoscience and Remote Sensing Letters*, IEEE, in print.

Battán, L.J., and C.F. Bohren, 1982: Radar Backscattering by Melting Snowflakes. *J. Appl. Meteor.*, **21**, 1937–1938.

Beard K.V., and C. Chuang, 1987: A new model for the equilibrium shape of raindrops. *J. Atmos. Sci.*, **56**, 2673-2683.

Bech, J., B. Codina, J. Lorente, and D. Bebbington, 2003: The sensitivity of single polarization weather radar beam blockage correction to variability in the vertical refractivity gradient. *J. Atmos. Oceanic Technol.*, **20**, 845–855.

Benjamin, S.G., D. Devenyi, S.S. Weygandt, et al., 2004: An hourly assimilation-forecast cycle: the RUC. *Mon Wea. Rev.*, **132**, 495-518.

Brandes, E.A., G. Zhang, and J. Vivekanandan, 2002: Experiments in rainfall estimation with a polarimetric radar in a subtropical environment. *J. Appl. Meteor.*, **41**, 674–685.

-----, and K. Ikeda, 2004: Freezing-level estimation with polarimetric radar. *J. App. Meteor.*, **43**, 1541–1553.

Bringi, V.N., V. Chandrasekar, N. Balakrishnan, and D. Zrnic, 1990: An examination of propagation effects on radar measurements at microwave frequencies. *J. Atmos. Oceanic Technol.*, **7**, 829-840.

-----, and -----, 2001: *Polarimetric doppler weather radar: principles and applications*. Cambridge University Press, 636 pp.

-----, -----, J. Hubbert, E. Gorgucci, W. Randeu, and M. Scoenhuber, 2003: Raindrop size distribution in different climate regimes from disdrometer and dual-polarized radar analysis. *J. Atmos. Sci.*, **60**, 354-365.

Brock F. V, K. C Crawford, R. L Elliott, G. W Cuperus, S. J Stadler, H. L Johnson, and M. D Eilts, 1995: The Oklahoma mesonet: A technical overview. *J. Atmos. Oceanic Technol.*, **12**, 5–19.

Chandrasekar, V., V. Bringi, N. Balakrishnan, and D. Zrnić, 1990: Error structure of multiparameter radar and surface measurements of rainfall. part III: specific differential phase. *J. Atmos. Oceanic Technol.*, **7**, 621–629.

-----, E. Gorgucci, and G. Scarchilli, 1993: Optimization of multiparameter radar estimates of rainfall. *J. Appl. Meteor.*, **32**, 1288–1293.

Ciach, G.J., 2003: Local random errors in tipping-bucket rain gauge measurements. *J. Atmos. Oceanic Technol.*, **20**, 752–759.

Cifelli R., W. A. Petersen, L. D. Carey, S. A. Rutledge, and M. A. F. Silva Dias, 2002: Radar observations of the kinematic, microphysical, and precipitation characteristics of two MCSs in TRMM LBA. *J. Geophys. Res.*, **107**, 8077, doi:10.1029/2000JD000264.

D’Amico, M.M.G., A.R. Holt, and Carlo Capsoni, 1998: An anisotropic model of the melting layer. *Radio Sci.*, **33**, 535-552.

Dinku, T., E. N. Anagnostou, and M. Borga, 2002: Improving radar-based estimation of rainfall over complex terrain. *J. Appl. Meteor*, **41**, 1163–1178.

Doviak R. J., and D. S. Zrnich, 1993: *Doppler radar and weather observations*. Academic Press, 562 pp.

Drummond, F.J., R.R. Rogers, S.A. Cohn, W.L. Ecklund, D.A. Carter and J.S. Wilson, 1996: A new look at the melting layer. *J. Atmos. Sci.*, **53**, 759–769.

Duchon C. E., and G. R. Essenberg, 2001: Comparative rainfall observations from pit and aboveground rain gauges with and without wind shields. *Water Resour. Res.*, **37**, 3253–3263.

Ekpenyong, B. E., and R. C. Srivastava, 1970: Radar characteristics of the melting layer—A theoretical study. Preprints, *14th Conf. on Radar Meteorology*, Tucson, AZ, Amer. Meteor. Soc., 161–166.

Fabry, F., G.L. Austin, and D. Tees, 1992: The accuracy of rainfall estimates by radar as a function of range. *Quart. J. Roy. Meteor. Soc.*, **118**, 435-453.

-----, and I. Zawadzki, 1995: Long-term observations of the melting layer of precipitation and their interpretation. *J. Atmos. Sci.*, **52**, 838-851.

-----, and W. Szyrmer, 1999: Modeling the melting layer. Part II: Electromagnetic. *J. Atmos. Sci.*, **56**, 3593 – 3600.

Fiebrich, C.A., D.L. Grimsley, R.A. McPherson, K.A. Kesler, and G.R. Essenberg, 2006: The value of routine site visits in managing and maintaining quality data from the Oklahoma mesonet. *J. Atmos. Oceanic Technol.*, **23**, 406–416.

Giangrande, S.E, and A.V. Ryzhkov, 2003: The quality of rainfall estimation with the polarimetric WSR-88D radar as a function of range. Preprints, 31st *International Conference on Radar Meteorology*, Seattle, Amer. Meteor. Soc., 357-360.

-----, and -----, 2004: Polarimetric method for bright band detection. Preprints, 11th *Conf. on Aviation, Range and Aerospace Meteorology*, Hyannis, Massachusetts. Amer. Meteor. Soc., CD-ROM, P5.8.

-----, and -----, 2005: Calibration of dual-polarization radar in the presence of partial beam blockage. *J. Atmos. Oceanic Technol.*, **22**, 1156–1166.

Goddard, J.W.F., J.Tan, and M. Thurai, 1994: Technique for calibration of meteorological radar using differential phase. *Electron. Lett.*, **30**, 166-167.

Goeke, S., and A. Waldvogel, 1998: Studies of snowflake aggregation efficiencies within the melting layer. *Conf. on Cloud Physics*. Everett, Wash., 458 – 461.

Gorgucci, E., G. Scarchilli, and V. Chandrasekar, 1999: A procedure to calibrate multiparameter weather radar using properties of the rain medium. *IEEE Trans. Geosci. Remote Sens.*, **37**, 269-276.

Glickman, T. S., Ed., 2000: *Glossary of Meteorology*. 2d ed. Amer. Meteor. Soc., 855 pp.

Gourley, J. J., and C. M. Calvert, 2003: Automated designation of the bright band using WSR-88D data. *Wea. Forecasting*, **18**, 585–598.

Hubbert, J.C., V.N. Bringi, and D. Brunkow, 2003: Studies of the polarimetric covariance matrix. Part I: calibration methodology. *J. Atmos. Oceanic Technol.*, **20**, 696-706.

Hunter, S.M, E. W. Holroyd, and C.L. Hartzell, 2001: Improvements to the WSR-88D snow accumulation algorithm. Preprints, *30th International Conference on Radar Meteorology*, Munich, Germany, Amer. Meteor. Soc., 716-718.

Jameson, A.R., 1991: A comparison of microwave techniques for measuring rainfall. *J. Appl. Meteor.*, **30**, 32–54.

Kitchen, M., 1997: Towards improved radar estimates of surface precipitation rate at long range. *Quart. J. Roy. Meteor. Soc.*, **123**,145-163.

Klaassen, W., 1988: Radar Observations and Simulation of the Melting Layer of Precipitation. *J. Atmos. Sci.*, **45**, 3741–3753.

Koistinen J., 1991: Operational correction of radar rainfall errors due to the vertical reflectivity profile. Preprints, *25th Int. Conf. on Radar Meteorology*, Paris, France, Amer. Meteor. Soc., 91–94.

Kovetz, A., and B. Olund, 1969: The effect of coalescence and condensation on rain formation in a cloud of finite vertical extent. *J. Atmos. Sci.*, **26**, 1060–1065.

Krajewski, W. F., and G. J. Ciach, 2005: Towards probabilistic quantitative precipitation WSR-88D algorithms: data analysis and development of ensemble model generator: phase 4. Report to Office of Hydrologic Development under NOAA Contract DG133W-02-CN-0089, 69 pp.

Kucera, P.A., W.F. Krajewski, and C.B. Young, 2004: Radar beam occultation studies using GIS and DEM technology: an example study of Guam. *J. Atmos. Oceanic Technol.*, **21**, 995-1006.

- Langston, C., and J. Zhang, 2004: An automated algorithm for radar beam occultation. Preprints, *11th Conf. on Aviation, Range and Aerospace Meteorology*, Hyannis, Massachusetts. Amer. Meteor. Soc., CD-ROM, P5.16
- Liu H., and V. Chandrasekar, 2000: Classification of hydrometeors based on polarimetric radar measurements: Developments of fuzzy logic and neuro-fuzzy systems, and in situ verification. *J. Atmos. Oceanic Technol.*, **17**, 140–164.
- Maddox, R.A., Zhang, J., Gourley, J. J., and Howard, K.W. 2002: Weather radar coverage over the contiguous United States. *Wea. Forecasting*, **17**, 927–934.
- Matrosov S. Y., D. E. Kingsmill, B. E. Martner, and F. M. Ralph, 2005: The utility of X-band polarimetric radar for quantitative estimates of rainfall parameters. *J. Hydrometeor.*, **6**, 248–262.
- May P. T., T. D. Keenan, D. S. Znić, L. D. Carey, and S. A. Rutledge, 1999: Polarimetric radar measurements of tropical rain at a 5-cm wavelength. *J. Appl. Meteor.*, **38**, 750–765.
- McPherson, R.A., C.A. Fiebrich, K.C. Crawford, R.L. Elliott, J.R. Kilby, D.L. Grimsley, J.E. Martinez, J.B. Basara, B.G. Illston, D.A. Morris, K.A. Kloesel, S.J. Stadler, A.D. Melvin, A.J. Sutherland, H. Shrivastava, J.D. Carlson, J.M.

- Wolfenbarger, J.P. Bostic, and D.B. Demko, 2007: Statewide monitoring of the mesoscale environment: a technical update on the Oklahoma mesonet. *J. Atmos. Oceanic Technol.*, **24**, 301–321.
- Meneghini, R., and L. Liao, 1996: Comparisons of cross sections for melting hydrometeors as derived from dielectric mixing formulas and a numerical method. *J. Appl. Meteor.*, **35**, 1658–1670.
- Mishchenko M. I., 2000: Calculation of the amplitude matrix for a nonspherical particle in a fixed orientation. *Appl. Opt.*, **39**, 1026–1031.
- Mitchell, D.L., 1988: Evolution of snow-size spectra in cyclonic storms. Part I: snow growth by vapor deposition and aggregation. *J. Atmos. Sci.*, **45**, 3431 – 3451.
- Mitra, S.K., O. Vohl, M. Ahr, and H.R. Pruppacher, 1990: A wind tunnel and theoretical study of the melting behavior of atmospheric ice particles. IV: Experiment and theory for snow flakes. *J. Atmos. Sci.*, **47**, 584 – 591.
- Mittermaier, M.P., and A.J. Illingworth, 2003: Comparison of model-derived and radar-observed freezing-level heights: Implications for vertical reflectivity profile-correction schemes. *Quart. J. Roy. Meteor. Soc.*, **129**, 83-95.

Park, H.-S., A. Ryzhkov, D. Zrnica, and K. Kim, 2007: Optimization of the matrix of weights in the polarimetric algorithm for classification of radar echoes. Preprints, 33rd Conf. on Radar Meteorology, Cairns, Australia, Amer. Meteor. Soc., CD-ROM, P11B.4.

Passarelli, R.E., 1978: An approximate analytical model of the vapor deposition and aggregation growth of snowflakes. *J. Atmos. Sci.*, **35**, 118 – 124.

Pruppacher, H.R., and J.D. Klett, 1998: *Microphysics of Clouds and Precipitation*, 2nd ed. Kluwer Academic Publishers, 954 pp.

Russchenberg, H. W. J., and L. P. Ligthart, 1996: Backscattering by and propagation through the melting layer of precipitation: a new polarimetric model. *IEEE Trans. Geosci. Remote Sens.*, **34**, 3–14.

Ryzhkov, A.V., and D.S. Zrnica, 1995: Precipitation and attenuation measurements at a 10-cm wavelength. *J. Appl. Meteor.*, **34**, 2121–2134.

-----, and -----, 1996: Assessment of rainfall measurement that uses specific differential phase. *J. Appl. Meteor.*, **35**, 2080–2090.

-----, and -----, 1998a: Discrimination between rain and snow with a polarimetric radar. *J. Appl. Meteor.*, **37**, 1228–1240.

- , and -----, 1998b: Polarimetric rainfall estimation in the presence of anomalous propagation. *J. Atmos. Oceanic Technol.*, **15**, 1320-1330.
- , 2001: Interpretation of polarimetric radar covariance matrix for meteorological scatterers: theoretical analysis. *J. Atmos. Oceanic Technol.*, **18**, 315-328.
- , T.J. Schuur, and D.S. Zrnice, 2001a: Radar rainfall estimation using different polarimetric algorithms. Preprints, *30th Int. Conf. On Radar Meteorology*, Munich, Germany, Amer. Meteor. Soc., 641-643.
- , -----, and -----, 2001b: Testing a polarimetric rainfall algorithm and comparison with a dense network of rain gauges. Preprints, *Fifth Int. Sym. On Hydrological Applications of Weather Radar – Radar Hydrology*, Kyoto, Japan. 159-164.
- , S. E. Giangrande, and D.S. Zrnice, 2002: Using multiparameter data to calibrate polarimetric weather radars in the presence of a partial beam blockage. *Proc. IGARSS 2002*, Toronto, Canada, 2820 - 2822.

- , and D. S. Zrníc, 2003: Discrimination between rain and snow with a polarimetric NEXRAD radar. Preprints, *31st Conference on Radar Meteorology*, Seattle, Washington, Amer. Meteor. Soc., 635-638.
- , S.E. Giangrande, and Terry J. Schuur, 2005a: Rainfall estimation with a polarimetric prototype of WSR-88D. *J. Appl. Meteorol.*, **44**, 502–515.
- , T. Schuur, D.W. Burgess, P.L. Heinselman, S.E. Giangrande, and D.S. Zrníc, 2005b: The joint polarization experiment: polarimetric rainfall measurements and hydrometeor classification. *Bull. Amer. Meteor. Soc.*, **86**, 809-824.
- , S.E. Giangrande, V.M. Melnikov, and T. J. Schuur, 2005c: Calibration issues of dual-polarization radar measurements. *J. Atmos. Oceanic Technol.*, **22**, 1138–1155.
- , T.J. Schuur, D.W. Burgess, and D.S. Zrníc, 2005d: Polarimetric tornado detection. *J. Appl. Meteor.*, **44**, 557-570.
- , 2007: The impact of beam broadening on the quality of radar polarimetric data. *J. Atmos. Oceanic Technol.*, **24**, 729 - 744.

-----, D.S. Zrníc, P. Zhang, J. Krause, H. Park, D. Hudak, J. Young, J.L. Alford, M. Knight, and J.W. Conway, 2007: Comparison of polarimetric algorithms for hydrometeor classification at S and C bands. Analysis of the performance in different climate regions. Preprints, *33rd Conf on Radar Meteorology*, Cairns, Australia, Amer. Meteor. Soc., CD-ROM, P10B.3.

Sanchez-Diezma R., I. Zawadzki, and D. Sempere-Torres, 2000: Identification of the bright band through the analysis of volumetric radar data. *J. Geophys. Res.*, **105**, 2225–2236.

Scarchilli, G., E. Gorgucci, and V. Chandrasekar, 1996: Self-consistency of polarization diversity measurement of rainfall. *IEEE Trans. Geosci. Remote Sens.*, **34**, 22-26.

Schuur, T., A. Ryzhkov, P. Heinselman, D. Zrníc, D. Burgess, and K. Scharfenberg, 2003: Observation and classification of echoes with the polarimetric WSR-88D radar. NSSL Report, 46 pp. Available online at:
http://www.nssl.noaa.gov/88d-upgrades/WSR-88D_reports.html

Seo, D.-J., J. Breidenbach, R. Fulton, D. Miller, T. O'Bannon, 2000: Real-time adjustment of range-dependent biases in WSR-88D rainfall estimates due to nonuniform vertical profile of reflectivity. *J. Hydrometeorol.*, **1**, 222–240.

- Shafer, M.A., C.A. Fiebrich, D.S. Arndt, S.E. Fredrickson, and T.W. Hughes, 2000: Quality assurance procedures in the Oklahoma mesonet network. *J. Atmos. Oceanic Technol.*, **17**, 474–494.
- Smith, J.A., D.-J. Seo, M.L. Baeck, and M.D. Hudlow, 1996: An intercomparison of NEXRAD precipitation estimates. *Water Resour. Res.*, **32**, 2035-2045.
- Smyth, T. J., and A.J. Illingworth, 1998: Correction for attenuation of radar reflectivity using polarization data. *Quart. J. Roy. Meteor. Soc.*, **124**, 2393-2415.
- Stewart, R.E., J.D. Marwitz, and J.C. Pace, 1984: Characteristics through the melting layer of stratiform clouds. *J. Atmos. Sci.*, **41**, 3227 – 3237.
- Super, A.B., and E.W. Holroyd, 1998: Snow accumulation algorithm for the WSR-88D radar: final report. Bureau of Reclamation Report R-98-05, Denver, CO, July, 75p.
- Tabary, P., A.L. Henaff, G. Vulpiani, J. Parent-du-Châlet, and J.J. Gourley, 2006: Melting layer characterization and identification with a C-band dual-polarization radar: a long-term analysis. Preprints, *Fourth European Conference on Radar Meteorology and Hydrology (ERAD) 2006*, Barcelona, Spain, 17-20.

- Tzivion (Tzitzvashvili), S., G. Feingold, and Z. Levin, 1987: An efficient numerical solution to the stochastic collection equation. *J. Atmos. Sci.*, **44**, 3139–3149.
- Vasiloff, S., 2001: WSR-88D performance in northern Utah during the winter of 1998 – 1999. Part I: adjustments to precipitation estimates. NWS Western Region Technical Attachment NO.01-02.
- Vivekanandan, J., D. S. Zrnić, S. M. Ellis, R. Oye, A. V. Ryzhkov, and J. Straka, 1999: Cloud microphysics retrieval using S-band dual-polarization radar measurements. *Bull. Amer. Meteor. Soc.*, **80**, 381–388.
- Vivekanandan, J., G. Zhang, S. Ellis, D. Rajopadhyaya, and S. Avery, 2003: Radar reflectivity calibration using differential propagation phase measurement. *Radio Sci.*, **38**, No 3, MAR 14-1-13.
- Willis, P.T., and A.J. Heymsfield, 1989: Structure of the melting layer in mesoscale convective system stratiform precipitation. *J. Atmos. Sci.*, **46**, 2008 – 2025.
- Wilson, J.W., and E.A. Brandes, 1979: Radar measurement of rainfall - a summary. *Bull. Amer. Meteor. Soc.*, **60**, 1048–1058.

WSR-88D Radar Operations Center, 2001: WSR-88D system specification.

Document Number 2810000D, Code Identification 0WY55, 31 October 2001,

190 pp.

Zawadzki, I.I., 1975: On radar-rainage comparison. *J. Appl. Meteor.*, **14**, 1430–1436.

-----, W. Szyrmer, C. Bell, and F. Fabry, 2005: Modeling of the melting layer. Part III: the density effect. *J. Atmos. Sci.*, **62**, 3705–3723.

-----, 2006: Sense and nonsense in radar QPE. *Fourth European Conference on Radar in Meteorology and Hydrology*. Barcelona, Spain, 18 – 22 Sept., 121 – 124.

Zrnica, D.S., N. Balakrishnan, C.L. Ziegler, V.N. Bringi, K. Aydin, and T. Matejka, 1993: Polarimetric signatures in the stratiform region of a mesoscale convective system. *J. App. Meteor.*, **32**, 678–693.

-----, 1996: Weather radar polarimetry - trends toward operational applications. *Bull. Amer. Meteor. Soc.*, **77**, 1529–1534.

-----, and A. Ryzhkov, 1996: Advantages of rain measurements using specific differential phase. *J. Atmos. Oceanic Technol.*, **13**, 454–464.

-----, and -----, 1999: Polarimetry for weather surveillance radars. *Bull. Amer. Meteor. Soc.*, **80**, 389–406.

-----, -----, J. Straka, Y. Liu, and J. Vivekanandan, 2001: Testing a procedure for automatic classification of hydrometeor types. *J. Atmos. Oceanic Technol.*, **18**, 892–913.

APPENDIX A: TABLES

Table 1: KOUN data listing and available verification for melting layer designation

| Event | ML Designation | RUC Hours | Radiosonde Source | Sonde Hour |
|----------------------------|--------------------------------|--------------------------------|--------------------------|----------------------|
| 21 May 2003 | 1236-1437 UTC | 1200-1500 UTC | NWS Norman, OK | 1200 UTC |
| 4 June 2003 | 1204-1839 UTC | 1200-1900 UTC | NWS Norman, OK | 1200 UTC |
| 11 June 2003 | 0056-0601 UTC | 0100-0600 UTC | NWS Norman, OK | 0000 UTC |
| 2 June 2004 | 2117-2210 UTC | 2100-2200 UTC | N/A | N/A |
| 3 June 2004 | 0201-0559 UTC | 0200-0600 UTC | N/A | N/A |
| 9 June 2004 | 0714-2359 UTC | 0700-2300 UTC | NWS Norman, OK | 1200 UTC 0000 UTC |
| 19 June 2004 | 1155-1837 UTC | 1100-1900 UTC | NWS Norman, OK | 1200 UTC |
| 20 June 2004 | 1628-1753 UTC | 1600-1800 UTC | TELEX MCAS | 1648 UTC |
| 21 June 2004 | 0936-1658 UTC | 0900-1700 UTC | NWS Norman, OK | 1200 UTC |
| 22 June 2004 | 0503-1410 UTC | 0500-1200 UTC | NWS Norman, OK | 1200 UTC |
| 14 November 2004 | 1917-2359 UTC | 1900-2300 UTC | NWS Norman, OK | 0000 UTC |
| 15 November 2004 | 0643-2025 UTC | 0700-2000 UTC | NWS Norman, OK | 1200 UTC |
| 18 November 2004 | 0029-0337 UTC 0553-0559 UTC | 0000-0400 UTC 0600 UTC | NWS Norman, OK | 0000 UTC |
| 6 February 2005 | 0122-1455 UTC | 0100-1500 UTC | NWS Norman, OK | 1200 UTC |
| 13 May 2005 | 0657-1253 UTC | 0700-1300 UTC | NWS Norman, OK | 1200 UTC |
| 4 June 2005 5 June 2005 | 2222-2359 UTC 0000-0259 UTC | 2200-2300 UTC 0000-0300 UTC | NWS Norman, OK | 0000 UTC |
| 13 June 2005 | 0112-0322 UTC 2140-2305 UTC | 0100-0300 UTC 2200-2300 UTC | NWS Norman, OK | 0000 UTC |
| 17 June 2005 | 0403-0501 UTC | 0400-0500 UTC | N/A | N/A |

Table 2: Listing of KOUN events and the hours of observation.

| Number | Date | Hours (UTC) | Event Type |
|--------|----------|-----------------------|-------------------------|
| 1. | 08/14/02 | 1 – 4 | MCS |
| 2. | 09/08/02 | 18 – 21 | Tropical Remnant |
| 3. | 09/09/02 | 16 – 17 | Tropical Remnant |
| 4. | 09/14/02 | 6 – 11 | MCS |
| 5. | 09/19/02 | 2 – 7 | MCS |
| 6. | 10/08/02 | 17 – 20, 22 – 23 | Widespread Stratiform |
| | 10/09/02 | 1 – 3, 4 – 5, 13 – 14 | |
| 7. | 10/19/02 | 19 – 20, 21 – 22 | Widespread Stratiform |
| 8. | 10/24/02 | 15 – 17, 19 – 21 | Widespread Stratiform |
| 9. | 10/28/02 | 19 – 20 | Widespread Stratiform |
| 10. | 12/03/02 | 22 – 23 | Stratiform / Ice NW OKC |
| | 12/04/02 | 1 – 3 | |
| 11. | 04/19/03 | 10 – 14 | MCS |
| 12. | 04/23/03 | 22 – 23 | Isolated Convection |
| 13. | 05/14/03 | 5 – 11 | Severe Convective Cells |
| 14. | 05/16/03 | 5 – 10 | MCS |
| 15. | 05/20/03 | 1 – 5 | Isolated Convection |
| 16. | 06/02/03 | 3 – 6 | MCS |
| 17. | 06/04/03 | 12 – 14, 15 – 17 | MCS |
| 18. | 06/05/03 | 10 – 15 | MCS |
| 19. | 06/06/03 | 2 – 7 | MCS |
| 20. | 06/11/03 | 0 – 1, 2 – 6 | MCS |
| 21. | 06/12/03 | 0 – 5 | MCS |
| 22. | 06/13/03 | 10 – 14 | Isolated Convection |
| 23. | 04/24/04 | 2 – 7 | MCS |
| 24. | 05/13/04 | 19 – 20 | MCS |
| 25. | 06/02/04 | 20 – 23 | MCS |
| 26. | 06/04/04 | 14 – 20 | Isolated Convection |
| 27. | 06/19/04 | 16 – 20 | MCS |
| 28. | 06/21/04 | 8 – 13 | MCS |
| 29. | 06/22/04 | 8 – 12 | MCS |
| 30. | 08/28/04 | 8 – 12 | MCS |
| 31. | 11/14/04 | 20 – 23 | Widespread Stratiform |
| 32. | 11/15/04 | 10 – 14 | Widespread Stratiform |
| 33. | 05/13/05 | 6 – 10 | MCS |
| 34. | 05/27/05 | 15 – 18 | Isolated Convection |
| 35. | 06/05/05 | 1 – 5 | MCS |
| 36. | 06/10/05 | 7 – 11 | MCS |
| 37. | 06/17/05 | 4 – 7 | MCS |
| 38. | 07/01/05 | 14 – 17 | MCS |
| 39. | 08/27/05 | 18 – 22 | Isolated Convection |
| 40. | 08/29/05 | 3 – 6 | Isolated Convection |
| 41. | 09/14/05 | 3 – 6 | MCS |
| 42. | 10/01/05 | 2 – 18 | MCS |
| 43. | 10/05/05 | 21 – 23 | MCS |
| | 10/06/05 | 0 – 3, 4 – 6 | |

Table 3: The results of echo classification for the Oklahoma Mesonet dataset. Percentages exclude nonecho/null classifications. $\langle R \rangle$ and $\langle Z_{DR} \rangle$ are mean values of rainfall rate (Z capped at 53 dBZ) and differential reflectivity over gage locations for the corresponding echo class. The standard NEXRAD $R(Z)$ relation (23) is used to estimate the relative contribution to the total radar-estimated rain depth in the far right column.

| Echo Category | # Observations | % Occurrence | $\langle R \rangle$ capped [mm hr ⁻¹] | $\langle Z_{DR} \rangle$ [dB] | % Contribution to R(Z) Rainfall |
|---------------|-------------------|-----------------|--|-------------------------------|--|
| GC / AP | 7736 | 9.79 | 2.88 | 0.62 | 5.94 |
| Biological | 11577 | 14.66 | 0.34 | 2.89 | 0.89 |
| Dry Snow | 4560 | 5.78 | 1.51 | 0.48 | 1.59 |
| Crystals | 1251 | 1.58 | 0.50 | 0.81 | 0.14 |
| Wet Snow | 9443 | 11.96 | 5.03 | 1.10 | 10.75 |
| Graupel | 2695 | 3.41 | 14.41 | 0.60 | 8.93 |
| Rain | 34016 | 43.08 | 3.68 | 0.83 | 28.9 |
| Big Drops | 4989 | 6.31 | 3.93 | 1.66 | 4.48 |
| Heavy Rain | 2224 | 2.82 | 58.58 | 2.11 | 29.7 |
| Rain / Hail | 460 | 0.58 | 82.33 | 1.15 | 8.65 |

Table 4: Listing of KOUN events and the hours of observation in the subset for which 0.0° and 0.5° rainfall results are examined.

| Number | Date | Hours (UTC) | Event Type |
|--------|----------|-------------|-----------------------|
| 1. | 06/11/03 | 0 – 6 | MCS |
| 2. | 06/19/04 | 16 – 18 | MCS |
| 3. | 06/22/04 | 7 – 12 | MCS |
| 4. | 11/14/04 | 20 – 23 | Widespread Stratiform |
| 5. | 11/15/04 | 10 – 14 | Widespread Stratiform |

Table 5: Values of ρ_{HV} and Z_{DR} for different aggregation intensities defined by factor C. Λ_r and Λ_s are the slopes of the bi-exponential distribution for rain and snow portions, respectively.

| C | Λ_r [mm^{-1}] | Λ_s [mm^{-1}] | ρ_{HV} | Z_{DR} [dB] |
|----------|---|---|--------------------------------------|--|
| 0 | 2.92 | 0.50 | 0.995 | 0.866 |
| 30 | 2.80 | 0.45 | 0.989 | 1.067 |
| 60 | 2.70 | 0.40 | 0.951 | 1.793 |
| 90 | 2.60 | 0.35 | 0.941 | 2.10 |
| 120 | 2.50 | 0.30 | 0.940 | 2.13 |

APPENDIX B: FIGURES

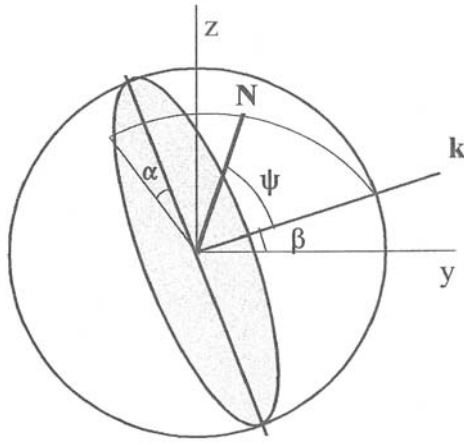


Fig. 1: Geometry of scattering as adapted from Ryzhkov (2001). Shaded area represents polarization plane. Direction N denotes orientation of the symmetry axis of the particle, k represents the direction of wave propagation, z is the true vertical, α denotes the canting angle and ψ is the orientation angle with respect to the direction of propagation k .

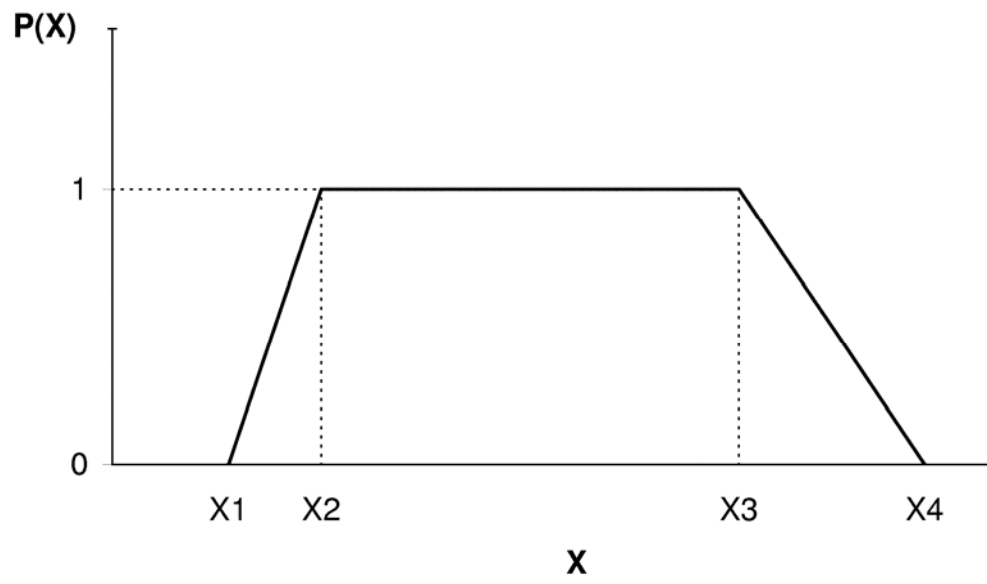


Fig. 2: Trapezoidal membership function shape.

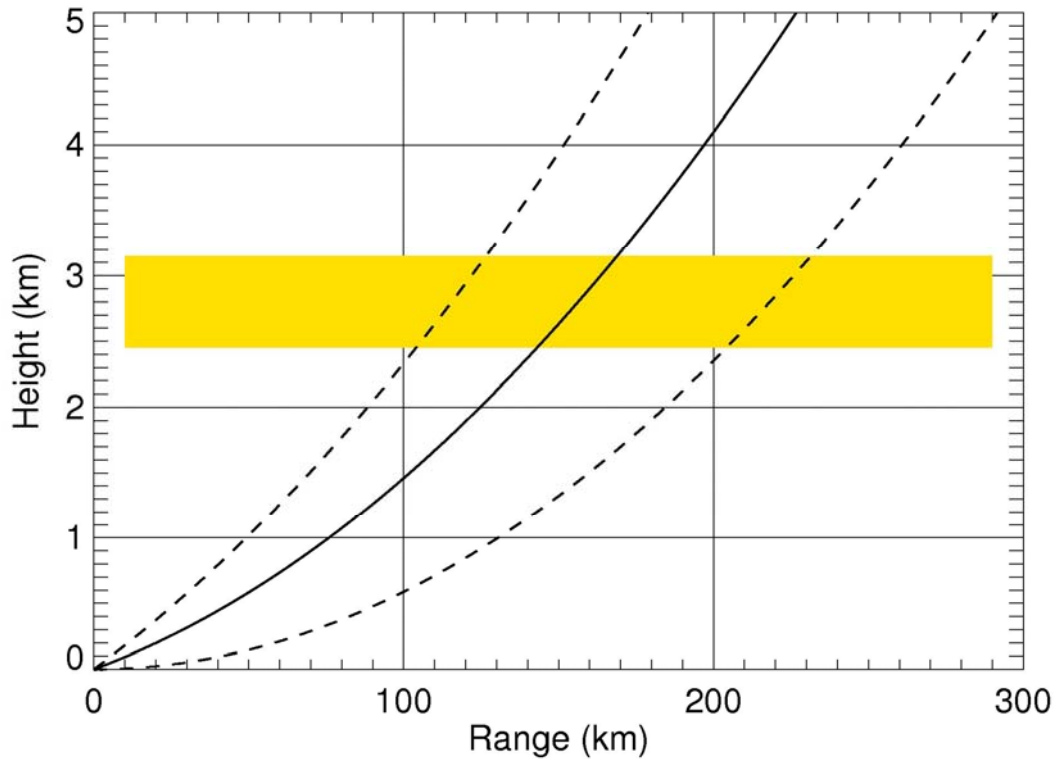


Fig. 3: Illustration of radar beam interaction with the melting layer. Solid curve represents the mean beam height of the 0.5° elevation angle tilt with a 1° beam width (bounded by dashed curves).

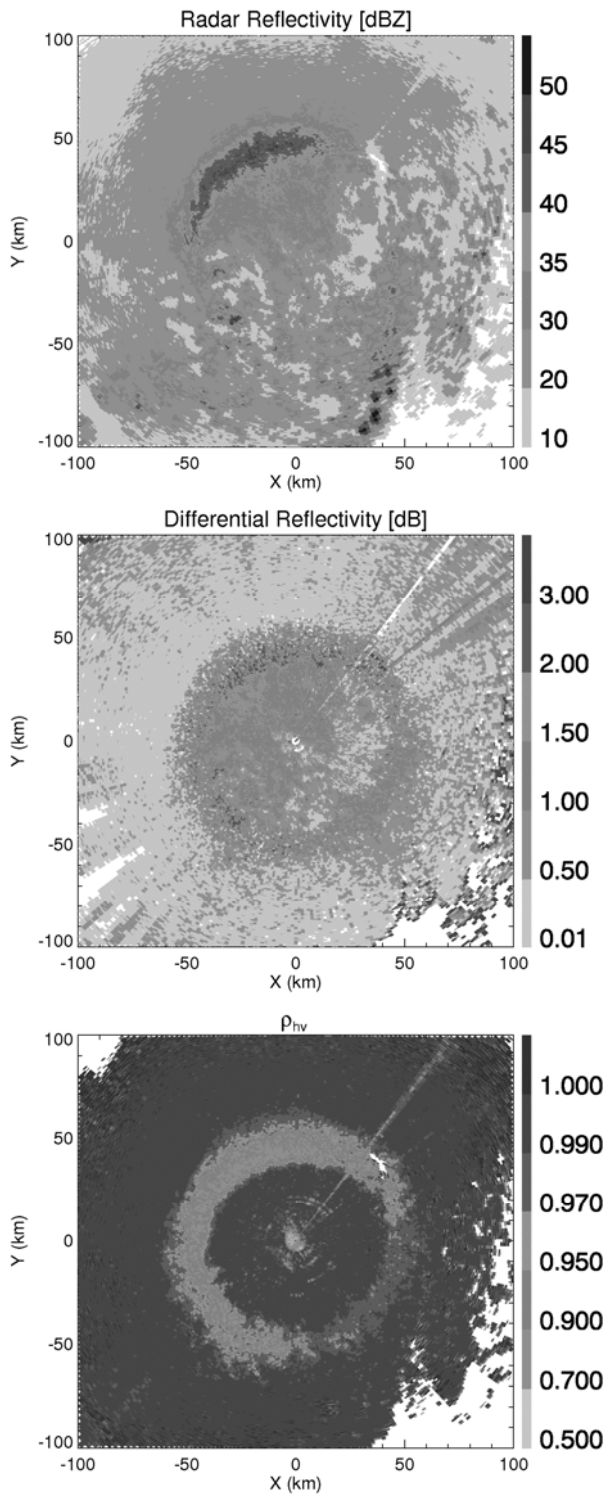


Fig. 4: KOUN measurement PPI images of Z, Z_{DR} , and ρ_{hv} on May 13, 2005 at the 4.5° elevation angle.

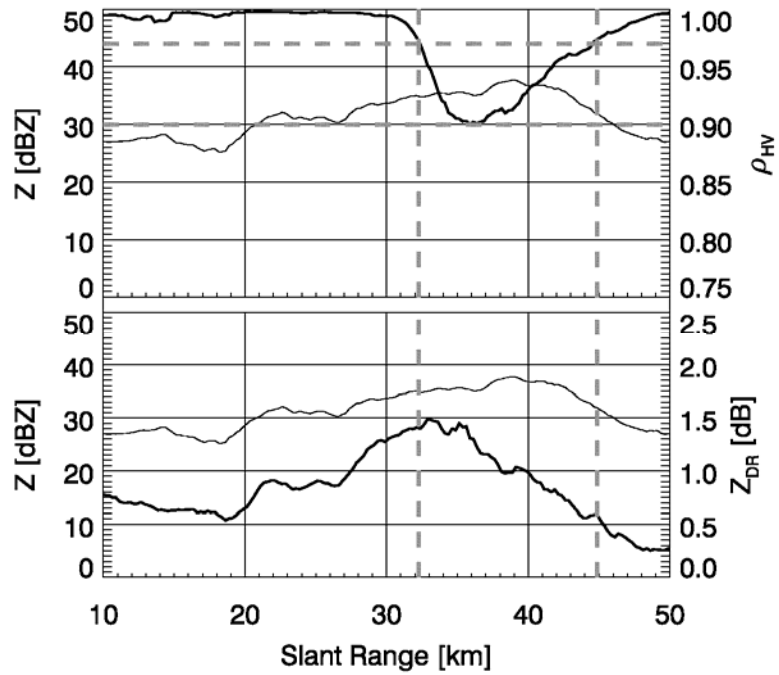


Fig. 5: An example of average slant range dependences of Z , Z_{DR} , and ρ_{hv} at the 4.5° elevation angle for the case illustrated in Fig. 4. Z measurements are displayed with thin solid lines, Z_{DR} and ρ_{hv} are displayed with thick solid lines. MLDA ρ_{hv} thresholds are depicted with dashed lines.

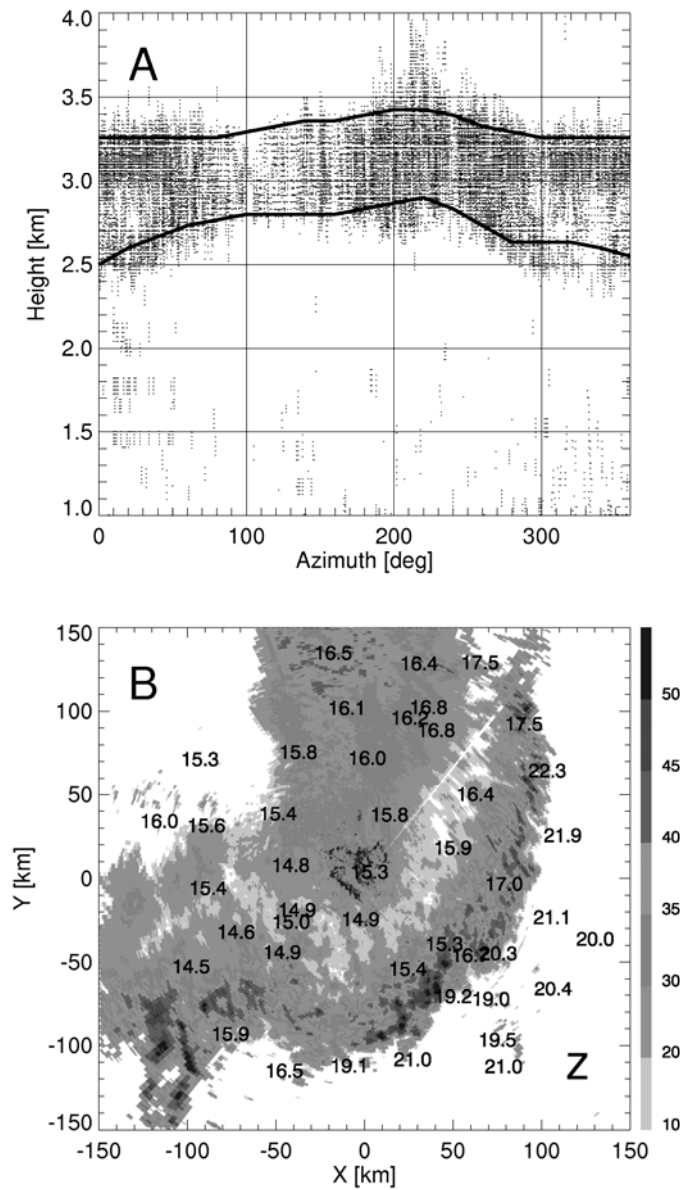


Fig. 6: (A) Example of ML points mapped on the height-azimuth plane. The 80% (ML top) and 20% (ML bottom) height contours are overlaid on the image in solid lines. (B) Corresponding surface Oklahoma Mesonet temperature (Celsius) and KOUN radar reflectivity factor from the 0.5° elevation angle. Highest surface temperatures and higher ML tops are located in directions ahead of the convective line.

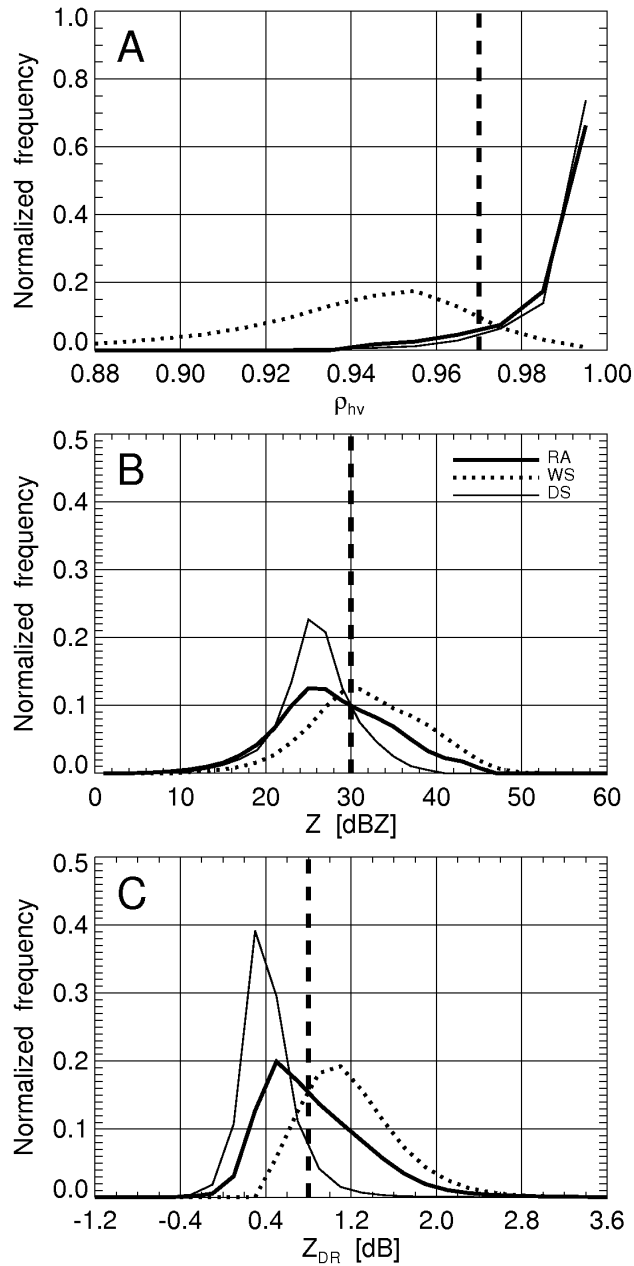


Fig. 7: Normalized histograms of KOUN radar measurements of (A) ρ_{hv} , (B) Z, and (C) Z_{DR} for wet snow (dotted line), dry snow (thin solid line) and light-to-moderate rain (thick solid line)(adapted from Park et al. (2007), 29 hours of observation). Vertical dashed lines indicate thresholds used in the MLDA.

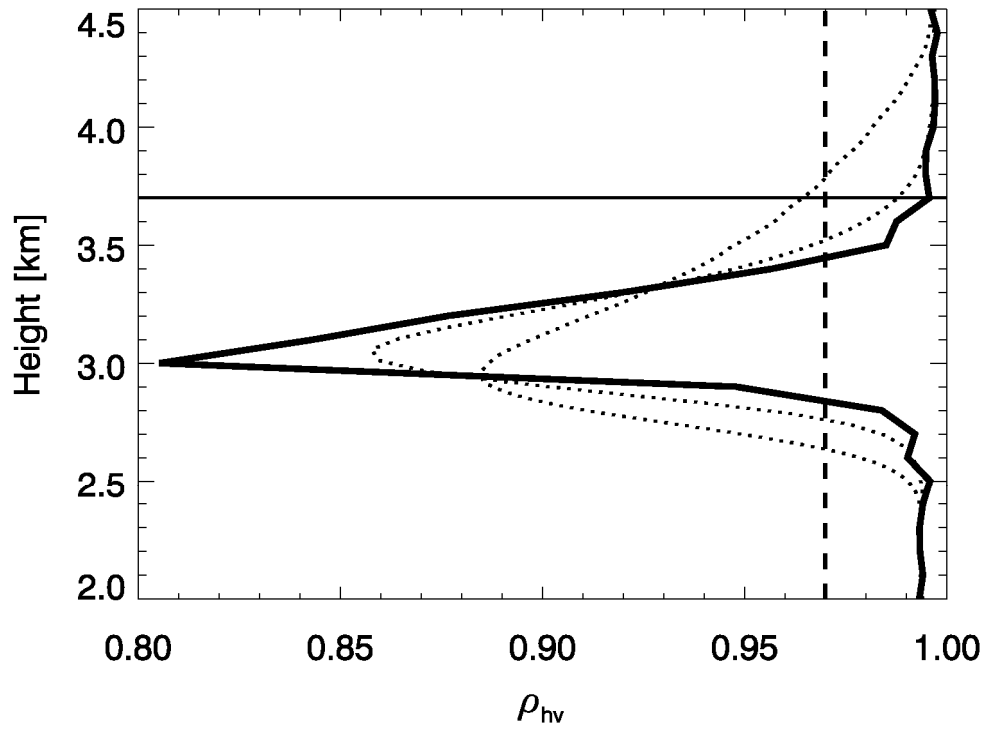


Fig. 8: Intrinsic model (thick solid line) and smoothed (dotted lines) vertical profiles of ρ_{hv} demonstrating the impacts of beam broadening and radial smoothing on polarimetric melting layer signatures at elevation angles 4.5° and 10.0° . Environmental melting level height is approximately 3.7 km (thin horizontal line).

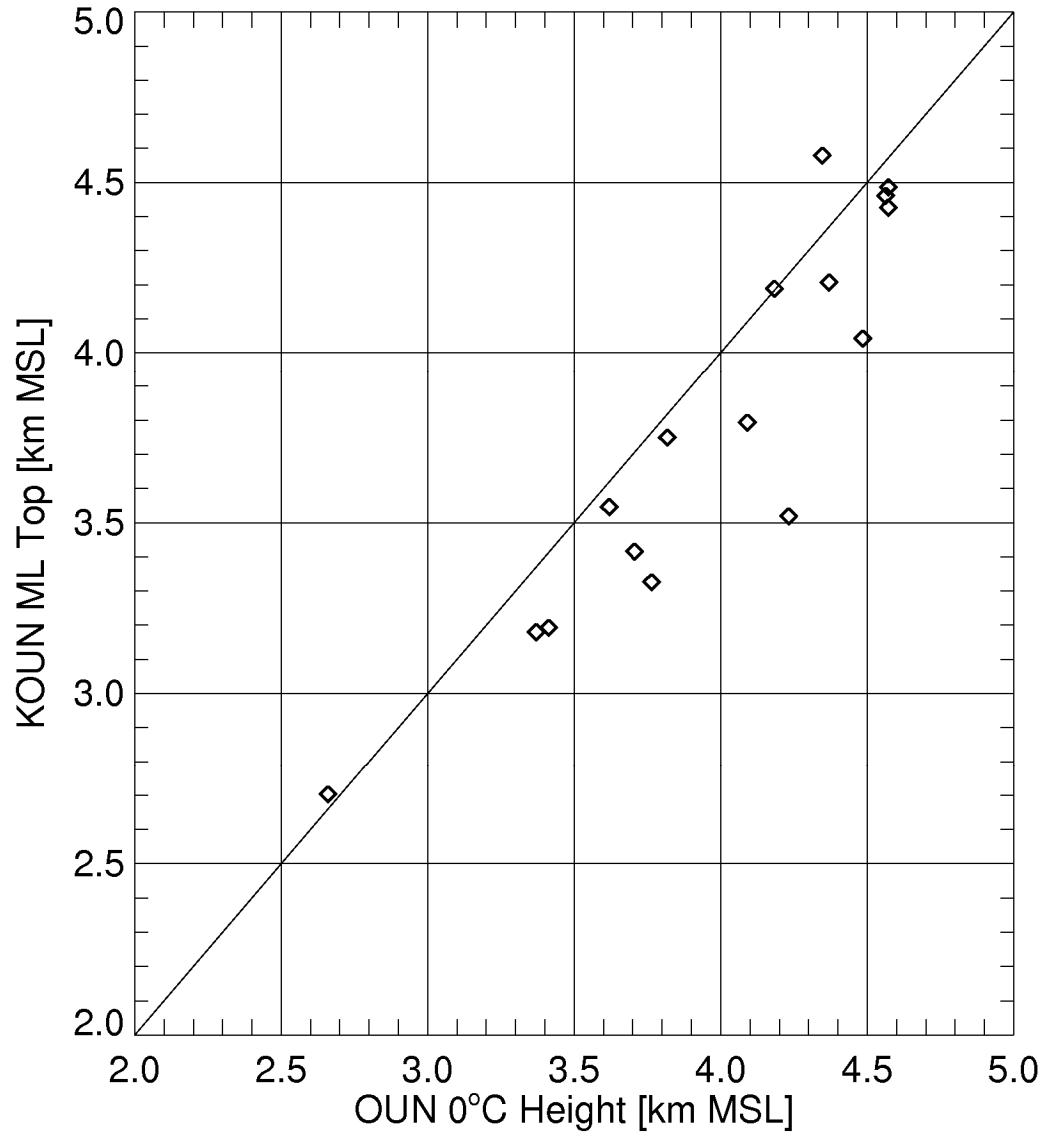


Fig. 9: Scatterplot of ML top heights obtained from the MLDA versus radiosonde-derived 0°C observations.

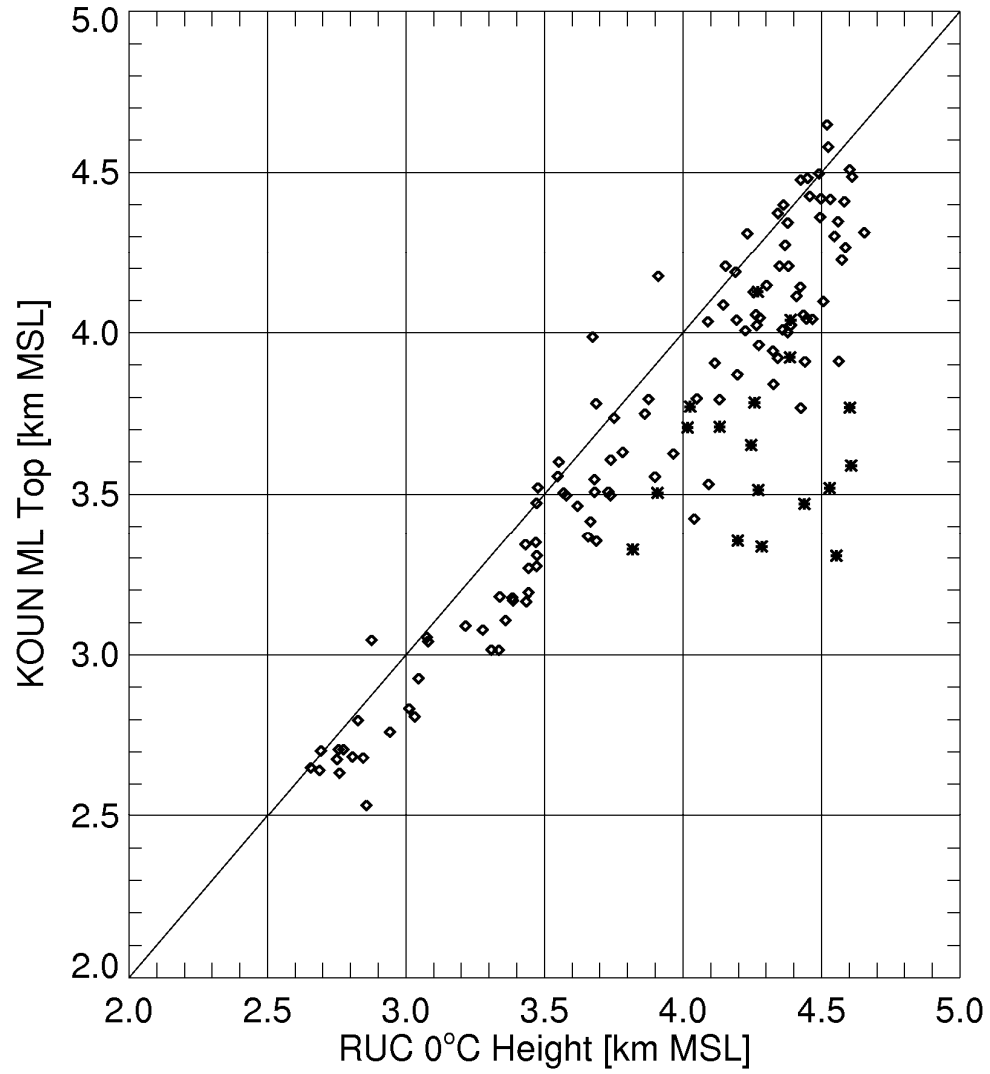


Fig. 10: As in Fig. 9, but utilizing RUC model analysis output temperatures for validation. Hours with questionable RUC or MLDA performance for convective events are noted with asterisks.

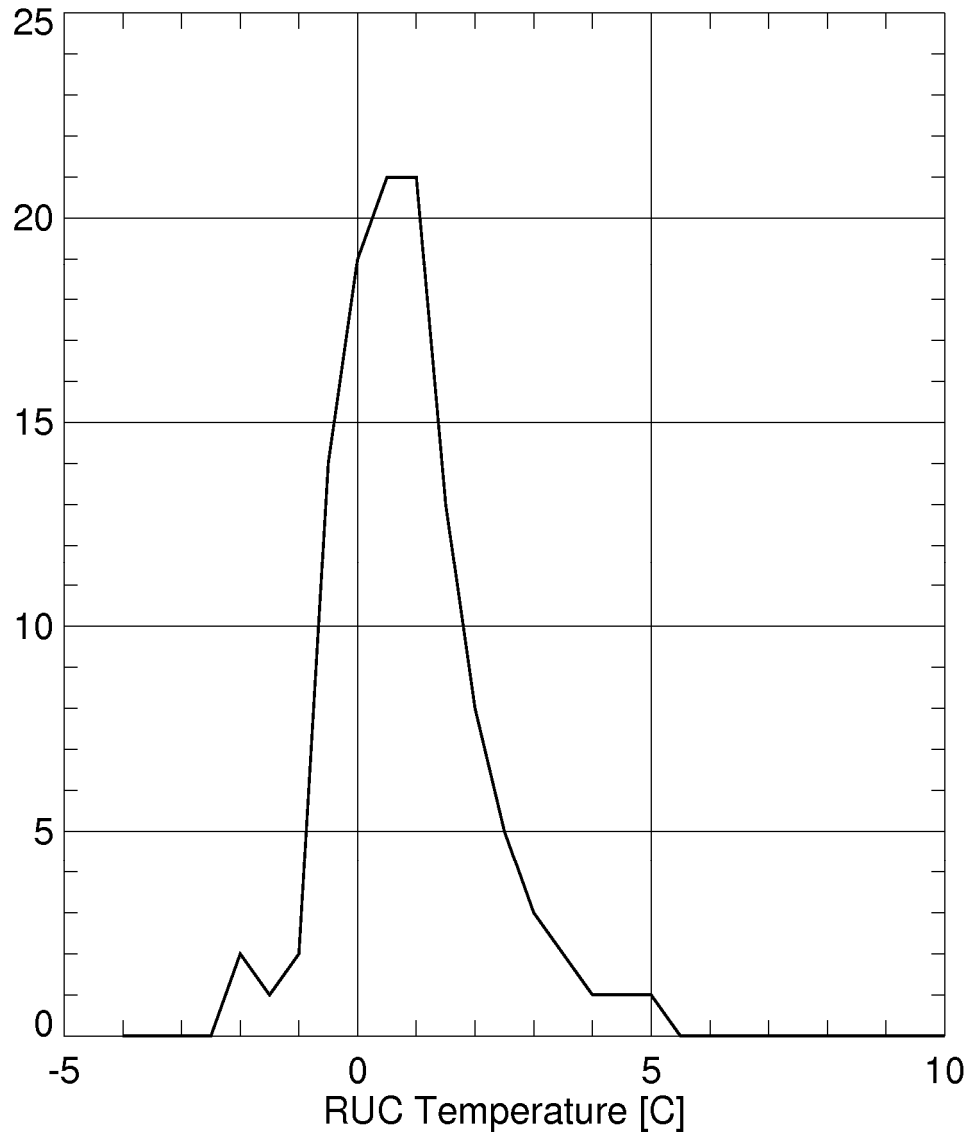


Fig. 11: Histogram of the temperature of the ML top retrieved from the radar as revealed by RUC model analysis output.

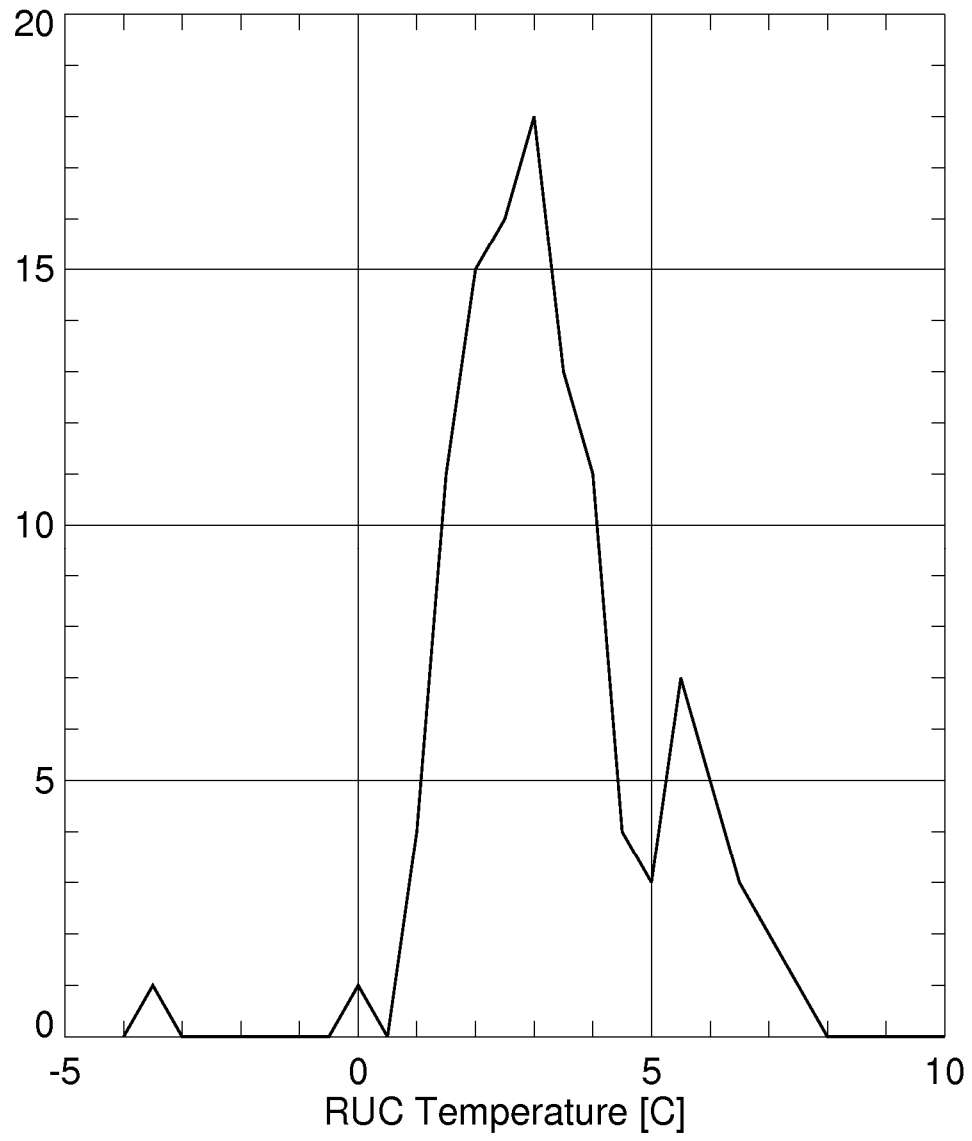


Fig 12: As in Fig. 11, but for ML bottom heights.

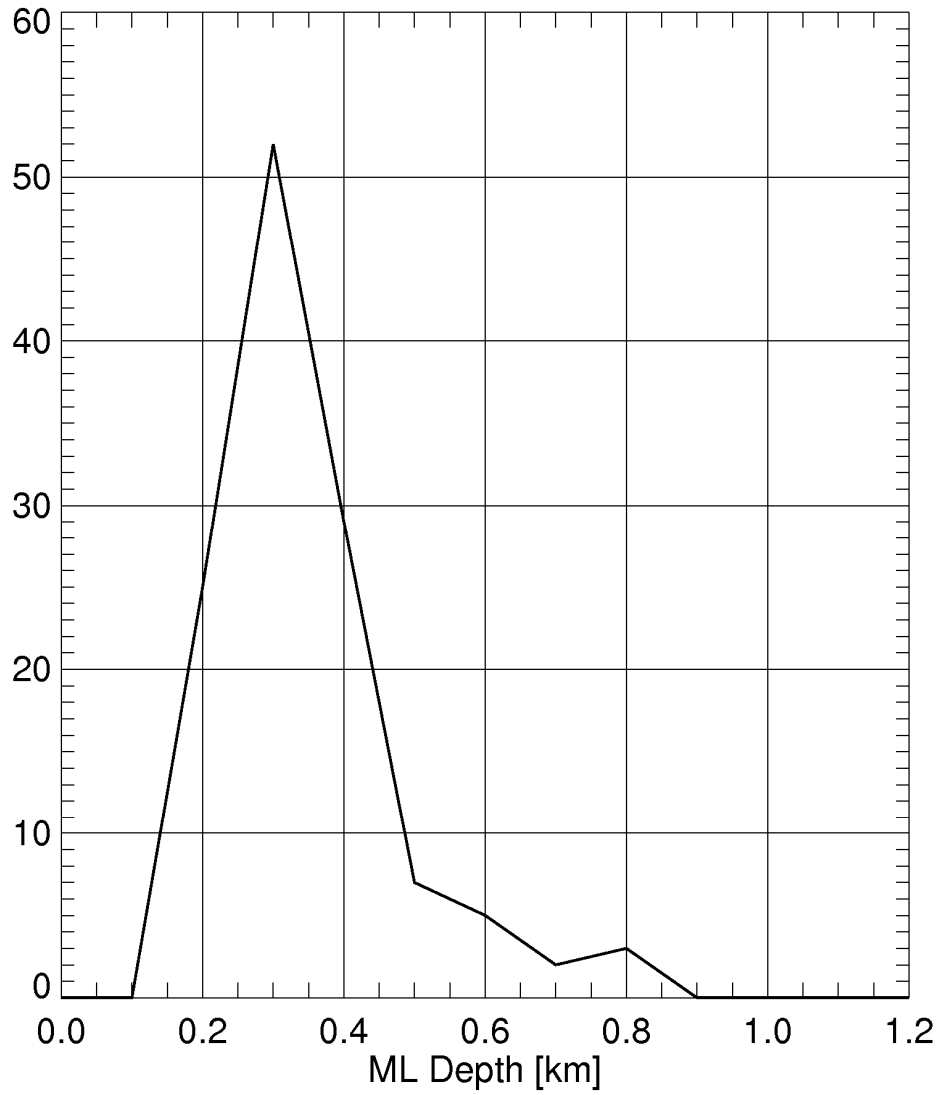


Fig. 13: Histogram of the ML thickness retrieved from the MLDA.

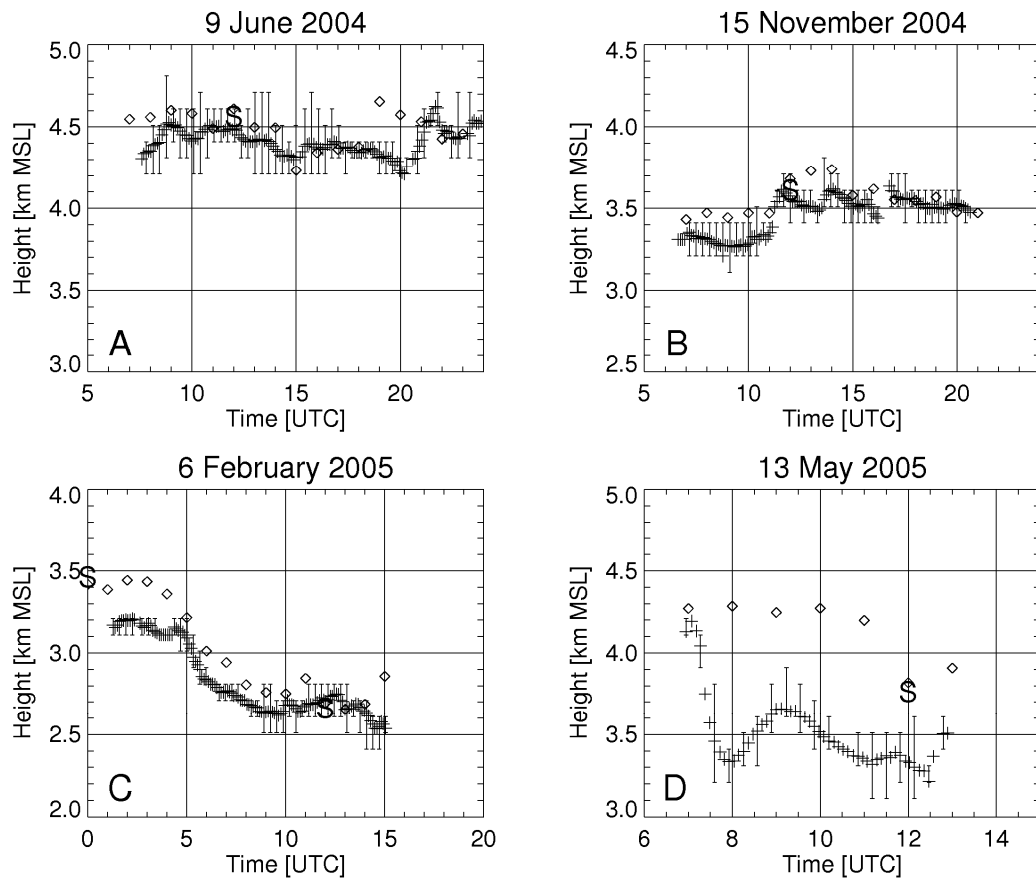


Fig. 14: Temporal dependencies of the height of the ML top estimated from the radar (crosses), RUC model output (diamonds) and soundings ('S' symbol, bottom of the symbol) for 4 different days of observation.

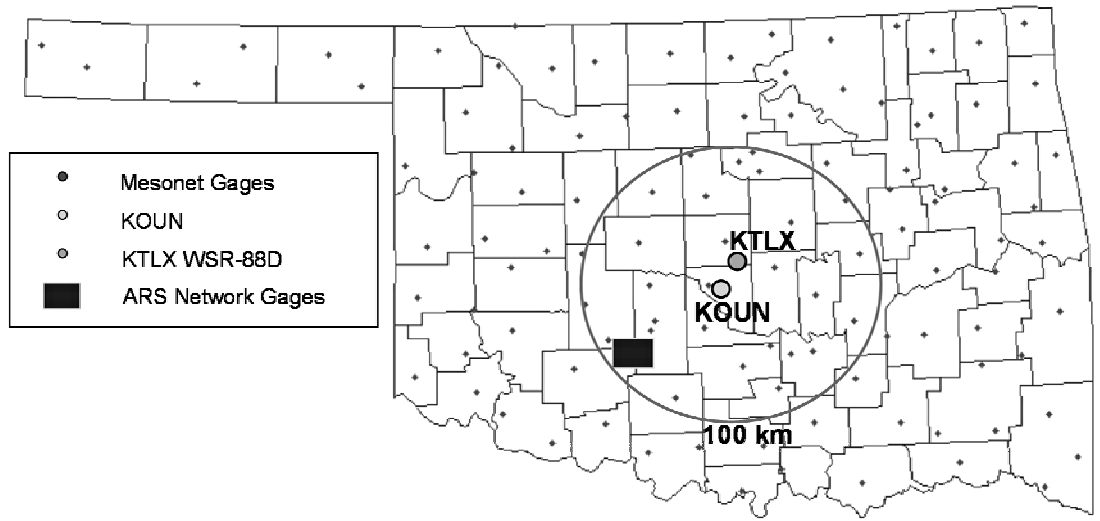


Fig. 15: A map of the observation network in central Oklahoma.

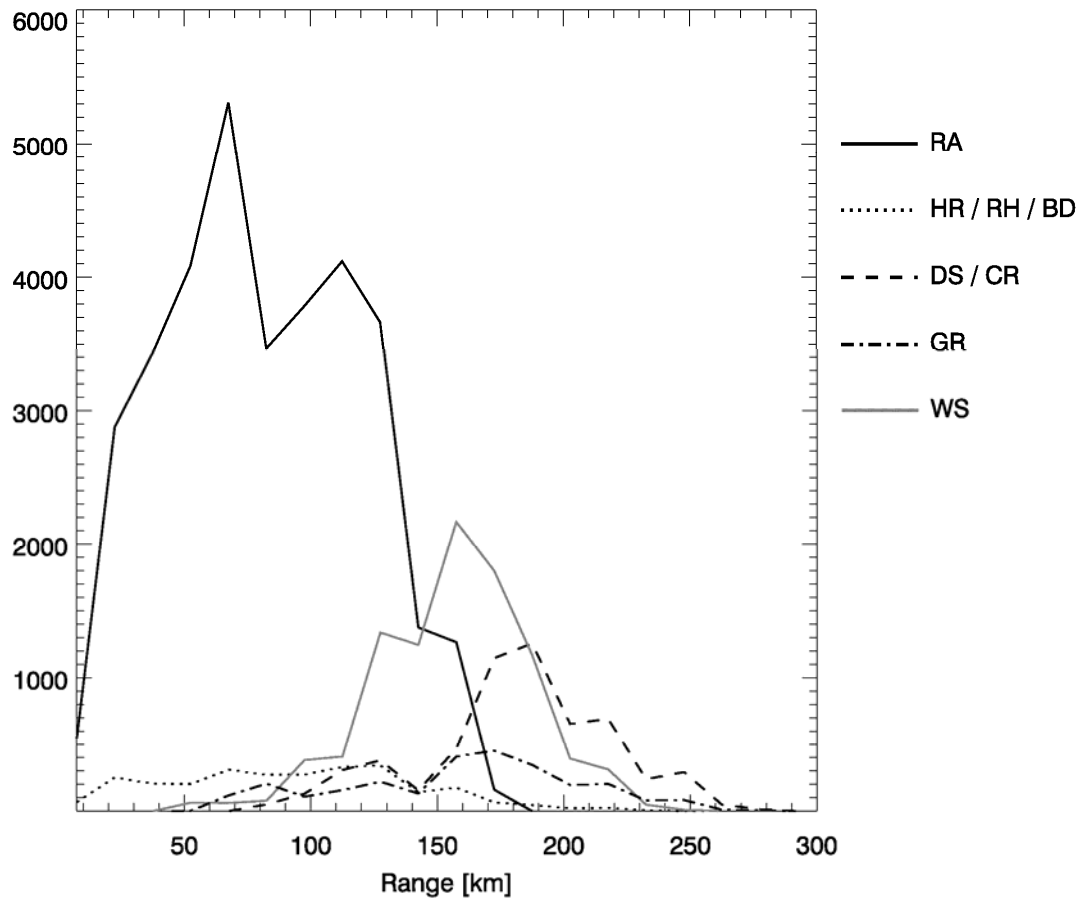


Fig. 16: Histogram of ranges associated with different classes of hydrometeors observed at the 0.5° elevation.

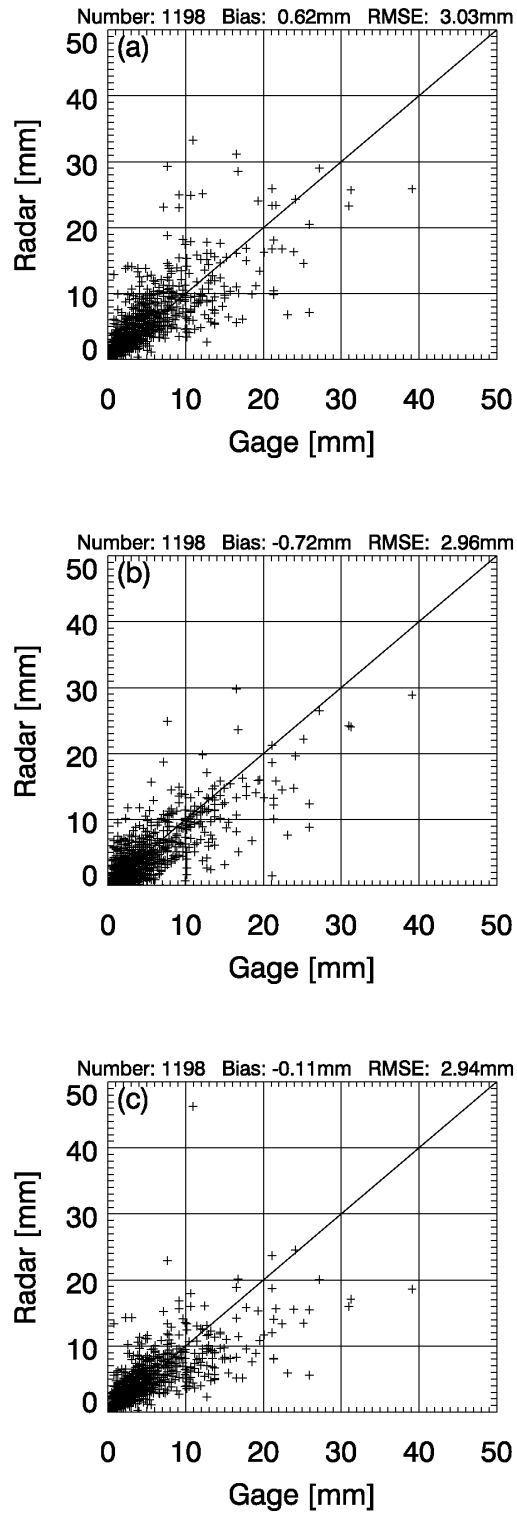


Fig. 17: Hourly radar-gage rainfall accumulation scatterplots for rain type I over Oklahoma Mesonet gage locations: (a) $R(Z)$, (b) $R(K_{DP})$, (c) $R(Z, Z_{DR})$.

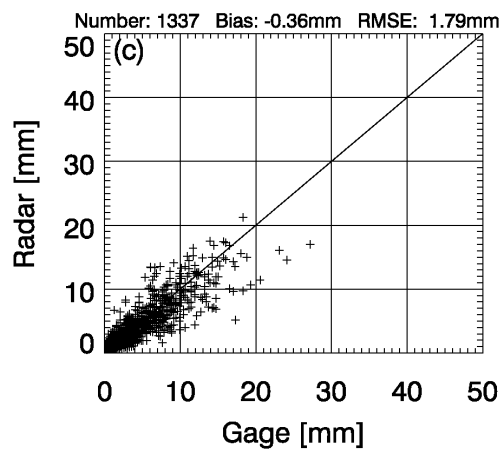
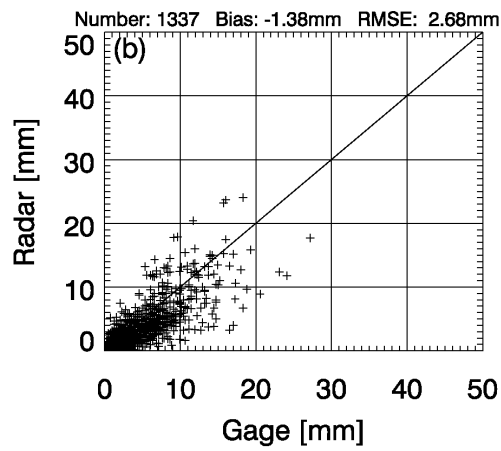
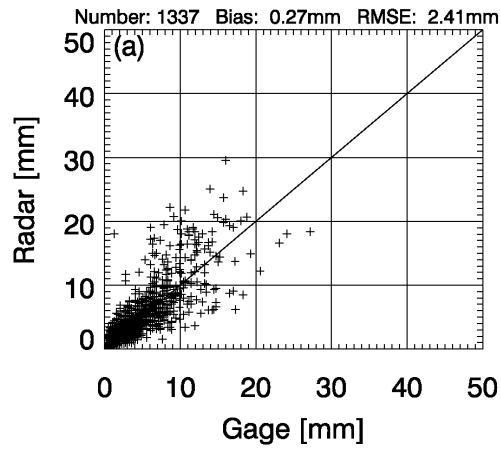


Fig. 18: Hourly radar-gage rainfall accumulation scatterplots for rain type I over ARS network gage locations: (a) $R(Z)$, (b) $R(K_{DP})$, (c) $R(Z, Z_{DR})$.

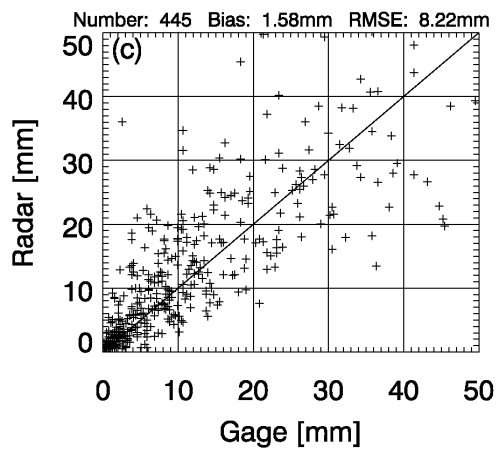
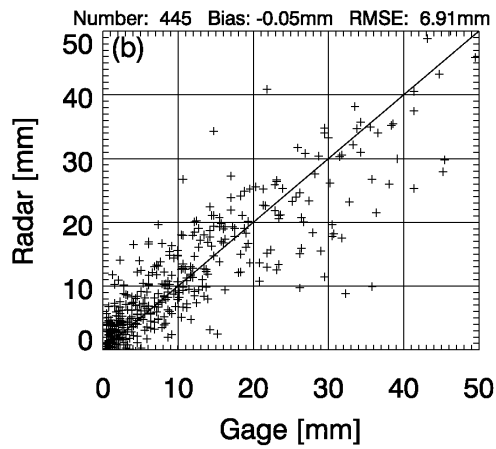
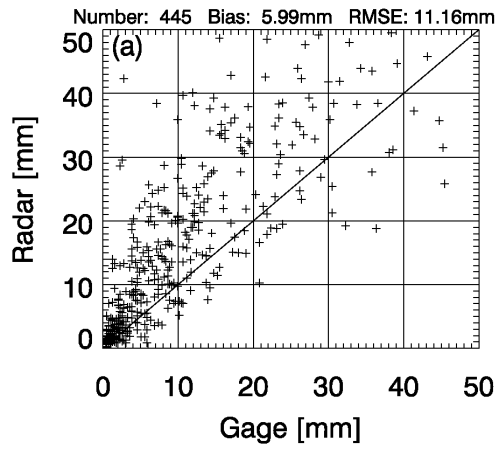


Fig. 19: As in Fig. 17, but for rain type II over Oklahoma Mesonet gages.

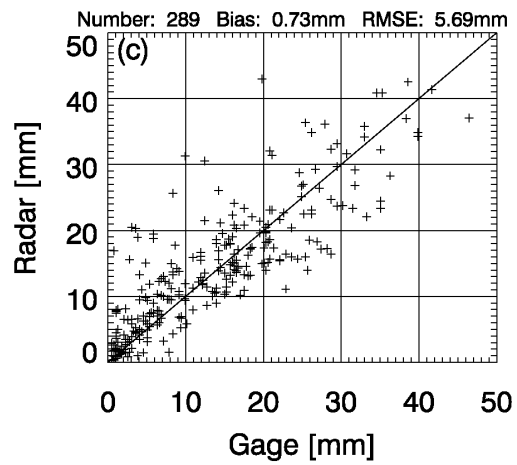
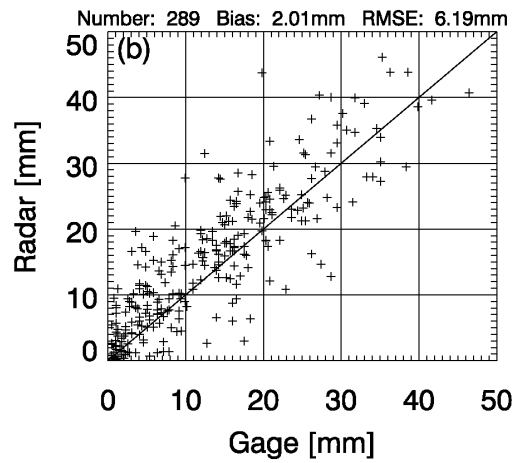
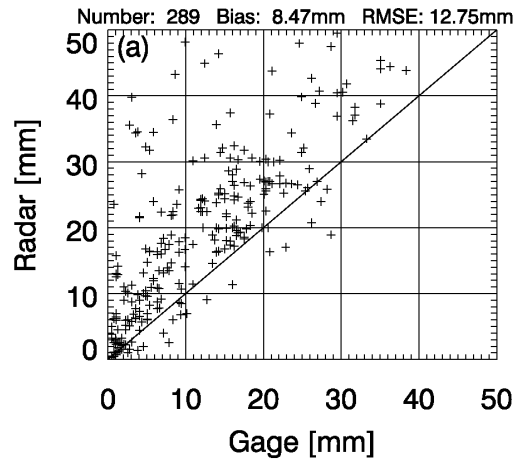


Fig. 20: As in Fig. 18, but for rain type II over ARS network gages.

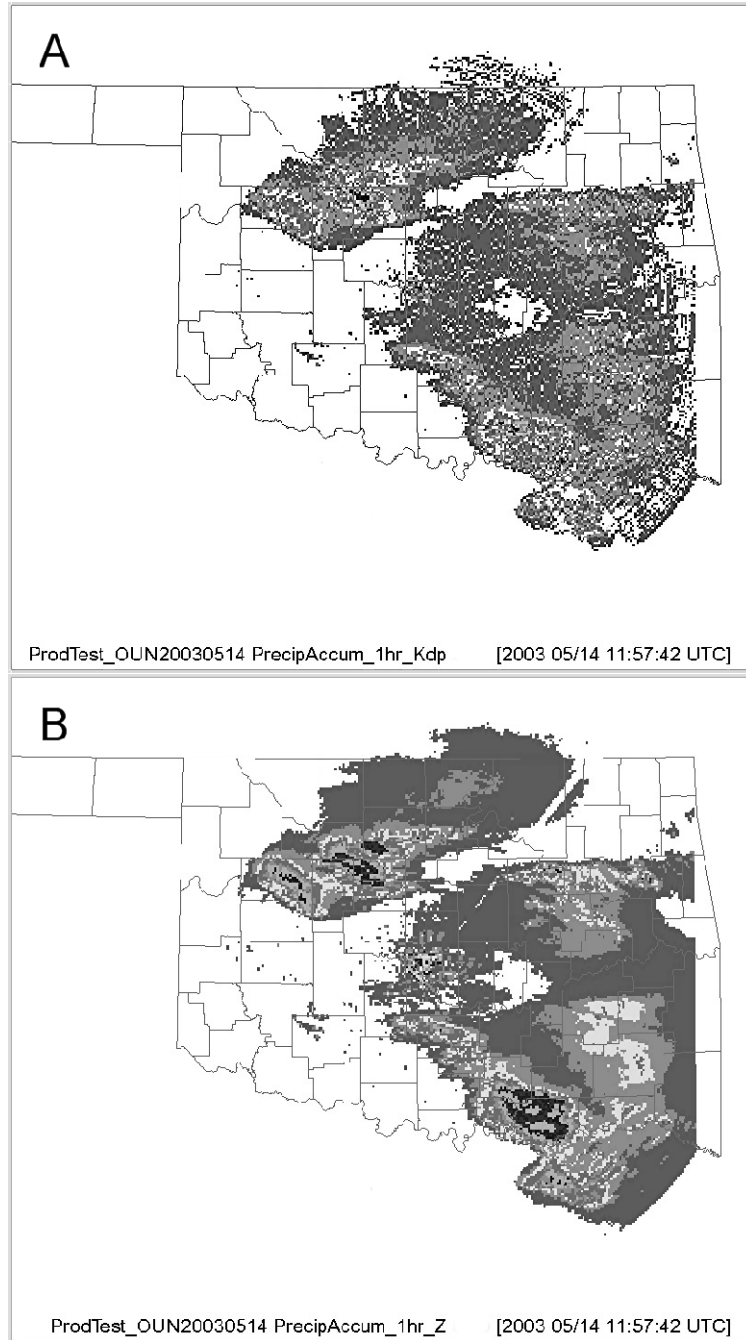


Fig. 21: An example of hourly rain accumulation maps obtained using an (a) $R(K_{DP})$ relation and (b) $R(Z)$ relation.

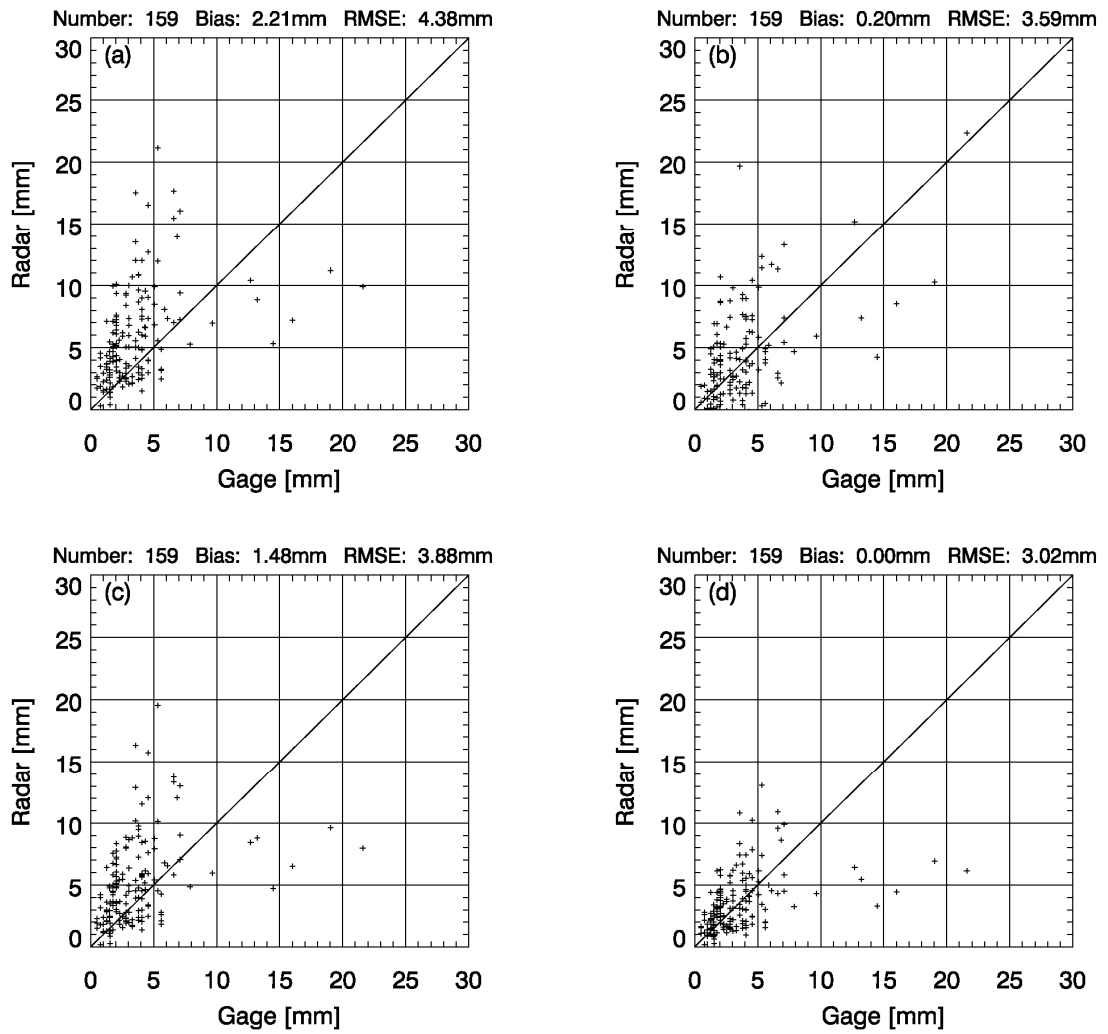


Fig. 22: As in Fig. 17, but for Wet Snow over Oklahoma Mesonet gages: (a) $R(Z)$, (b) $R(K_{DP})$, (c) $R(Z, Z_{DR})$, and (d) $0.6 \cdot R(Z)$ that minimizes bias.

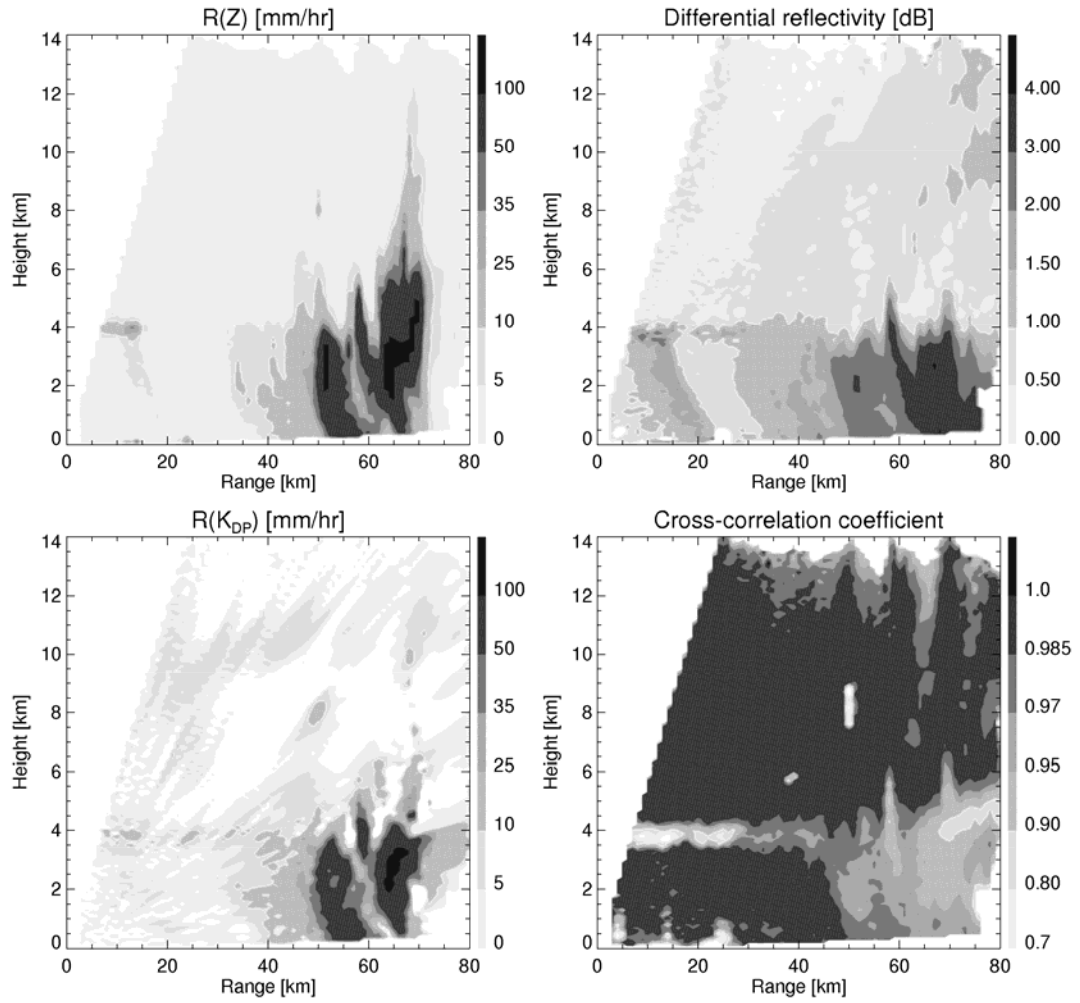


Fig. 23: Vertical cross-section of $R(Z)$, Z_{DR} , $R(K_{DP})$ and ρ_{HV} through a thunderstorm illustrating loose connection between $R(K_{DP})$ and Z_{DR} aloft and rain at the surface.

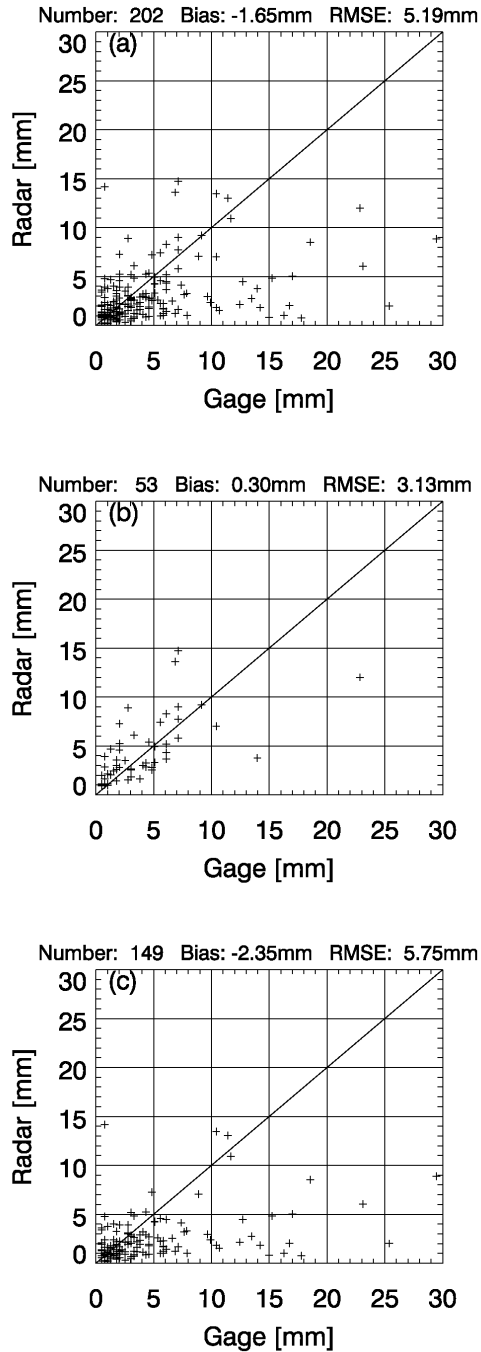


Fig. 24: Performance of the conventional R(Z) algorithm if Dry Snow and Crystals are identified in the radar resolution volume; (a) All distances and heights of the radar volume are included, (b) the radar volume is at or below the freezing level, (c) the radar volume is above the freezing level.

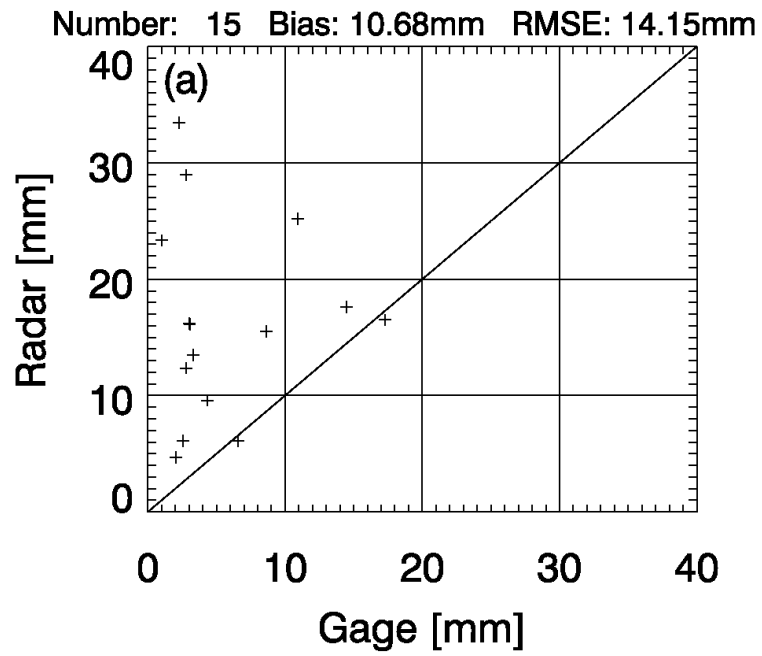


Fig. 25: Performance of the conventional R(Z) algorithm if the radar volume is filled with graupel or hail and is located above the freezing level.

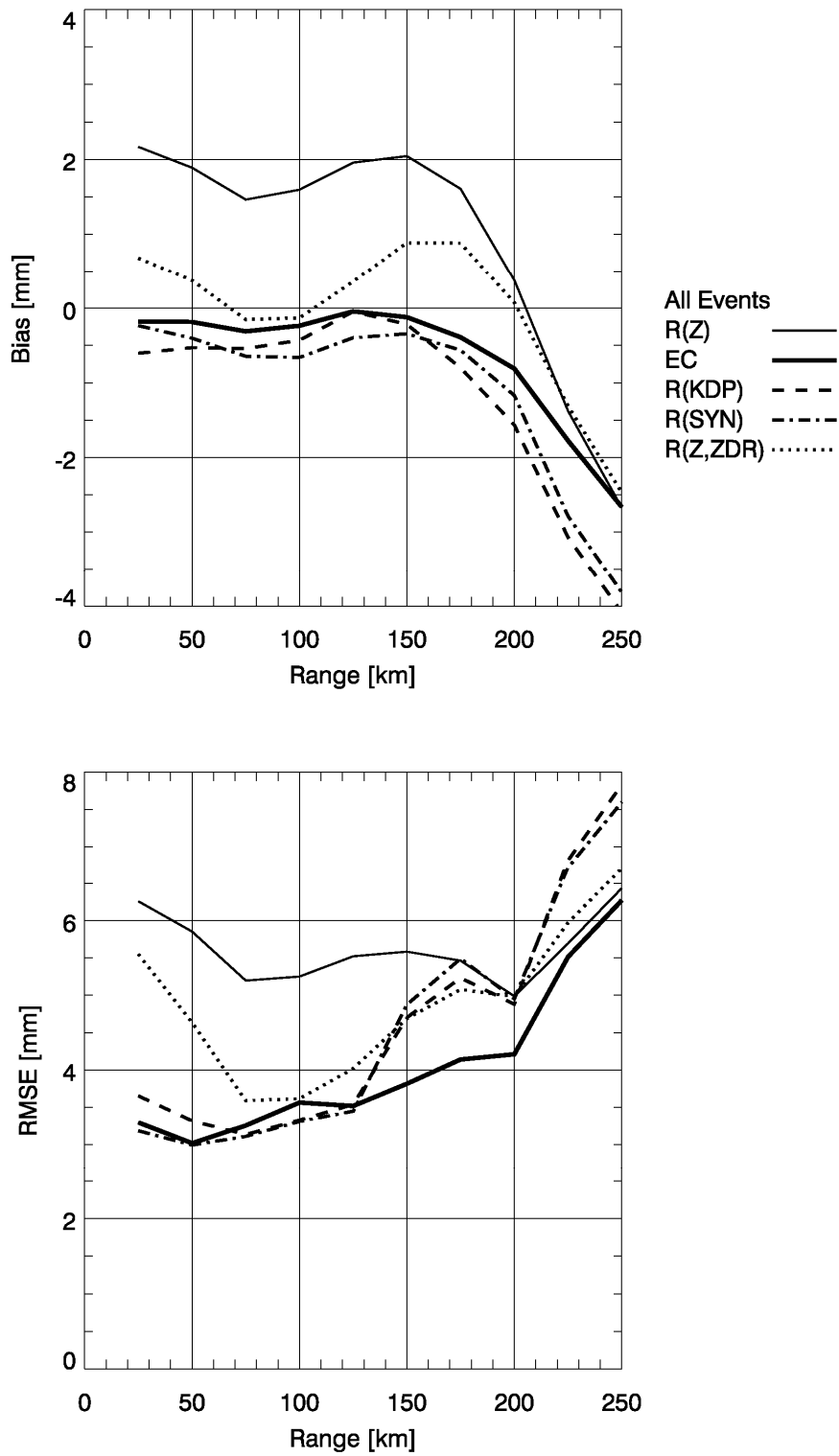


Fig. 26: Mean bias (top) and RMS error (bottom) of different radar estimates as a function of range (43 rain events, 179 hours of observation).

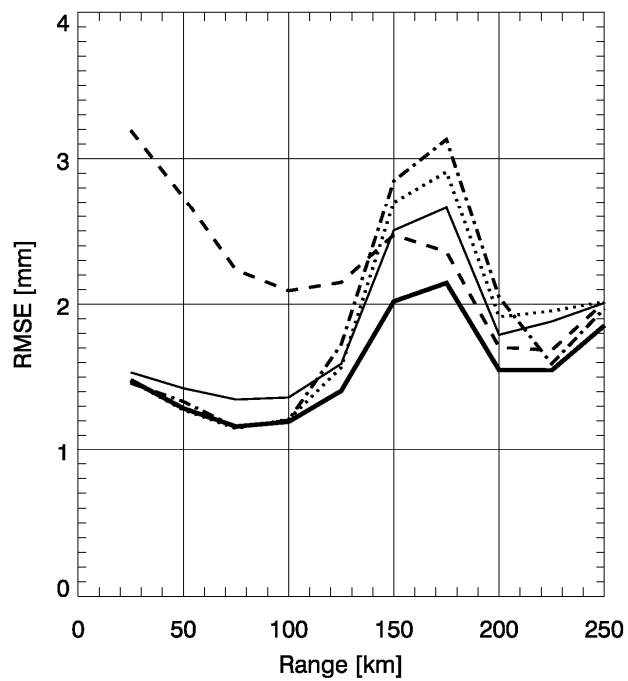
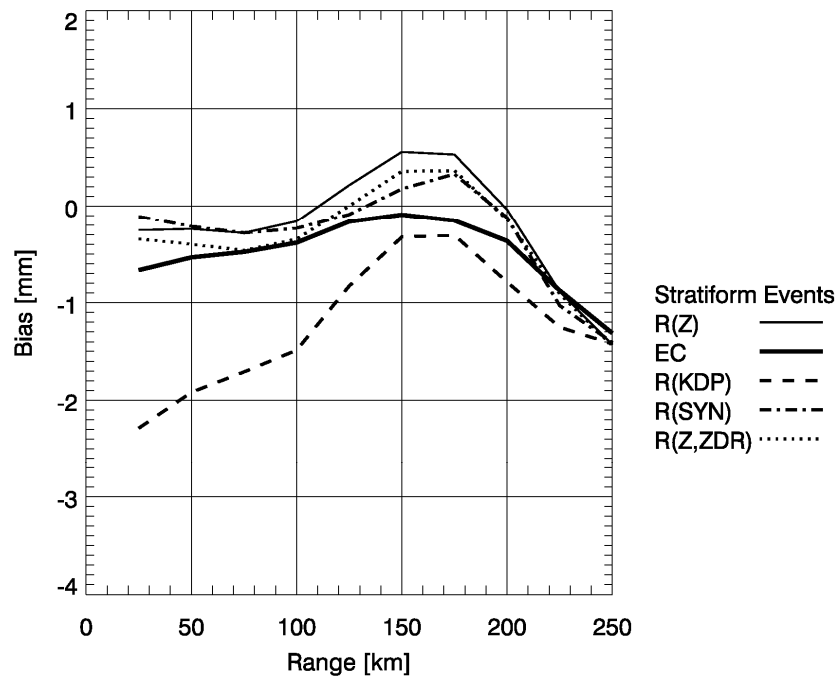


Fig. 27: As in Fig. 26, but for stratiform events with an absence of convective signatures (9 rain events, 26 hours of observation).

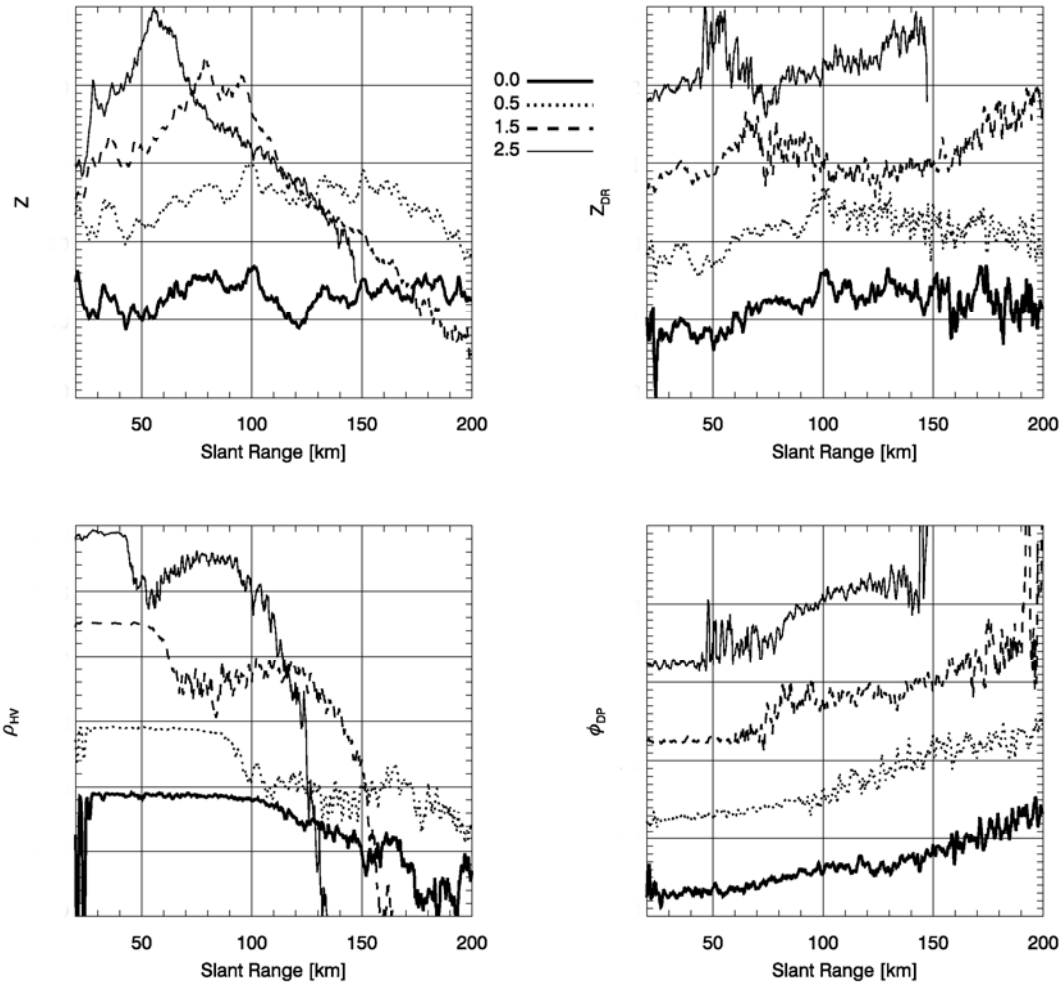


Fig. 28: Polarimetric variables for various elevation angles measured at the 110° azimuth for the 11/18/04 case. Tick marks in Z (Z_{DR}) plots represent 1 dB (0.1 dB). ρ_{HV} is plotted with 0.01 tick marks. Tick marks in Φ_{DP} profiles are in 1° increments.

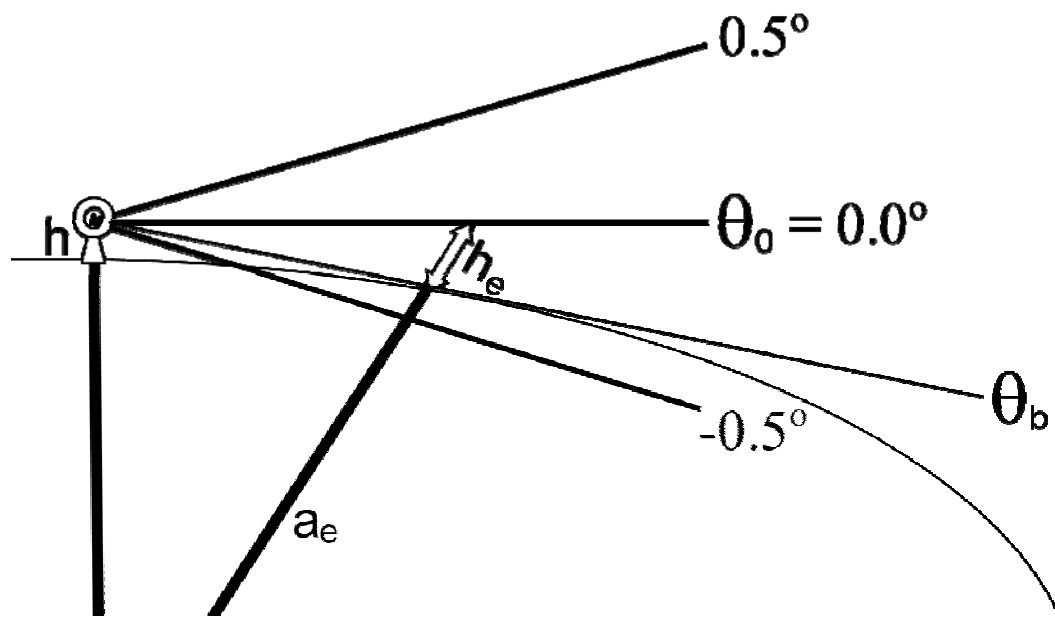


Fig. 29: Illustration of the beam blockage cause by the surface. θ_0 is the elevation angle at the middle of the beam (here drawn as 0.0°), θ_b is the elevation angle for the top of the blocking obstacle, h is the height of the radar tower, a_e is the effective radius of the earth, h_e is the equivalent mean beam height above the surface.

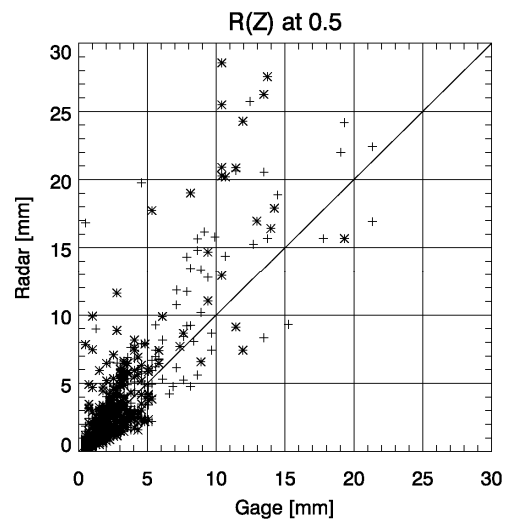
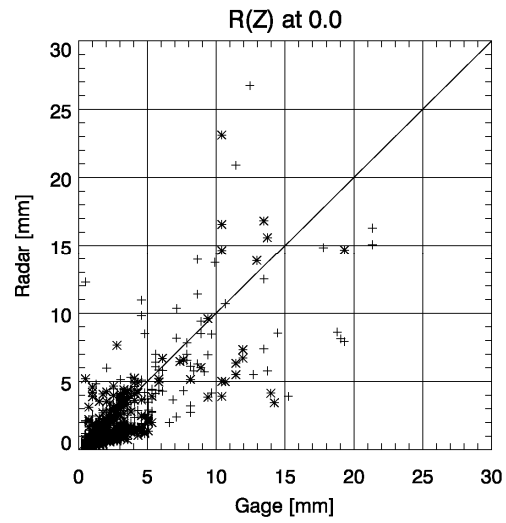


Fig 30: Hourly radar-gage rainfall accumulation scatterplots over ARS (cross-hairs) and Oklahoma Mesonet (stars) network gage locations for the $R(Z)$ relation at the 0.0° tilt and the 0.5° tilt.

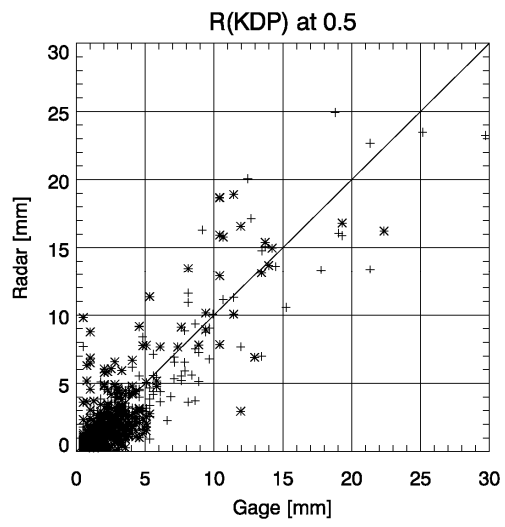
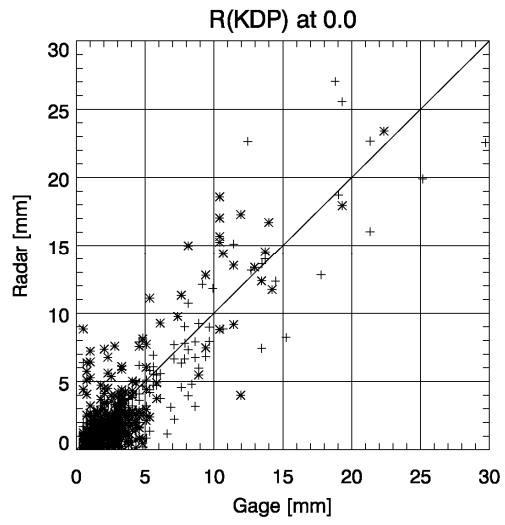


Fig. 31: As in Fig. 30, but for $R(K_{DP})$.



Fig. 32: Image of the Cimarron radar taken during the Fall of 2002. Top left corner image shows the radar after an ice storm in February 2003.

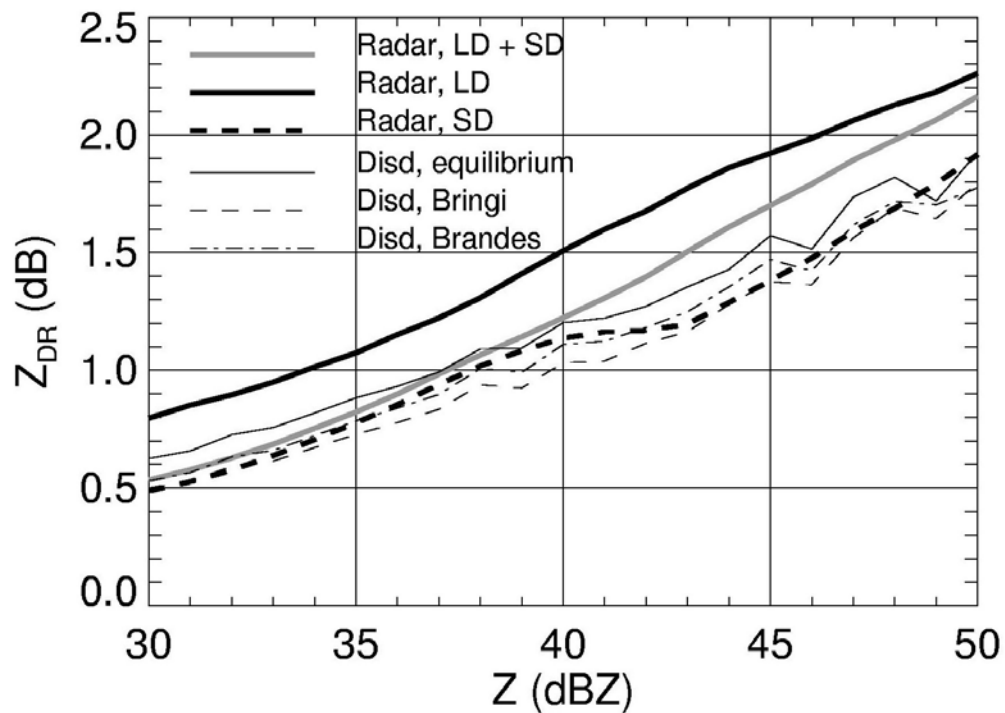


Fig. 33: Mean Z - Z_{DR} dependencies obtained from the radar for different rain regimes and from the disdrometer using different assumptions about raindrop shapes. “Radar” curves are derived from the KOUN WSR-88D measurements. “Disd” curves are based on the 2D video disdrometer statistics. “LD” and “SD” curves correspond to rain regimes dominated by large and small drops, respectively. Simulations from disdrometer measurements are made using assumptions about drop shape following Beard and Chuang (1987) measurements, Brandes et al. (2002), and Bringi et al. (2003).

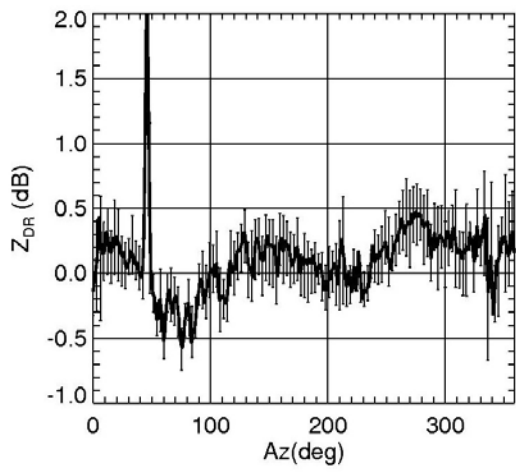
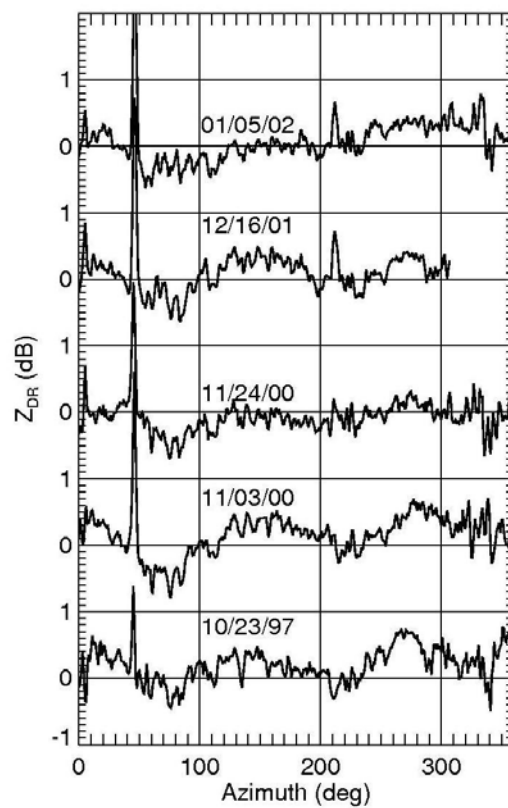


Fig. 34: (a) Azimuthal dependencies of Z_{DR} measured by the Cimarron radar at the 0.5° elevation angle for 5 rain events. (b) Mean azimuthal dependence for these events. Error bars indicate the range of Z_{DR} variations for all cases.

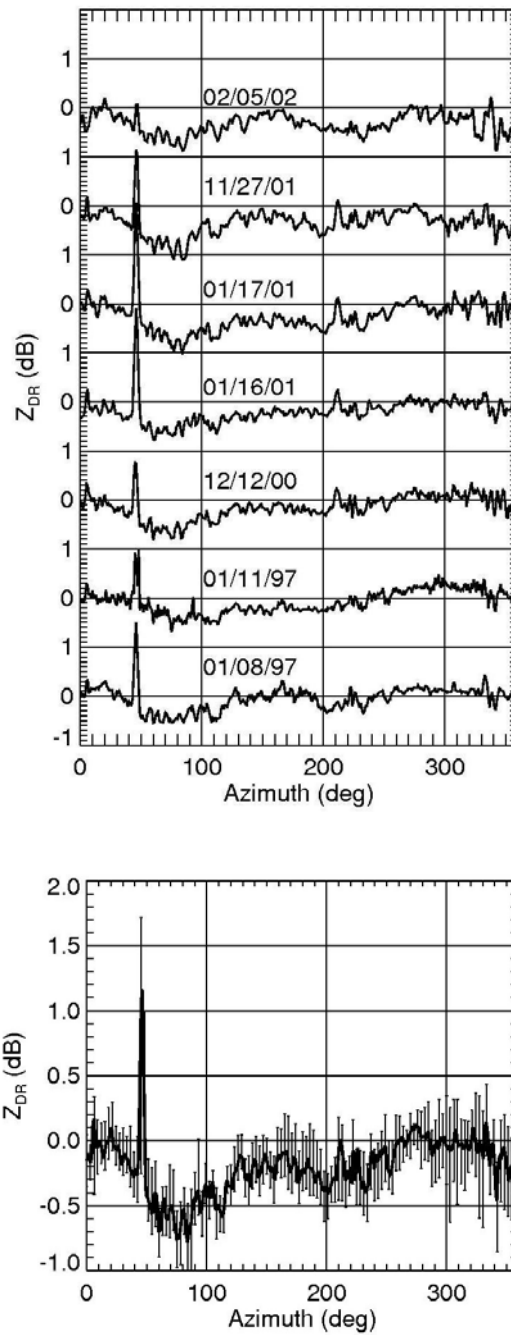


Fig. 35: Same as Fig. 34, but for 7 snow events.

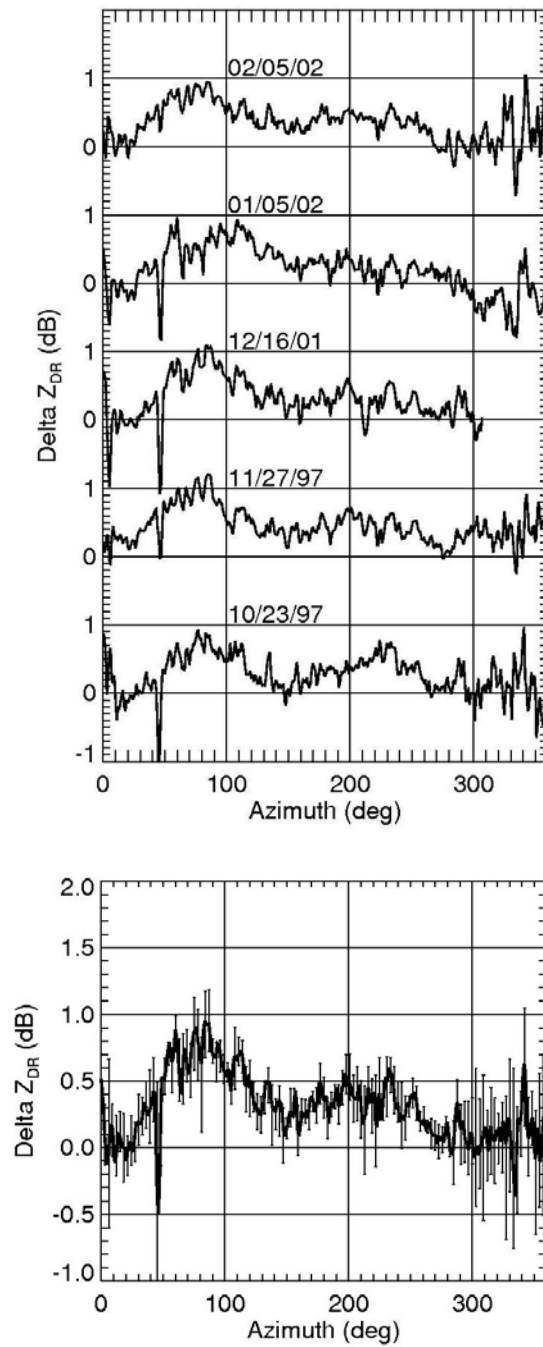


Fig. 36: (a) Difference between the mean azimuthal dependencies of Z_{DR} at the 1.5° and 0.5° elevation angles for 5 events. (b) Mean azimuthal dependence for all 5 events. Error bars indicate the range of variation in the difference field.

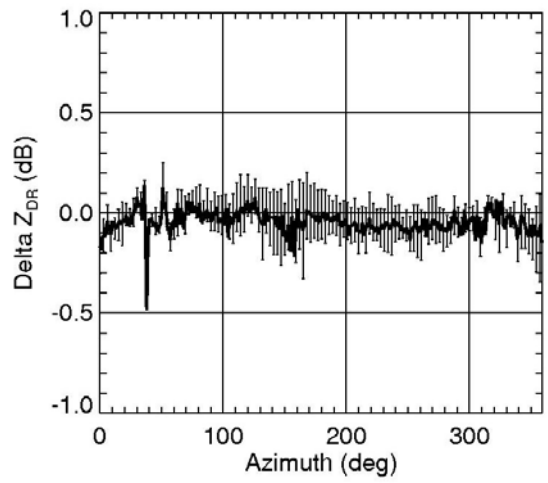
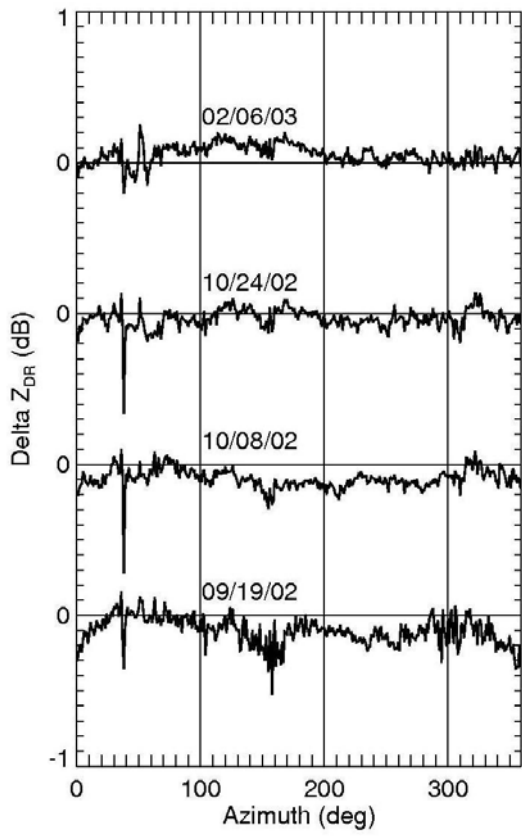


Fig. 37: Same as Fig. 36, but for 4 events observed by the KOUN radar.

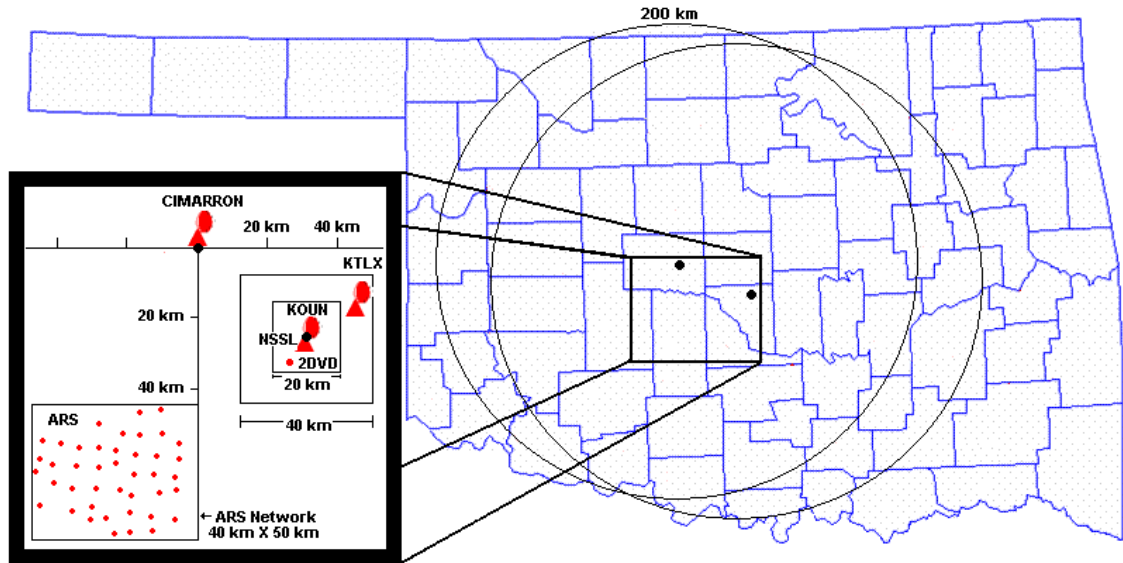


Fig. 38: Location of radars and the ARS network rain gauges in central Oklahoma.

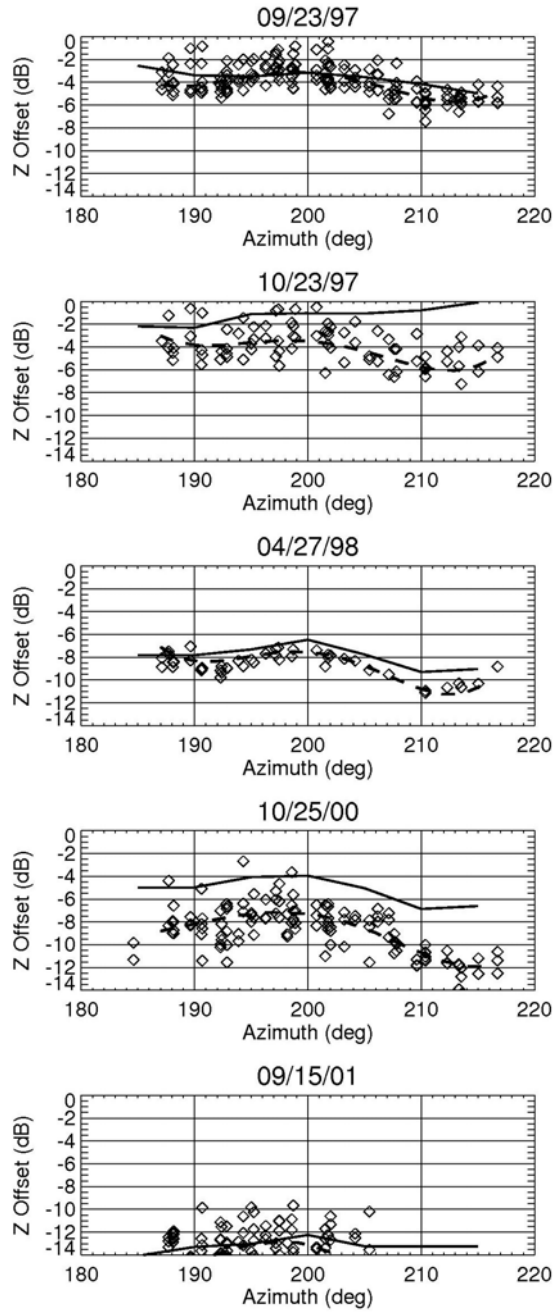


Fig. 39: Bias of Z measured by the Cimarron radar as a function of azimuth for 5 rain events. Diamonds and dashed lines indicate results of direct comparisons of Z from the Cimarron and WSR-88D data. The solid curves represent results of consistency-based retrievals.

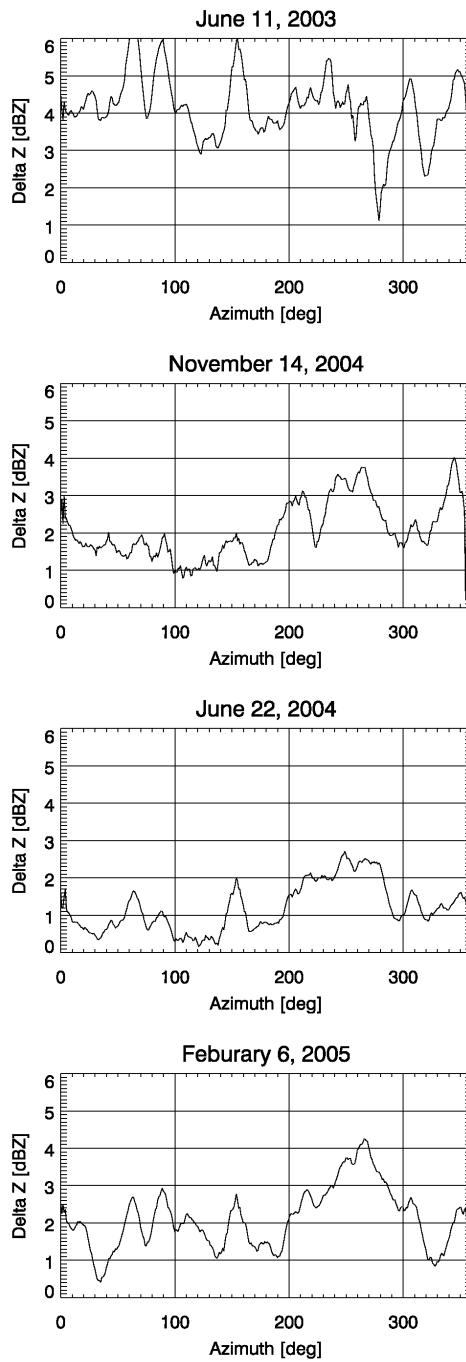


Fig. 40: Relative bias of Z as determined from the difference of $R(K_{DP})$ and $R(Z)$ rainrates projected into Z as a function of azimuth for 4 rain events.

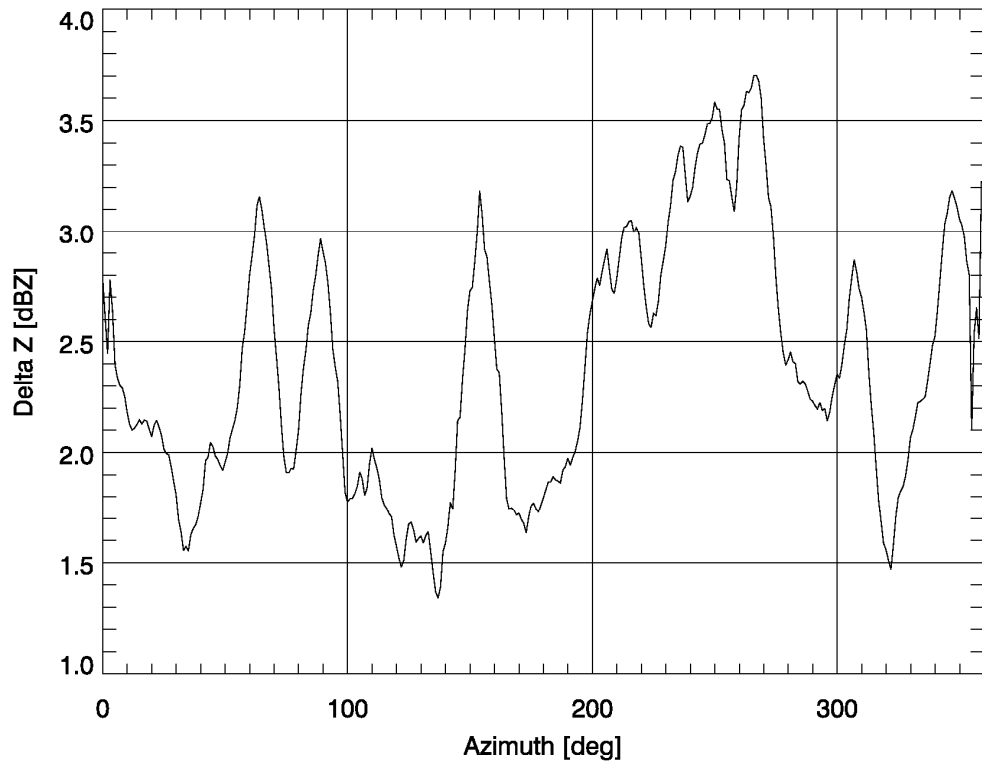


Fig. 41: Mean azimuthal dependence of the Z bias for the events featured in Fig. 38.

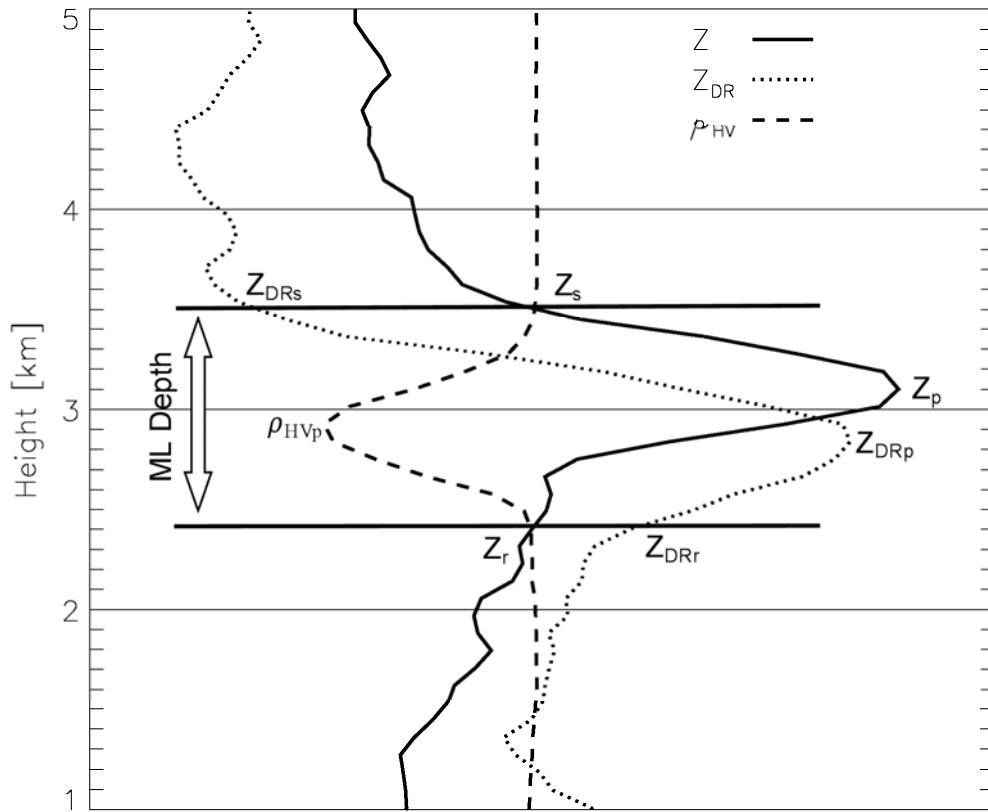


Fig. 42: Diagram of polarimetric measurement profiles and several parameters that are extracted from these profiles.

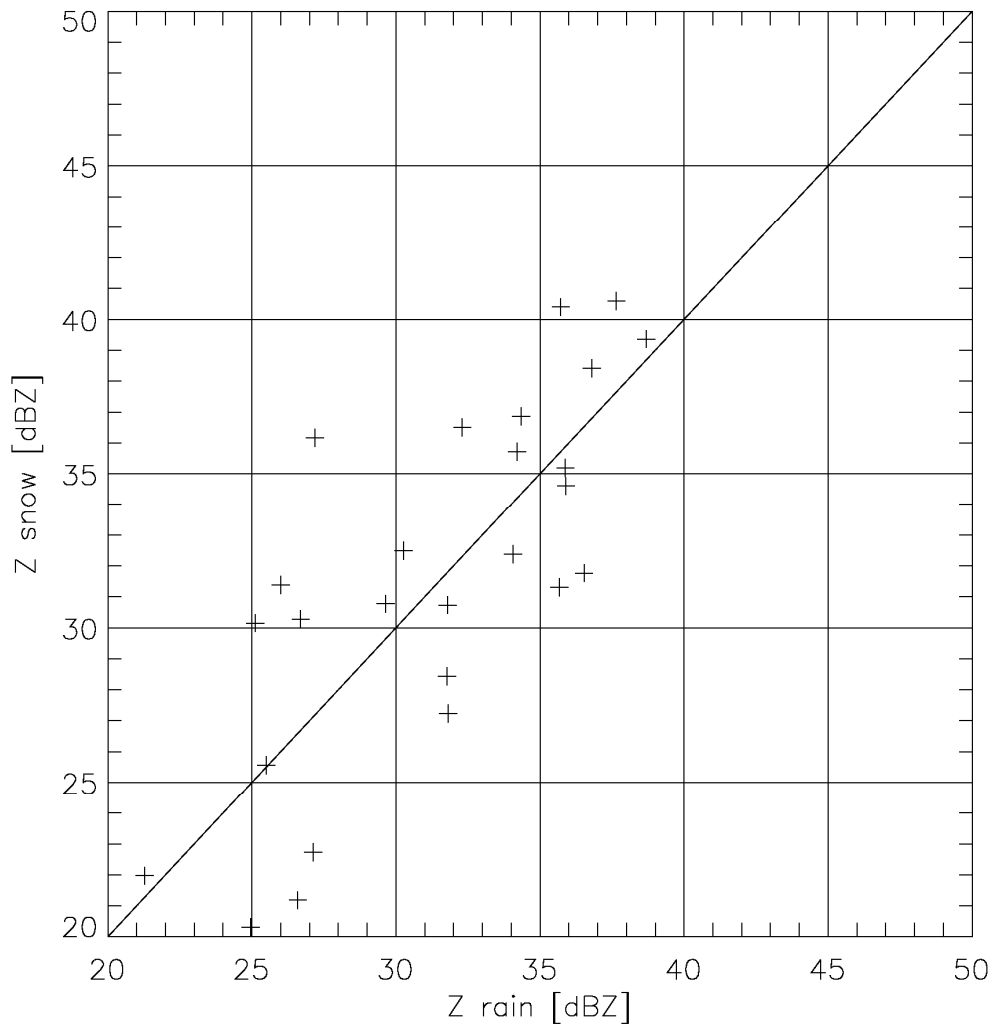


Fig. 43: Scatterplot of the Z in snow versus the value of Z in the rain beneath the melting layer as revealed from analysis of 30 typical profiles of polarimetric radar variables in 10 different storms with pronounced bright band observed with the NSSL's S-band polarimetric radar.

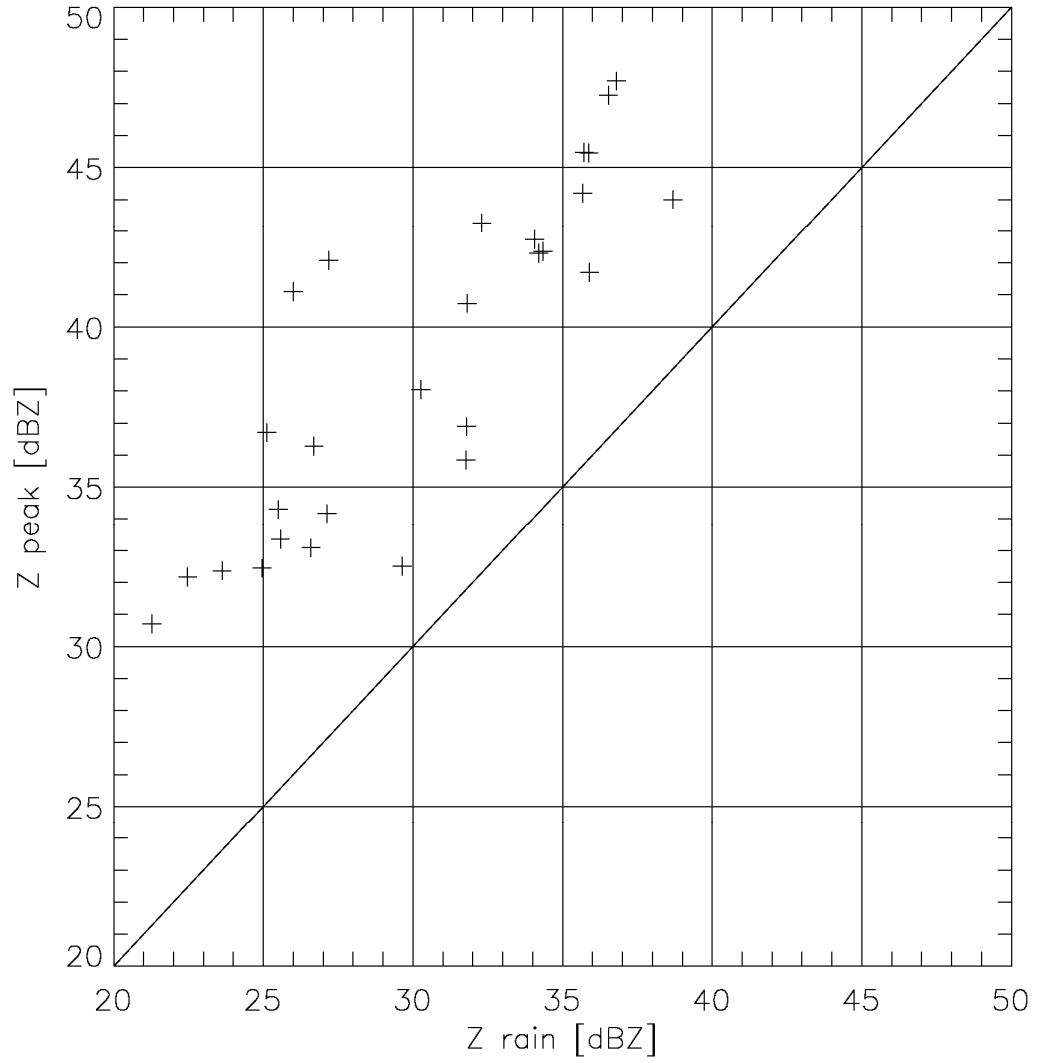


Fig. 44: Scatterplot of Z in rain versus the peak value of Z within the melting layer as in Fig. 43.

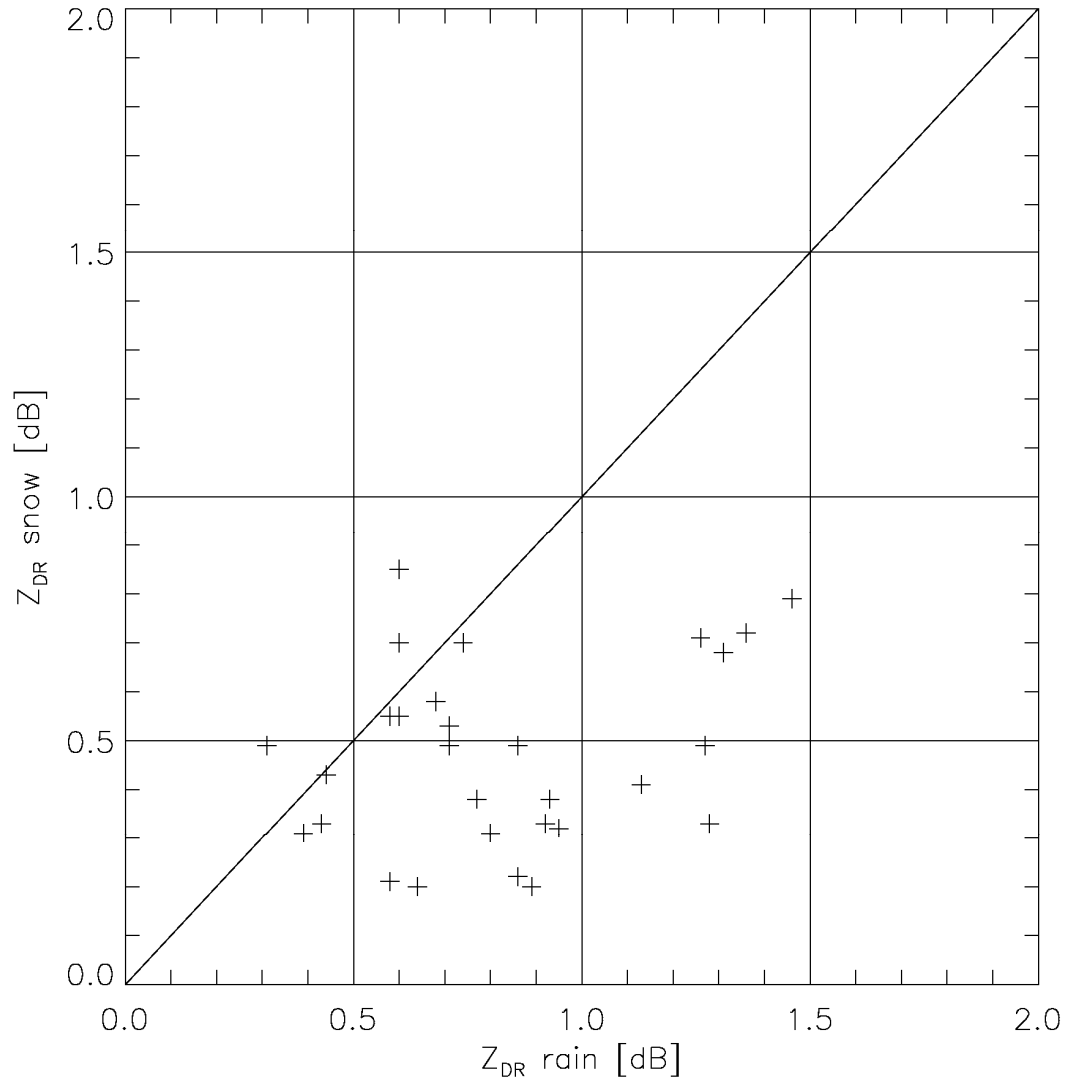


Fig. 45: Scatterplot of Z_{DR} in snow versus Z_{DR} in rain beneath the melting layer as in Fig. 43.

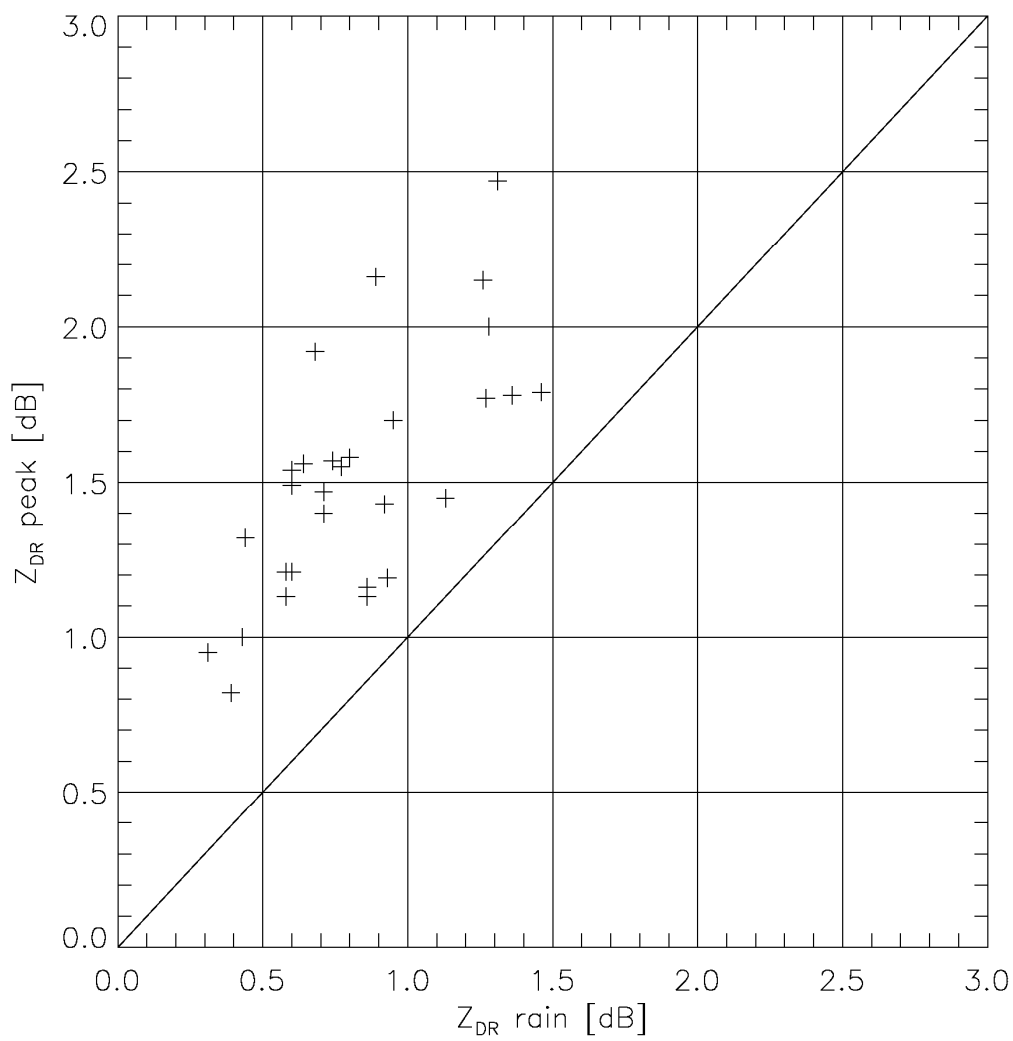


Fig. 46: As in Fig. 43, the scatterplot of the Z_{DR} in rain versus the peak in Z_{DR} within the melting layer.

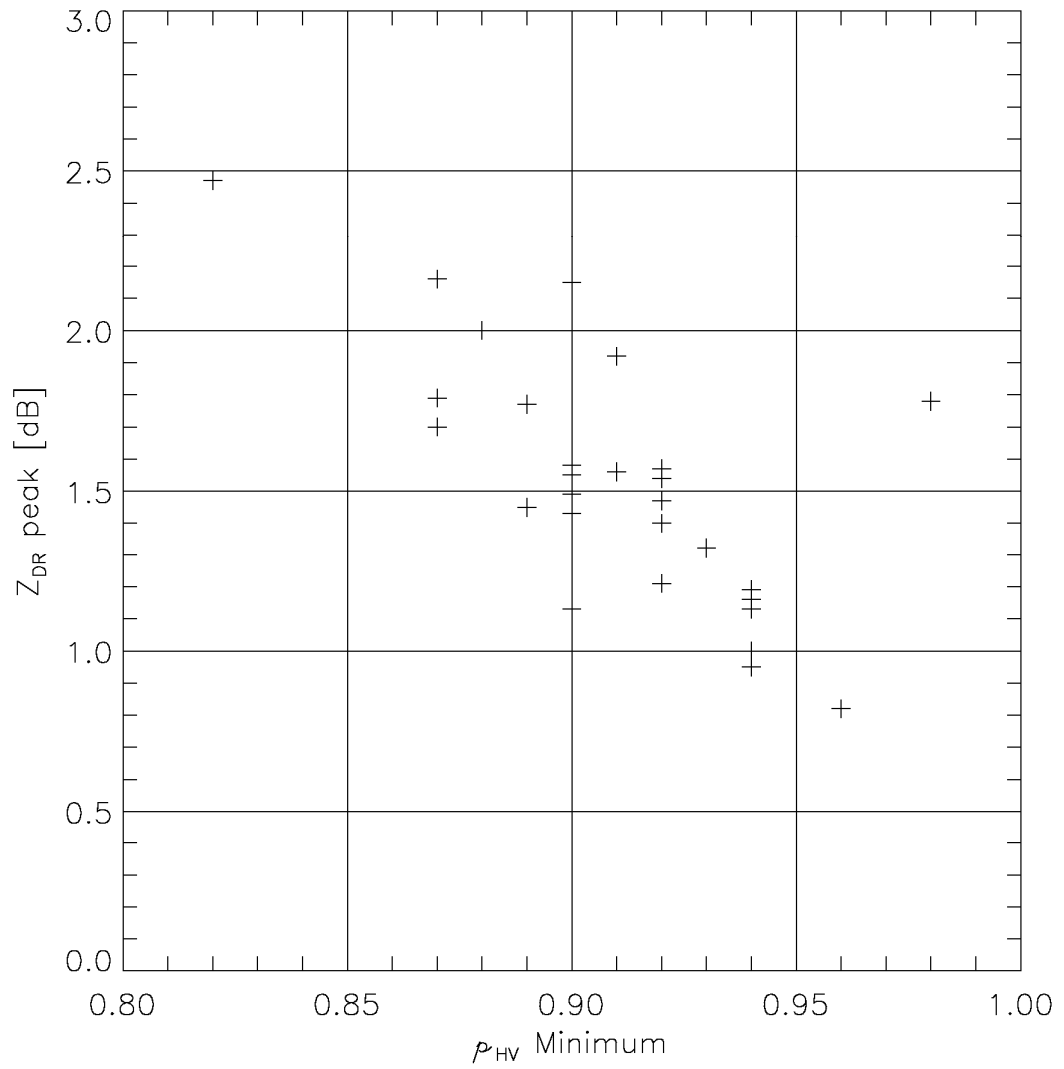


Fig. 47: As in Fig. 43, the scatterplot of the Z_{DR} peak within the melting layer versus the minimum in ρ_{HV}.

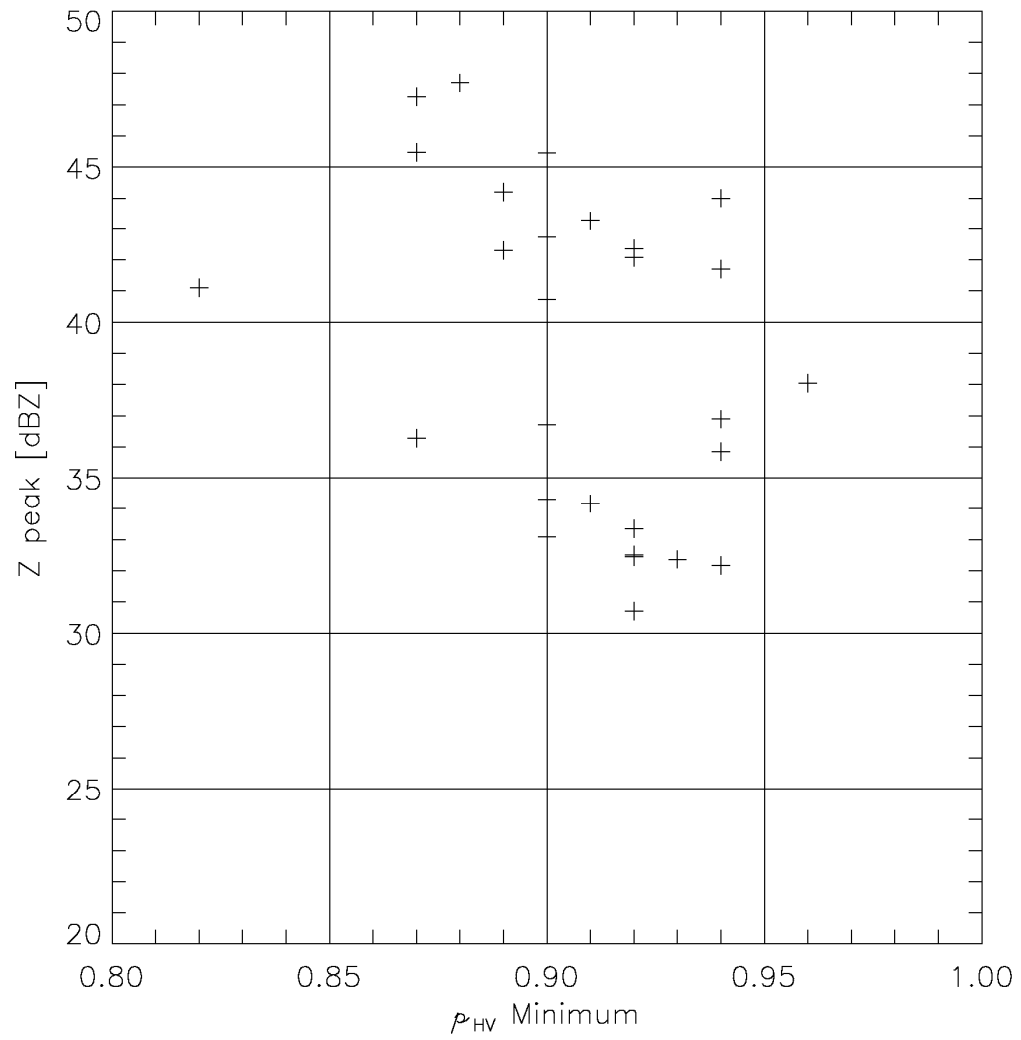


Fig. 48: As in Fig. 43, the scatterplot of the Z peak within the melting layer versus the minimum in ρ_{HV} .

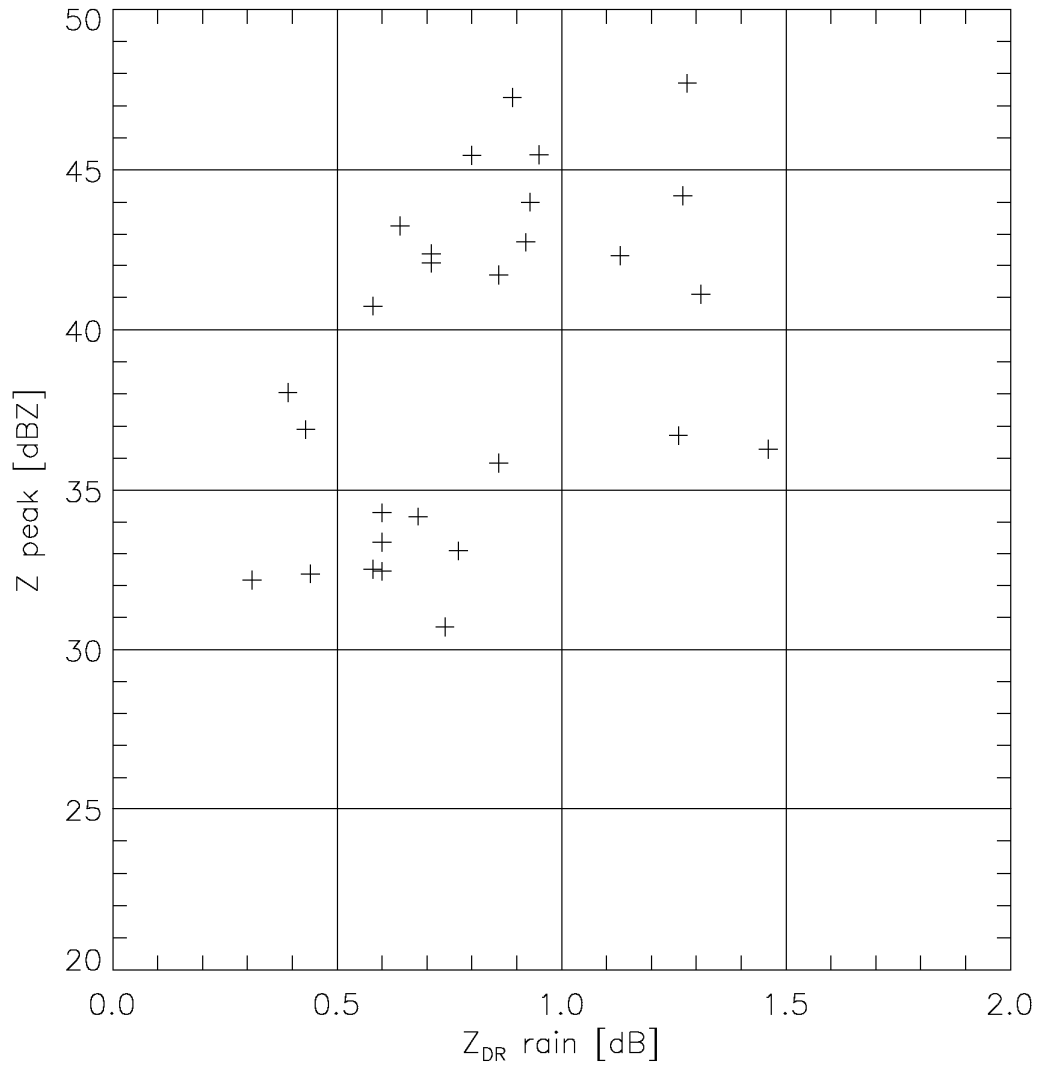


Fig. 49: As in Fig. 43, the scatterplot of the Z peak within the melting layer versus the value of Z_{DR} in rain beneath.

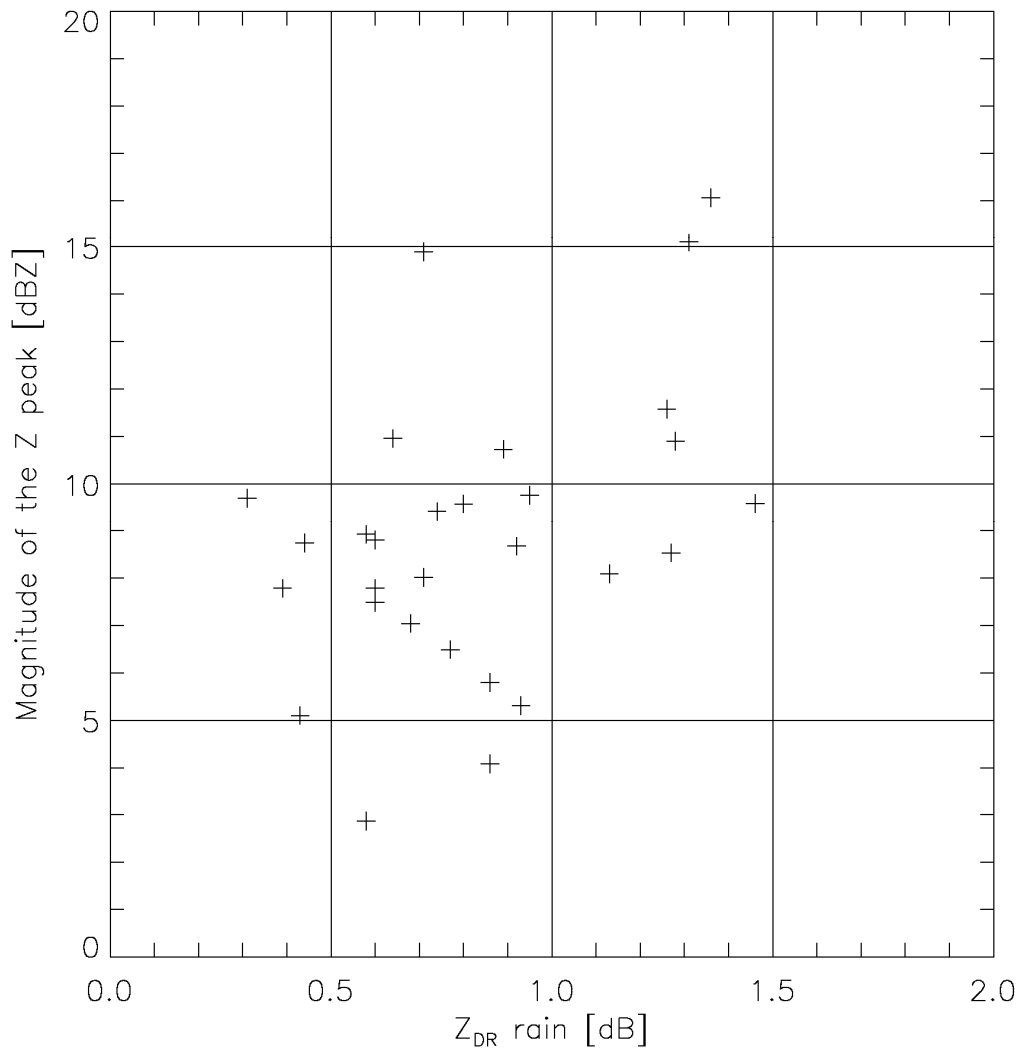


Fig. 50: As in Fig. 43, the scatterplot of the enhancement in Z within the melting layer versus the Z_{DR} in the rain beneath

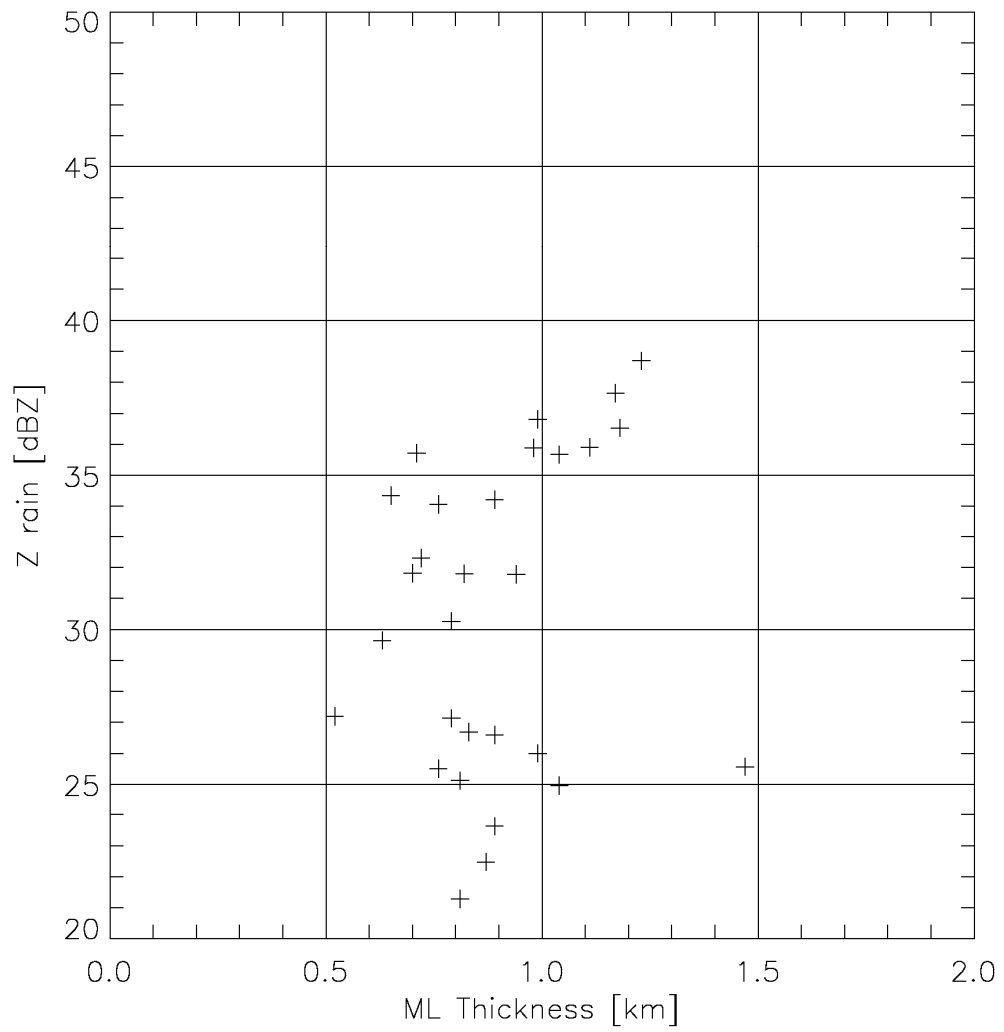


Fig. 51: As in Fig. 43, the scatterplot of melting layer thickness versus the value of Z in rain.

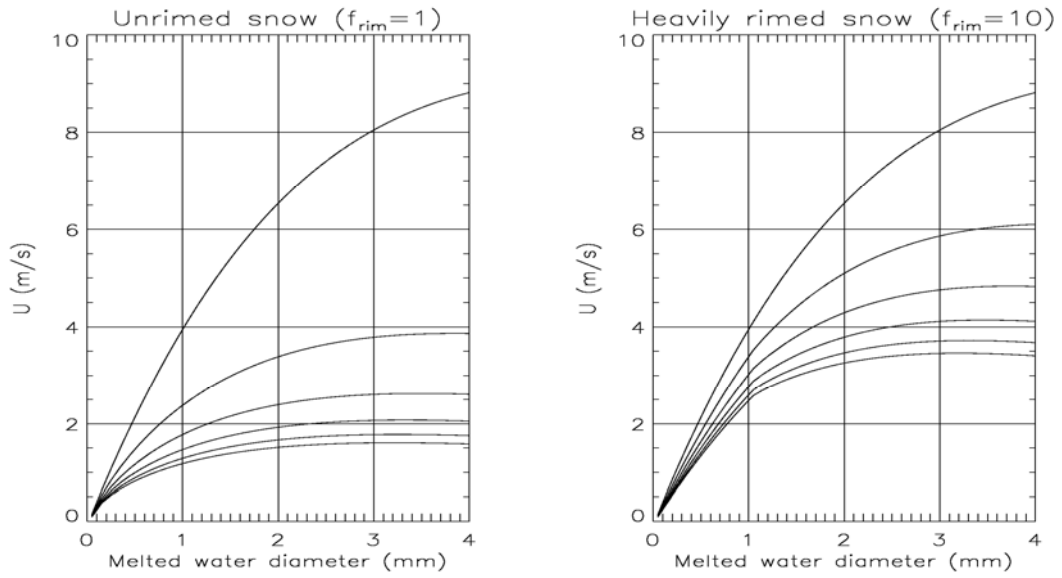


Fig. 53: Terminal velocity of melting snowflakes as a function of melted water diameter for six values of mass water fraction: 0, 20, 40, 60, 80, and 100% in the case of unrimed and heavily rimed snow.

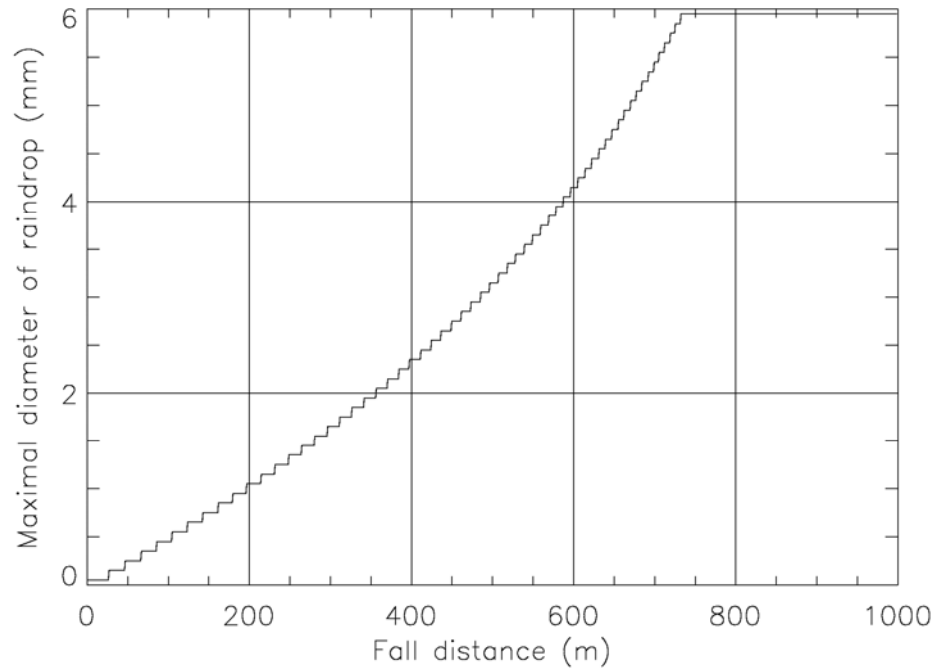


Fig. 54: Maximal diameter of raindrops versus fall distances from the top of the melting layer. Rainrate R is set at 5 mm hr^{-1} .

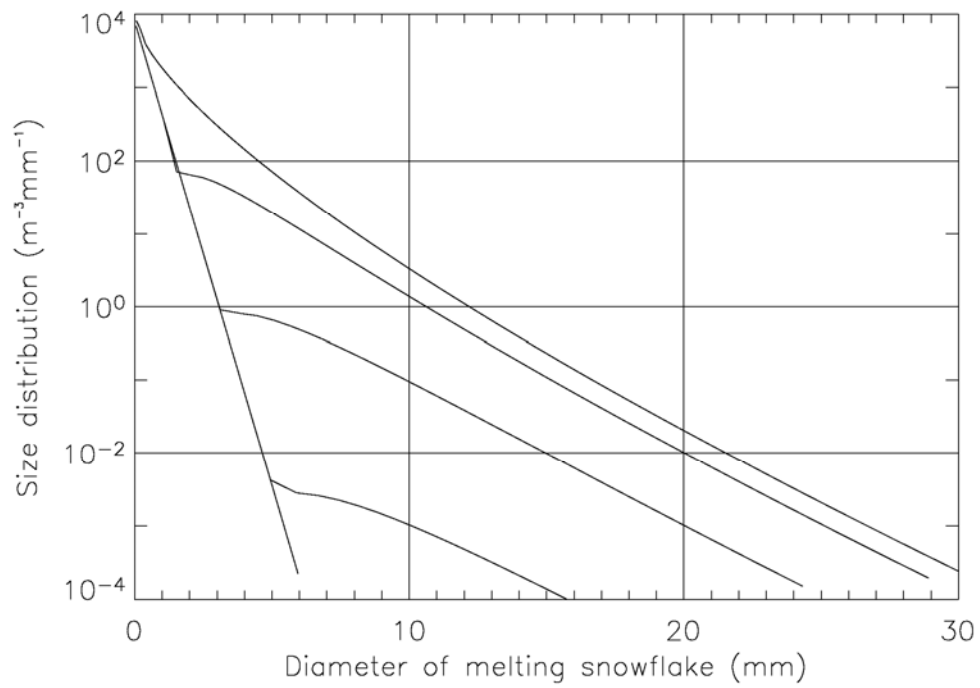


Fig. 55: Size distributions of raindrops and partially melted snowflakes at the top of the melting layer (upper curve) and at the levels 200, 400, 600, and 800 m below the top.

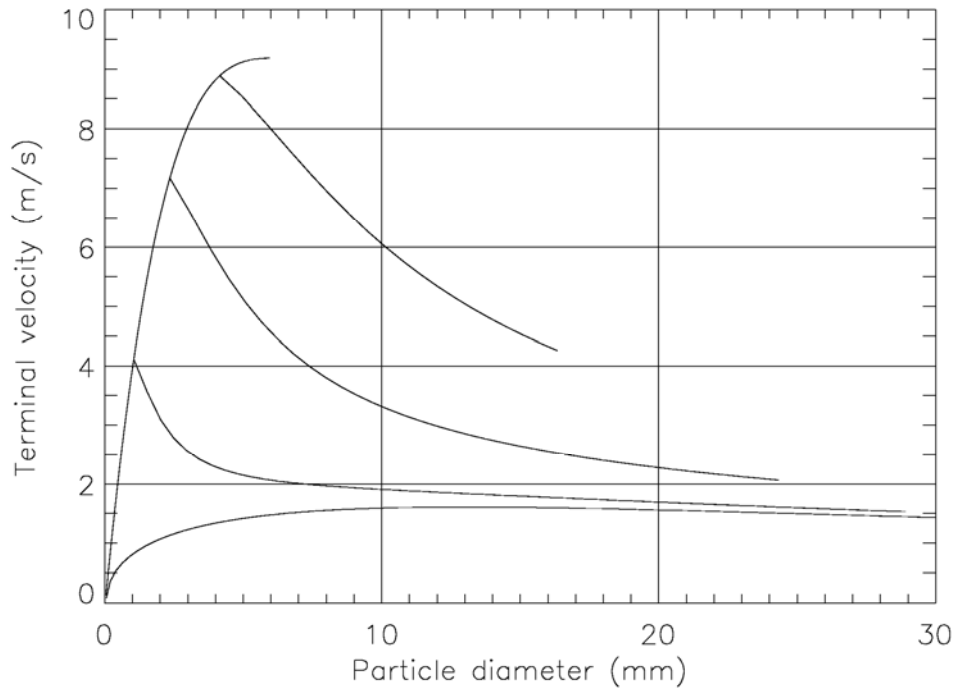


Fig. 56: Terminal velocities of raindrops and partially melted snowflakes at the top of the melting layer (bottom curve) and at the levels 200, 400, 600, and 800 m below the top. Rainrate R is set at 5 mm hr^{-1} .

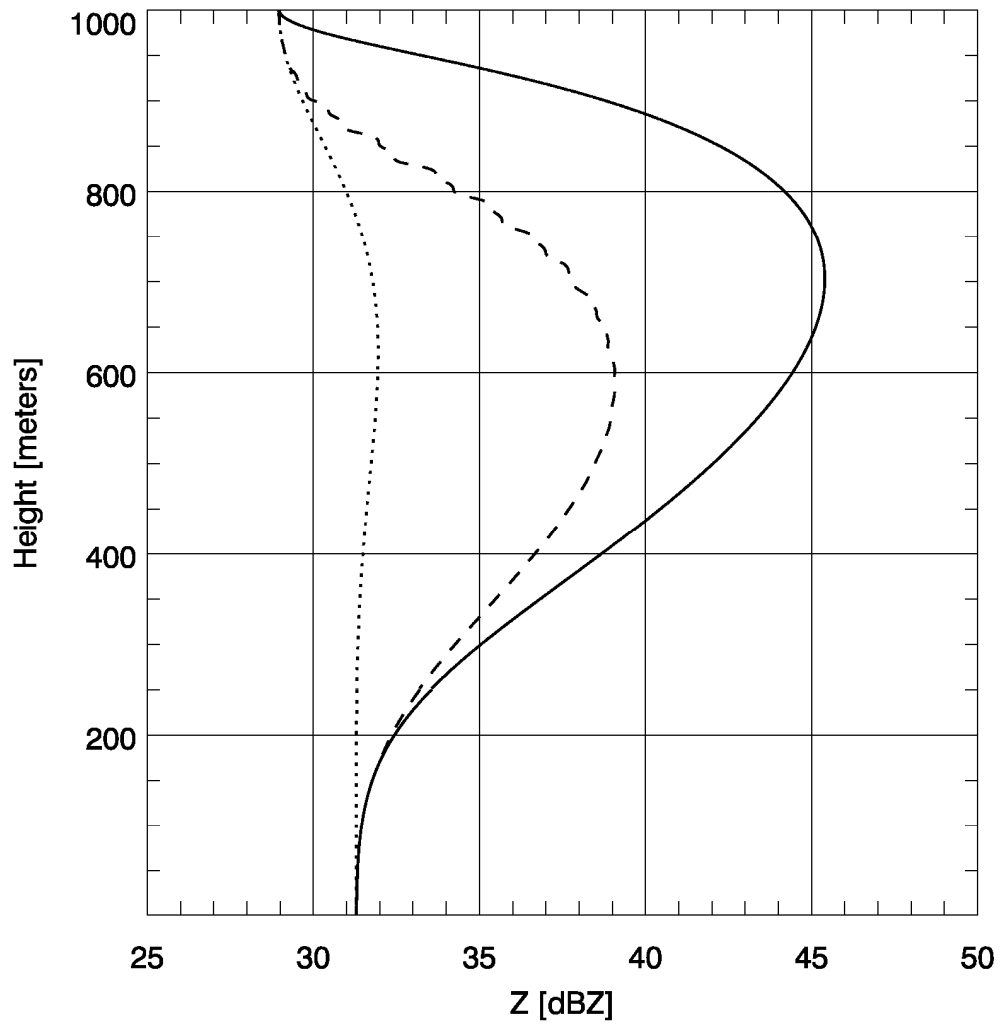


Fig. 57: Model profiles of Z_H through the melting layer. Z_H based on dielectric Model A (water with snow inclusions) is depicted with a solid line, Model B (snow with water inclusions) is depicted with a dotted line, and Model C (mixture of Models A,B) is depicted with a dashed lines. Rain rate is 3 mm hr^{-1} .

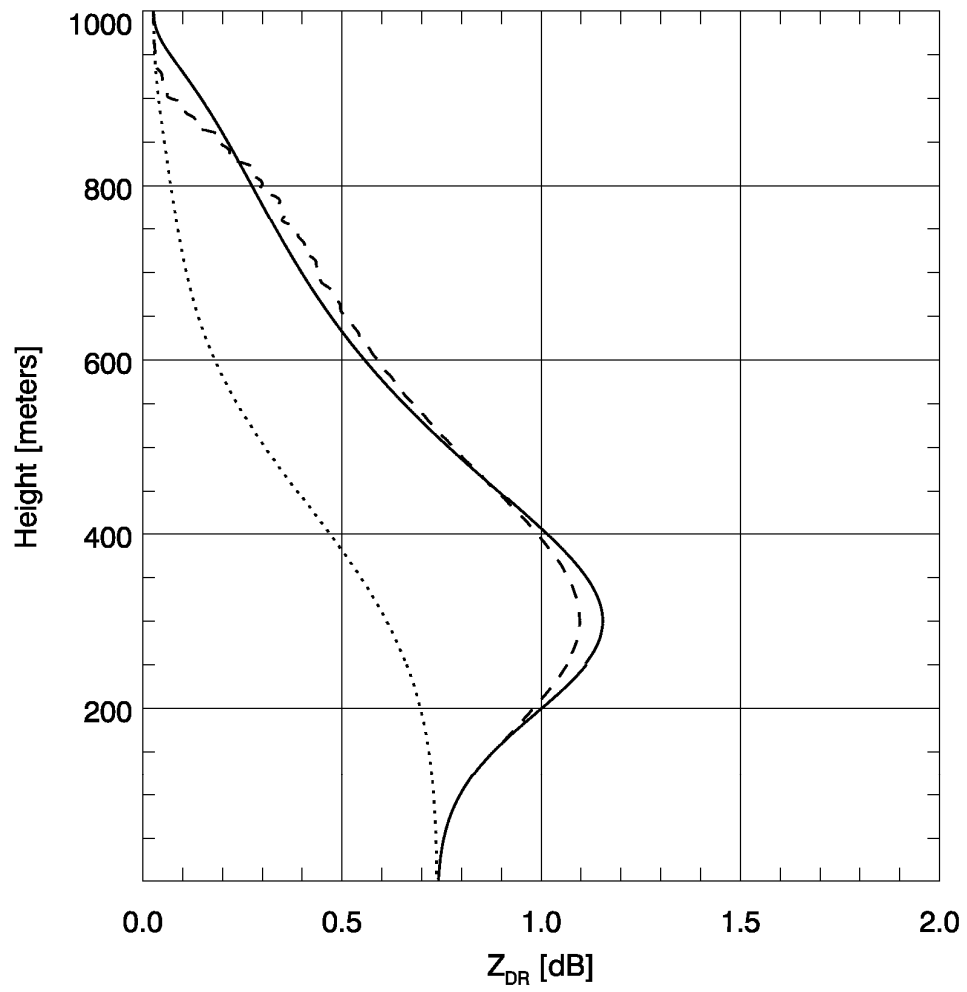


Fig. 58: As in Fig. 57, but for model profiles of Z_{DR} through the melting layer.

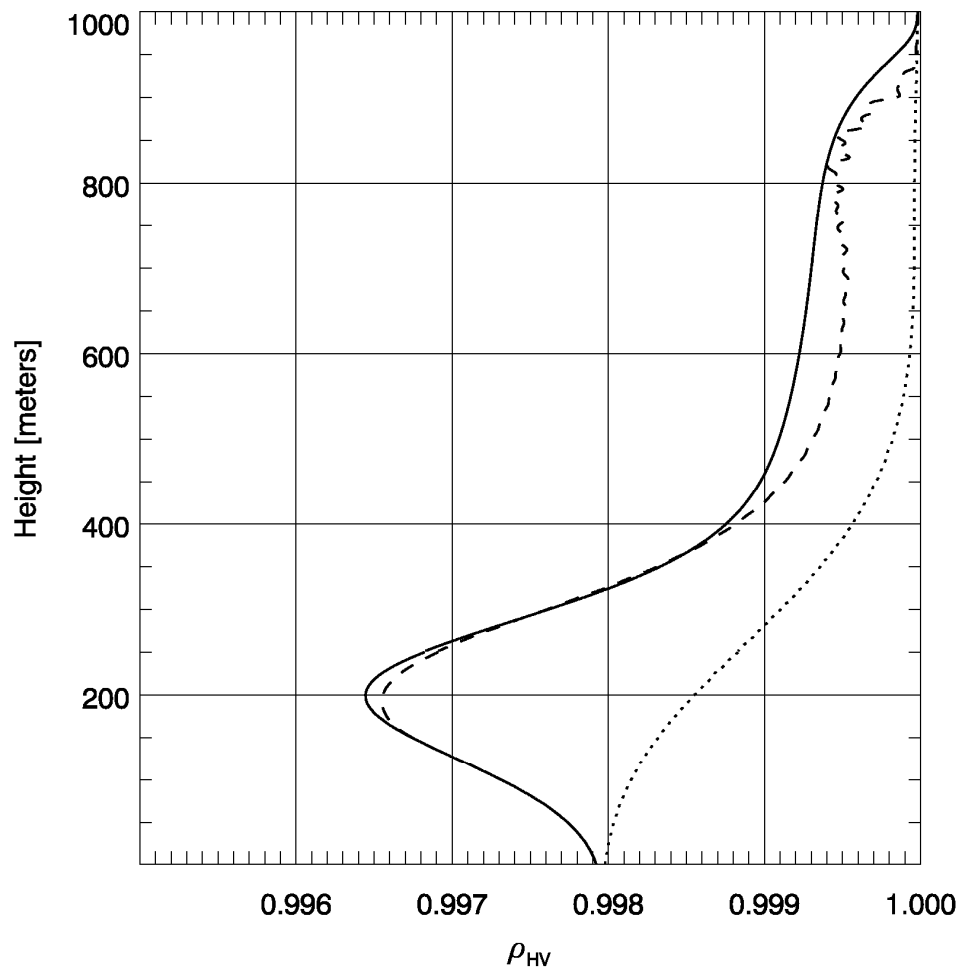


Fig. 59: As in Fig. 57, but for model profiles of ρ_{HV} through the melting layer.

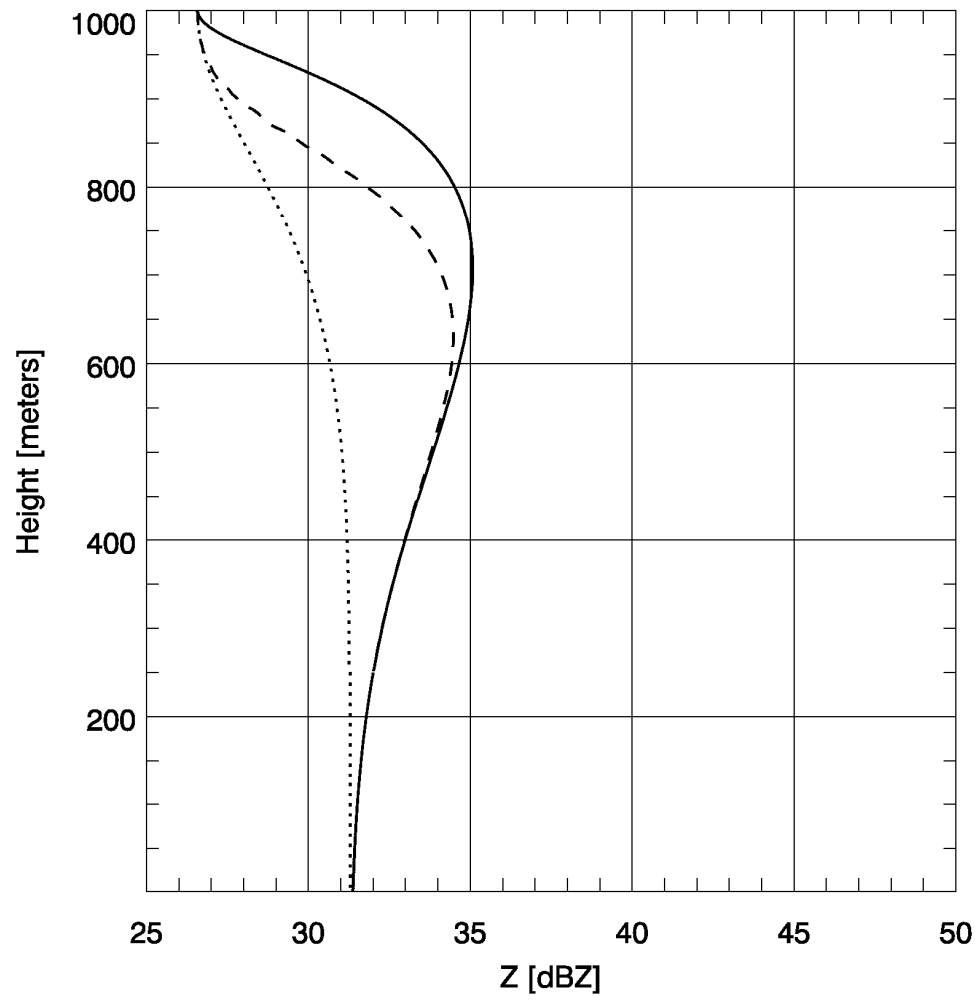


Fig. 60: As in Fig. 57, model profiles of Z_H for heavily rimed particles entering the melting layer.

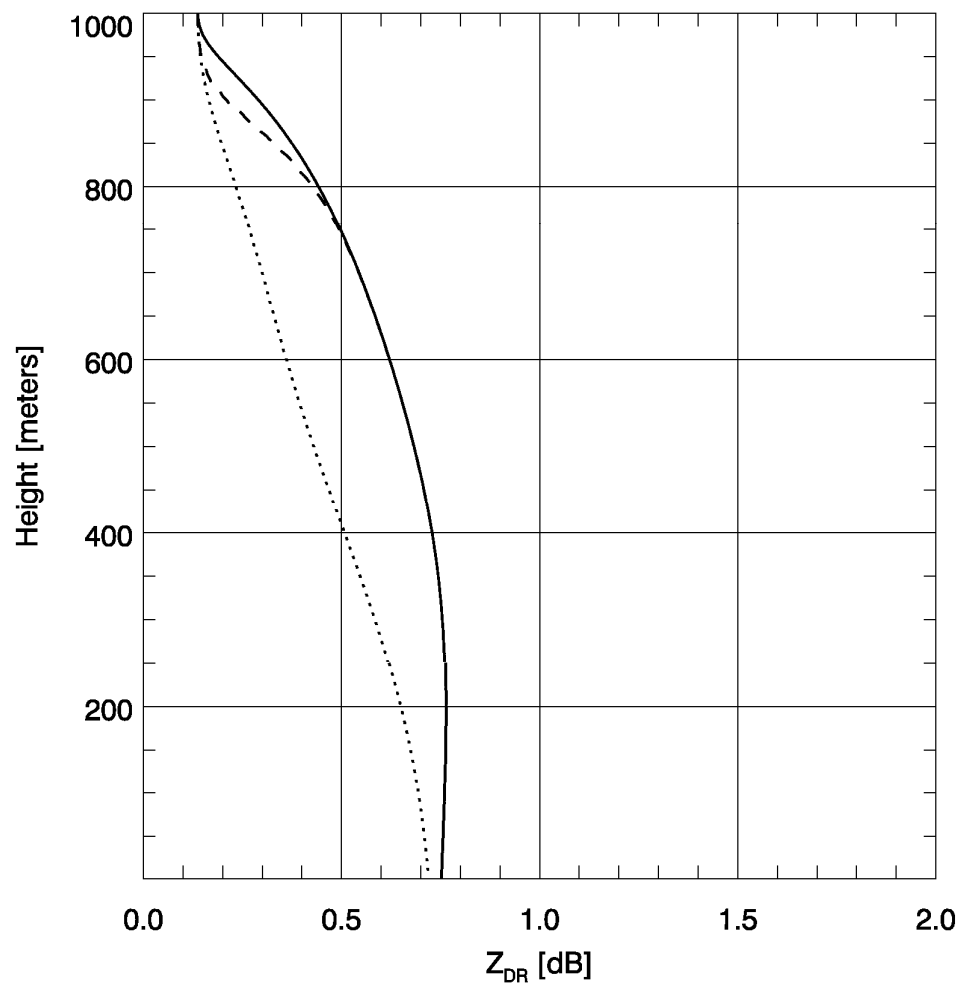


Fig. 61: As in Fig. 57, model profiles of Z_{DR} for heavily rimed particles entering the melting layer.

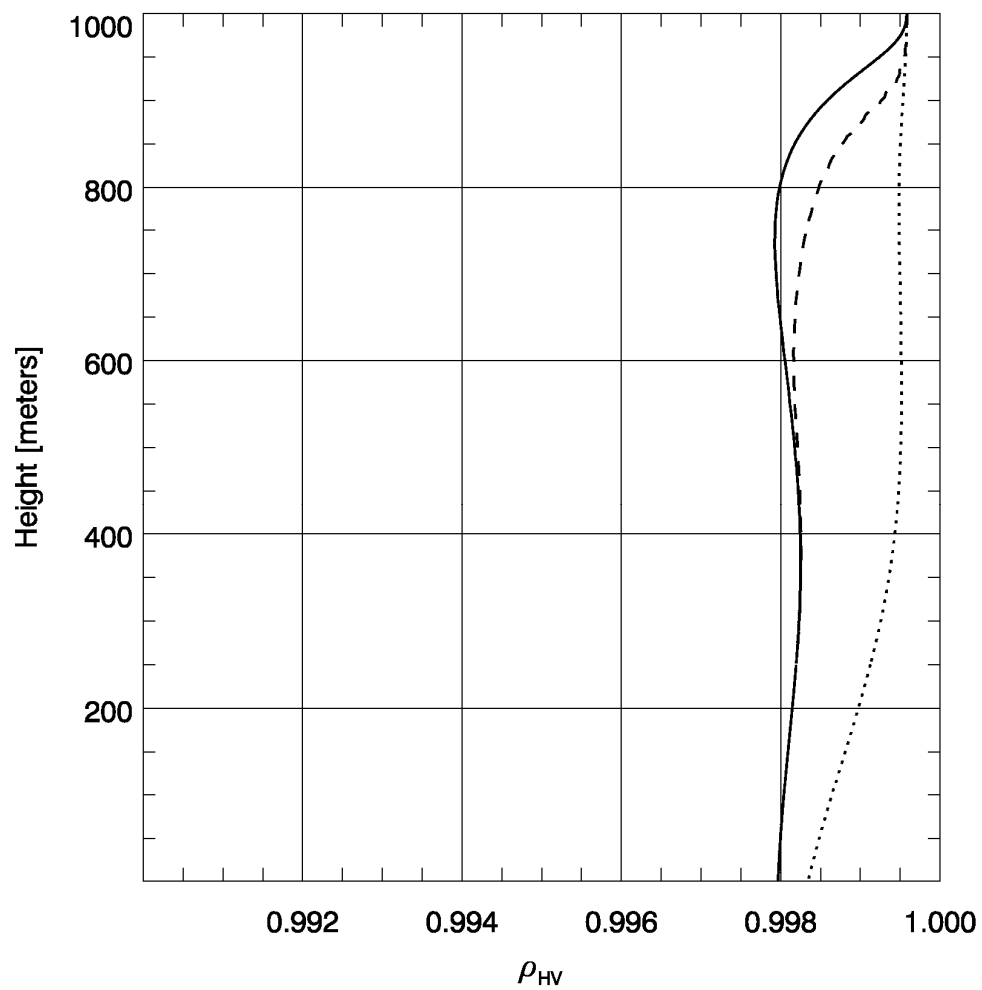


Fig. 62: As in Fig. 57, model profiles of ρ_{HV} for heavily rimed particles entering the melting layer.

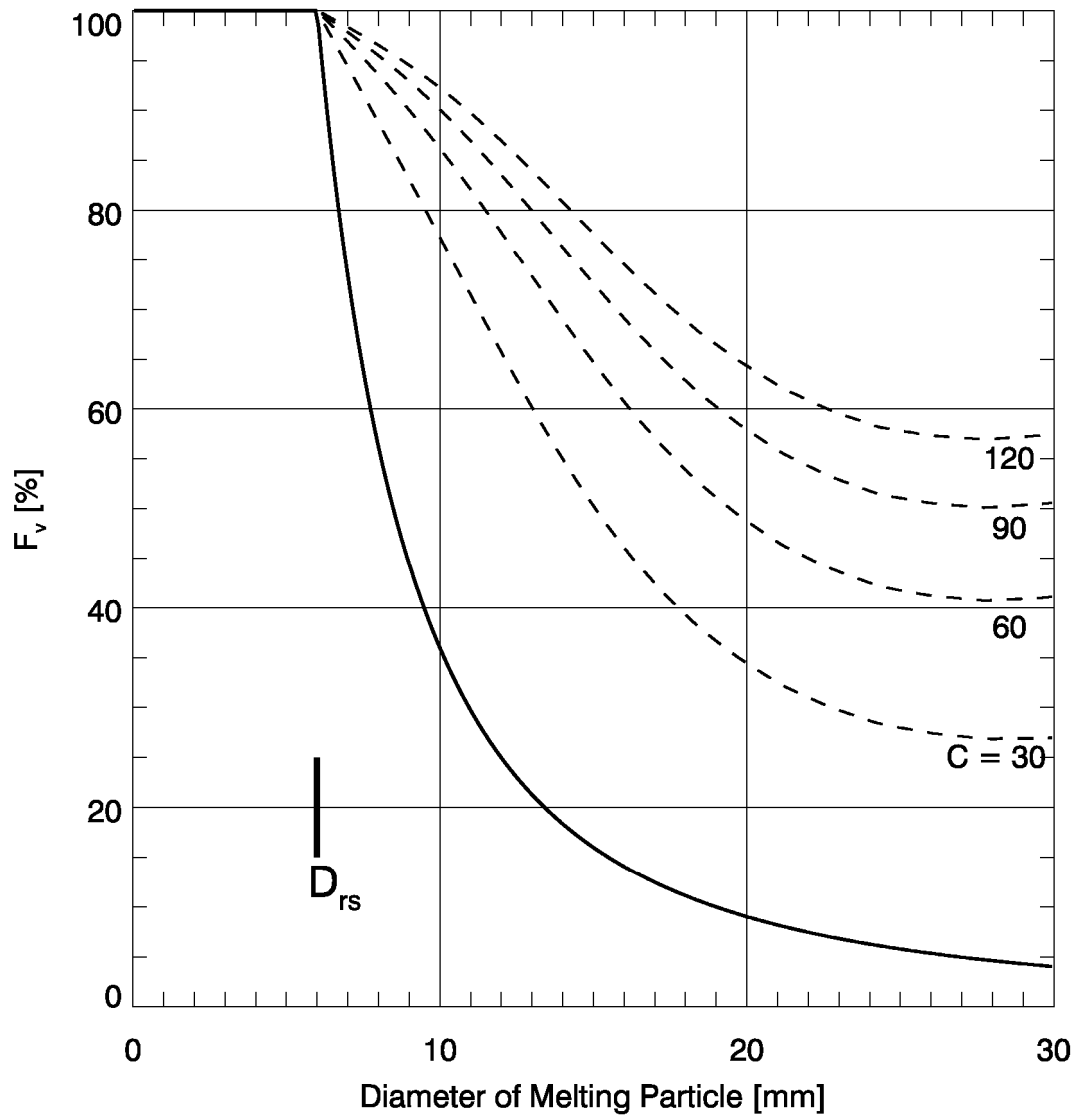


Fig. 63: Volume fraction of water dependence on melting particle diameter. The maximal size of raindrops D_{rs} is 6 mm. Solid curve is the dependence that matches well with the thermodynamic model in Eq. (90). Dashed lines are for increasing aggregation factors as in Eq. (107).

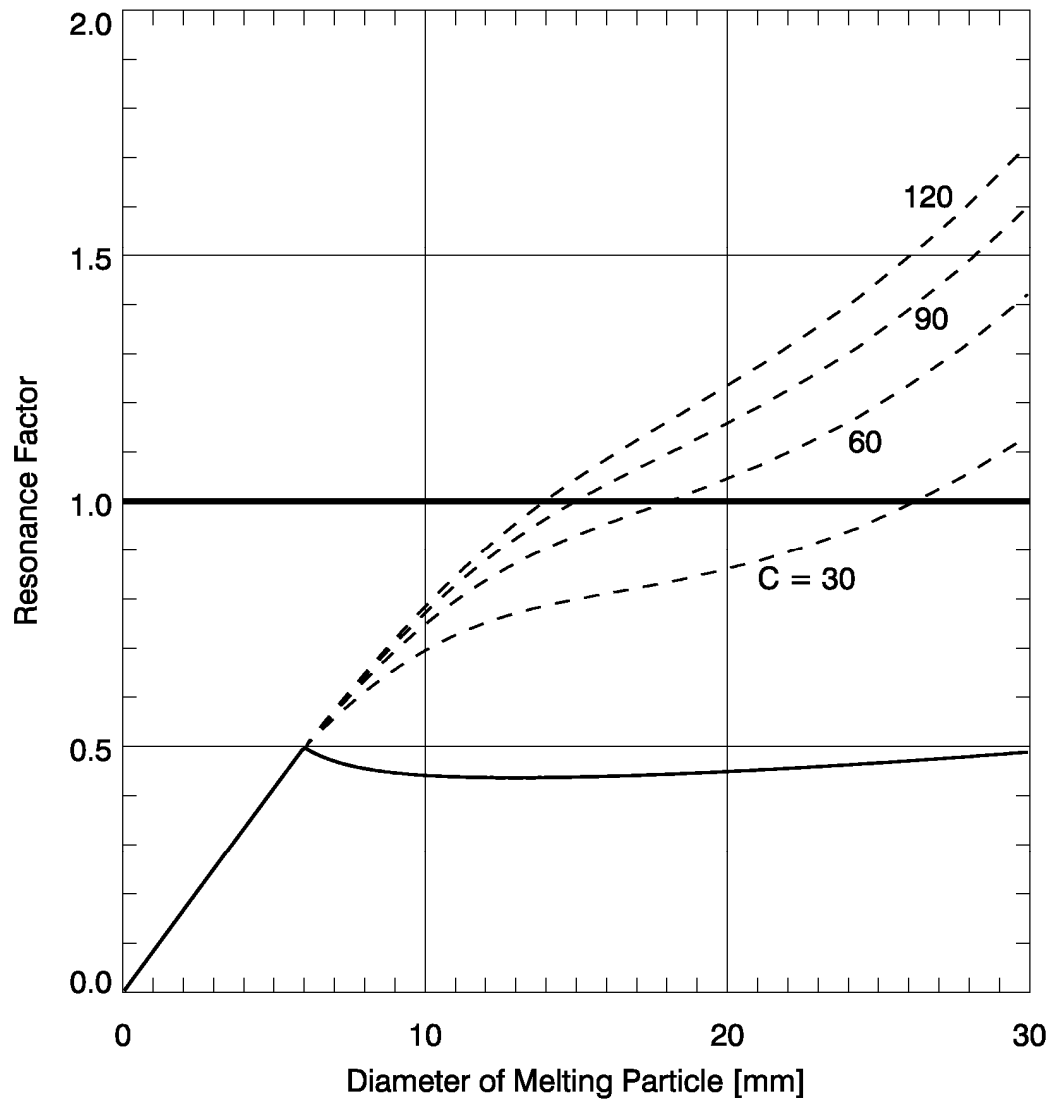


Fig. 64: Resonance factor $D_m |\epsilon_m|^{1/2} / \lambda$ dependence on melting particle diameter. Solid curve corresponds to dielectric constants determined using the output of the thermodynamic model without aggregation. Dashed lines are for increasing aggregation factors.

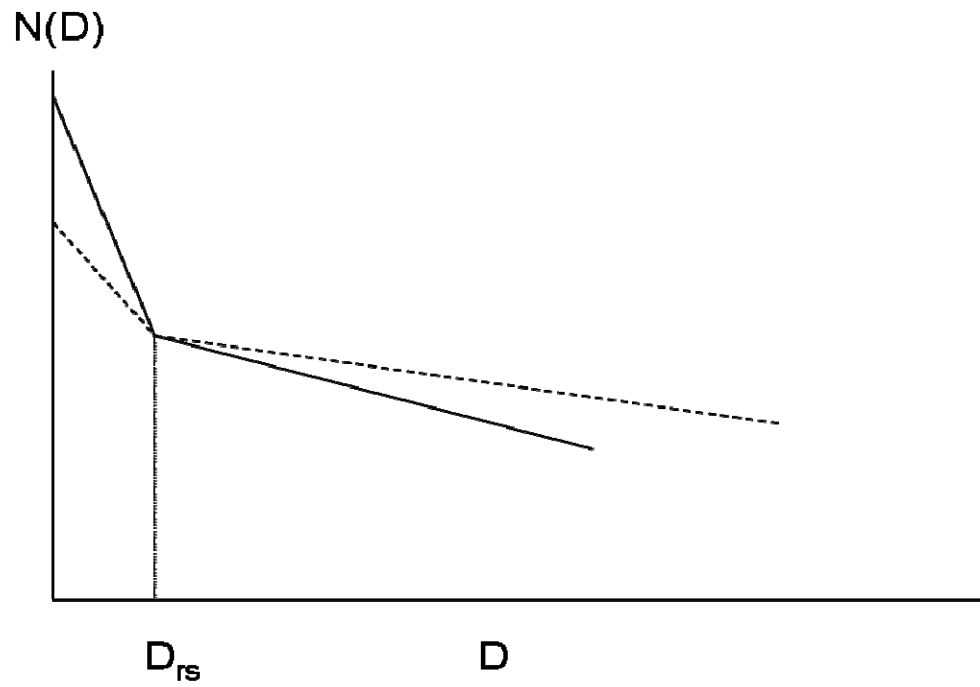


Fig. 65: Modification of the bi-exponential particle size distribution via aggregation.